Computer simulation of aggregation and gelation in colloidal suspensions

Mark D. Haw

A thesis submitted in fulfilment of the requirements

for the degree of Doctor of Philosophy

to the

University of Edinburgh

1996

Abstract

Aggregation and gelation in colloidal suspensions are studied by computer simulation using the diffusion-limited cluster aggregation (DLCA) model. By studying the structure of the aggregating system in detail using computational methods analogous to scattering experiments, direct comparison is made with recent scattering experiments on fast colloidal aggregation. The simple DLCA model is shown to reproduce many features observed in experiments, including the appearance of an intense scattering peak at small angle or large length-scale, which is shown to correspond with a density modulation in the aggregating system at the inter-cluster length scale. The calculated scattering function is examined in detail by studying the structure of individual aggregates, the arrangement of aggregates in the system, and the effect of aggregate size-position correlations. The scaling properties of the scattering function are examined and simulation results compared to experiments. More direct investigation of scaling in the system is carried out by comparing the time evolution of various length scales. The DLCA model is extended to allow thermal restructuring of aggregates. In this 'reversible' model the typical morphology of the system varies from a near-fluid-like state with no long-lived large aggregates, through a system of near-compact clusters, to a near-space-filling gel made from locally compact filaments which are ramified at longer length scales. The irreversible DLCA model is thus the strong-bonding limit of this more general model of particle aggregation.

Ackowledgements

In carrying out the work described in this thesis I have of course benefitted greatly from the advice and support of many people. Of particular help was the work on one of the simulation algorithms carried out by Malcolm Sievwright as part of an undergraduate project. I would like to thank my Supervisors, P. N. Pusey and W. C. K. Poon, for their guidance, teaching and encouragement, and for careful readings of drafts of the thesis, and Patrick Warren and John Earnshaw for helpful discussions.

Many thanks are due to the following: 'Ginger' Gus Pirie for discussions (one or two of them even scientific) and mild bigotry; 'Uncle' Steve Ilett for chemical insight, KB food-testing and reminiscences of Peterboro in the Golden Age; 'Big' Veronique Trappe for the Continental Outlook; 'Dynamic' Phil Segre for a delightful blend of scientific expertise and golfing stories; 'Euro' Oliver Behrend for pancakes and an inability to navigate through forest; 'Young' Steve Meeker for The Alternative Approach To The PhD; 'Manky' Marieta Soliva for her boundless enthusiasm; and 'I got Mum Pregnant too' Floyd Chui for Real Taiwanese Home Cooking. There are undoubtedly other important people I haven't mentioned, who will be insulted. But don't worry, I'm sure you're not half as insulted as those I have mentioned.

Finally of course I thank my Mum and Dad and family for support and financial donations to a good cause. This thesis is dedicated to my Grandmother, Mrs. F. Haw.

... conjectured it, as men of science
from certain derangements in their calculations
will conjecture the existence of a star
that no telescope has revealed.

Arnold Bennet
'The Pretty Lady'

Contents

Chapter 1

Introduction: Aggregation and gelation in colloids

Abstract

In this Chapter we introduce colloidal suspensions and the phenomena of aggregation and gelation in colloids. Typical methods in colloidal experiments are described, including the principles of scattering experiments. We briefly summarise the experimental literature dealing with colloidal aggregation. The concepts and analytical methods of fractal geometry are introduced and their relevance to aggregating colloidal systems discussed. Finally gelation, the filling of the macroscopic system by an assembly of ramified aggregates, is shown to be a natural consequence of fractal aggregation.

1.1 Colloidal suspensions

In this thesis we study particle aggregation in colloidal suspensions by computer simulation. There are many examples of colloidal suspensions in physics, chemistry, biology and industry, in many of which colloidal particles are subject to attractive interparticle interactions and form *aggregates*. The structure of such aggregates, the kinetics of

their growth, and the interactions between aggregates have been the subject of substantial study in physics, especially over the past few years. Here we study the structure and kinetics of particle aggregation via a simple simulation model, using methods of analysis by which direct comparisons with experiments may be made. The main initial motivation for this work comes from a number of experiments in which scattering methods have been used to study the structure of aggregating colloids. These experiments have been carried out in a wide range of colloidal systems demonstrating some striking 'universal' results which are not dependent on the details of the system.

We discuss key experiments in more detail below. First, to provide a background to the simulations, we briefly introduce colloidal suspensions and the main experimental methods used to study aggregation in colloids. Chapter 2 describes the simulation algorithm. In Chapters 3, 4 and 5 we describe our results in detail, and we summarise our findings and conclude in Chapter 6.

A colloidal suspension is a suspension of particles in a fluid. Usually the term 'colloidal' is restricted to particles with radii a in the range $10^{-9}m < a \leq 10^{-6}m$. The lower limit of this size range corresponds to the length scale below which quantum effects become important; theoretical treatments of colloidal suspensions generally exclude any consideration of quantum phenomena. The upper limit corresponds to the length scale above which particle motion in the suspension tends to be dominated by convective effects. In the colloidal size range then, the most dominant contribution to particle dynamics is *Brownian motion.* In a certain sense the study of colloidal systems is very much the study of Brownian motion.

1.1.1 Brownian motion

Brownian motion is a random, diffusive motion. A Brownian particle can be thought of as moving in a series of small 'steps' of random length and direction. This 'random' step-motion of the colloidal particle results from the large number of collisions between the (relatively large) particle and the molecules of the surrounding fluid. At any instant very large numbers of molecules collide with the particle from all directions. Any small

imbalance in the numbers of molecules coming from different directions will lead to a very small resultant impulse which drives the particle a very small 'step' in some direction. The continual fluctuation in the molecular motions and collisions means that the direction and strength of the resultant impulses on the particle vary continuously in an effectively random manner.

Thus Brownian motion can be modelled quite simply by a 'random walk'. The particle moves by a consecutive series of small steps in randomly chosen directions. The key result of such a motion is that the total resultant displacement over time of the particle increases not linearly[1] but with the square root of time; a particle starting at the origin at time $t = 0$ and moving one random walk step of length l per unit time, has a displacement from the origin s given by (on average)

$$s \sim l\sqrt{t}. \tag{1.1}$$

A random-walk trajectory 'explores' much more space than a linear trajectory (Figure 1.1). In other words in a random walk from point A to point B, a large region of the space between A and B is visited by the particle.

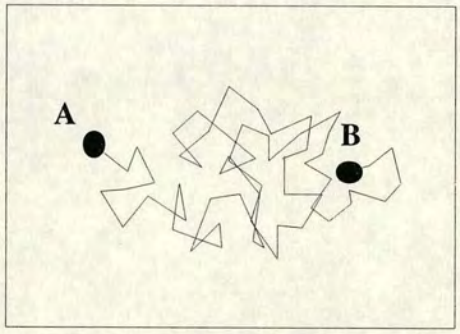

Figure 1.1. A particle travels between points A and B by Brownian motion. The random walk 'explores' substantially more space than would a linear trajectory.

[1] A particle moving along a *ballistic* trajectory (i.e. a straight line) with a constant speed v moves a distance $s = vt$ in time t.

1.1.2 Real and 'model' colloidal suspensions

Colloidal particles can be many different shapes, from spheres to thin rods, to ovoids, to flattened discs, to completely irregular particles. The particles in a suspension may also be many different sizes. The particles may interact with each other in various ways, these interactions also being dependent on the solvent medium. The whole suspension may be subject to macroscopic stresses and shears, as well as to particle concentration or temperature gradients. The system may be subject to external fields such as gravitational or magnetic fields. Thus the range of conditions under which colloidal suspensions appear is wide, and many variables can be involved in determining the behaviour of a given colloidal system.

Colloids are important in industry and technology. Many natural substances occur in colloidal form, especially biological substances such as foods (e.g. milk, chocolate [1]) and animal products (e.g. blood). Paints and inks are examples of important industrial colloids. Natural and industrial colloids can be very complex systems, and development of technologies often proceeds by trial and error rather than through a clear understanding of the complex physics and chemistry of the particular colloidal system.

Current theoretical models of colloidal suspensions generally involve simple model systems. More complicated models rapidly become mathematically intractable. Computer simulations are of substantial use, because they allow direct control of the complexity of a system as well as offering the possibility of making direct measurements of quantities which are important to theoretical models but sometimes difficult to measure experimentally. However it is desirable that some kind of similar 'model' colloidal system can be studied experimentally, so that theory and simulation can keep in touch with real phenomena. This sort of experimental model system has been approached quite closely over the past two decades, with the introduction of methods of chemically synthesising regularly-shaped and regularly-sized colloidal particles with well-defined interactions, whose behaviour is also stable over a long period of time (see below).

From the point of view of basic physics, a particularly attractive possibility is that the

study of simple model colloidal systems may lead to a better understanding of 'particle' phenomena on the much smaller *atomic* length scale; this is sometimes known as the 'colloid-atom analogy'. Because colloidal particles are orders of magnitude larger than atoms, phenomena such as phase transitions (crystallization, phase separation, etc.) generally occur on time scales orders of magnitude *longer* in colloids compared to atomic systems. If one could study a colloidal system which was sufficiently simple that the analogy with atomic systems was reasonable, one could then make observations and carry out experiments which in atomic systems would be very difficult or impossible. For instance, the kinetics of crystallization in colloidal systems can be studied quite easily (the time scale for crystallization might typically be minutes to hours) [2, 3] whereas in atomic systems (e.g. the crystallization of a metal) the process is so fast that experiments are very difficult to carry out.

1.1.3 The hard sphere

A simple theoretical system for which some approximate results can be obtained analytically is the *hard sphere* model. In this model, colloidal particles behave like billiard balls; they do not interact with each other except to 'bounce' rigidly apart on collision.

An experimental system similar to the theoretical hard sphere system would be of great use in validating the most basic ideas behind current theories of colloidal suspensions. Over recent years methods of particle synthesis (e.g. emulsion polymerisation) have been developed which can provide well-characterised systems of (nearly) monodisperse (single size) spherical particles [4] with a size polydispersity as low as 1%-5%. Methods of stabilisation of such particles, to counteract the strong attractive van der Waals forces which otherwise would lead to irreversible aggregation of the suspension, have also been developed, so that good experimental approximations to the hard sphere are now available.

1.1.4 Stabilisation

Strong attractive van der Waals forces between colloidal particles arise from the addition of the fluctuating molecular dipole-induced dipole interactions within each particle [5], which lead to an irreversible fast aggregation of the particles in the suspension. In order to study aggregation under more controlled (and reversible) conditions, there are various methods by which the suspension may be stabilised against the Van der Waals forces.

A common method is *charge* stabilisation. A colloidal particle may have ionisable surface groups which, when the colloid is dispersed in a polar solvent (e.g. water), will dissociate from the surface, feeding ions into the solution. The dissociation of ions from the particle surface leaves the particle with a net surface charge. Such *charged* colloidal particles thus interact through Coulomb (electrostatic) forces. Because all the particles have the same sign charge, their 'bare' interaction would be repulsive and, in principle, long-ranged. However, the ions dissociated into the solvent, while diffusing away by Brownian motion, tend to form a surrounding 'diffuse layer' of charge opposite in sign to the particle surface charge. Ions already present in solution may mix with this layer. The effect of the diffuse charge layer is to *screen* the intrinsically long-ranged and repulsive electrostatic interparticle potential. The net interaction between the double-layer enclosed particles is still repulsive, but its range depends upon the solvent conditions. The electrostatic repulsive forces stabilise the particle suspension against the van der Waals forces, as long as the range of the double-layer repulsive potential is larger than the range of the van der Waals attraction and the repulsion is strong enough (the probability of a particle having enough kinetic energy to overcome the repulsion is low). The degree of screening—the magnitude of the resultant repulsive force between particles and the range of the interaction—may be varied experimentally by changing the salt content of the solvent, a method which is sometimes used to induce and control aggregation behaviour (see for example [6, 7]).

A second method is *steric* stabilisation. Here, polymer chains are anchored onto the surface of the colloidal particle forming a polymer shell which acts as a 'cushion', keeping

particles apart. When two particles' polymer-chain 'shells' approach, their interaction depends upon the solvent conditions. The structure of a polymer chain in a solvent is determined by the interaction between the monomers of the polymer chain and the solvent [8]. In a 'good' solvent the chains are 'swollen', that is parts of the chain tend to avoid each other (entropically or energetically the monomers in the polymer 'prefer' to be surrounded by solvent rather than other monomers); in this case entanglement of two separate chains is very unfavoured. Thus when the colloidal particles approach each other their polymer chain coatings give rise to a strong repulsion and the particles are forced apart again. Typically, for a short-chain stabilising polymer, the effective interparticle potential of such a system is short-ranged and very steeply repulsive (the repulsion of the polymer chains grows very fast over a very small distance), so that the interaction of sterically-stabilised particles can be a good experimental approximation to the hard sphere model.

In a 'bad' solvent the polymer chain coatings of the particles collapse to a more compact structure (monomers 'prefer' to be near other monomers rather than solvent molecules), and entanglement or close approach of chains connected to neighbour particles is no longer strongly disfavoured. The colloidal particles feel no repulsion when they approach each other closely, and may come within range of the van der Waals attraction[2]. Therefore changing the solvent quality (with respect to the grafted polymer chains) can be a useful method of inducing aggregation in sterically-stabilised colloids (e.g. [9, 10]). A change of solvent quality is often achieved by changing temperature.

1.1.5 Aggregation in colloids

In many colloidal systems attractive interparticle forces lead to *aggregation*. Many naturally occurring colloidal systems, such as foodstuffs (e.g. cottage cheese) [1], are subject to aggregation phenomena; particles are attracted to each other and tend to form clumps or clusters. It is often a major problem of manufacturing or processing

[2]Monomers in the coating polymers of *different* particles will also tend to 'prefer' to be near monomers of other chains as well as their own, giving rise to an additional effective attraction between the particles.

industries to *stop* aggregation, that is to keep a colloidal suspension stable. Conversely aggregation in some products is an important and desirable process which gives the system its textures, rheological properties, etc. Therefore from a technological point of view it is clearly important, whether we want to start aggregation or stop it, to understand what is happening in the colloidal system during the aggregation process.

Aggregation in colloids is also interesting from a basic physics perspective. There are clear similarities between the behaviour of an aggregating system of particles and the behaviour of systems undergoing first-order phase transitions such as phase separation in fluids or alloys. These similarities have become particularly evident from computer simulation work, where the structure of systems can be viewed directly, and clear qualitative similarities between structures from widely varying models are found.

Various experimental methods may be employed to induce and study aggregation behaviour in colloidal systems. Reduction of the range of electric double-layer screening in charged colloids and changing solvent quality in sterically-stabilised colloids have already been mentioned. Another common method is to create a 'depletion interaction' between colloidal particles. This may be done, for example, by adding non-adsorbing polymer to a stable colloidal suspension (e.g. a 'hard sphere' sterically-stabilised colloid [11, 12, 13]). The free polymer chains in the solvent exert an osmotic pressure on the colloidal particles. A free colloidal particle feels no *net* force due to the surrounding polymer (assuming fluctuations in polymer chain density average out on the scale of the particle). However, consider what happens if two particles approach each other closely (Figure 1.2). If the particles happen to come less than a certain distance apart ($\sim$ the radius of gyration of the polymer chain) then polymer chains are effectively excluded or *depleted* from the region between the particles. Then the forces exerted on the outer surfaces of the particles by the polymer are greater than the forces exerted in the depleted region between the two particles. This results in a *net* force tending to push the two particles together. If the force is strong enough (which depends on the polymer pressure, and therefore the concentration of polymer in the system) long-lived 'bonds' between particles can result.

The colloid-polymer system has been studied quite extensively both theoretically [14,

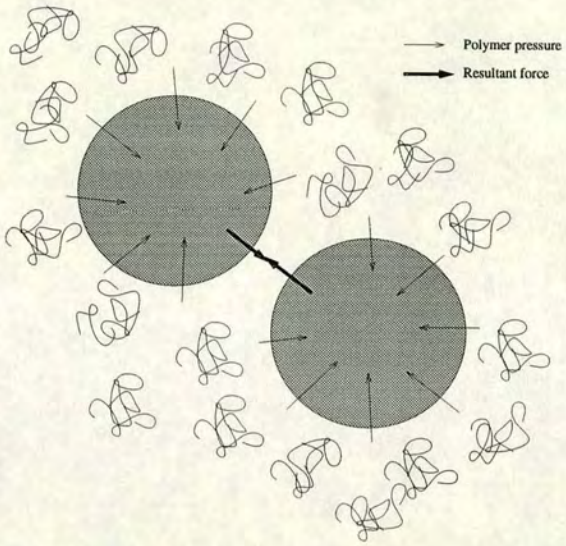

Figure 1.2. Depletion-induced attractive force between nearby colloidal particles in a colloid-polymer mixture.

15] and experimentally [11, 12, 16]. The effective interparticle potential range and depth are easily varied by changing respectively the ratio of the size of the colloidal particle to the size (radius of gyration) of the polymer, and the concentration of free polymer in the system. The potential is purely attractive and typical experiments [11, 16] have involved potentials of 'depths' of a few k_BT (the average thermal kinetic energy of the particles). Thus the colloid-polymer mixture is a good candidate for the study of 'weak' and reversible aggregation in colloids (Chapter 4).

The depletion interaction model has also been applied to the binary colloidal suspension, that is a suspension of colloidal particles of *two sizes*. The smaller particles play a similar role to that of the free polymer chains in the colloid-polymer mixture; again small particles are excluded from regions between the larger particles when the large particles approach each other; a net force driving the large particles together is exerted by the small particles. Actually the phase behaviour of such binary mixtures of colloidal particles is extremely rich [17]; the aggregation behaviour is only one small element of the binary suspension problem. Studies of this kind of system have been reported recently by Dinsmore and co-workers [18] and by Imhof and Dhont [19].

1.2 The structure of a colloidal suspension

A common quantitative measure of structure in the colloidal suspension is the *pair correlation function* or pair distribution function, denoted $g(\mathbf{r})$. This quantity appears frequently in theoretical models, and is also accessible in experiment via direct observation or (indirectly) via scattering techniques (see section 1.3). It may be taken as a basic measure of the structure of a suspension.

Given a particle at some origin, $g(\mathbf{r})$ is proportional to the probability that there is a particle at position vector $\mathbf{r}$ measured from the origin. The pair correlation function therefore meaures spatial correlations in particle positions. In a crystal structure where particle positions are highly correlated, $g(\mathbf{r})$ is high for certain lattice vectors $\{\mathbf{r}\}$ which define the crystal structure. In a colloidal fluid (a disordered structure) $g(\mathbf{r})$ typically shows weak short-range oscillations which decay at longer range, indicating that the fluid has some short-range correlation but that the positions of particles at large separation are not correlated. Interparticle correlations increase as the concentration of a system or as the interaction strengths or ranges increase. For example the simple hard sphere model system shows a transition from a disordered fluid structure to a highly-ordered crystal in a narrow concentration (volume fraction) range near 50%.

In isotropic, homogeneous disordered systems (e.g. colloidal fluids) the pair correlation function is a function of distance r ($r = |\mathbf{r}|$). $g(r)$ is then defined through

$$g(r)\rho dV = n(r, dV) \tag{1.2}$$

where $n(r, dV)$ is the number of particles in the volume element dV at distance r from the particle at the 'origin', and ρ is the average number density of the system. Thus dr is the width of the circular (two dimensions, 2D) or spherical (three dimensions, 3D) shell of volume dV. ($dV = 2\pi r dr$ in 2D, $4\pi r^2 dr$ in 3D.) In practice when measuring g(r) directly one computes a spatial average of $g(r)$ by taking each particle in turn as the 'origin' and counting the number of other particles in the circular or spherical shells dV at distances r. For a *disordered* system $g(r)$ fluctuates about the value 1.0, because the density of particles in the shells fluctuates about the average system density ρ;

the system is homogeneous on length scales beyond the range of the weak short-range correlations.

The $g(r)$ function is of prime interest in experiment and theory, since it describes the structure of the colloidal system. Sometimes, for instance when it is possible to use microscopy to directly observe particles in a suspension [20] (which usually can only be done with large particles and at low particle concentrations), $g(r)$ can be directly computed. However, more often the experimentalist obtains information about $g(r)$ and structure in the system using *scattering methods*. The basis of the measurement of structure by scattering is discussed in the next section. Thereafter the connection between scattering and the $g(r)$ function is demonstrated.

1.3 Scattering

Scattering is perhaps the most common experimental method used to investigate the structure of colloidal suspensions. An excellent and very thorough introduction to the theory of scattering is given by Kerker [21]. In this short discussion we will consider specifically the scattering of visible light, though the general principles of scattering methods apply to any electromagnetic radiation. In addition to light-scattering, the scattering of X-rays is also often used in experiments. However because of the typical size-range of colloidal particles (in relation to the wavelength of the scattering radiation), light-scattering is probably the most common method of studying structure in colloid physics. For example, the crystal lattice parameters in typical 'hard-sphere' colloidal crystals are of such a dimension that the crystal planes' Bragg scattering peaks fall in the visible wavelength range, giving colloidal crystals their striking colours and iridescence [22, 23].

1.3.1 Scattering from a single large particle

In what follows we shall make certain assumptions about the scattering conditions, under which the analysis of scattering data is considerably simplified. We assume

first that the colloidal particles are large relative to the wavelength of the light but that the refractive index difference or *scattering contrast* (between the particle and the surrounding solvent) is small. Thus the following condition, usually known as the *Rayleigh-Debye* (or Rayleigh-Gans-Debye) condition, is satisfied:

$$2ka(m-1) << 1, \tag{1.3}$$

where $k = 2\pi/\lambda$ is the propagation constant for the incident radiation of wavelength λ, a is the radius of the colloidal particle, and m is the relative refractive index or scattering contrast, equal to the ratio of the refractive index of the particle to the refractive index of the surrounding fluid. The physical relevance of this condition is discussed below.

A further assumption we make is that the scattering particle is constructed from a non-absorbing dielectric material. Mathematically this means that the relative refractive index m is a real quantity. For scattering by conductors (or absorbing dielectrics) the theory becomes substantially more complex [21], but it is often the case that experimental (model) colloidal suspensions involve dielectric particles. (Note, however, that some experiments have been carried out with conducting colloidal gold particles [24, 25, 26].)

Now consider light incident upon a 'large' particle of arbitrary shape (Figure 1.3). We imagine the particle divided up into small volume elements each of which scatters incident light. The physical meaning of the Rayleigh-Debye condition (1.3) is that light incident at any of the elemental volumes is not affected by the presence of the rest of the particle—this is why we require $m \approx 1$. Thus each volume scatters the 'same' incident light. (The equivalent condition in quantum phenomena is usually termed the first Born approximation or the *single scattering* approximation.) Each elemental volume acts as a *Rayleigh scatterer*, that is a small (compared to λ) scattering volume which scatters *isotropically* according to Rayleigh theory [21]. The total scattered field from the set of elemental volumes at some distant point O (Figure 1.3) is equal to the sum of the electric fields scattered from each elemental scattering volume. In other words, under Rayleigh-Debye conditions, the scattering at some angle from a large particle is

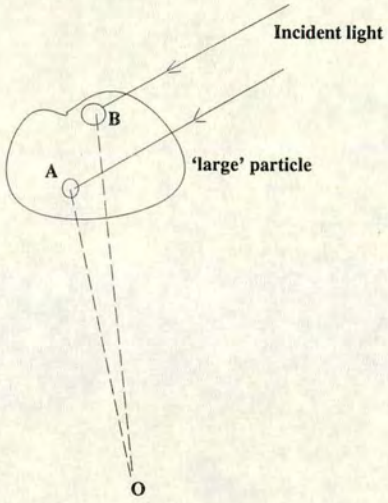

Figure 1.3. The scattering from a 'large' particle under the Rayleigh-Debye condition. The relative refractive index is small so that the incident wave is the same throughout the particle (single scattering approximation); the particle is large so that it can be considered a set of small volumes, each of which scatters like a small Rayleigh scatterer. Scattered fields from A and B interfere at (distant) observation point O.

given by the interference of fields scattered from all parts of the particle. The wave (electric field) scattered by point A may be written as

$$E_A = K exp(i\delta_A) \tag{1.4}$$

where K is the (Rayleigh scattering) amplitude of the scattered wave (which depends on the relative refractive index and the incident wavelength) and δ_A is the phase of the wave scattered from A (relative to some 'reference' phase, for instance the phase of the incident wave). δ_A is determined only by the position (relative to some origin) of the elemental volume at A. The total scattered field at O is therefore the sum of terms as in equation (1.4) scattered from all elemental volumes making up the particle:

$$E_O = K \int_V exp(i\delta_{dV_i}) dV \tag{1.5}$$

where δ_{dV_i} is the phase of the wave scattered from volume element dV_i. The scattered intensity is given by the square modulus of the field.

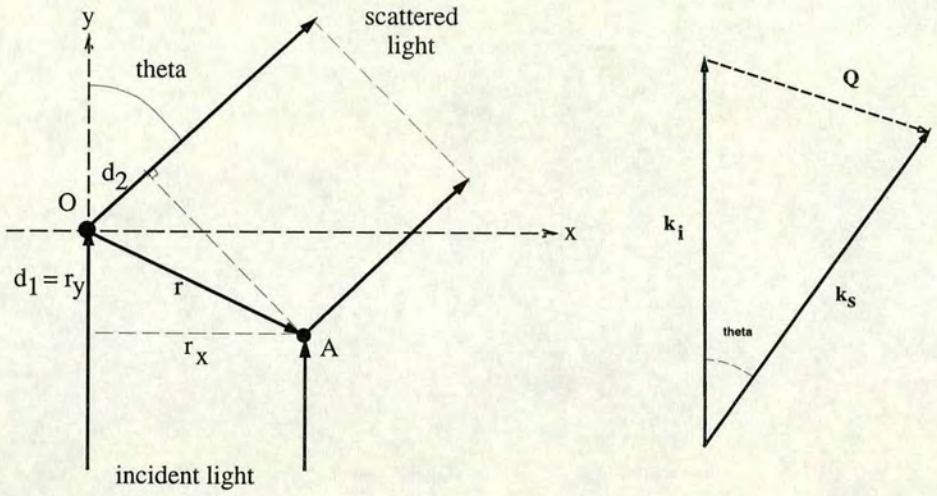

Figure 1.4. The interference of two waves scattered at angle θ by two points O and A, at relative position vector $\mathbf{r}$. For simplicity the problem is illustrated in two dimensions, and the y-axis is set parallel to the incident direction. The total 'extra' distance travelled by the wave scattered at O is $d_1 + d_2$. On the right we show the geometry of the incident and scattered waves $\mathbf{k_i}$ and $\mathbf{k_s}$ and the scattering vector $\mathbf{Q}$.

The problem now is to determine the relative phases $\{\delta_{dV}\}$. For simplicity we consider a 2D geometry, though the result is identical in three dimensions. The relative phases of the waves scattered from different points may be derived in terms of the relative positions of the scatterers and the scattering angle θ as in Figure 1.4. Incident light is scattered at points O and A. The total 'extra' distance travelled by the wave scattered at O is

$$D = d_1 + d_2 = r_y + d_2.$$

Some trigonometry shows that d_2 is given by

$$d_2 = r_x sin\theta - r_y cos\theta$$

so that the total phase difference of the two scattered waves, $\delta = 2\pi D/\lambda$, is :

$$\delta = \frac{2\pi}{\lambda}[r_y(1 - cos\theta) + r_x sin\theta]. \tag{1.6}$$

Equation (1.6) thus relates the phase difference to the components of the relative

position vector $\mathbf{r}$ and to the scattering angle θ. The phase difference of the waves scattered from points O and A may further be written in terms of a *scattering vector* $\mathbf{Q}$ as follows. Define $\mathbf{Q}$ such that δ is given by the dot product of the scattering vector and the relative position $\mathbf{r}$:

$$\delta = \mathbf{Q} \,.\, \mathbf{r} \,. \tag{1.7}$$

Equating (1.6) and (1.7), $\mathbf{Q}$ has components (in this geometry)

$$Q_x = \frac{2\pi}{\lambda} sin\theta \tag{1.8}$$

and

$$Q_y = \frac{2\pi}{\lambda}(1 - cos\theta). \tag{1.9}$$

Finally from (1.8) and (1.9) the magnitude of $\mathbf{Q}$ is given by

$$Q = \frac{4\pi}{\lambda} sin(\theta/2). \tag{1.10}$$

(Equation (1.10) uses the trigonometric identity $cos\theta = cos(2 \times (\theta/2)) = 1 - 2sin^2\theta/2$.)

Equation (1.5) for the total field scattered by the particle may now be written in terms of the scattering vector and an integration over the positions (relative to some origin) of all the 'elemental volumes' making up the particle:

$$E = K \int_V exp(i\mathbf{Q}.\mathbf{r}) \;\; d^3r. \tag{1.11}$$

As written, Equation (1.11) assumes that the large particle is internally homogeneous—all the elemental volumes have the same relative refractive index or scattering contrast. The relative refractive index m is then absorbed into the constant K. Alternatively we can write

$$E = K' \int_V (m(\mathbf{r}) - 1) exp(i\mathbf{Q}.\mathbf{r}) \;\; d^3r \tag{1.12}$$

if instead the relative refractive index m is a function of position, $m = m(\mathbf{r})$.

1.3.2 Scattering by a suspension of particles

We now employ the same principle as above, that the total scattered field is given by the interference sum of fields scattered from different parts of the scattering volume, to obtain the scattering from a *system* of particles (e.g. a suspension of colloidal particles). Consider a scattering volume consisting of a system of particles whose centres of mass are at a set of coordinates $\{\mathbf{r}\}$. Electromagnetic radiation scatters from each particle at some angle θ and is detected at a distant point P (the point should be distant so that the scattering angle θ to the point from each part of the sample is approximately the same—this is usually called 'far-field' or Fraunhofer scattering). Now the amplitudes of the scattered waves from each particle will add coherently in exactly the same way as the scattering from different elemental volumes in a single particle. (We still require that each particle scatters the same (previously unscattered) incident field, in other words that particles do not re-scatter waves already scattered by other particles. Such *multiple scattering* can become a serious problem in experiments at high particle concentration.) The scattered waves have a set of phase differences determined by the *relative positions of the particles* in the suspension. Thus a scattering measurement provides information on the *interparticle structure* of the system of particles.

Using the relation given above for the phases of the scattered waves, we can write for the instantaneous total field scattered by a system of N particles at a given angle θ

$$E(\mathbf{Q}) = \sum_{j=1}^{N} b_j(\mathbf{Q}) exp(i\mathbf{Q}.\mathbf{r}_j), \tag{1.13}$$

where $\mathbf{Q}$ is the scattering vector as defined above, with magnitude $Q = \frac{4\pi}{\lambda} sin(\theta/2)$, the $\mathbf{r}_j$ are the particle (centre of mass) coordinates, and $b_j(\mathbf{Q})$ is the scattering amplitude of the particle j. Each $b_j(\mathbf{Q})$ is given by equation (1.11) or (1.12). In general the particles may be different shapes and sizes and have different density distributions (relative refractive index functions $m(\mathbf{r})$) so that the $b_j(\mathbf{Q})$ may be quite different. The instantaneous total scattered intensity is given by the square modulus of the electric field:

$$I(\mathbf{Q},t)) = |E(\mathbf{Q},t)|^2. \tag{1.14}$$

In typical experiments (for instance involving disordered systems or 'powder' polycrystalline colloidal crystals) the *measured* intensity as a function of scattering vector magnitude Q or scattering angle is an average (an *ensemble* average in polycrystalline systems, a *time* average in disordered systems):

$$< I(\mathbf{Q}) >=< \sum_{j=1}^{N}\sum_{k=1}^{N} b_j(\mathbf{Q})b_k(\mathbf{Q})exp[i\mathbf{Q}.(\mathbf{r}_j - \mathbf{r}_k)] > . \tag{1.15}$$

This averaging is simply a consequence (in disordered systems) of the finite time over which a single measurement of intensity is taken, or (in polycrystalline systems) of the random distribution of crystallite orientations.

If, as is often assumed for model colloidal suspensions [2], the particles are the same shape and size, and are furthermore isotropic so that $b_j(\mathbf{Q}) = b_j(Q)$, then all particles have the same scattering function $b_j(Q) \equiv b(Q)$. In this case the amplitude term can be removed from the summation:

$$< I(\mathbf{Q}) >= N|b(Q)|^2 \sum_{j=1}^{N}\sum_{k=1}^{N} < exp[i\mathbf{Q}.(\mathbf{r}_j - \mathbf{r}_k)] >, \tag{1.16}$$

and the scattering function can be written

$$I(\mathbf{Q}) = NP(Q)S(\mathbf{Q}). \tag{1.17}$$

Equation (1.17) represents a *separation* of the scattered intensity into two components, the so-called *form factor* $P(Q)$ and *structure factor* $S(\mathbf{Q})$. The form factor describes the scattering by an individual particle, the structure factor describes the interparticle structure of the system of particles. This separation of scattering is frequently used in the study of model colloidal systems where the particles are reasonably monodisperse and identically-shaped [2]. In such an experiment one can measure the form factor by measuring the scattering from a very dilute suspension in which interparticle structure is negligible ($S(\mathbf{Q}) = 1$)[3]. Then measurement of the total scattered intensity $I(\mathbf{Q})$ and

[3]For a system where the particle positions are completely uncorrelated, the sum of random cosine and sine terms in the exponential in equation (1.16) evaluates to zero except for the 'self term' $j = k$, so that the sum simply gives the number of particles; equation (1.17) then implies $S(\mathbf{Q}) = 1$.

division by $P(Q)$ leads to (within a multiplicative constant) the interparticle structure factor $S(\mathbf{Q})$.

1.3.3 Pair correlation and scattering

We show now how the structure factor $S(\mathbf{Q})$ is related to the particle pair correlation function, which in turn directly describes the structure of the system. According to equation (1.16) the structure factor of a system of N particles in a volume V is given by

$$S(\mathbf{Q}) = \frac{1}{N} \sum_{j=1}^{N} \sum_{k=1}^{N} < exp[i\mathbf{Q}.(\mathbf{r}_j - \mathbf{r}_k)] > . \tag{1.18}$$

Extracting the 'self term' $j = k$ we obtain

$$S(\mathbf{Q}) = 1 + \frac{1}{N} \sum_{j=1}^{N} \sum_{k \neq j}^{N} < exp[i\mathbf{Q}.(\mathbf{r}_j - \mathbf{r}_k)] > . \tag{1.19}$$

Now the summation term can be written in terms of the pair correlation function $g(\mathbf{r}_1, \mathbf{r}_2)$ by converting to an integral over all pairs of positions $\mathbf{r}_1$ and $\mathbf{r}_2$ (since $g(r)$ essentially 'counts' how many pairs of particles per unit volume there are at separation $r = |\mathbf{r}_1 - \mathbf{r}_2|$) :

$$S(\mathbf{Q}) = 1 + \frac{1}{N} \frac{N(N-1)}{V^2} \int d^3\mathbf{r}_1 \int d^3\mathbf{r}_2 \; g(\mathbf{r}_1, \mathbf{r}_2) \; exp[i\mathbf{Q}.(\mathbf{r}_1 - \mathbf{r}_2)]. \tag{1.20}$$

(The number of particles in volume element $d^3\mathbf{r}_1$ at $\mathbf{r}_1$ is $Nd^3\mathbf{r}_1/V$; the number in volume element $d^3\mathbf{r}_2$ at $\mathbf{r}_2$ *given that there is a particle at* $\mathbf{r}_1$ is $(N-1)d^3\mathbf{r}_2/V$.) For large N, $N - 1 \simeq N$. Further, by assuming that the pair correlation function $g(\mathbf{r}_1, \mathbf{r}_2)$ depends only on the difference $\mathbf{r}_{12} = \mathbf{r}_1 - \mathbf{r}_2$, the integral over $\mathbf{r}_1$ may be evaluated to give a term equal to the total system volume V. Lastly, we assume the system is isotropic such that the pair correlation function depends only on the magnitude of the pair separation, $g(\mathbf{r}_{12}) = g(r)$. Thus we arrive at an equation directly relating the structure factor as measured in scattering experiments to the pair correlation function

describing the real-space structure of the system of particles:

$$S(Q) = 1 + \frac{N}{V} \int g(r)\ exp(i\mathbf{Q}.\mathbf{r})\ d^3r. \tag{1.21}$$

A 'forward scattering' term δS_0 is usually removed from equation (1.21) giving

$$S(Q) = \delta S_0 + 1 + \frac{N}{V} \int [g(r) - 1]\ exp(i\mathbf{Q}.\mathbf{r})\ d^3r. \tag{1.22}$$

The 'forward scattering' term is the scattered intensity at $Q \to 0$ and may be identified with the scattering by the *entire system*. It is not observable in experiment; the largest length scale which is in principle observable is the largest dimension L of the scattering volume, $Q_{min} \simeq 2\pi/L$, and only for $Q < Q_{min}$ does δQ_0 have any effect on $S(Q)$ [27].

In practice scattering experiments are usually easier than direct observation of $g(r)$, thus the common experimental problem is the 'inverse transform' problem: given a measured $I(Q)$, obtain the function $g(r)$.

In Chapter 2 we return to scattering methods when we discuss the analogous *calculation* of scattering data from simulated aggregating systems.

1.4 Experimental studies of colloidal aggregation

Aggregation phenomena are widespread in experimentally studied colloidal systems. A major motivation for the work in this thesis is to attempt to model colloidal aggregation from a fundamental point of view which excludes as far as possible the particular details of any one experimental system. In fact similar experiments have now been carried out in a wide range of systems, and an intriguing picture of the 'universal' aspects of aggregation is emerging.

The concepts of *fractal geometry* have turned out to be of central importance in colloidal aggregation phenomena. A full introduction to the relevant aspects of fractals is deferred until section 1.5; first, in this section a short summary of recent important experimental work in colloidal aggregation is provided.

Probably the earliest study of particle aggregation phenomena to be interpreted in terms of the concepts of fractal geometry was the work of Forrest and Witten [28] on smoke-particle aggregates. It was shown subsequently by Witten and Sander [29] that a simple aggregation model could be employed to understand the structure of the aggregates. Thereafter some universal properties of particle aggregation models (that the *fractal dimension* of aggregates, for instance, appeared to be almost independent of many model details) were demonstrated in computer simulations [30, 31]. In fact by this stage simulations were rather outpacing experimental studies. Details of the development of particle aggregation simulations are given in Chapter 2.

After the smoke-particle work of Forrest and Witten, the earliest demonstrations of fractal geometry in more strictly *colloidal* (i.e. solid particles in a liquid suspension) aggregation began to appear around 1984. Schaefer and co-workers [32] showed by light and X-ray scattering that aggregates of small silica particles had fractal structure. Weitz and Oliveria [33] analysed projections of electron microscope images to show that aggregating gold colloids formed fractal clusters with dimension close to that of simulations [34]. Of particular interest in subsequent studies were two-dimensional (2D) experiments [7, 35, 36, 37, 38], because in these experiments the aggregates could often be directly visualized and compared to pictures from simulations. 2D experiments usually utilize the confinement of particles to air-water interfaces [7, 35, 37], where large surface forces ensure that thermal fluctuations in particle energy are never likely to enable the particles to escape the interface. Charged particles confined between conducting plates, and attracted to the plates by application of an AC electric field, have also been used [36]. Skjeltorp [38] used a system of quite large particles physically confined between two plates. In these experiments the 2D structures of aggregates are often analysed, if any analysis beyond visual observation is attempted, by discretizing and digitizing video frames, so that in fact the data from 2D experiments often come in identical form to that from simulations. For example, calculation from digitized images of the pair correlation function $g(r)$ was carried out by Armstrong and co-workers [37]; in fact in this system both short-range fractal structure (with exponent d_f agreeing well with simulations) and longer-range denser packing (the onset of gelation, see below) were observed.

Studies of aggregation may be divided into three broad areas: structural, kinetic, and dynamic. Structural information may be obtained directly (as in 2D experiments, from visual observation and analysis) or, as is usually necessary in 3D experiments, via scattering methods. Single-particle and collective dynamics in aggregating colloids may be studied using dynamic scattering methods, e.g. dynamic light scattering (DLS); essentially one derives information on the diffusion of particles and clusters in the system by measuring the decay in time of (instantaneous) interparticle spatial correlations.

Kinetic studies (i.e. the evolution of structure) involve measurement of the rate of growth of aggregates, and also of the time evolution of the distribution of aggregate sizes. The rate of growth of aggregates is sometimes derived from scattering measurements [39][4]. Mass distributions are often obtained by counting particles in (digitized) images, a method which is clearly much simpler for 2D experiments. Kinetic, structural and dynamic aspects were considered by Lin and co-workers [26, 40] in a variety of different systems, thus demonstrating some 'universal' system-independent aspects of colloidal aggregation. The kinetics of aggregation was studied for colloidal gold by Weitz and Lin [41] by analysing electron-microscope images; Hurd and Schaefer [35], Robinson and Earnshaw [7] and Feder and co-workers [42] also studied the kinetics of aggregation in various 2D colloidal systems via the aggregate mass distribution and the aggregate growth rate (the average cluster mass). The aggregation kinetics of *macroscopic* (i.e. non-Brownian) particles was studied by Roussel and co-workers [43]; despite the apparent difference between Brownian and non-Brownian systems their results show remarkable similarities to colloidal experiments and simulations. The kinetics of aggregation of particles with a long-range magnetic attraction was studied by Helgesen and co-workers [44].

Studies of single-particle dynamics and collective dynamics of aggregates in aggregating colloids are fewer, due partly to the greater experimental effort and more complex analytical techniques required, but probably also because a substantial amount of

[4]Through the mass-dependence of the single-cluster form factor, when it can be measured; see Chapter 3.

structural information is usually a prerequisite to the interpretation of dynamic measurements. Lin and co-workers [26, 40] used dynamic light scattering to study various charged colloidal systems; aggregating colloid-polymer mixtures have been studied, again by DLS, by Pirie and co-workers [11, 16].

1.4.1 Light scattering experiments

In recent years a number of important experiments studying aggregation in well-characterised colloidal systems has been carried out, leading to a clearer picture of phenomena common to aggregating systems as diverse as aggregating charged colloids [6, 39, 45, 46, 47], silica hydrogels [48], aggregating emulsions [49, 50], and aggregating colloid-polymer mixtures [11, 13, 16, 51]. That very similar observations (see below) are made in such a wide range of systems has provided a major part of the motivation for our simulations. These experiments have in common the use of small-angle light scattering (SALS) to obtain structural information throughout the aggregation process. The 2D experiments of Robinson and Earnshaw [7, 52] obtain the analogue of scattering measurements by calculation from digitized images.

Scattering techniques are of great use in studying the evolution of structure in colloidal systems. Roughly speaking, measurement of scattered intensity at scattering vector (magnitude) Q provides information about structures around length scale $l \sim 2\pi/Q$ (see equation (1.21)). Strong scattering at a given length scale indicates the presence of 'important' correlations of particle positions at this scale. The magnitude Q is related to the experimental scattering angle according to equation (1.10) as shown in section 1.3. To study aggregates or structure at *large* length scales, it is thus necessary to measure $I(Q)$ at *small* Q or small angle. Hence the technique of 'small-angle light scattering'. There are equivalent techniques, of course, for small-angle X-ray scattering (SAXS) and small-angle neutron scattering (SANS).

A key element in the recent progress in SALS experiments in colloids has been the development and better availability of good equipment for measuring scattering at very small angles and with good time-resolution. Experimentally one requires very

'clean' (laser) sources and colloidal samples free of large-scale contaminants like dust which naturally scatter at small angles. The use of video cameras and recorders to collect data over a large range of angles at one instant has become widespread, since often the systems studied undergo very fast structural changes. The extensive series of experiments of Carpineti and co-workers [6, 39, 45, 46, 47] were made possible by the construction of a very sensitive electronic sensor consisting of a large-area network of photodiodes.

1.4.2 The 'small-angle peak' in $I(Q)$

A major result from the recent SALS experiments [11, 16, 45, 46, 47, 49, 52] is the observation of a strong peak in the scattered intensity $I(Q)$ at small but non-zero angle (large length scale). As the aggregation proceeds this small-angle peak both increases in intensity and moves to smaller angle (smaller scattering vector magnitude Q). Presumably the peak indicates some *growing* 'dominant' length scale related to the growth of structures within the suspension. In some experiments [11, 45, 49] at late time the scattering peak 'freezes', no longer brightening or moving to smaller angle; this is accompanied by a marked slowing in the dynamical behaviour of the system, as indicated by a slowing of the fluctuations in the scattered speckle pattern (measured quantitatively by DLS by Pirie and co-workers [11, 16]). This late-time behaviour is presumably due to *gelation*, as further discussed below.

It seems that a number of earlier experiments [6, 26, 32, 48] failed to indicate the presence of a *peak* at small scattering angle, but rather gave scattering patterns interpreted as the scattering by *single* aggregates. It was thus something of a surprise to many that SALS studies of colloidal aggregation did not always give simply 'single fractal' scattering patterns. In fact the interpretation, even at the most qualitative level, of the presence of the peak in $I(Q)$ at $Q > 0$, was far from clear in the experimental literature. That there is a 'characteristic' or 'dominant' length scale in the aggregating system is clear from the scattering data; what physical features this length scale corresponds to, what elements of the qualitative 'aggregation model' are important in determining the details of the scattering, and what determines the evolution in time of the scattering

function, are questions upon which the experimental references are so far inconclusive. Simulations, as will be seen, provide some more precise answers, though perhaps a general theory is still somewhat distant.

The qualitative similarities between the colloidal SALS observations and small-angle scattering studies of a diverse range of systems from polymer mixtures [53] to binary fluids [54] are striking. Scattering behaviour similar to that described above, with a moving, growing peak in $I(Q)$ at $Q > 0$, has long been familiar from studies of unstable and metastable systems (simple liquids, binary fluids etc.) undergoing spinodal decomposition and classical nucleation [55]. Even colloidal crystallization studies have generated similar SALS results [56]. Thus the recent SALS experiments on aggregating colloids have suggested that there may be some fundamental link between particle aggregation processes and phase separation in general. There is a reasonably clear conceptual similarity between phase separation and particle aggregation. In the aggregation model initially small spatial fluctuations in particle density or distribution grow, as particles aggregate into clusters. In models of phase separation in unstable or metastable systems, similar fluctuations in density grow into macroscopic separate phases. 'Scattering functions' have often been calculated in the analysis of simulations of phase separation [57, 58, 59], and qualitatively similar scattering behaviour is observed. Indeed even theoretical approaches tend to obtain information on scattering rather than direct spatial information, since often the functional equations of phase transition theory are easier to handle in their Fourier-transformed disguises [60]. Mathematically $S(Q)$ is just the Fourier transform of the pair correlation function $g(r)$ (equation (1.21)).

1.4.3 Gelation

As mentioned, in some experiments interesting late-time behaviour is observed. For example, experiments measuring the dynamics of particle and aggregate motion in colloid-polymer mixtures [11] have demonstrated that, at late time, a 'pinning' or 'freezing' phenomenon can occur. Diffusion in the system slows down dramatically and 'frozen' (non-decaying on the experimental time-scale) density fluctuations are

observed. These effects seem likely to be due to gelation, that is the formation of a single macroscopic aggregate which spans the entire suspension. This is further consistent with the observation that the peak in the scattering function $I(Q)$ 'freezes' at a given, non-zero scattering vector, implying that further growth of aggregates is inhibited. Similar 'pinning' effects have been observed in other rather different systems, e.g. in polymer mixtures [53], and have been attributed there too to the 'frustration' of further growth by the formation of a large system-filling structure. Why space-filling aggregates should appear in dilute colloidal suspensions requires a consideration of the internal *fractal* structure of the aggregates, which is discussed in the next section.

1.5 Fractals

When aggregation occurs in the colloidal system, aggregates or *clusters* of particles are formed. In both experiments and simulations these particle clusters have been convincingly shown to have a *fractal* structure. In this section some of the mathematical concepts of fractals are introduced.

1.5.1 Self-similarity and length scales

A fractal is a *self similar* object. This means that it is *invariant to changes in scale.* An object with rotational symmetry, for instance a circle, is invariant to changes in orientation, i.e. is invariant under rotational transformations. A fractal, then, has *scaling symmetry*; scale transformations, for instance a doubling of the object's overall size, leave the structure of the object unchanged. Consider the fractal in Figure 1.5(a). If we cut a portion out of the object, and rescale the portion so that it is the same overall size as the original object, we see that the original object and the rescaled part remain similar (Figure 1.5(b)). (In the case of a 'perfect' deterministic or 'mathematical' fractal the rescaled cut and the original object would be identical. In real physical situations it is more common to find *statistical* fractals, in which case the similarity is statistical rather than exact—'average' measures of structure are scale-invariant.)

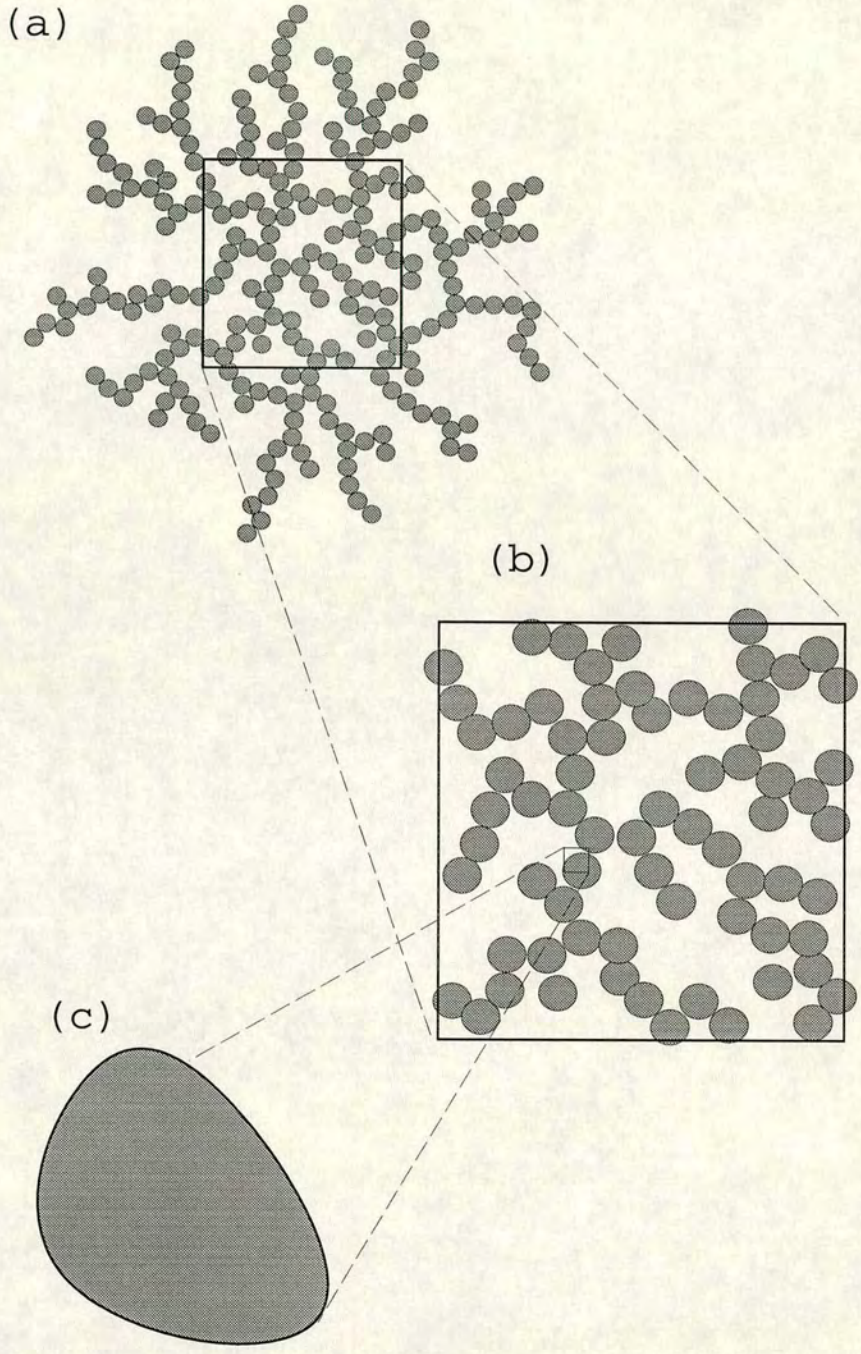

Figure 1.5. Self-similarity: a portion is cut out of a fractal cluster of small 'particles' (a), and rescaled (b). On this length scale the fractal structure is self-similar. But on the scale of the 'particle' the rescaled structure is not similar to the original (c).

A 'perfect' fractal is completely invariant under any change of scale. This means that we could cut smaller and smaller portions out of our original object, and rescale them by correspondingly larger and larger factors, and the rescaled and original versions would still have the same structure. However, it is clear from Figure 1.5 that at some lower length scale the scale-invariance fails. In physical situations there is always a lower limit to the size of portion we can cut out of the fractal (or equivalently an upper limit to the rescaling factor). At some small size the object is actually made up of small 'monomers'. If we cut a portion out of the *inside* of one of these monomers and rescale it, we just get a bigger monomer, whose internal structure certainly is not similar to the internal structure of the original cluster. Thus on length scales smaller than the individual monomers, the object is *not* fractal.

Similarly in real situations there is also an upper limit to fractal structure. This is often just the overall size of the object; we cannot cut a portion out of the object bigger than the object itself.

Thus a *perfect* fractal is both an infinitely large, and an infinitely fine object. The existence in physical situations of the lower and upper limits of fractal structure has important consequences for colloidal aggregation.

1.5.2 Measuring fractal aggregates

Fractal dimension, mass fractals, surface fractals

A fundamental number in all studies of fractal structures is the *fractal dimension.* It tells us how 'dense' an object is (or how 'fractal' it is).

Consider an object in D dimensions with some characteristic size R. Further, assume this object is internally homogeneous or compact—that is, its density is a constant, independent of its size. The volume of the object is given by the size raised to the power D, and because its density ρ is uniform the object has a mass given by

$$M_{compact} \sim R^D \rho \sim R^D. \tag{1.23}$$

Now consider a *mass* or *volume fractal* object (Figure 1.6). If we draw larger and larger circles from the centre of the object, and count the number of 'particles' inside each circle (i.e. measure the 'mass' of the object at a range of values of size R) we find that the 'mass' scales with the radius again as a power law, but this time with an exponent $d_f < D$:

$$M_{fractal} \sim R^{d_f}. \tag{1.24}$$

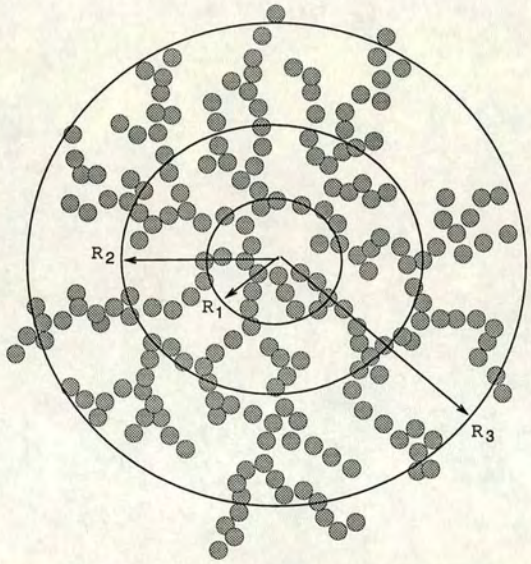

Figure 1.6. A 2D fractal cluster of small 'particles'. The total mass inside a circle of radius R scales not as R^2 (as it would for a homogeneous 2D object) but as R^{d_f}, where the fractal dimension $d_f < 2$. The density $\rho(R) \sim R^{d_f}/R^2 \sim R^{d_f - D}$; in other words when measured on an increasing scale the apparent density of the object decreases.

A *surface* fractal [24] is internally compact or homogeneous (not fractal), but has a fractal surface. The surface area of a 3D object with a fractal surface is related to the object's size R not by $A \sim R^2$ but by $A \sim R^{d_s}$, where d_s is the *surface fractal dimension*, with $3 - 1 < d_s < 3$.

The density of a fractal

Since the 'volume' of the mass fractal (the area of the circles in Figure 1.6) still

scales with the radius with exponent D, equation (1.24) can be written in another way which demonstrates an important result for the density of a fractal. Clearly $(mass) = (volume) \times (density)$ so that equation (1.23) is still obeyed:

$$M_{fractal} \sim R^D \rho. \tag{1.25}$$

But now to satisfy equations (1.24) and (1.25) we find that *the density ρ must be a function of R*,

$$\rho = \rho(R) \sim R^{d_f - D}. \tag{1.26}$$

The density $\rho(R)$ is the density of the object *measured on the length scale R*. So as we increase the radius of our measuring circle in Figure 1.6 we find that the density we measure (the mass inside the circle divided by the area of the circle) *decreases*. For a homogeneous or compact object, of course the measured density would be independent of the length scale we measure at.

More mathematical details of fractals, and a host of other dimensions and exponents, are discussed in Mandelbrot's book [61]. Vicsek's book [62] is a better introduction to the uses of fractal geometry in the particular area of colloidal (and other mesoscopic) physics.

1.6 Gels and gelation

Because there is a fair amount of leeway in the use of the term 'gel' in the literature, it is important to be clear on what we mean by 'gel'. The most common approach is to define the gel from a rheological point of view; a sample is called a gel if it displays a finite (non-zero) yield stress, that is it behaves (under low stress/strain conditions) like a solid, having a non-zero elastic modulus. (Above the yield stress the gel structure breaks apart and, usually, the sample behaves like a fluid again.) This is a definition of the gel familiar from polymer systems.

However in this work rheological behaviour, though it is certainly of great interest, will not be studied, and so the rheological definition of gelation is not used. Rather in

this thesis we will define a *colloidal gel* simply as a *space-filling structure of colloidal particles.* In the colloidal gel, the *microscopic* particles have collectively formed a structure which fills (or 'spans') the *macroscopic* sample. In this section we show how gelation or space-filling is a natural consequence of the growth of fractal structures.

1.6.1 Space-filling by fractals

Why should gelation occur in an aggregating particle system ? How can space be filled by a suspension of particles whose volume fraction is often very low ? In the simplest approach, gelation can be shown to be a direct consequence of the fractal geometry of the particle aggregates.

Consider a region of a colloidal suspension (Figure 1.7). The region contains N particles in a volume V. The volume fraction of the sample (the fraction of volume occupied by the particles) is related to the number of particles by

$$\Phi \sim \frac{Na^D}{V} \tag{1.27}$$

where a is the particle radius and D is the dimension of space (usually 2 or 3). The radius of the region shown is $R_u \sim V^{1/D}$, so that

$$R_u \sim a\left(\frac{N}{\Phi}\right)^{1/D} . \tag{1.28}$$

Now make a single fractal aggregate of some given fractal dimension d_f from these N particles (the right-hand pictures in Figure 1.7). From the equations of fractal geometry (1.24) and (1.26) the radius of the aggregate, R_a, scales with its mass (N) with an exponent equal to the reciprocal of the fractal dimension d_f :

$$R_a \sim aN^{1/d_f} \tag{1.29}$$

From (1.28) and (1.29) it is clear that the radius of the aggregate scales with a *higher power* of the number of particles than does the radius of the original region of the suspension ($1/d_f > 1/D$ because $d_f < D$). Thus if we consider a growing aggregate,

its radius R_a *grows faster than the radius of the region,* R_u*, originally occupied by its constituent particles.* This is a direct consequence of the object having dimension $d_f < D$. Furthermore, for some region of size $R_u = R_{gel}$ containing N_{gel} particles, the resulting aggregate radius will reach the radius of the original region. If the macroscopic system is filled with such regions (i.e. aggregates grow at more or less the same rate throughout the macroscopic system) then near this point aggregates throughout the system will begin to contact each other—a macroscopic system-spanning structure is formed. While there is still a lot of 'empty' space in voids inside the aggregates, nevertheless the system of aggregates has formed a space-filling gel.

The above 'model' of cluster gelation is a rather simplistic approach. For instance, it incorporates no information on *how* the aggregates grow (we simply assume a fractal dimension $d_f < D$). It assumes that all the aggregates grow at the same rate (are all the same size at a given time). It ignores the possibility that aggregates might not contact each other as soon as they grow to the gel size R_{gel}, but rather might overlap and interpenetrate each other. Anisotropy of aggregates may have significant effects. The simple model says nothing, moreover, about the spatial cluster-cluster structure.

However the argument does supply us with the prediction that gelation *must* occur in any irreversible aggregation (provided the sample is large enough). This is a point sometimes confusingly discussed in the literature. It is important to realise that with this model there is no 'critical gelation concentration' below which the system-spanning gel will not form—*unless the total number of particles* $N < N_{gel}$. In other words, in a small system it is possible to finish with a single cluster which does not span the system—but this is really a finite size effect. For example Allain and Jouhier [63] report a *critical gel concentration* for a 2D aggregation experiment. But this is simply due to the small size of their experiment—below some concentration with a given system size there are simply not enough particles for the system spanning gel to form. The 'critical gelation concentration' depends then on the system size.

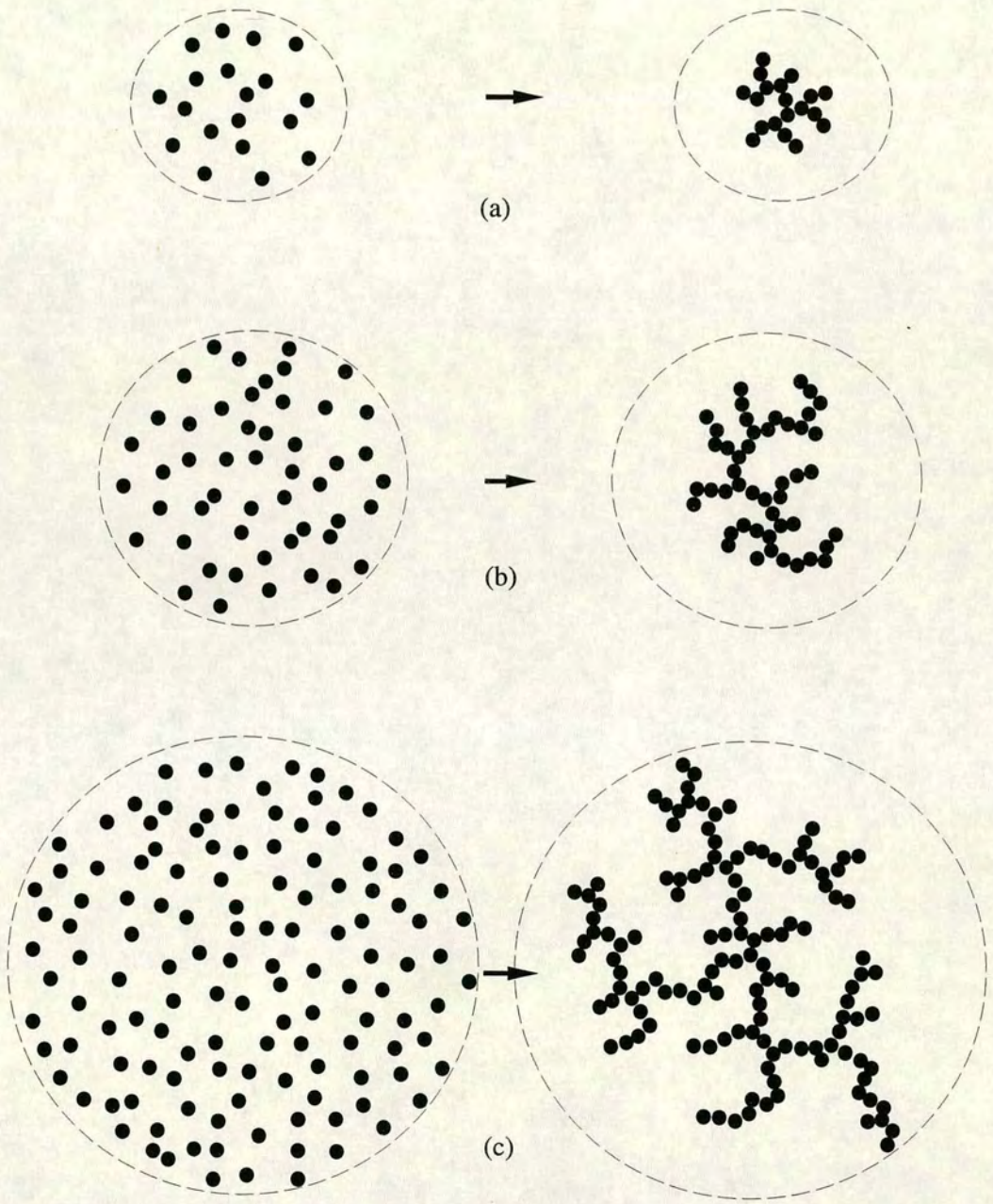

Figure 1.7. Simple picture of space-filling or gelation due to fractal growth. In (a) the small cluster is substantially smaller than the region within which its unaggregated particles were originally contained. In (b) a larger region gives a larger aggregate. In (c) the aggregate, whose radius grows quicker than the radius of the region originally containing its particles, is now the same size as the original region. In a system filled with aggregating regions like this, the clusters begin to contact each other across the macroscopic system; the system-spanning gel is formed.

1.6.2 The effect of concentration

According to the above argument there will be some average size of clusters R_{gel} at which the aggregates fill up space and contact each other to form the gel. The particle gel is thus made up of an assembly of fractal clusters, of average size R_{gel}. Therefore the range of length scales over which the gel has a fractal structure is limited, at the lower length scale by the size of the colloidal monomers (Figure 1.5) and at the upper length scale by the *gel cluster size* R_{gel}. Despite its apparent limitations we can try to use the simple model above to predict how the gel cluster size R_{gel} depends on the system density.

According to the above model the gel is formed when the radius R_a of the 'typical' aggregate of N particles reaches the radius of the region which initially contained the unaggregated particles, R_u (Figure 1.7(c)). R_a is related to N through

$$N \sim (R_a/a)^{d_f}$$

where a is the radius of the monomers making up the aggregate. So

$$R_a \sim aN^{1/d_f}.$$

The N unaggregated particles, at volume fraction Φ, initially occupied a region of radius R_u, where N and R_u are related by

$$N \sim \frac{V\Phi}{a^D} \sim \left(\frac{R_u}{a}\right)^D \Phi.$$

Equating the two expressions for N we can relate the radius of the aggregate to the radius of the region its N particles originally occupied:

$$\left(\frac{R_a}{a}\right)^{d_f} \simeq \left(\frac{R_u}{a}\right)^D \Phi.$$

The 'gel cluster' appears when the aggregate reaches the size of the unaggregated

region, $R_a = R_u \equiv R_{gel}$:

$$R_{gel}/a \sim \Phi^{\frac{1}{d_f - D}}. \tag{1.30}$$

Since $d_f < D$, increasing the volume fraction Φ leads to a decrease in R_{gel}: *The fractal clusters making up the gel are smaller at higher particle concentration.* In experiment, the fractal structure of the clusters making up the gel will become less evident for higher volume fraction systems. Indeed, at some high enough volume fraction, the upper and lower limits of the fractal structure will become equal, at which point the gel will have no fractal structure whatsoever. While early (mostly low volume fraction) simulation studies of aggregation tended to concentrate on the fractal character of aggregates [30, 31] it is clear that at higher volume fraction fractal concepts cannot fully describe the aggregate or gel structure. Furthermore, analyses which concentrate solely on estimating single statistics like the fractal dimension become less useful. For such limited fractal 'regimes' as will be found at high volume fractions, it is more difficult to define the meaning of the fractal dimension even when it is measured [64]. Since d_f is an exponent in a power law, if the range of fractal structure covers much less than an order of magnitude then the estimation of d_f becomes very problematic.

Various authors have estimated R_{gel} in experiments and measured its dependence on system density [46, 49]. Experimental results follow relation (1.30) reasonably well at least at low density. Bibette and co-workers [49] found that, in 3D systems above volume fraction $\Phi \approx 0.01$, R_{gel} no longer followed the scaling of (1.30). In contrast, Gonzalez and Ramirez-Santiago [65] found that the scaling worked up to $\Phi \approx 0.08$ in cluster aggregation simulations.

1.6.3 Length scales and depletion zones

We end with a second look at gelation and the effect of the fractal structure of aggregates, with particular attention to the concepts of *depletion zones* and *characteristic length scales* in the aggregating system. We consider here a very simple picture of the aggregating or phase-separating system, in which the system is made up of regions of higher than average density ($\rho_c > \rho_0$) and regions of lower than average density

($\rho_d < \rho_0$). This picture has been applied to phase-separating systems (see e.g. [66]) and to colloidal aggregation [45, 47, 67]. Before the aggregation or phase-separation commences the system is homogeneous, with the average density ρ_0. As the separation or aggregation proceeds, regions of higher density are created (clusters or aggregates, in the case of particle aggregation). Mass conservation of course implies that regions of lower density must then also appear, since the overall average density in the system must remain constant. The specific picture of particle aggregation is then that clusters are formed which are surrounded by *depleted regions* or depletion zones.

This picture is considered in some detail for a phase-separating system by Koch and co-workers [68]. Consider a (highly) simplified two-dimensional model consisting of a single high-density region or 'droplet' embedded in a system at overall average number density ρ_0 (Figure 1.8). Internally the droplet has number density $\rho_c > \rho_0$, and is surrounded by a depleted zone with number density $\rho_d < \rho_0$. The depleted zone is in turn surrounded by the homogeneous 'bulk' system with density ρ_0. The total mass within the depletion zone radius R_2 is given by

$$M(R_2) \sim R_2^2 \rho_0 \tag{1.31}$$

since mass must be conserved in the system as a whole. Now the mass within R_2 may also be written in terms of the mass of the droplet and the mass in the depletion zone:

$$M(R_2) \sim R_1^2 \rho_c + (R_2^2 \rho_d - R_1^2 \rho_d), \tag{1.32}$$

where R_1 is the radius of the droplet. Equating the two expressions gives a relation between R_1 and R_2 :

$$R_2 \sim \left(\frac{\rho_c - \rho_d}{\rho_0 - \rho_d} \right)^{1/2} R_1. \tag{1.33}$$

R_2 and R_1 are functions of time; as the phase-separation continues the droplet grows. Equation (1.33) shows that *the radius of the depletion zone is proportional to the radius of the droplet.* If one considers the radius of the droplet to be a 'characteristic length scale' in the problem, then the only other length scale, the radius of the depletion zone, is simply proportional to it; in other words a single length is characteristic of the system.

Koch and co-workers [68] demonstrate the consequences of this idea by calculating the pair correlation function $g(r)$ of a simulated phase-separating system and showing that rescaling all lengths by the time-dependent droplet length scale generates a *time-independent scaling form* for $g(r)$. As the phase-separation proceeds the typical droplet and depletion zone (as measured from the $g(r)$ function) simply expand by the same factor.

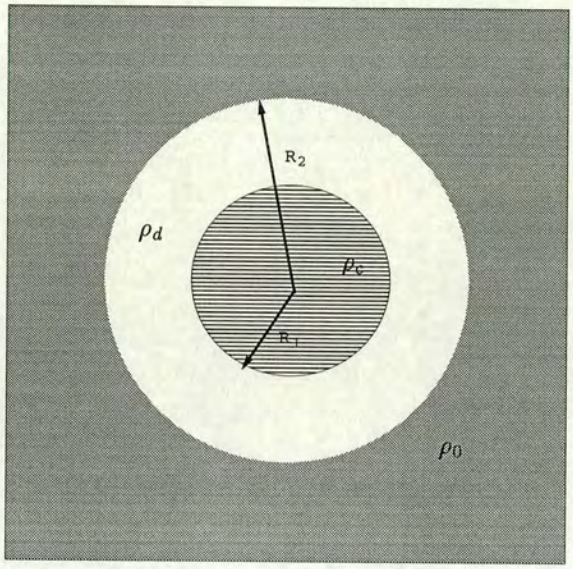

Figure 1.8. A 'droplet' with higher than average density ρ_c is surrounded by a depleted region of lower than average density, ρ_d, embedded in the homogeneous bulk with average density ρ_0. The radii of the droplet and depleted region are R_1 and R_2 respectively.

The key assumption in equation (1.33) is that the droplet is homogeneous or compact; it has *constant* (length independent) density ρ_c. But consider now the case of a growing *fractal cluster* in an equivalent very simple model of aggregation. As has been shown in previous sections (see e.g. Figure 1.7) the 'average' density of a fractal cluster ρ_f is not a constant, but depends on the size of the cluster R_1. A fractal cluster of radius R_1 made up of particles with radius a has a mass given by

$$M(R_1) \sim (R_1/a)^{d_f}$$

where $d_f < 2$ is the fractal dimension of the cluster. The density of the fractal cluster is $\rho_f(R_1) \sim (R_1/a)^{d_f}/R_1^2$ (in 2D). Inserting this expression in equation (1.33) we obtain

for the scaling of the depletion zone radius with the cluster radius[5]:

$$R_2 \sim \left(\frac{(R_1/a)^{d_f} R_1^{-2} - \rho_d}{\rho_0 - \rho_d} \right)^{1/2} R_1 \tag{1.34}$$

Thus the *time dependence* of the cluster radius is not the same as the time dependence of the depletion zone radius. In fact, because $d_f < 2$ ($d_f < D$ in general for D-dimensional space) the *radius of the cluster grows faster than the radius of the depletion zone.*

Equation (1.34) demonstrates again that at any finite system density ρ_0 the growing cluster will 'fill up' space; gelation will occur. Furthermore it implies that the two length scales in the problem, the typical cluster radius and the typical depletion zone radius, grow at different rates, so that a single length scale is not enough to characterise the system. According to this model scaling such as that demonstrated for the phase-separating (compact droplet) system of Koch and co-workers [68] will not work. The same conclusion is reached concerning fractal aggregation by Sciortino and co-workers [67, 69] using a more realistic diffusion model, who claim that when *apparent* scaling is observed in fractal aggregation it is most probably due to limitations in the experimental resolution. But one immediately obvious assumption in the interpretation of equation (1.34) which may not be justified is that the depletion zone is homogeneous with uniform density ρ_d. Furthermore the equation assumes that ρ_d is independent of time, an assumption which our results indicate is not supported in fractal aggregation (Chapters 3 and 4).

Experimental light-scattering measurements on aggregating colloids [16, 45, 47, 52] have shown that scaling (of the scattering function) *does* appear to work quite convincingly, at least over some limited time-regime during the aggregation. Thus it remains an open question whether the simple model of the aggregating system as described above, and indeed the simple model of gelation, do correctly describe the experimental aggregating system. We investigate the scaling properties of the scattering function and of various lengths in the simulation system in the following Chapters.

[5]The number densities ρ_d and ρ_0 have dimensions of inverse volume (area in 2D) so that the expression remains dimensionally consistent.

Chapter 2

Simulation of aggregation

Abstract

In this chapter we introduce the cluster-cluster aggregation computer simulation model of colloidal aggregation. The implementation of the model as used in this thesis is described in detail. Some general details of the main methods of analysis are given, as well as a short summary of methods and results of previous simulations of the cluster aggregation model.

2.1 Computer simulation of aggregation

2.1.1 First simulations

Aggregation processes are widespread in colloidal physics, and have been studied experimentally for a long time. However, not until the late 1960's did computers become available which were powerful enough to enable any reasonable attempt at simulating aggregation processes. An early example of the simulation of aggregation in particle systems appears in the work of Sutherland and co-workers [70]. Aggregating particles were observed to form apparently amorphous structures in a simulation of *ballistic*

cluster aggregation[1]. At this time quantitative methods of analysing the structure of these 'amorphous' aggregates were not available. Only when the development of the concepts of *fractal geometry* (Chapter 1) had advanced sufficiently could quantitative progress be made.

In 1979 Forrest and Witten [28] introduced some of the concepts of fractal geometry [61] into their analyses of experimental images of smoke-particle aggregates. Subsequently Witten and Sander [29] developed the *diffusion-limited aggregation* (DLA) simulation model of particle aggregation. In the DLA model a single particle diffuses (i.e. moves by random walk) through a system, at the centre of which is positioned a stationary 'seed' particle. The diffusing particle eventually collides with and becomes attached to the central seed. Thereafter another particle diffuses into the volume, collides with and joins the growing central aggregate, and so on. The resulting aggregate was shown by Witten and Sander to have a *fractal* structure [29]. The fractal dimension d_f was found to compare quite well to similar measurements from the smoke-particle aggregation experiments.

From this moment the field of computer simulation of particle aggregation grew rapidly. A number of quite different experimental systems have been shown to be described well by the Witten-Sander DLA model (at least from visual observation or according to statistics like the fractal dimension) [71]. However the physical processes involved in aggregation in *colloidal* systems seemed unlikely to be very close to the 'particle-seed' aggregation model of DLA, which involves the growth of a single central aggregate. Rather in colloidal systems it is more reasonable to consider growth as occuring throughout the suspension, by the aggregation of the monomer colloidal particles and the continuing diffusion and coagulation of the growing aggregates.

Hence the introduction of the *cluster-cluster aggregation* (CCA) simulation model. In fact this 'new' model was similar to that early model of Sutherland and co-workers [70]. In biophysics the model had already been studied by Finegold [72] in an attempt to simulate the aggregation of particles within membranes; Ref. [72] gives further

[1]Particles and clusters were moved along ballistic or straight-line trajectories, hence these simulations do not apply precisely to most colloidal systems in which the dominant particle motion is Brownian

references demonstrating the importance of particle aggregation phenomena in the biological field.

2.1.2 Cluster-cluster aggregation

Meakin [30] and Kolb and co-workers [31] separately and simultaneously reported studies of the two-dimensional *diffusion-limited cluster-cluster aggregation* (DLCA) simulation model in 1983. In this model a number of particles diffuse simultaneously through a system. When two particles collide, they immediately stick together, and subsequently diffuse as a *cluster*. Similarly when clusters collide they stick and diffuse as larger combined clusters. Thus structures of greater and greater size are built up throughout the system volume. Because collisions immediately lead to 'bonding', this variant of the model is called *diffusion limited*; growth is limited by the rates of diffusion of clusters through the system. In a variant of the model, *reaction-limited cluster aggregation* (RLCA), particles do not stick immediately upon collision, but rather bonds are formed with some probability $P << 1$. DLCA thus models particle aggregation when there is no repulsive part to the interparticle potential (Figure 2.1); in the RLCA model some kinetic 'barrier' must be overcome before the particles can approach closely enough to permanently bond.

Unlike in the DLA model, in DLCA and RLCA there is no central 'seed' and there are a number of clusters diffusing in the system at any one time. This is a better physical model of *colloidal* aggregation processes. It allows a finite system concentration or volume fraction to be defined. Eventually, if the simulation is continued for long enough, all particles will belong to a final single cluster. That large clusters appear which may 'fill' the system also leads to the possibility of modelling gelation (Chapter 1).

In this work we consider only the DLCA model. In principle the RLCA model may be treated as a generalisation of DLCA by introducing the sticking probability parameter P. However it has been shown both in experiment [7, 39] and in simulation studies [73, 74] that reaction-limited aggregation is rather more complex than one might initially expect. For example, as clusters grow larger, in collisions they become more likely to

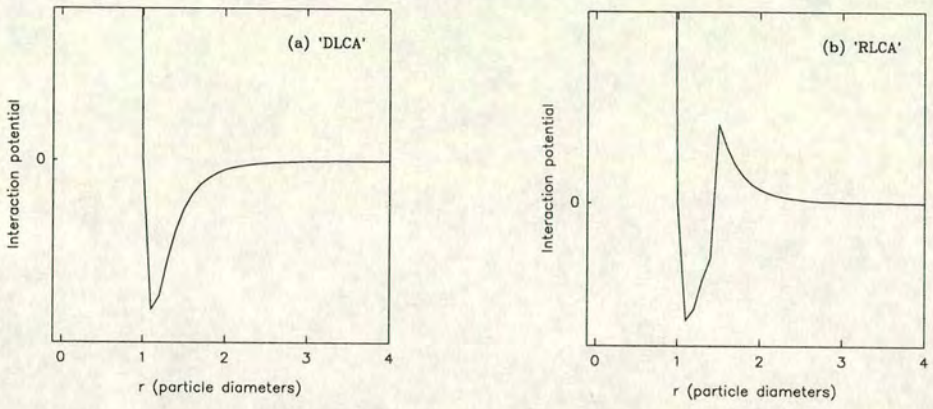

Figure 2.1. Schematic forms of the interparticle potential for diffusion-limited (DLCA) and reaction-limited (RLCA) aggregation conditions. (a) In DLCA the potential features an attractive 'well' (potential < 0); (b) in RLCA there is a repulsive 'barrier' outside the attractive well. An approaching particle must have enough kinetic (thermal) energy to surmount this repulsive barrier if it is to reach the attractive part of the potential and form a 'bond'.

contact neighbouring clusters at many points, thus generating a 'crossover' from RLCA to conditions more typical of DLCA.

2.2 Implementation of the DLCA model

The model used in this work is close to a 'standard' implementation of the DLCA simulation. In principle the DLCA model is quite simple. This has the advantage that it may describe (at least qualitatively) phenomena observed in a very wide range of systems in which the details of the physical system are thus demonstrated be unimportant to the fundamental processes of aggregation. Moreover, the process of particle and cluster diffusion as modelled in the simulations remains physically close to the real phenomenon. However the simplicity of the model may also mean that some phenomena, which do depend on details not included in the simulation, will not be observed. In fact, as will be described, the very simple DLCA model does appear to apply to a wide range of quite diverse physical systems, at least to a first approximation.

2.2.1 Continuum and lattice models

In this thesis DLCA simulations have been implemented both in a continuum (or 'off-lattice') and in a lattice-based model[2]. In the lattice-based model particles are constrained to occupy the sites of a square (in 2D) or simple cubic (in 3D) lattice. Diffusion 'moves' are always of one lattice site in one of the lattice directions. Particles can only bond with nearest-neighbours (i.e. there is no bonding between diagonal neighbours). The use of the lattice reduces computation time enormously, but it does impose some limitations on the short-range structure of aggregates. The implications of the use of the lattice are studied in Chapter 3 by comparing results from the lattice-model with results from the continuum model. Due to constraints on computational resources, it has been possible to implement the off-lattice model only in 2D and for relatively small systems.

2.2.2 The simulation box

The simulation system is represented by a square (2D) or cubic (3D) 'box' with side-length L. In the simulations *periodic boundary conditions* are imposed. We imagine the finite simulated box to be surrounded by replicas of itself (Figure 2.2). If a particle moves out of the simulated box on one side, its 'image' moves back into the box at the opposite side. In this way a much larger (conceptually 'infinite') system is approximated. There are important implications of the use of periodic boundaries for the structures formed in the aggregating system, especially when clusters or particles appear with size approaching the size of the box; these are discussed in more detail in section 2.6.1.

2.2.3 Volume fraction and number density

The initial configuration of the simulation system is generated as follows. A number of particles N is placed randomly (without overlap) into the box. The box size L and/or

[2] An original small-scale 2D version of the lattice-based algorithm was written by M. Sievwright as part of an undergraduate project.

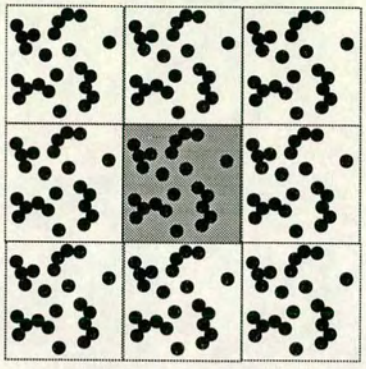

Figure 2.2. Use of periodic boundary conditions effectively means simulating a large (infinite) system as if it were 'tiled' with replicas of the 'real' system. Only the shaded central box is actually simulated.

the number of particles N are determined by the *particle volume fraction* or *number density* required for the experiment. In the continuum or off-lattice model, the particle area fraction Φ (all off-lattice simulations are in 2D) is defined as the fraction of the total area of the box which is occupied by particles (circular discs):

$$\Phi = \frac{N\pi a^2}{L^2} \tag{2.1}$$

where a is the particle radius. In the lattice-based simulations, a more appropriate variable is the *particle number density*, ρ. For a lattice where the (3D) box contains L^3 lattice sites, the number density ρ is the fraction of lattice sites which is occupied by a particle:

$$\rho = \frac{N}{L^3}. \tag{2.2}$$

A particle 'fills' a whole lattice site. Therefore the definitions of a 'particle' on-lattice and off-lattice are not exactly equivalent.

2.2.4 Initial structure

We require that there is no extraneous structure or order in the initial distribution of particles before aggregation commences which might persist into the aggregation

simulation and give rise to spurious aggregate structures or incorrect kinetics. Thus, having placed the particles randomly in the simulation box, an initialisation procedure is carried out in order to guarantee that the system immediately prior to aggregation has (as near as possible) the structure of a 'hard sphere' colloidal fluid. The initialisation routine employed is based on standard Monte Carlo techniques [75]. A particle is picked at random, and a random 'move' is attempted, that is a move of the particle a certain distance l in a random direction. If the move would result in an overlap with another particle, it is rejected. If not, the particle is moved to the new position. Another particle is picked at random, and the process is repeated.

In the lattice-based simulations the move distance l is constrained to be one lattice spacing (one particle diameter). In the continuum simulation a value of l is selected which gives the best compromise between the number of steps required to initialise the system structure and the number of attempted steps which are rejected because of overlaps. Longer steps would mean the particle distribution is changed more at each step, thus the 'equilibrium' fluid structure is approached faster; however longer steps are also more likely to lead to overlaps and rejected moves. In practice selecting a step length l which gives an 'acceptance ratio' (fraction of attempted moves which do not result in overlap) of approximately 70% was found to be a good compromise. The value of l giving approximately this ratio (at the particle area fractions studied, $\Phi = 0.1$ and $\Phi = 0.3$) was $l = 0.2d$ where d is the particle diameter.

One requires some way to tell when the system structure is sufficiently close to the equilibrium hard sphere fluid. In initial simulations the *scattering function* (see Chapter 1) of the system of particles was calculated at intervals during the initialisation. The calculation of the scattering function from simulation data is described in section 2.3. The initialisation was continued until there were no longer significant changes in the scattering function (apart from statistical fluctuations). In subsequent simulations at least this number of initialisation steps was carried out before the aggregation commenced. In some cases the number of initialisation steps was also varied to check for any remaining effects of the starting configuration. In general it was found that

between 1000 and 5000 steps per particle[3] was adequate for the large lattice-based simulations. In the continuum simulations the number of equilibration steps was 1000 per particle. In practice the initialisation routine did not represent a significant fraction of the total run-time.

2.2.5 Cluster aggregation

After initialisation the particles continue diffusing through the system but now the aggregation commences: colliding particles and clusters stick together. In practice a list is maintained of all particles and clusters in the system. At the beginning of each time step the list is randomly resorted, so that the particles and clusters are moved in a random order, to reduce any possible effects of non-simultaneous motion. Taking each particle or cluster in the list in order, a random 'move' is selected, a check for collisions with other clusters is made, and any colliding clusters are 'combined' such that they subsequently diffuse as a single cluster.

The move procedure differs according to whether the simulation is lattice-based or off-lattice. In the off-lattice case, random (x,y) components for the move are calculated from a Gaussian distribution with mean zero and standard deviation σ. σ determines the *mean* magnitude of the move. Scaling of the mean magnitude of moves with cluster mass, to simulate the slower diffusion of larger clusters, is discussed below.

In the lattice-based model, moves are restricted to a length of a whole lattice spacing (equal to a particle diameter d), and to one of the lattice directions (4 in 2D and 6 in 3D). In this case a move direction is chosen at random, the probabilities of all directions being equal. The slowing down of larger clusters by scaling the frequency of moves for different-sized clusters is described below.

Before particle positions are updated according to the generated random move a check is made whether, during the move, the moving particle or cluster will collide with any other particle or cluster (when moving a *cluster* we must, of course, update the

[3] Particles are selected randomly so that *on average* each particle was moved this number of steps during initialisation.

positions of all the cluster's particles). Again the implementation of the collision check differs between the lattice-based and continuum simulations.

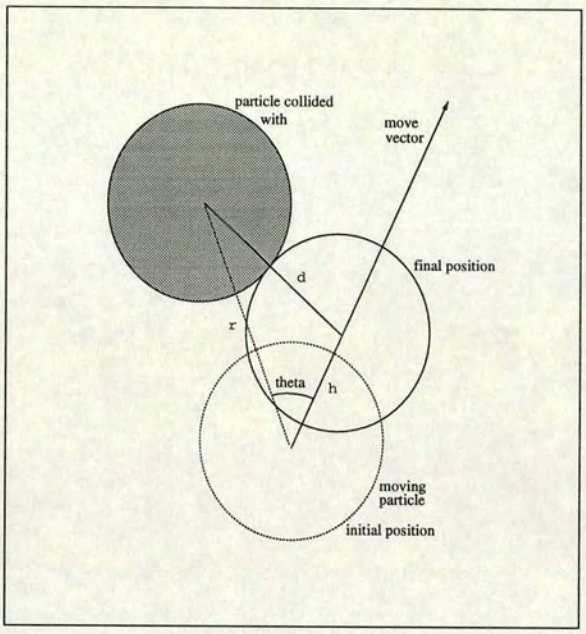

Figure 2.3. Detection of a collision between a moving particle and a nearby stationary particle, in the off-lattice simulation model. In the Figure the length of the move vector is exaggerated for clarity; in the simulations the vector is typically about 3% of a particle diameter.

Moving and collision in continuum

In the off-lattice case, detection of collisions involves solving a quadratic equation relating the position of the moving particle and the positions of *each* other particle with which the moving particle may collide. The situation is illustrated in Figure 2.3. From the Figure we have

$$h^2 - h.2rcos\theta + r^2 - d^2 = 0 \tag{2.3}$$

where h is the distance along the move vector at which the particles collide, r is the initial separation of the two particles, d is the distance between the particle centres at collision (i.e. a particle diameter) and θ is the angle between the move vector and the line joining the centres of the two particles at their initial positions. To detect a

collision this equation is solved for h. Positive real roots h less than the length of the move vector indicate a collision. (If the equation has no real positive roots, this means there is no collision; negative roots are 'collisions' along the move vector in the opposite direction to the move, and therefore are also ignored.) A naive approach is to solve for h for *all* pairs of moving–not moving particles (remembering that for a moving cluster, every particle in the cluster is moving, and each must be checked for collisions in turn). Then if there is a collision, the original move length is replaced with the distance to the *first* collision (the smallest value of h, the 'first' collision along the move vector). All particles in the moving cluster are then moved this distance along the move vector, so that the moving cluster and the 'hit' cluster are just touching. The two clusters are then 'combined' using a cluster-number label, such that they subsequently diffuse as a single cluster.

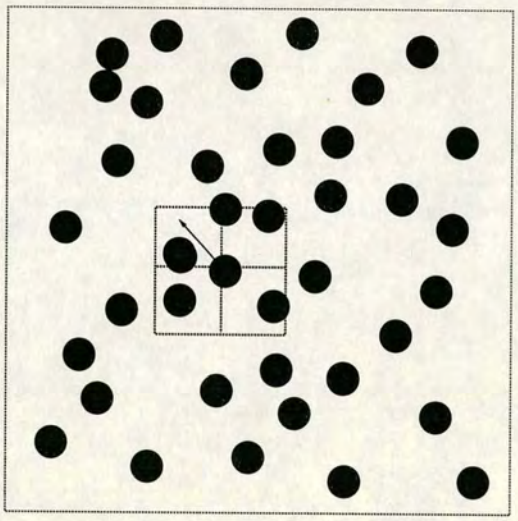

Figure 2.4. A particle with a given move vector (shown by the arrow) will move through only those 'cells' of the system shown by the dashed lines. The particle cannot possibly collide with particles outside these cells, so collision detection need only be carried out for those particles within the four cells.

However, it is clear from Figure 2.4 that a moving cluster cannot collide with absolutely *any* other particle in the system, since some particles are much further away than the maximum possible length of the move. We only really need solve the quadratic to look for collisions with 'nearby' particles and clusters. (In fact the meaning of 'nearby'

changes as the moving entities grow in size, which has important implications for the problem, as described in section 2.6.1.) Therefore the efficiency of the algorithm may be improved by selecting only 'nearby' not-moving neighbours with which to check for collision. In practice we use a method sometimes called the 'link-cell' [4]. The simulation box is divided up into smaller cubes (3D) or squares (2D). For each sub-box an 'occupier list' is maintained, that is a list of all clusters *any part of which* is inside the sub-box. When a cluster is moved, the sub-boxes through which any part of it will pass are identified, and only those other clusters listed in the given sub-boxes' occupier lists need be checked for collision. This improves the efficiency of the algorithm immensely, especially in the earliest stages when many small clusters are present which occupy perhaps only one or two sub-boxes; almost all the system can be excluded then from the collision check.

Moving and collision on-lattice

In the lattice-based simulation, detection of collisions is much simpler, since particles can occupy only fixed lattice sites. (The lattice is maintained as an array in program memory, so that the continuum method's quadratic equation solution step is replaced by a simple memory look-up.) *After* a particle or cluster is moved, all the moving cluster's nearest-neighbour lattice sites are examined. By nearest-neighbour we mean the four sites in the $\pm x$ and $\pm y$ directions (in 2D) or the six sites in the $\pm x$, $\pm y$ and $\pm z$ directions in 3D. For all the neighbour sites which are occupied by particles of other clusters, we must now 'join' the clusters so that they subsequently diffuse as a single cluster. This is achieved using a cluster-number label as in the off-lattice algorithm.

2.2.6 Scaling of cluster movement with cluster size

For a single spherical particle in a solvent, a free translational diffusion coefficient D may be defined through the Stokes-Einstein relation

$$D = \frac{k_B T}{6\pi\eta a}$$

[4] A classic example of Opaque Name Syndrome.

where T is the temperature, η is the solvent viscosity, a is the particle radius and k_B is Boltzmann's constant. Thus the diffusion coefficient is inversely proportional to the radius of the particle. It is reasonable to expect that cluster size will have an effect on the *cluster* diffusion coefficient D_{cl} in the DLCA model. It is intuitively apparent that larger clusters will diffuse at a slower rate. Therefore we impose a scaling of the diffusion rate of clusters in the simulation according to cluster radii. Using the cluster *radius of gyration* as a characteristic radius, we assume that the above Stokes-Einstein scaling is reasonable also for ramified clusters [76], that is to say the translational diffusion coefficient of a cluster is scaled in inverse proportion to its radius of gyration:

$$D_{cl} \sim r_g^{\delta} \tag{2.4}$$

with $\delta = -1$. The cluster radius of gyration r_g is defined by

$$r_g = \frac{1}{n_c} \sum_{i}^{n_c} (\mathbf{r}_i - \mathbf{r}_c)^2 \tag{2.5}$$

where the $\mathbf{r}_i$ are the coordinates of the particles in the cluster, n_c is the number of particles in the cluster, and $\mathbf{r}_c$ is the cluster centre of mass.

Therefore the cluster diffusion rate slows down in inverse proportion to the cluster radius. Once again, the implementation of the scaling of the diffusion of clusters of different sizes differs between the continuum and lattice-based simulations.

Diffusion scaling in continuum

In the continuum case, the scaling of the diffusion of clusters is conceptually simpler than for the lattice-based model. When generating a random move for a cluster, the random components of the move are calculated from a Gaussian distribution whose width (i.e. standard deviation σ) is set according to the required diffusion coefficient. For larger clusters we reduce the width, and therefore the *mean magnitude* of the move. All clusters still move every step (in contrast to the on-lattice case, see below).

Diffusion scaling on-lattice

For the lattice-based simulation, each diffusion step must be a whole lattice spacing. Therefore the length of the random walk step cannot be reduced for larger clusters in order to slow their diffusion. Alternatively, their diffusion can be slowed *on average* by simply moving the larger clusters *less often* than the smaller clusters. In practice the probability that a cluster will move at the current step is calculated. The probability is inversely proportional to the square root of the cluster radius (thus the diffusion coefficient D_{cl} is inversely proportional to the radius). A random number is generated from a uniform distribution between zero and one. If this random number is less than the move probability, the cluster is allowed to move; otherwise the 'attempted' move is rejected, and the cluster is left where it is for the current simulation step.

Diffusion coefficient of monomers and dimers

The definition of the radius of gyration r_g in equation (2.5) leads to a value $r_g = 0$ for monomers (i.e. single particles). Thus a somewhat arbitrary value must be selected for the radius of gyration of monomers. The most obvious approach, which is followed here, is to set $r_g = a$, the particle radius. But it should be noted from equation (2.5) that two-particle clusters or dimers (whose centres are always exactly one particle diameter apart) also have $r_g = a$. Therefore in the simulations monomers and dimers have the same radius of gyration and the same diffusion coefficient D_{cl}.

2.2.7 Time

Time t in the simulation is counted in simulation steps from the initiation of the aggregation. A simulation step is defined as one move for *every* cluster (including, in the on-lattice case, *attempted* moves of larger clusters even if rejected as described above). Thus while times t do not refer to any 'real' time scale (for which we would have to specify details of the aggregating system such as particle radius a, solvent viscosity η, etc.) the time scale is in itself physically defined.

Lattice effect on 'start time'

There is an important effect of the use of the lattice on simulating the *early time*

regime of the aggregation. When particles are placed randomly on the lattice, some particles will inevitably occupy neighbouring lattice sites (even after the equilibration procedure). These neighbouring particles therefore form clusters, so that the system already contains some clusters at the 'start' of the aggregation, $t = 0$. By contrast the continuum system initially consists only of monomers. In terms of kinetics, our results suggest that this effect can be simply considered as a 'shift' of the simulation start time, so that $t = 0$ in the lattice simulations corresponds to $t > 0$ in the continuum simulations. The degree of clustering at the start time in the lattice model depends on the system number density. As the density is increased larger and larger clusters of monomers appear in the initial configuration. Therefore *there is always an early time regime which cannot be studied in the lattice model*, and the extent of this early time regime *depends on number density.* In this work one consequence of the use of the lattice model in most of the simulations is that there are certain early-time phenomena (see Chapters 3 to 5) which may be observed only in simulations at low number density.

The initial procedure of randomly placing particles at the sites of the lattice is an example of the *percolation problem* [77]. The clusters formed by the random placing of particles on the lattice are often termed 'percolation clusters'. The structure of the percolation clusters is likely to be different to the structure of clusters growing by the DLCA process. This implies that the structure of the clusters 'pre-existing' in the initial configuration is somewhat different to what would be expected had these clusters really been built via the DLCA process[5]. For *small* pre-existing clusters this problem is not too important, because the structure of small clusters is dominated by the underlying lattice structure anyway. But there exists a *critical percolation density* ρ_P at which the initial configuration contains (on average for a finite system) a *percolating cluster* which spans the whole system [77]. Near ρ_P the initial configuration will contain very large clusters whose structure differs from DLCA clusters. The use of the lattice thus imposes a second constraint: as well as a density-dependent lower limit to the time regime we can study, there is an upper limit to number density which can be studied, above which significant 'percolation-like' structural effects are expected.

[5]The clusters in the *equilibrated* initial configuration are not exactly 'percolation clusters' due to the Monte Carlo equilibration, but they are not DLCA clusters either.

In this thesis we have studied number densities up to $\rho = 0.3$ in 2D and $\rho = 0.1$ in 3D, both maxima reasonably well below the respective square/cubic lattice critical percolation densities of $\rho_P \approx 0.59$ in 2D and $\rho_P \approx 0.31$ in 3D [77]. Effects of the lattice on structure and kinetics are studied via the calculated scattering functions in Chapter 3. In practice the lattice does not seriously affect structure beyond the smallest length scales. As has been mentioned, the main effect on kinetics is the 'shift' of the lattice start time relative to the continuum $t = 0$.

2.2.8 Move length in the continuum model

In the off-lattice simulations it is necessary to choose a random-walk step-length l_0, the mean magnitude of the random walk steps of the diffusing monomers at the start of the aggregation. As larger clusters appear their diffusion is scaled according to equation (2.4). The basic monomer random walk step length must be small enough to reasonably approximate Brownian motion, but large enough that the simulation does not take an impractical amount of time to run. The step-length l_0 was selected by carrying out some initial tests with different step lengths and studying the kinetics of the aggregation via the time evolution of the average mass. First tests were carried out with a step-length $l_0 = 10\%$ of the particle diameter d. To ensure against spurious effects on the growth kinetics due to using too large a step, the step-length was reduced until no further changes in the kinetics (as measured by the average mass versus time) were observed. In practice for the 2D off-lattice simulations at area fraction $\rho = 0.3$ a value of $l_0 = 0.033d$ was arrived at. Therefore the largest (mean magnitude) step-length in the continuum simulation was set to 3.3% of the particle diameter (for all area fractions).

2.2.9 Rotational diffusion

In real colloidal systems, particles undergo not only translational diffusion but also *rotational* diffusion. This also applies of course to clusters in aggregating colloidal systems. The addition of many small 'random' rotations of the cluster, due to the fluctuations

in the impacts of surrounding solvent molecules, results in the cluster carrying out a 'rotational random walk' as well as a translational random walk. However no attempt has been made to include rotational motions of clusters in these simulations. Rotations in the continuum model would involve a number of quite complex calculations, while in the lattice model would be very difficult to implement at all.

According to the rotational diffusion equivalent of the Stokes-Einstein relation, the rotational diffusion constant (the *angular* diffusion constant) is inversely proportional to the *cube* of the radius of the particle:

$$D_{rot} = \frac{k_B T}{8\pi\eta a^3}$$

If we assume this scaling applies also to clusters of particles, rotational diffusion is comparable to translational diffusion only for the motion of the outermost particles of the cluster. Meakin [78] has studied the effects of rotational diffusion in the DLCA model, concluding that for physically reasonable rotational diffusion rates (i.e. slower than translational diffusion) there are no major effects on cluster structure, at least according to the estimated fractal dimension. *Intercluster* structural effects of rotational diffusion may become more important at high particle concentration when a system of well-separated clusters is never realised (see Chapter 3).

2.2.10 Hydrodynamic effects

Part of the interaction between colloidal particles and the surrounding solvent is taken into account in the simulation model by modelling the Brownian motion of the colloidal particles using a random walk. However, the hydrodynamic behaviour of the solvent leads to other solvent-mediated interparticle interactions which are in principle many-body and long-ranged. These hydrodynamic interactions are not taken into account in the DLCA model. Computational limitations mean we cannot hope to simulate the fluid molecules as well as the colloidal particles if we are to study reasonably large

aggregating systems[6].

2.2.11 Reversible bonding

It has been noted above that bonding between colliding particles and clusters is immediate and irreversible. This is equivalent to assuming that there is an infinite 'sticking potential' exactly at 'touching' distance which irreversibly bonds two colliding particles together. (The bonds are also assumed then to be rigid.) In this thesis the effects of *reversible* bonding, that is of a finite interparticle potential, are also investigated. Discussion of this extension of the DLCA model is deferred until Chapter 4.

2.3 Analysis of structure by 'scattering' methods

As has been described in the previous Chapter, scattering is one of the most useful and most common experimental methods in colloids. Because so many experiments use scattering methods to investigate structure and dynamics in colloidal suspensions, it makes sense to use analogous methods to analyse results from computer simulation. Calculation of the scattering function at different stages of the aggregation provides a good way to directly compare simulation and experiment. Thus substantial use is made of 'scattering methods' in the analysis of simulation results in this thesis. Chapter 1 gives details of the physical basis of scattering theory including derivations of the scattering intensity from single particles and systems of particles. Here we describe some computational details of the calculation of the scattering function $I(\mathbf{Q})$ from the simulation data.

[6] One possible approach currently the subject of substantial study is the use of 'Lattice-Boltzmann' methods to simulate the hydrodynamic behaviour of the solvent; see e.g. [79].

2.3.1 Calculation of the scattering function from particle coordinates

In the simulated system we have a set of coordinates representing the positions of the centres of colloidal particles in the simulation box. As discussed in the previous Chapter, the instantaneous amplitude of the electric field of light scattered by a system of N particles at a set of coordinate vectors $\{\mathbf{r}\}$ is given by

$$E(\mathbf{Q}) = \sum_{j}^{N} b_j(\mathbf{Q}) exp[i\mathbf{Q}.\mathbf{r}_j] \tag{2.6}$$

where $\mathbf{Q}$ is the scattering vector and $b_j(\mathbf{Q})$ is the ($\mathbf{Q}$ dependent) amplitude of the field scattered by particle j. The instantaneous *intensity* of scattered light measured is the square modulus of the electric field:

$$I(\mathbf{Q}) = |\sum_{j}^{N} b_j(\mathbf{Q}) exp[i\mathbf{Q}.\mathbf{r}_j]|^2 \tag{2.7}$$

It is straightforward therefore to calculate the scattering function $I(\mathbf{Q})$ from particle configurations generated during the simulation. Since we are not interested in the internal structure of the particles, in the calculation the particles are treated as 'delta functions'; we compute the scattered intensity using equation (2.7) putting $b_j(\mathbf{Q}) = 1$.

The use of a square (2D) or cubic (3D) simulation box with periodic boundary conditions has important implications for the calculation of the scattering function. The scattering wavevector must be *continuous* at the periodic boundaries. For a simulation box of side L (area $L \times L$ in 2D, volume $L \times L \times L$ in 3D) the scattering vector components which satisfy continuity at the periodic boundaries in each dimension are given by

$$Q = \pm 2n\pi/L, \tag{2.8}$$

where n is an integer. The *reciprocal space* represented by the set of allowed scattering vectors consists of a square (in 2D) or cubic (in 3D) lattice of points, with lattice spacing $2\pi/L$. The *resolution* of features in the scattering pattern therefore depends

on the system size L. It follows too that the *smallest* scattering vector component in each dimension which can be calculated is also determined by L, $Q_{min} = 2\pi/L$. This is equivalent to the obvious point that we cannot see any structure *larger* than the simulation box.

In principle there is no upper limit Q_{max} on the scattering vector magnitude (there is no upper limit on n in equation (2.8)). However, for $Q \geq 2\pi/d$, where d is the diameter of a particle (or a lattice spacing in the lattice-based simulations) the scattering function 'probes' structures on length scales of d and smaller. In a real scattering experiment at this length scale one would be studying the internal structure of the colloidal particles. But in the simulation the particles are 'structureless'. Therefore we usually do not calculate $I(\mathbf{Q})$ for $|Q|$ beyond $|Q|_{max} \approx \pi/d$.

Scattering function in the lattice-based model

At the length scale of the lattice parameter in the lattice-based simulation, the *lattice structure* is *imposed* on the system. Therefore when the scattering function is calculated the lattice structure is observed at this length scale. The lattice is a regular crystal (square in 2D or simple cubic in 3D) and corresponding strong Bragg diffraction peaks appear in the scattering function (Figure 2.5). We therefore cannot study aggregate structure on these small length scales, since the aggregates are forced to have the lattice structure. On larger length scales, the structure will approximate closer and closer the continuum. (An examination of the effects of the lattice on the structure and scattering functions of the simulated system is given in Chapter 3.)

The use of the lattice has a very important practical consequence for calculation of the scattering intensity. As is shown in Chapter 1, $I(\mathbf{Q})$ is the Fourier transform of the particle distribution. On a lattice, we have a *discrete* particle distribution. This means that we can use a very efficient method to calculate the scattering function, the *discrete Fast Fourier Transform* (FFT) algorithm [80]. This is a well-known algorithm which makes use of identities in the discrete calculation of the exponential phase factors in the scattering sum to reduce the number of calculations required; it also reduces the *scaling* of the calculation time with the number of particles. Therefore it is possible

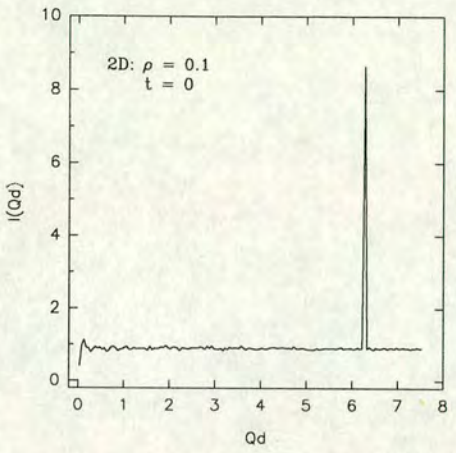

Figure 2.5. The scattering function $I(Qd)$ (where d is the particle diameter) calculated for the initial (time $t = 0$) configuration of a 2D lattice-based simulation at number density $\rho = 0.1$. The underlying square-lattice structure (with lattice parameter d) gives rise to a strong peak in $I(Q)$ at $Q = 2\pi/d$.

in reasonable time to calculate the scattering function of much larger lattice-based systems. (The computation time for the direct calculation of the sum of phase factors in equation (2.7) scales at best as the number of particles N multiplied by the number of Q vectors. The number of Q vectors scales with the square (in 2D) of the system size L, giving a best scaling overall of N^2, so the calculation becomes very time-consuming for large systems.) The off-lattice simulations use continuum coordinates and the scattering functions are calculated directly; this is practicable for the small off-lattice systems studied here, but the N^2 scaling means it becomes very time-consuming even for quite small increases in the number of particles. In fact some authors 'convert' a set of continuum coordinates into discrete coordinates in order to calculate the scattering function using the FFT (e.g. Ref. [81]).

2.4 Cluster aggregation–review of previous work

Here we describe some previous implementations of the CCA model and discuss some important results reported in the literature. There are a number of review articles which cover many aspects of simulations with the cluster-cluster aggregation model in

more detail (see for example Refs. [82, 83]), while Ref. [62] gives a wider introduction to the application of fractals to growth phenomena.

2.4.1 Cluster structure

One the first major results to emerge from simulations of the DLCA model was an estimate of the fractal dimension of DLCA clusters. This provided a first test of the validity of the model in a wide range of experimental systems. Various methods have been used to obtain estimates of d_f, from the mass-radius relation $M \sim R_g^{d_f}$, to density correlation functions and particle distribution functions. From the earliest two-dimensional simulations Meakin [30] obtained an estimate $d_f \simeq 1.45 \pm 0.05$; Kolb and co-workers [31] obtained $d_f \simeq 1.38 \pm 0.06$. Further work with larger systems, and higher-dimensional implementations of the model [34], have led to the following generally 'accepted' estimates of the fractal dimension d_f in 2D and 3D DLCA:

2D: $d_{f,DLCA} = 1.42 \pm 0.05$

3D: $d_{f,DLCA} = 1.78 \pm 0.05$.

Compared to the fractal dimensions of DLA clusters ($d_f \simeq 1.7$ in 2D and $d_f \simeq 2.5$ in 3D [29, 84]) these values are rather low; this means that DLCA clusters tend to be more ramified than DLA (particle-cluster) aggregates. This is intuitively reasonable given that in DLCA both objects are ramified clusters and the likelihood that they will deeply interpenetrate each other is much lower than in DLA, where a small particle encounters a large cluster.

In most of the literature the above values of fractal dimension are taken to be *universal.* In fact this is part of the attraction of the fractal aggregation model, in that in a wide range of experiments, the details of whose systems are often very different, still a 'universal' value is found for the fractal dimension. This means that the structures formed in these systems are not dependent at all on many details of the system. A number of experiments in quite a wide range of systems have found values of d_f close to the DLCA simulation estimates [6, 7, 16, 49]. All this encourages one to think that

aggregation is a near-universal process which can be characterised entirely by a single statistic, the fractal dimension. However as we shall show, more detailed analyses generally indicate that in most practical cases the fractal dimension tells at best only part of the story.

2.4.2 Mass distribution

The evolution of the cluster mass distribution in the DLCA model has been studied in some detail in simulation [82, 85, 86] and compared with experimental measurements in various systems (e.g. [7, 41, 87]). Qualitatively it is often observed that a distribution initially peaked at small clusters (monomers) develops into a broad 'bell-shaped' distribution, with a (sometimes very broad) peak which moves to larger and larger mass as the aggregation proceeds. The monomers and small clusters are 'soaked up' in collisions to form larger clusters.

However in simulations the behaviour of the mass distribution has been shown to depend quite strongly on how the clusters in the system diffuse, specifically on the prescription relating a cluster's diffusion constant D_{cl} to its mass m [82, 86]. If one writes

$$D_{cl}(m) \sim m^{\gamma} \tag{2.9}$$

then different values of γ lead to major qualitative changes in the form of the mass distribution. Meakin and co-workers [86] showed that a 'critical' value $\gamma = \gamma_c$ exists in DLCA. For $\gamma > \gamma_c$ a peak in the mass distribution at $m > 1$ does not develop, rather the distribution is a monotonically decreasing function (a power-law out to some time-dependent cut-off mass). Monomers and small clusters tend to dominate the mass distribution at all times. At $\gamma = \gamma_c$ the distribution is more or less flat out to a quite steep cutoff at a mass which increases with time. A value of $\gamma_c \approx -0.27$ has been reported for 2D simulations and a value $\gamma_c \approx -0.55$ for 3D [82, 86]. For $\gamma < \gamma_c$, the peaked bell-shaped distribution is formed, and as long as $\gamma < \gamma_c$ the form of the distribution is more or less insensitive to the precise value of γ.

In many simulations the prescription

$$D_{cl}(m) \sim m^{-1/d_f} \tag{2.10}$$

is employed (though in this case one needs, of course, to 'guess' d_f before running the simulation). This is equivalent to writing

$$D_{cl}(R_g) \sim R_g^{\delta} \tag{2.11}$$

with $\delta = -1$, as in equation (2.4), where R_g is the radius of gyration, because for a fractal cluster $R_g \sim m^{1/d_f}$. This in turn is equivalent to a 'Stokes-Einstein' type relation where the diffusion constant of a cluster is inversely proportional to its radius. Meakin and co-workers [76] calculated the translational friction coefficient of clusters in DLCA simulations (using a hydrodynamic approximation to the diffusion tensor) and showed that Equation (2.10) was a reasonable scaling of the diffusion constant $D_{cl}(m)$. Note that using $\gamma = -1/d_f$ implies that $\gamma < \gamma_c$ (using the values of d_f given in section 2.4.1).

The Smoluchowski equation

The starting point in many analytical and numerical studies of aggregation has been the *Smoluchowski equation* [88], which essentially expresses simply the conservation of mass in the aggregating system:

$$\frac{dc_k}{dt} = \frac{1}{2}\sum_{i+j=k} K_{ij}c_i c_j - \sum_{j=1}^{\infty} K_{kj}c_j. \tag{2.12}$$

c_k, the concentration of clusters of mass k, *increases* if smaller clusters aggregate to make new clusters of mass k, and *decreases* if k-clusters aggregate with other clusters to make new clusters of mass $> k$. The relative rates of these events depend on the concentrations of clusters of all the different sizes, *and on the 'kernel' terms* K_{ij}. K_{ij} expresses the 'co-reactivity' of clusters of masses i and j, that is the probability of such clusters aggregating. Equation (2.12) is quite general; it is in the kernel terms that the physical description of the particular process is hidden. Thus what appears a simple

statement of the conservation of mass has led to a wealth of investigations in particle aggregation [89, 90, 91] as well as in many other fields of physics (see e.g. Ref. [89] for references in turn from astrophysics, cell biology, etc.).

A few general forms of the kernel K_{ij} have been proposed. Given such a form, investigation of aggregation via the Smoluchowski equation then normally takes the form of numerical study of the evolution of the distribution of cluster masses. In Ref. [92] Cabane gives a short summary of the generic form of the mass distribution for various important kernels. Basically kernels may be classified in terms of the relative probabilities of aggregation of clusters of different sizes: for instance, whether small cluster-small cluster reactions dominate the aggregation, whether large clusters are more likely to combine with smaller clusters or clusters of roughly similar size, and so on. Botet and Jullien [90] have attempted to derive the size distribution analytically by considering the probabilities of collision events directly.

An important limitation of the Smoluchowski equation is that it ignores all *structure* in the system. The probabilities of reactions are assumed in equation (2.12) to be proportional to the average concentrations c_k (i.e. the Smoluchowski equation is a 'mean field' theory). For example it is assumed in the first term of the equation that a cluster of size j may combine with *any* cluster of size i in the system to make a cluster of size k (usually the kernal K_{ij} is considered a function only of i and j, i.e. not a spatially varying function). But in reality in systems at finite density, steric constraints imply that a given cluster is less likely to reach a cluster far away than to collide with a cluster nearby. This spatial dependence of collision probabilities must also increase with system density, as aggregates become more confined by their neighbours. Thus generally the Smoluchowski equation is expected to be truly valid only in the limit of vanishing density. Of course the equation also ignores the *geometry* of aggregates; combination probabilities may also depend on the structure of the aggregates themselves. An attempt to take account of aggregate geometry is discussed in Ref. [89]. Spatial dependence might be built into the kernels K_{ij} by making some assumption about size-position correlations in the system. We consider size-position correlation in the DLCA model in Chapter 4.

Finally the Smoluchowski equation as written here and as most frequently studied describes an *irreversible* aggregation; aggregates cannot fragment to make groups of smaller aggregates. A number of studies has been reported of a Smoluchowski-type equation including *fragmentation kernels* F_{ij} as well as aggregation kernels K_{ij} [93, 94, 95]. Generally such a reversible aggregation system is found to approach a dynamic equilibrium where the effects of the collapse of clusters and of the growth of clusters are balanced.

2.4.3 Hierarchical model

In some implementations of the DLCA model, a so-called 'hierarchical' method has been employed [34]. In this method, clusters and particles are not positioned in space. Instead, a list of clusters is maintained, each individual cluster structure being recorded by storing a list of particle coordinates relative to the cluster centre. At a given stage of the aggregation, a pair of clusters is randomly selected from the list. One of these clusters is placed stationary at the centre of a 'box', and the other cluster is allowed to diffuse in the box until it contacts the stationary cluster. At this point the clusters are 'joined' and the set of particle coordinates relative to the new combined cluster's centre recalculated. Another pair of clusters is selected from the list, and the two clusters joined, and so on. One may use various rules for selection of pairs of clusters from the list (probabilities of selection may be proportional to the cluster sizes, for instance, or a *monodisperse* aggregation may be forced by, at each stage, always selecting each cluster once in a pair, so that at each stage the number of clusters halves and the average cluster mass doubles).

While this model is sometimes computationally more efficient, it has the disadvantage that it is essentially always a *zero density* model. There is no *intercluster* spatial structure. By selecting clusters randomly from the list, one is assuming that any one cluster can collide with any other cluster. In this way it is similar to the Smoluchowski equation approach (section 2.4.2); mass-dependent selection probabilities then correspond to the kernel terms K_{ij}. The lack of intercluster spatial structure is only a reasonable assumption in the limit of very low density, where clusters can effectively explore almost

all space without colliding because the rate of collision is so low. In any real system the arrangement of clusters in space will create steric constraints, such that one cluster cannot approach another elsewhere in the system because there are other clusters in the way. This is especially true at high system density. Furthermore, as fractal clusters grow in a system at finite density they progressively fill more space (Chapter 1); the hierarchical model cannot include this effect.

2.4.4 Reaction-limited aggregation

In the diffusion-limited cluster aggregation (and diffusion-limited particle aggregation or DLA) models it is assumed that particles and clusters stick immediately on collision. In the *reaction-limited* cluster-aggregation variant, a sticking probability $P_{stick} < 1$ is implemented. When particles collide they are not automatically 'bonded', rather bonds form only with probability P_{stick}. Otherwise the clusters remain separate and continue to diffuse independently. This model is more relevant to some experimental situations, where the interparticle potential features a 'barrier' to aggregation (Figure 2.1). Approaching particles will only get close enough to 'fall into' each other's attractive potential well if they have enough kinetic energy to surmount the repulsive energy barrier.

In both experiment [7, 39] and simulation the structure of aggregates formed under 'reaction-limited' conditions has been shown to differ somewhat from aggregates formed under diffusion-limited conditions. In particular the fractal dimension for RLCA clusters is found to be somewhat higher than DLCA [96]:

2D: $d_{f,RLCA} = 1.55 \pm 0.06$

3D: $d_{f,RLCA} = 2.0 \pm 0.06$

There are also significant differences in kinetics and mass distribution [7, 41, 97]. The average mass is found to increase *exponentially* with time rather than algebraically. The mass distribution generally does not feature a peak or bell-shape under any conditions. Structural differences have been demonstrated in light-scattering experiments; some

RLCA-type experimental systems do not show a peak in the small-angle scattered intensity [46]. Others systems do show a peak [52], but the peak does not have the same scaling properties as in DLCA (see Chapter 1). 'Scattering' peaks have been demonstrated in RLCA simulations [65] but again the scaling properties differ from DLCA. Topological differences between RLCA and DLCA have also been studied [98, 99].

2.4.5 Other models

Finally we briefly mention a few other studies of aggregation. Debierre and Turban [100] have studied *chain-chain* aggregation, using a modified DLCA model where only the end monomers of chains are 'sticky'. Ansell and Dickinson [101, 102] have simulated aggregation with a *Brownian dynamics* algorithm, which conceptually can be made more realistic than the DLCA model (one can introduce hydrodynamic approximations, finite-range interactions, etc.). The disadvantage of Brownian dynamics methods is that currently only relatively small systems can be studied with realistic computational resources. Dickinson has also studied particle gelation in such a small-scale Brownian dynamics model [103]. Voss reported a study of 'multiparticle aggregation' [104], a kind of hybrid DLA/DLCA model in which many particles diffuse in a system containing a single DLA-type growing cluster. The effect of repulsive as well as attractive interactions in an RLCA system was studied by Meakin and Muthukumar [105]. Botet and Jullien [106] measured the anisotropy of DLCA clusters. *Reversible* aggregation has been considered by a number of authors in various models [93]-[95],[107]-[113] and is studied in more detail in this thesis (Chapter 4). Recently the study of the scattering properties of the DLCA system has become popular [65, 81],[114]-[119], due to the rather striking and unexpected results of recent experiments, as we have described in Chapter 1. We study in detail the structure of the DLCA system by such 'scattering methods' in the next Chapter.

2.5 Density effects in DLCA

A question which remains largely unaddressed is the behaviour of the DLCA model at high volume fraction [82]. This is important because many experimental and industrially important colloidal systems are at high volume fraction.

Indications from the first simulations were that the cluster structure, as measured by the fractal dimension, was the same in a range of system densities. Certainly simulations with particle volume (or area) fractions $\Phi \leq 0.1$ give identical estimates of d_f to within statistical error. However, a few studies have shown that the situation is not quite as simple. The 'best accepted' values of d_f have been found in low-density simulations (often simulations employing 'hierarchical' methods which are essentially equivalent to the zero-density limit, see above) [30, 31, 34]. There is some evidence from a study by Kolb and Herrmann [120] that at higher density the fractal dimension of clusters increases (to $d_f \simeq 1.75$ in 2D simulations at number density $\rho \approx 0.3$). The same authors also studied a model where effectively $\rho \to 1$, in which structural details were found to depend on the diffusivity of clusters [121].

Perhaps more important though than the structure of individual clusters is the effect of increasing volume fraction on the structure of the system as a whole. As discussed in Chapter 1, the irreversibly aggregating system consisting of growing fractal clusters will always be subject to gelation. Herrmann and Kolb [122] studied the average separation of clusters and showed that, after an initial increase in the 'aggregation' regime, this began to decrease as gelation was approached; in other words the clusters began to fill space. The simplest structural picture predicts that the gel is an assembly of fractal clusters which, as space is filled, begin to 'pack' near-homogeneously (or perhaps percolate the system, see e.g. Ref. [123]). The typical size of the 'gel clusters' depends strongly on the system density (equation (1.30)). At higher density the fractal clusters in the gel are smaller; space is filled before they can grow very large. Therefore *measuring* the fractal dimension of the clusters becomes far more difficult in systems at high density (one is trying to estimate an exponent for a power-law function often over considerably less than a decade). Indeed it might be said that the concept of

fractal structure becomes less useful since the clusters may be so small as to barely be fractals at all. Clearly a simple (or not so simple) determination of the fractal dimension of clusters in a high density system is not enough to fully characterise the structure of the system. The structure of the system as a whole (i.e. over the full range of length scales) will be of utmost importance when considering such properties as flow, porosity, response to stresses, and so on [124, 125]. The advantage of analysis by 'scattering methods' [65, 81],[114]-[119] is exactly this, that structure may be studied on all length scales.

2.6 Finite size and lattice effects

2.6.1 Periodic boundary conditions

In these simulations a large (macroscopic) system of aggregating particles is modelled by simulating a small 'real' system and applying *periodic boundary conditions*. The macroscopic system is considered as a large contiguous set of 'replicas' of the small system. For instance we can think of a two-dimensional macroscopic system as being 'tiled' by replicas of the small simulated system (Figure 2.2). If an object moves out of the small box on one side its 'image' reappears on the opposite side.

The basic assumption made when employing periodic boundary conditions is that the macroscopic system is *homogeneous* on length scales of the 'real' simulation box and larger. The macroscopic system is 'tiled' *homogeneously* with replicas of the small simulated system. If in the macroscopic system there is any important inhomogeneous structure (or indeed important *interaction*, between in our case, say, clusters) at length scales larger than the small system, it will not be properly simulated.

The cluster aggregation problem contains an intrinsically growing length scale. As the aggregation proceeds the size of the clusters increases. While the interparticle interaction appears at first sight to be confined to very short range (i.e. the particles only 'feel' each other, or stick, when they touch), still because clusters diffuse as a whole there is an effective longer-range interaction between particles in the same cluster. The

range of this interaction increases with time as the clusters grow. If the simulation is continued for long enough clusters of the size of the simulation box will appear. Beyond this scale clusters are *forced to be homogeneous by the periodic boundary conditions* (they add homogeneously to 'images' in neighbouring replicas of the system). Now, if just below the scale of the simulation box the large cluster is already homogeneous then there is no problem. But if at the box scale the cluster is still inhomogeneous (e.g. still growing fractally) then there is an artificial change in the cluster structure at the scale of the simulation box, the cluster going from inhomogeneous to homogeneous.

Gelation

The above argument has important implications for the study of gelation in the simulation. In the simple picture presented in Chapter 1 the gel is a homogeneous assembly of smaller fractal clusters. According to equation (1.30) the typical size of the *fractal units* of the gel, R_{gel}, depends strongly on system density. Now if our simulation box size is smaller than R_{gel}, it is clear the structure of the gel cannot be correctly obtained. At late time a *single* large fractal cluster, instead of a close-packed assembly of smaller fractals, will fill the simulation box. This is *not* a 'proper' gel. However at higher density the gel clusters are smaller (equation (1.30)). If the simulation system is larger than the gel cluster size, the simulated gel will have the correct structure, the homogeneous assembly of smaller fractal clusters.

Therefore in practice, because of limitations on computational power, it is difficult to obtain such a 'correct' gel structure except at quite high system density. In this thesis then the gel structure has been investigated only in systems at high density. This is anyway the situation most relevant to those experiments and industrial applications where gelation is important.

2.6.2 Diffusion on lattice

Diffusion 'steps' on the lattice are constrained to be of a whole particle diameter, which is considerably larger than the Brownian 'step' of a real physical system. The nature of the random walk means that a longer step simply corresponds to a large number of small

steps, implying that for a single isolated particle the length of the individual steps is not important. However in a concentrated system (e.g. the high number density systems considered here) the use of such a long diffusion step may cause problems, because the moving particle may collide with a nearby particle before it has had time to carry out a 'proper' diffusive motion. In the high number density lattice systems we have studied, aggregation may be seen to be very fast (see Chapter 3) implying that many particles are not able to carry out many diffusion steps before joining other particles in aggregates. However, examination of the kinetics of the aggregation (as measured for instance by the growth of the scattering peak, see Chapter 3) does not indicate any substantial differences between kinetics in the lattice-based simulations and the continuum simulations (once the time steps are rescaled to be equivalent). In addition other authors have reported off-lattice simulations whose results do not differ in any obvious way with the same results obtained in these simulations [81]. (There is also no particular evidence, for instance, of a lattice effect on the cluster fractal dimension $d_{f,DLCA}$.) Undoubtedly more important than lattice effects are the finite system-size structural effects discussed in the previous subsection.

Chapter 3

Structure of the DLCA system

Abstract

The peak in the scattering function of the aggregating system, reported for many experimental aggregating colloidal systems and also observed in the calculated 'scattering' function of the simulated system, is shown to correspond to the characteristic outer radius of a 'depletion zone' around clusters. Approximate time-independent scaling of the scattering functions, as observed in experiments, is demonstrated by the simulations, but only over a limited region of time. At high number densities and at early time in lower densities the scattering functions may be scaled only with a scaling exponent much lower than the 'accepted' DLCA fractal dimension. The structure of individual clusters and the arrangement of clusters within the system are studied by calculating cluster 'form factors' and cluster positional 'structure factors'. Scaling of the structure factor indicates that the cluster arrangement has a time independent form which simply 'expands' to longer length scales as the aggregation proceeds. Analysis of the 'separation' of the scattering function into internal cluster correlations and cross-cluster correlations indicates that the scattering function depends in a complex way on cluster structure, cluster arrangement, cluster mass distribution and the *spatial* distribution of masses.

3.1 Simulations

In this Chapter we study the structure and kinetics of the DLCA aggregation model in both two and three dimensions, at a range of particle number densities/area fractions. We calculate scattering functions, equivalent to the scattered intensity measured in scattering experiments, in order to compare results of the model directly with experiments. By computing pair correlation functions for the simulation system the features of the scattering function are related to features of the real-space structure of the system. The development of structure in the system is considered by examining the evolution of the full scattering function, the 'form factor' of individual clusters, and the 'structure factor' of the cluster positions.

Table 3.1 summarises the simulations discussed in this Chapter, including details of volume fractions, system sizes, total run times, and so on.

Density	System size L	No. particles	total run time	single cluster ?
(a) 2D, lattice-based				
0.01	500	2500	50000	No
0.1	300	9000	16799	Yes
	500	25000	19435	Yes
0.3	100	3000	125	Yes
	300	27000	394	Yes
	500	75000	244	Yes
(b) 3D, lattice-based				
0.01	70	3430	5468	Yes
0.05	70	17150	596	Yes
0.1	70	34300	118	Yes
(c) 2D, off-lattice				
0.1	89.7	1024	900000	No
0.3	51.8	1024	60000	Yes

Table 3.1. Details of lattice-based and continuum (off-lattice) simulations. System size L is in particle diameters; run time is in simulation steps. Where repeat simulations have been run in the same systems, typical example total run times are given. The final column indicates whether the run was continued until all particles belonged to a single cluster.

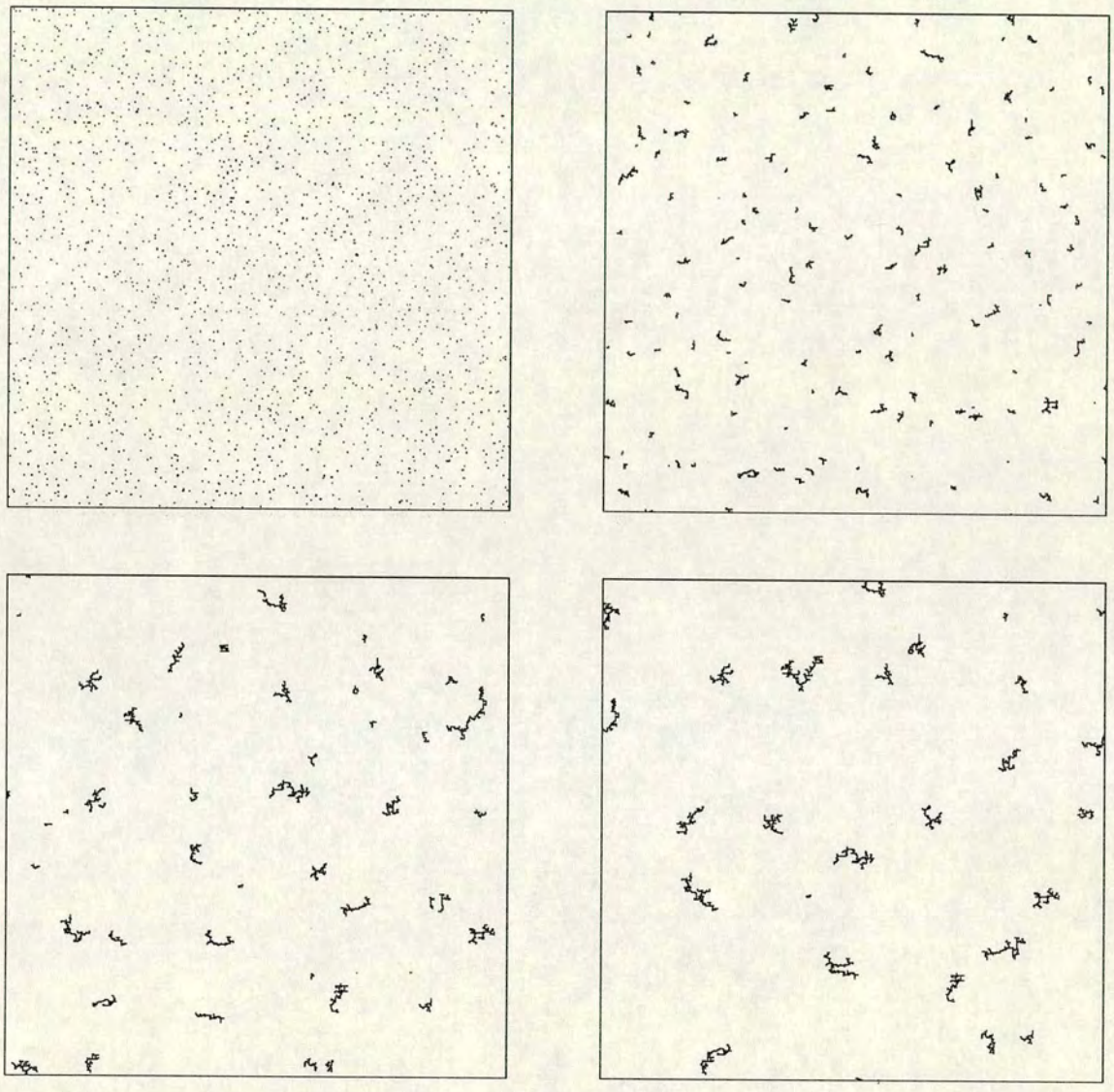

Figure 3.1. The lattice-based 2D aggregating system, with system size $L = 500$ and number density $\rho = 0.01$. Times shown are $t = 10$, $t = 3000$, $t = 10000$ and $t = 20000$ simulation steps.

3.1.1 Visual representation of the aggregating system

Pictures of the 2D and 3D DLCA simulation systems at various densities and times are shown in Figures 3.1, 3.2, 3.3, 3.4 and 3.5. (In the 3D pictures, for clarity the particles are drawn as circles around 80% smaller than the true particle size. The 3D pictures demonstrate convincingly the difficulties faced in experiment and simulation alike when trying to image three-dimensional systems.)

Qualitative differences between 'low-density' and 'high-density' systems are immediately apparent from the 2D pictures. At the low densities, the system consists of a 'sol' of separate, well-defined fractal clusters. At least in intermediate time visual observation would suggest that the typical structure of these clusters does not change as they coalesce and grow; quantitative structural measures (the calculation of cluster form factors, see section 3.3.2) confirm this. The lower density pictures compare well with experimental images (e.g. Refs. [7, 52]). The high-density system (e.g. number density $\rho = 0.3$ in 2D) looks rather different. The system is so full of particles that well-defined separate clusters cannot form. From the earliest times the cluster size and cluster separation are comparable, and very quickly the clusters fill the system. The total run time to obtain a single cluster at $\rho = 0.3$ in 2D is typically only $t_g \sim 300-400$ simulation steps, compared to $t_g > 10000$ steps for $\rho = 0.1$. In 3D too, at the final stage the high density system (Figure 3.5) is 'filled' by the final cluster, while at lower density (Figure 3.4) the system is much more open, containing a single isolated cluster.

At high density, a high degree of *shape correlation* between neighbouring clusters is also visible. As they grow clusters are competing for 'growth material'. This generates roughly correlated neighbouring surfaces or perimeters. Shape correlation leads to the clearly visible system of 'channels' running through the high-density system. A similar channel effect has been remarked upon in experimental studies of 2D aggregating colloids [99]. The effect of shape correlations on the scattering properties of the aggregating system will be returned to later in this Chapter and in Chapter 4.

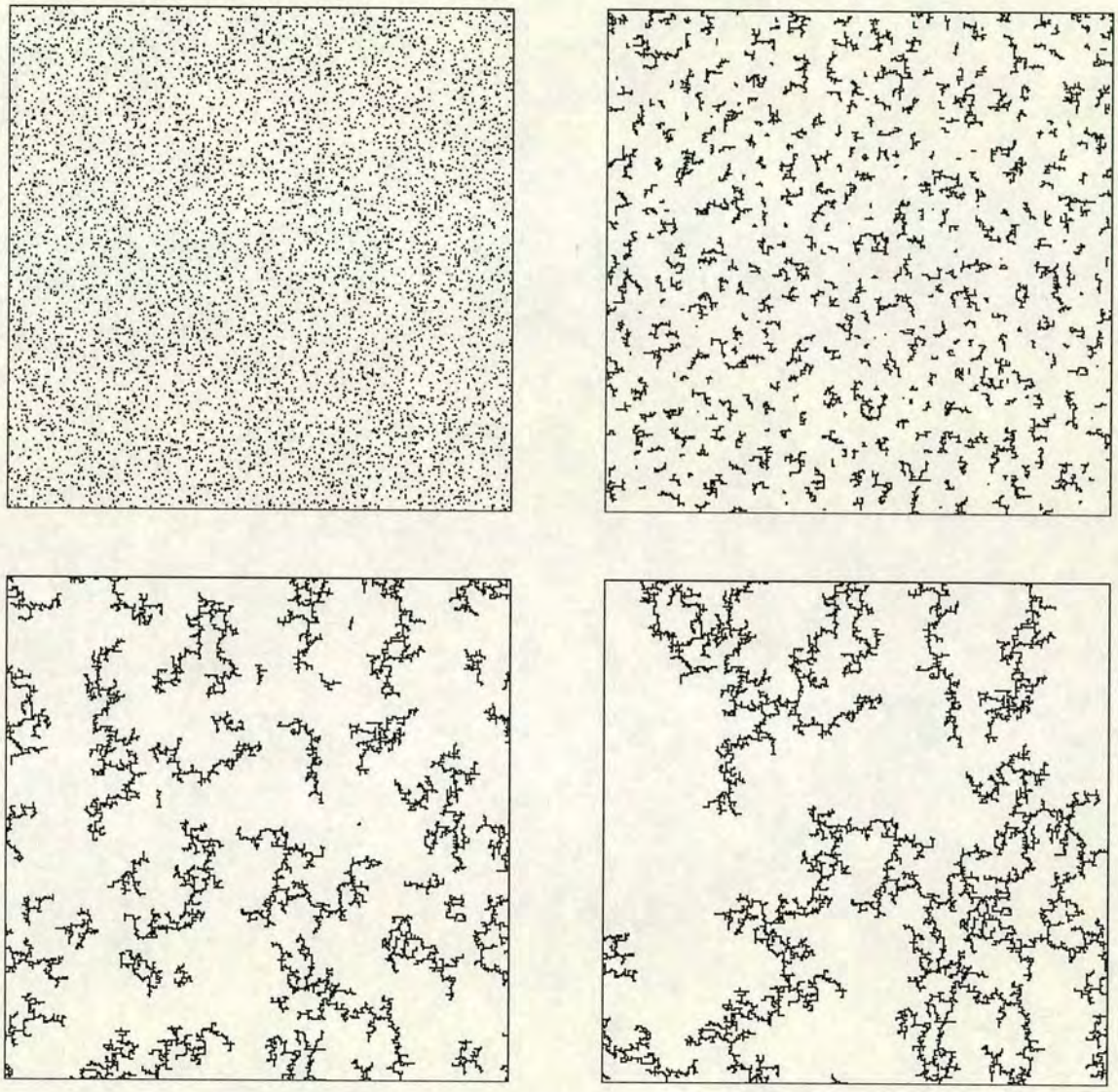

Figure 3.2. The lattice-based 2D aggregating system, with system size $L = 300$ and number density $\rho = 0.1$. Times shown are $t = 1$, $t = 100$, $t = 1000$ and $t = 16799$ simulation steps. At the final time all the particles belong to a single fractal cluster.

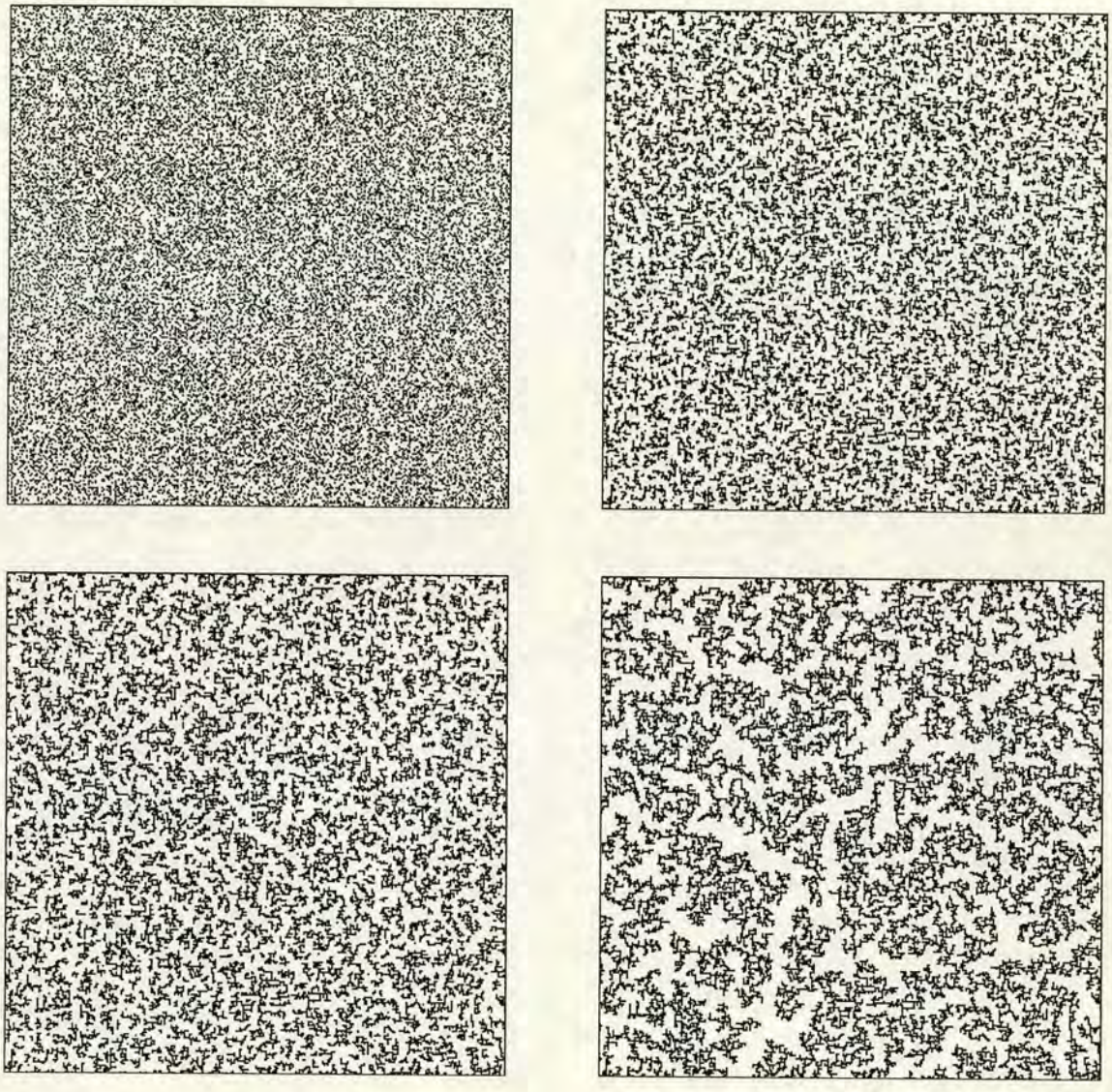

Figure 3.3. The lattice-based 2D aggregating system, with system size $L = 300$ and number density $\rho = 0.3$. Times shown are $t = 0$, $t = 5$, $t = 10$ and $t = 394$ simulation steps. At the final time all the particles belong to a single cluster, whose structure is fractal at short length scales but near-homogeneous at longer lengths (see text).

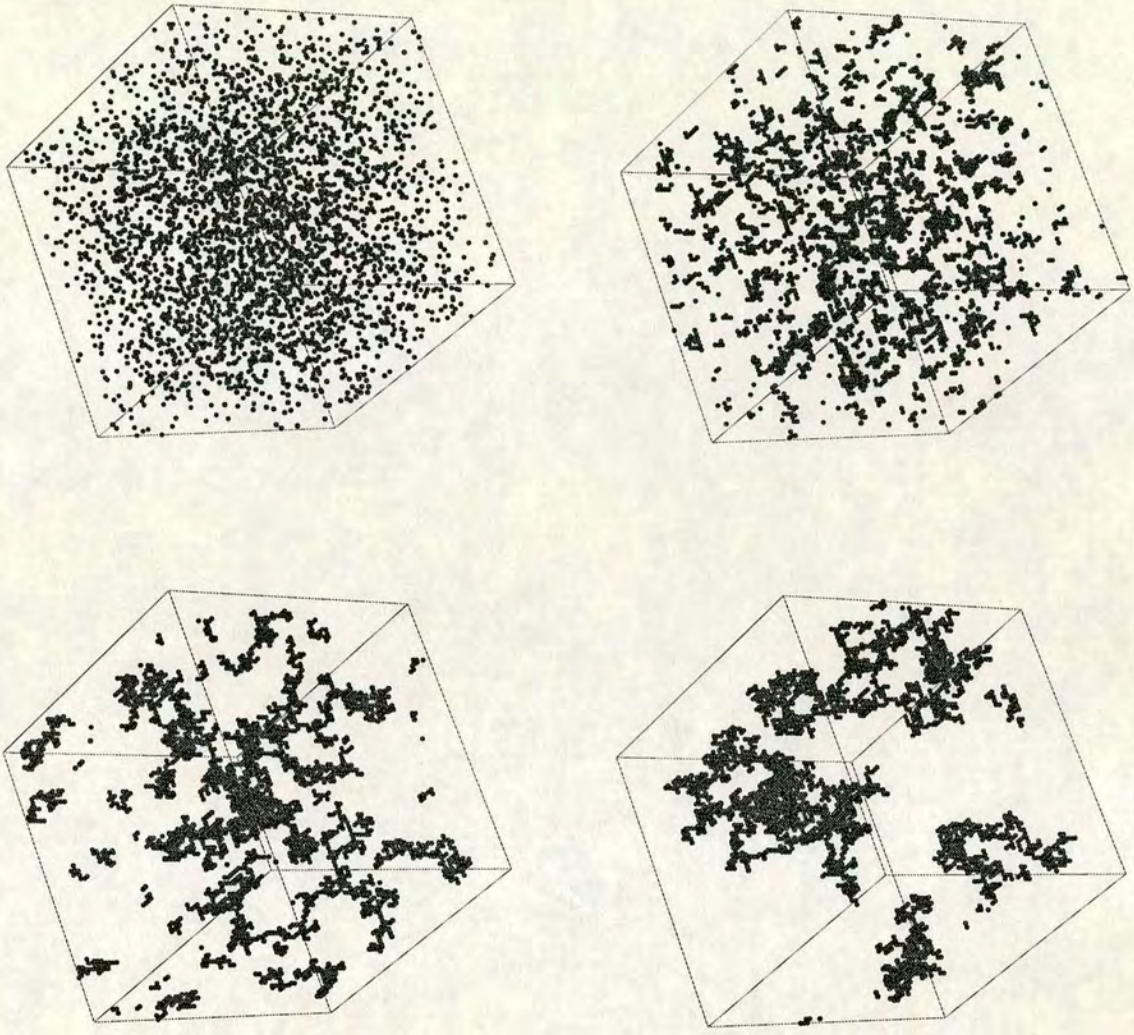

Figure 3.4. The lattice-based 3D aggregating system, with system size $L = 70$ and number density $\rho = 0.01$. Times shown are $t = 0$, $t = 100$, $t = 500$ and $t = 5468$ simulation steps. At the final time all the particles belong to a single cluster (connected around the periodic boundaries).

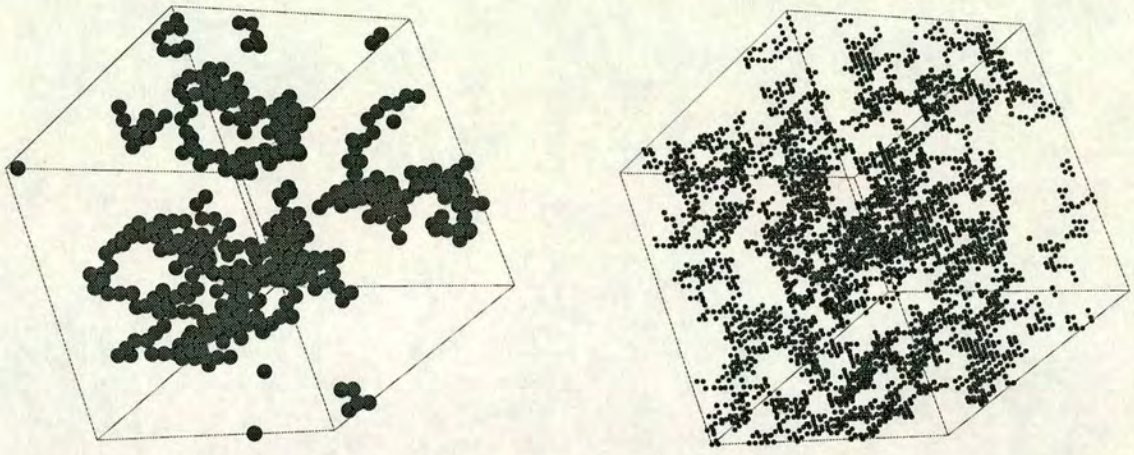

Figure 3.5. The lattice-based 3D aggregating system, with system size $L = 70$ and number density $\rho = 0.05$. Shown here are 'cut-outs' of parts of the system, on the left for time $t = 50$, a cube of side-length $l = 20$ cut out from the full system (with $L = 70$); on the right for time $t = 596$ (the 'gel time' for this run), a cube of side-length $l = 40$.

3.2 The scattering function

3.2.1 Calculation of $I(\mathbf{Q})$

As described in Chapters 1 and 2, we calculate the scattering function $I(\mathbf{Q})$ of the simulated system from

$$I(\mathbf{Q}) = \frac{1}{N} \sum_{j}^{N} \sum_{k}^{N} b_j(\mathbf{Q}) b_k(\mathbf{Q}) exp[i\mathbf{Q}.(\mathbf{r}_j - \mathbf{r}_k)]. \tag{3.1}$$

Note that the $1/N$ factor (N is the number of particles) is introduced in our calculations in order that the scattering functions from simulations with different system sizes L may be compared. (In experiments the scattering volume is usually a constant, defined as it is by the dimensions of the incident laser beam.) $I(\mathbf{Q})$ can be observed on the reciprocal-space lattice (defined by the set of allowed scattering vectors $\mathbf{Q}$) by plotting the equivalent of a *speckle pattern*. In such a pattern the amplitude $I(\mathbf{Q})$ of the scattering function at each coordinate $\mathbf{Q}$ on the reciprocal lattice (the scattered intensity at a given reciprocal lattice vector in a real scattering experiment) is represented

by a dot drawn with an area proportional to $I(\mathbf{Q})$. Figure 3.6 shows an example of an evolving speckle pattern calculated from a 2D simulation. For comparison, an example of an experimental scattering pattern, from a (3D) experiment on an aggregating colloid-polymer mixture [16], is given in Figure 3.7[1].

Immediately it is clear that the simulation structure gives a scattering pattern qualitatively similar to that observed in many experiments (see for example [54]); we see a bright ring of scattered light which shrinks to smaller angle and increases in intensity as the aggregation proceeds. Qualitatively similar behaviour is observed at all number densities in both 2D and 3D systems.

Circularly- or spherically-averaged plots of the scattering function $I(Q)$ versus scattering vector magnitude $Q = |\mathbf{Q}|$, for various densities in 2D and 3D systems are shown in Figures 3.8 and 3.9. (In the plots the x-axis is in units of $Q \times d$ where d is the particle diameter; since Q is measured in inverse particle diameters, Qd is then a dimensionless quantity. For on-lattice models the particle diameter is equal to the lattice parameter.) The circularly/spherically averaged function is calculated by averaging the values of $I(Q)$ for all reciprocal space vectors $\mathbf{Q}$ with magnitude between $Q - \delta Q$ and Q. We average $I(\mathbf{Q})$ in a circular annulus (2D) or spherical shell (3D) of width δQ, with an annulus/shell 'bin' width between $\delta Q = 0.012$ and 0.1 (particle diameters)$^{-1}$. The bin width has been chosen to give the best compromise between resolution of features in the scattering pattern and averaging over enough reciprocal lattice points to give reasonably noise-free data. Further, in some cases $I(Q)$ has been calculated from averages over a number (< 10) of repeat runs of the simulation (under identical conditions but with a new set of random numbers), in order to reduce noise in the scattering pattern.

From the circularly/spherically-averaged plots the development of the small-angle or small-Q peak in the scattering function is evident. The peak increases in intensity and moves to smaller Q, in qualitative agreement with the behaviour observed in experiments [11, 16, 45, 49, 50, 52]. One way to study quantitatively the evolution in time of the system structure is to measure peak positions Q_m and peak amplitudes $I(Q_m)$ as functions of time. We return to this more detailed analysis in section 3.4.

[1] The picture was kindly provided by A. D. Pirie.

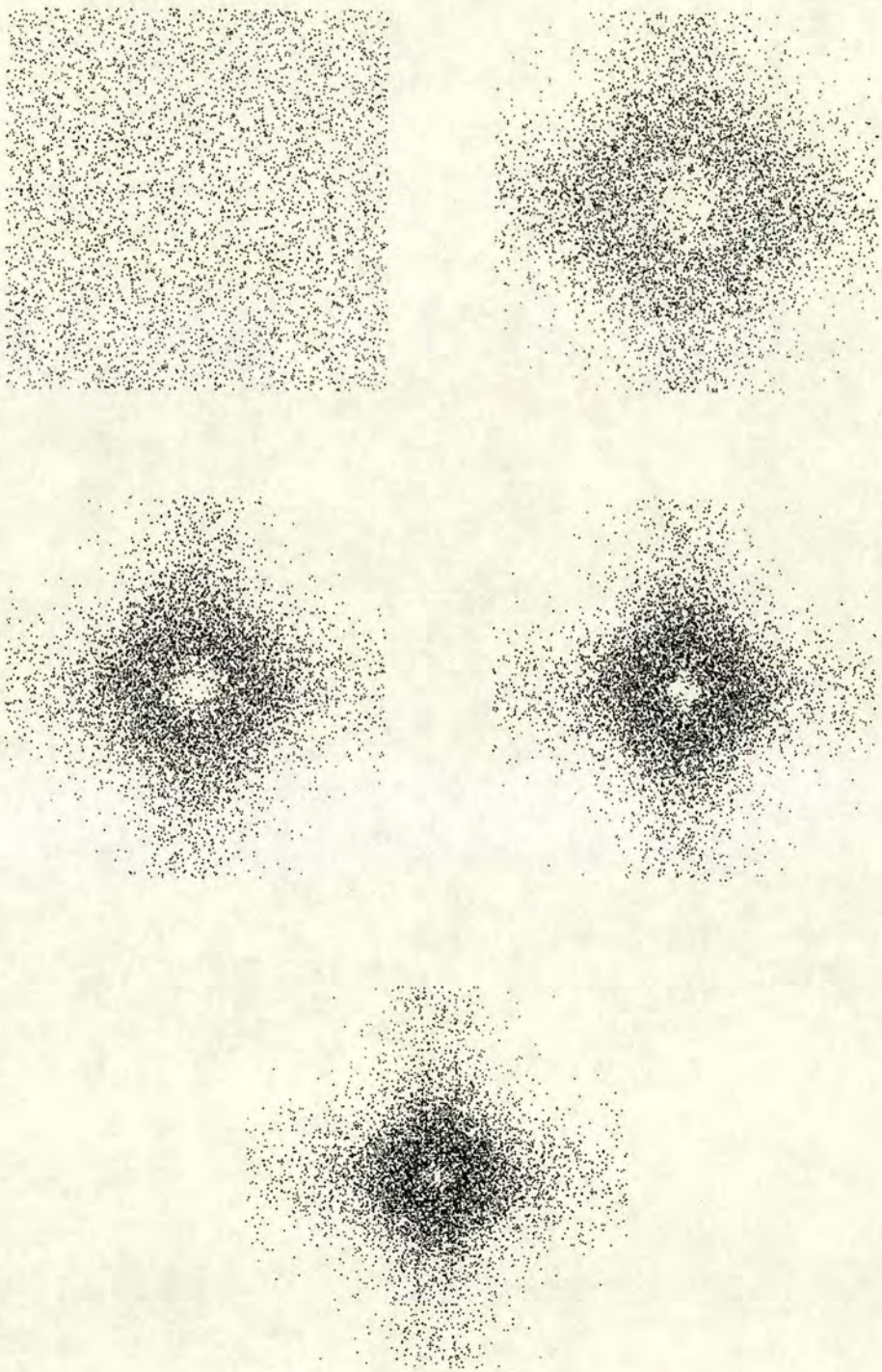

Figure 3.6. 'Speckle' patterns $I(\mathbf{Q})$ from a 2D lattice-based simulation at number density $\rho = 0.3$, system size $L = 300$, for times $t = 0$, $t = 1$, $t = 3$, $t = 5$ and $t = 10$ simulation steps. $I(\mathbf{Q})$ is calculated on the grid of reciprocal lattice points, with lattice parameter $\delta Q = 2\pi/L$ and extent $-\pi/d < q_x, q_y < \pi/d$ (d is the particle diameter or lattice spacing). The bottom left corner of each plot is at $\mathbf{Q} = (-\pi/d, -\pi/d)$, the origin $\mathbf{Q} = 0$ is in the centre and the top right corner is $\mathbf{Q} = (\pi/d, \pi/d)$. The 'cross-like' patterns are discussed in the text.

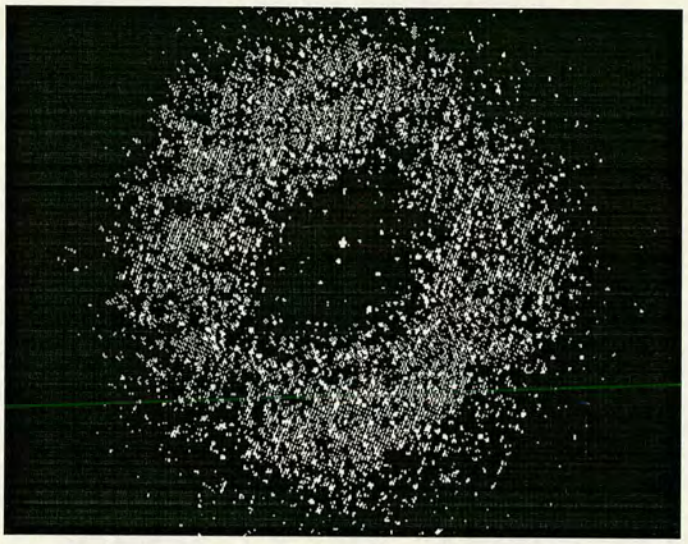

Figure 3.7. Speckle pattern of scattered light from a small-angle light-scattering experiment on an aggregating colloid-polymer mixture (a suspension of sterically stabilised polymethylmethacrylate colloidal spheres, with non-adsorbing polystyrene). The experiments are described in Ref. [16].

3.2.2 Lattice effects on $I(\mathbf{Q})$

As discussed previously (Chapter 2) in the lattice-based simulations the lattice structure is imposed on the system at short length scales comparable to the lattice parameter d. This has observable effects on the scattering function $I(\mathbf{Q})$, as can be seen clearly in the speckle patterns in Figure 3.6. The lattice structure which the clusters are forced to adopt at small length scale gives rise to increased scattering intensity along the reciprocal space axes, at large scattering vector magnitude (away from the centre of the speckle patterns), giving the cross-like patterns in the speckle plots.

The use of the lattice does not appear to have a substantial effect on the time evolution of the scattering functions however, as is shown in section 3.4 where data from the lattice-based simulations are compared in more detail with data from the off-lattice model.

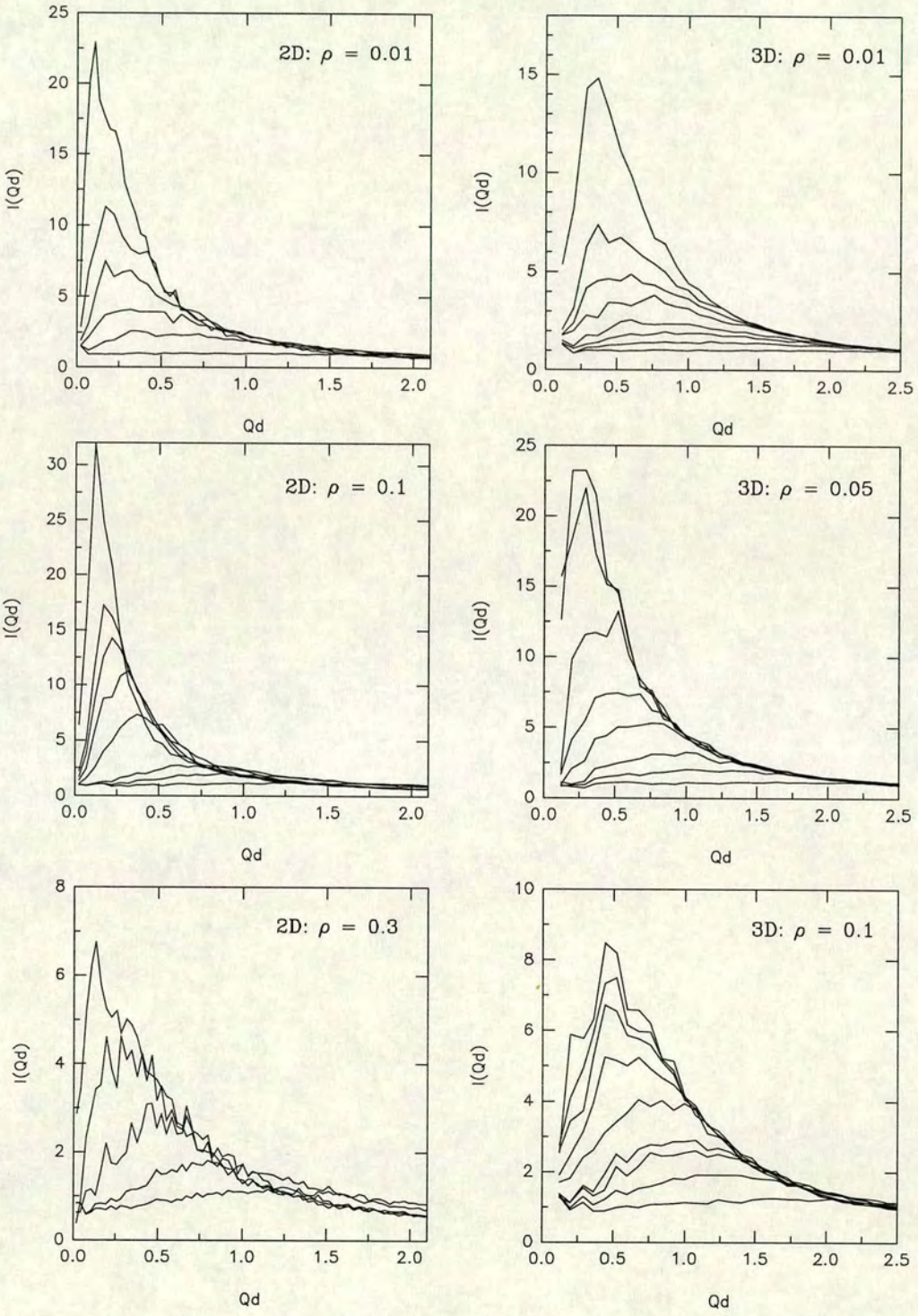

Figure 3.8. Circularly-averaged calculated scattering functions $I(Q)$ for lattice-based DLCA simulations in 2D and 3D. The 2D system size is $L = 500$, the 3D size is $L = 70$. 2D number densities are $\rho = 0.01$, $\rho = 0.1$ and $\rho = 0.3$. 3D number densities are $\rho = 0.01$, $\rho = 0.05$ and $\rho = 0.1$. As time increases the peak moves to smaller Qd and increases in intensity.

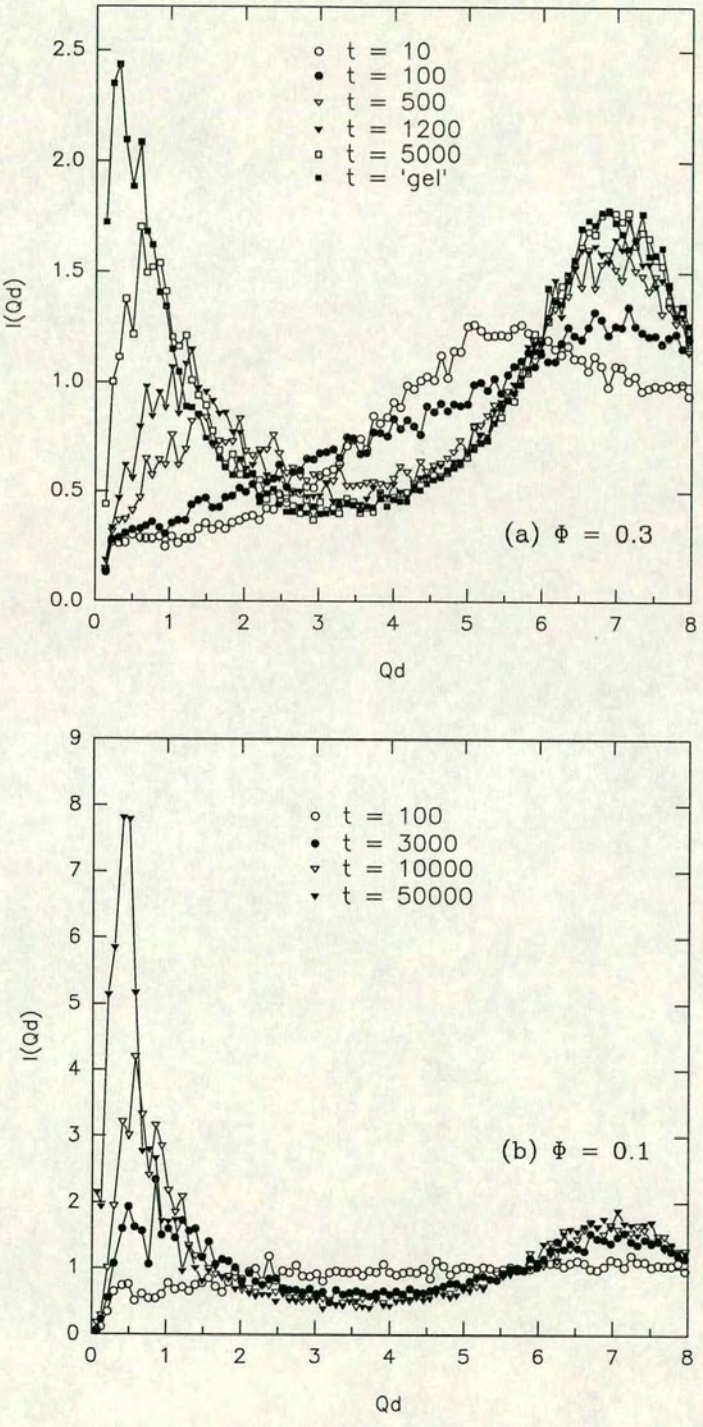

Figure 3.9. Circularly-averaged calculated scattering functions $I(Q)$ for off-lattice DLCA simulations in 2D. The 2D system size is $L \approx 51.8$ for area fraction $\Phi = 0.3$ and $L \approx 89.9$ for $\Phi = 0.1$.

3.2.3 Pair correlation function and depletion zones

The main question raised by results of recent scattering experiments on aggregating colloidal systems [11, 16, 45, 49, 52] is, what structural feature in the aggregating system gives rise to the peak in $I(Q)$? The existence of a peak in the scattering function implies that there is a characteristic or dominant length scale of structures in the system. However, due to the difficulty of direct observation in most experimental systems, it has not been clearly demonstrated from experiment exactly what structural features on this length scale there are in the aggregating system.

Discussions of the concept of 'depletion zones' surrounding growing clusters in the context of phase-separating systems appear in the literature as long ago as the 1960s [21, 66]. In this picture the system is occupied by clusters, that is areas of higher than average density, each separate and surrounded by an area of lower-than average density. The large clusters, which diffuse more slowly than the smaller clusters, essentially 'drain' particles and smaller clusters from the surrounding regions, thus generating depleted zones between large clusters.

While this concept has become reasonably well-accepted, direct observation from aggregation experiments has proved difficult. Two-dimensional experiments are of particular use here, because the problems of trying to image by microscopy through a macroscopic 3D system are avoided. In simulation, depletion zones have been convincingly demonstrated in the *pair correlation functions* of phase-separating fluids and fluid mixtures calculated from molecular dynamics (MD) and Brownian dynamics (BD) simulations [68, 126, 127]. However, definite demonstration of the DLCA aggregating system as composed of clusters surrounded by 'depletion zones' has not until very recently been forthcoming. In our work [117] (and in simultaneous work elsewhere [65]) it has recently been shown that calculation of the pair correlation function $g(r)$ of the DLCA simulation system may be used to demonstrate the existence of depletion zones[2], and indeed this analysis allows a *quantitative* determination of what physical feature the 'characteristic' length indicated by the scattering functions corresponds to.

[2]Though depletion zones in the density correlation function $C(r)$ may be visible even in some of the first DLCA simulations, e.g. [30].

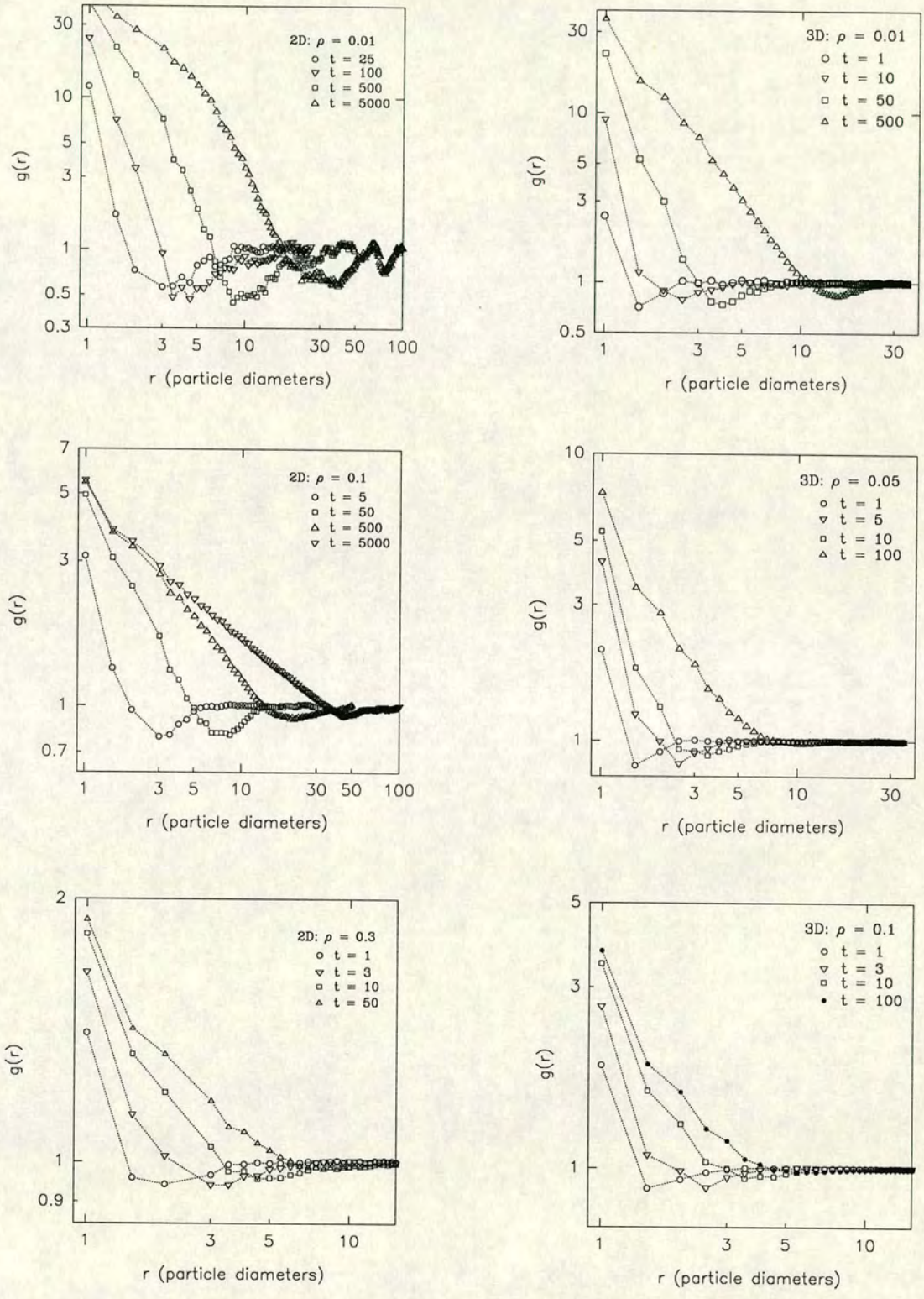

Figure 3.10. Circularly-averaged pair distribution functions $g(r)$ for lattice-based DLCA simulations in 2D and 3D. The 2D system size is $L = 300$ for number densities $\rho = 0.1$ and $\rho = 0.3$, and $L = 500$ for $\rho = 0.01$. The 3D system size is $L = 70$ for all number densities. The $g(r)$ functions are circularly/spherically averaged in 'bins' of width $\delta r = 0.5$ particle diameters.

The pair correlation function $g(r)$ is defined and described in Chapter 1. Some plots of $g(r)$ for 2D and 3D systems at various number densities, showing the evolution of the function in time as the aggregation proceeds, are given in Figure 3.10. In these plots the $g(r)$ function is circularly- (2D) or spherically-averaged (3D) by averaging $g(\mathbf{r})$ values in circular or spherical 'bins' of width $\delta r = 0.5$ particle diameters. The function is further averaged, as described in Chapter 1, by treating each particle in turn as the 'origin' for the calculation of $g(r)$.

$g(r)$ for particle aggregation simulations has been studied to some extent before (e.g. [101, 102, 103]). However as pointed out in Ref. [68], the short-length scale oscillations in the function can sometimes mask or divert attention from the larger features, e.g. the depletion zone (see below). Some degree of 'coarse graining' is necessary, for instance we use a relatively large 'bin width' $\delta r = 0.5$ diameters. In contrast, in Ref. [103] a bin width $\delta r = 0.2$ is used, which allows resolution of short-length scale features but also 'confuses' the plot such that the depletion zone is not so clearly visible.

Some particular features of $g(r)$ for the aggregating system are immediately apparent. First, the function quickly develops a peak at $r = 1.0$ particle diameters, which is sometimes called the 'touching' peak; it corresponds to particles bonded together at a distance of two particle radii. This peak appears and grows quite quickly, indicating the clustering of particles. The growth of this peak then slows at later time indicating that the average *local* structure in the system, that is the structure of nearest neighbours, becomes nearly constant. The short-length scale structure is quickly established. Because the clusters are fractals, more particles or clusters are quite unlikely to penetrate close to *most* of the particles in a given cluster, due to the *screening* effect of the fractal structure. Moreover, when two fractals collide, in this irreversibly- and rigidly-bonding model they tend to bond at only one point, so that collisions tend not to affect the local environment of *most* of the particles. Thus in the irreversible model on average the structure local to any given particle does not change very much through the later stages of the aggregation.

We can use the $g(r)$ function to estimate the average number of nearest (bonded) neighbours of the particles. From the definition of $g(r)$ we have that $g(1)$ is related to

$n(1)$, the average number of nearest neighbours, by

$$n(1) = 2\pi\rho g(1)dr. \tag{3.2}$$

A rough estimate of the 'limit' of $g(1)$ from the 2D plots in Figure 3.10 gives $n(1) \approx 1.6$ ($g(1) \approx 50$) for $\rho = 0.01$ and $n(1) \approx 1.9$ for $\rho = 0.1$ and 0.3 ($g(1) \approx 6$ and $g(1) \approx 2$ respectively). In 3D we find $n(1) \approx 3.1$ ($g(1) \approx 50$, $\rho = 0.01$), $n(1) \approx 2.8$ ($g(1) \approx 9$, $\rho = 0.05$) and $n(1) \approx 3.1$ ($g(1) \approx 5$, $\rho = 0.1$). These values are reasonable for ramified aggregates.

A second feature of the $g(r)$ functions is the presence of a *minimum* at intermediate length scale. Between the touching peak and the minimum, the $g(r)$ function typically measures structure 'inside' the cluster[3]. Roughly beyond the extremities of the typical cluster then there is a dip in the pair correlation function—at this distance from any typical particle, it is *less likely than average that we will find another particle.* In other words, typically there is a 'depleted zone' around clusters, a zone of lower than average density. Thus this is a direct observation of the existence of depletion zones around clusters in the DLCA system.

3.2.4 The scattering peak and the depletion zone

Various rather loose definitions of the correspondence between the scattering peak position and physical lengths in the aggregating system have been given in the literature. For instance the peak in the scattering function has often been said to indicate the 'average cluster size'. However, in experiments with aggregating emulsions [49] where there was a clear distinction between the size of clusters and the distance between clusters, and it was found that the cluster size was far too small to be associated with the scattering peak. It has alternatively been postulated [47, 49] that some kind of ordering of the arrangement of clusters may be responsible for the small-Q peak in the scattering function. The possibility of an ordered arrangement of clusters is investigated further

[3]Though note that since we are averaging $g(r)$ by using *every* particle as origin, the $g(r)$ function cannot be precisely interpreted this way; it is more of an average environment, or correlation, 'seen' by any particle.

in section 3.3.3.

A more quantitative and precise definition of the length scale indicated by the scattering peak would clarify the situation. To relate features in the scattering function to physical lengths in the system it is natural to consider the pair correlation function, since the scattering function is essentially the Fourier transform of $g(r)$ (see Chapter 1):

$$I(\mathbf{Q}) \propto \int [g(\mathbf{r}) - 1] exp(i\mathbf{Q}.\mathbf{r}) d\mathbf{r}. \tag{3.3}$$

The simulation results here indicate that the scattering peak length scale is not the size of clusters, but rather is *the radius of the cluster-plus-depletion-zone 'object'*. This is demonstrated by comparing the length scale equivalent to the peak in the scattering function, l_q, to the pair correlation function $g(r)$. If the scattering peak is at scattering vector $Q_m(t)$ at time t then the corresponding equivalent length scale is given by

$$l_q(t) = 2\pi / Q_m(t) \tag{3.4}$$

(where $l_q(t)$ is in particle diameters, since here the scattering vector Q is always measured in inverse particle diameters). In Figure 3.11 plots of the pair correlation function are given with the length scale $l_q(t)$ for the corresponding time indicated on each of the curves. It is clearly seen from the plots that l_q is approximately equivalent to *the outer radius of the depletion zone* in the pair correlation function. This appears to be true throughout the aggregation. Therefore the precise meaning of the peak *position* in the scattering function can be better defined now: there is a peak in the scattering function at a scattering vector equivalent to the length scale of the outer radius of the depletion zone around clusters. It is this typical cluster surrounded by its depletion zone which gives rise to the 'characteristic' length scale indicated by the scattering function.

If one assumes that there is *only one 'characteristic' length scale in the aggregating system*, to which all other physical lengths are simply proportional, then it may be argued that the above distinction between cluster size, cluster separation, and any other lengths, is not so important. This idea of a single characteristic length scale

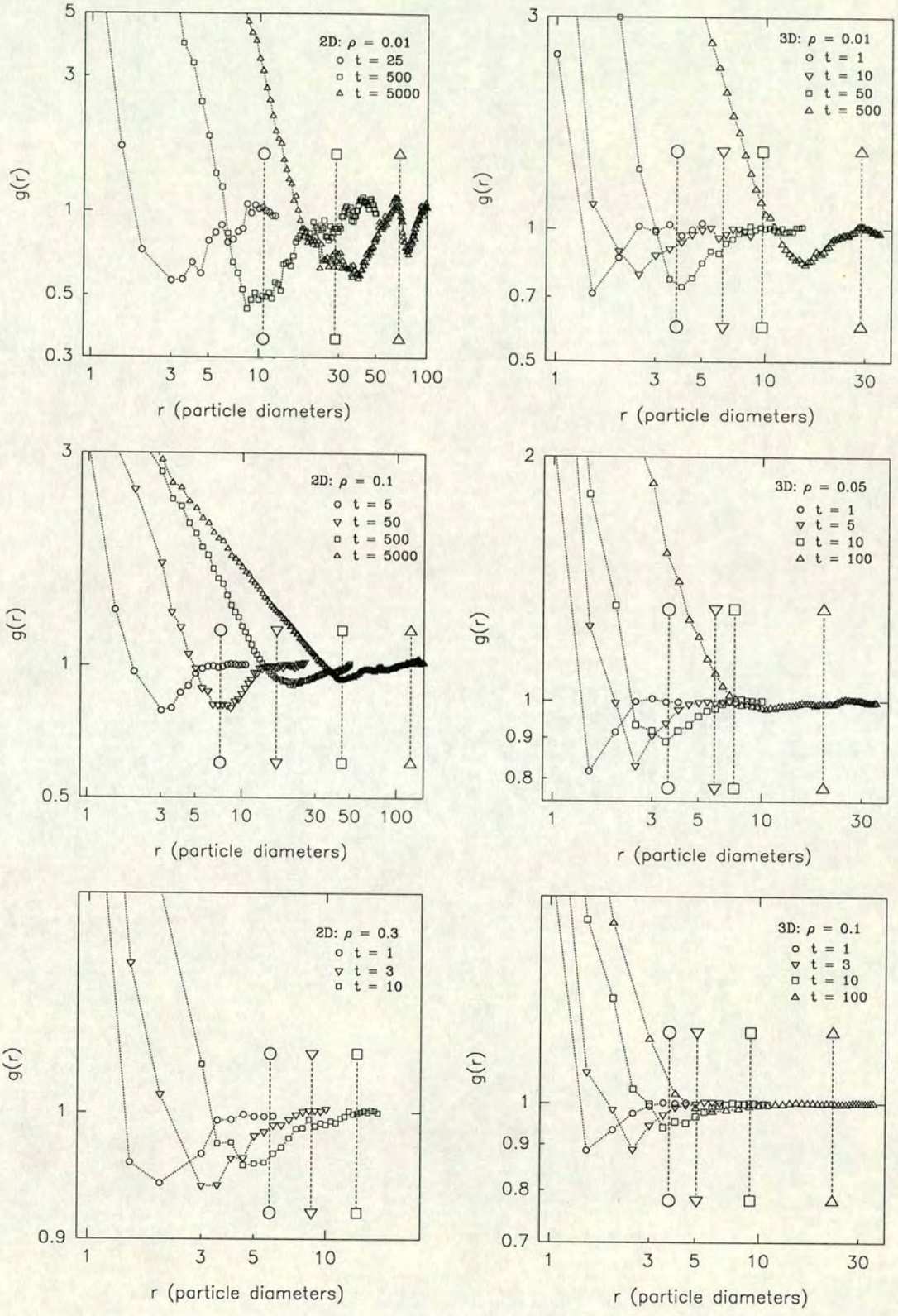

Figure 3.11. Pair distribution functions $g(r)$ from lattice-based DLCA simulations, with the length scales $l_q(t) = 2\pi/Q_m(t)$ indicated. The peak in the scattering function $I(Q)$ at $Q = Q_m$ corresponds to a length scale of the outer radius of the depletion zone in $g(r)$.

is at the heart of *scaling hypotheses* which have been proposed and to some extent demonstrated for colloidal aggregation [45, 52, 69, 81, 117]. Investigation of the scaling hypothesis as applied to scattering data is presented in section 3.5. A direct comparison of the scaling of various lengths in the aggregating system [117] is reported in Chapter 5.

3.3 Cluster structure and inter-cluster structure

3.3.1 'Separation' of scattering

To describe the structure of a system consisting of a collection of objects it is sometimes a useful approach to describe separately the *internal structure of the individual objects* and the *arrangement of the objects* in the system. This approach is commonly used in the interpretation of scattering patterns from experimental colloidal systems. The system is considered as made up of an assembly of 'scatterers'. If, as is often assumed to be the case in model colloidal systems, the scatterers are identical, then the full scattering intensity (equation 3.1) may be factorised into two components:

$$I(\mathbf{Q}) = P(\mathbf{Q})S(\mathbf{Q}). \tag{3.5}$$

(Note that in (3.5) we have dropped the N from equation 1.17 of Chapter 1, since in practice in order to compare results from different system sizes we 'normalise' $I(Q)$ by $1/N$, equation (3.1).) $P(\mathbf{Q})$ is the scattering function or *form factor* of the object—$P(Q)$ measures the internal structure of the object. $S(\mathbf{Q})$, the *structure factor*, measures the arrangement of the objects in the system. A detailed description of this kind of 'separation' of scattering into form factor and structure factor, particularly for experiments in model colloids, is given in Ref. [2].

For the factorisation in equation (3.5) to work, various conditions must be met. As already mentioned, ideally the scatterers must be identical (so that an identical factor $P(Q)$ may be removed from the scattering function). Certain situations have been considered (e.g. for polydisperse spherical colloids) in which an 'average' form factor can be defined, and the separation thus modified [128]-[133]. Even under these extensions,

the separation requires essentially that *all correlations between different clusters* are contained in $S(\mathbf{Q})$; in other words in the case of polydisperse particles, it is expected that any correlation between the size of particles and their relative positions would cause the breakdown of the factorisation in equation (3.5). Similarly in the case of a system of growing objects, such as in particle aggregation, any correlation between the positions of particles in separate clusters must be contained in $S(\mathbf{Q})$; this condition might break down if, for instance, the growing shapes of nearby clusters were somehow dependent on each other.

In this section, we calculate the form factor of the 'typical cluster' in the DLCA aggregating system, and the cluster positional structure factor of the system of aggregates. Regardless of whether the separation of scattering according to equation (3.5) works or not, the form factor provides information on the evolution of the structure of individual clusters as the aggregation proceeds; and the structure factor tells us how the clusters are arranged in the system and how this arrangement develops with time. The form factor may be compared with models of scattering by fractals, providing more information on the fractal dimension, etc. The calculated structure factor may be compared with theoretical predictions for models such as the hard sphere fluid to see if the *effective interactions* between the clusters may be further clarified. These analyses thus provide a rather more detailed picture of the nature of the aggregating system.

3.3.2 Cluster form factor

The form factor of a single cluster of particles is obtained from equation (3.1), where as usual in the simulation analysis we treat the particles as 'delta functions' with particle scattering functions $b_j = 1$, by inserting into the equation the set of coordinates $\{\mathbf{r}_k\}$ of the particles of the given cluster k. Thus the form factor $P_k(\mathbf{Q})$ of cluster k is calculated from

$$P_k(\mathbf{Q}) = \frac{1}{M_k} \left| \sum_j^{M_k} exp(i\mathbf{Q}.\mathbf{r}_j) \right|^2 , \tag{3.6}$$

where M_k is the mass (number of particles) of the cluster and $\mathbf{Q}$ is the scattering vector. Circular or spherical averaging can be used as before to obtain $P(Q)$, where Q is the

magnitude of the scattering vector. Of course $P(\mathbf{Q})$ depends on the shape of the cluster. Circular/spherical averaging $P(\mathbf{Q})$ for a single cluster may not be tenable if a cluster is highly anisotropic, as indeed evidence from experiments [7] and simulations [106] suggests that DLCA clusters are. For the purposes of calculating an *average* form factor however, that is the scattering function of a 'typical' cluster in the DLCA simulation, one may assume that anisotropy of clusters does not affect the calculation as long as one can average over a substantial number of clusters, *and* as long as the orientation of different clusters is independent. If these conditions are not met one will not be sampling enough differently-oriented clusters, and the circularly/spherically-averaged $P(Q)$ function will be more difficult to interpret as the orientational information will be 'buried' inside it.

Form factor of a fractal cluster

A simple form is expected for the scattering function of a (circularly or spherically symmetric) fractal object [24, 92, 134]:

$$P(Q) \sim Q^{-d_f} \qquad (Q_l < Q << Q_u) \tag{3.7}$$

$$P(Q) \to M \qquad (Q \to 0) \tag{3.8}$$

where M is the cluster mass, d_f is the fractal dimension of the cluster and Q_l and Q_u are the lower and upper (reciprocal space) cut-offs respectively; Q_l corresponds to a length scale of the size of the cluster, Q_u to the size of the 'monomers' making up the cluster. A more detailed functional form which has been used to fit experimental light-scattering data for aggregating colloidal systems [6] is given by the 'Fisher-Burford' (FB) expression [134][4]:

$$P(Q) = \frac{A}{[1 + 2Q^2R_g^2/3d_f]^{d_f/2}}. \tag{3.9}$$

R_g is a measure of the cluster radius, d_f is the fractal dimension, and A is proportional to the cluster mass [47]. This function includes both the power-law region $P(Q) \sim Q^{-d_f}$

[4] This phenomenological form for the scattering function was first used by Fisher and Burford [135] in examining scattering by systems at the critical point.

at larger Q and the 'rollover' to the near-constant region as Q approaches zero:

$$P(Q \to 0) \to A(1 - \frac{Q^2 R_g^2}{3}). \tag{3.10}$$

Plotting P *vs.* QR_g demonstrates that the 'rollover' corresponds approximately to $QR_g = 1$, or $Q_l \approx 2\pi/R_g$ (see Figure 3.14).

Average form factor

There are various ways in which an average form factor $P(Q,t)$ of all clusters in the system at a given time t may be calculated. The most obvious is to simply add the scattering intensity calculated for all individual clusters and divide by the total number of particles:

$$P(\mathbf{Q},t) = \frac{\sum_k^{N_c} \left| \sum_j^{M_k} exp(i\mathbf{Q}.\mathbf{r}_{jk}) \right|^2}{\sum_k^{N_c} M_k}, \tag{3.11}$$

where N_c is the number of clusters at time t, and $\mathbf{r}_{jk}$ is the position of the j^{th} particle of cluster k. This approach is equivalent to weighting each (normalised) individual cluster's form factor (equation (3.6)) by the mass of the cluster, that is

$$P(Q,t) = \frac{1}{\sum_k^{N_c} M_k} \sum_k^{N_c} M_k P_k(Q,t). \tag{3.12}$$

This means that larger clusters tend to contribute more to the average. An equivalent average to equation (3.11) has been used previously, for example in the analysis of scattering data from and theoretical models of polydisperse hard spheres [128, 129, 130].

Results–evolution of cluster structure

Examples of average cluster form factors are given on log-log plots in Figure 3.12 for 2D and 3D simulations at various number densities and times. P is plotted against Qd where d is the particle diameter. Since monomers are treated as 'delta functions' in the scattering equations, for an initial system consisting only of monomers we would have $P(Q, t = 0) = 1.0$. In fact for the lattice-based runs there are always some small clusters of particles even at time $t = 0$ (Chapter 2). As the aggregation proceeds the scattering by the 'typical cluster' increases at small Q, indicating the growth of larger

and larger structures. The shape of the calculated form factors may be compared with equation (3.7). Generally we do see a region $P(Q < Q_l) \rightarrow const$ and a 'power-law' region for $Q > Q_l$.

By calculating the average form factor as the aggregation proceeds we can see how the typical cluster structure evolves. For $Q > Q_l$ the scattering function is expected to follow a power-law in Q as in equation (3.7). In fact on the log-log plots it is clear that through early times the average form factor does not show a constant power-law exponent. At such early times the average includes a range of small clusters which show little fractal structure. At later time $P(Q > Q_l)$ does approach a power-law with a constant exponent as the system evolves into a collection of large fractal clusters. Estimation of the power-law exponent from this power-law region is sometimes used to obtain an estimate of the fractal dimension of the clusters. We have tried this analysis for the 2D data (for 3D data we use the more complete FB expression for the cluster form factor, as has been used in experiments—see below); results are given in Table 3.2. In any case, it should be remembered that the estimation of fractal dimension from the average form factor involves averaging over clusters whose structures may vary. This applies to estimates of d_f from mass-radius plots too (Chapter 5); and of course to most experimental measures of the fractal dimension of real systems, whether obtained by imaging or scattering methods.

At the lower densities in 2D ($\rho = 0.01$ and $\rho = 0.1$) the $P(Q)$ curves show reasonable single power-law regions, though there is some curvature especially at late times, probably due to the smaller and smaller number of clusters included in the average (so that orientational effects may become important). There is some variation in estimated exponents d_f from different times, but no clear trends, so that in Table 3.2 we include 'averages' or 'typical' values of d_f with error bars indicating the extent of the variations in time. We find $d_f \approx 1.4$, which compares well with previous low-density estimates from the mass-radius relation [30, 31, 34].

The results from the $\rho = 0.3$ system are more complex, however. From the earliest times there is substantial curvature in the $P(Q)$ function and no clear single power-law region. A 'rough' fit to early time data ($t = 10$, ignoring or 'averaging over', if you

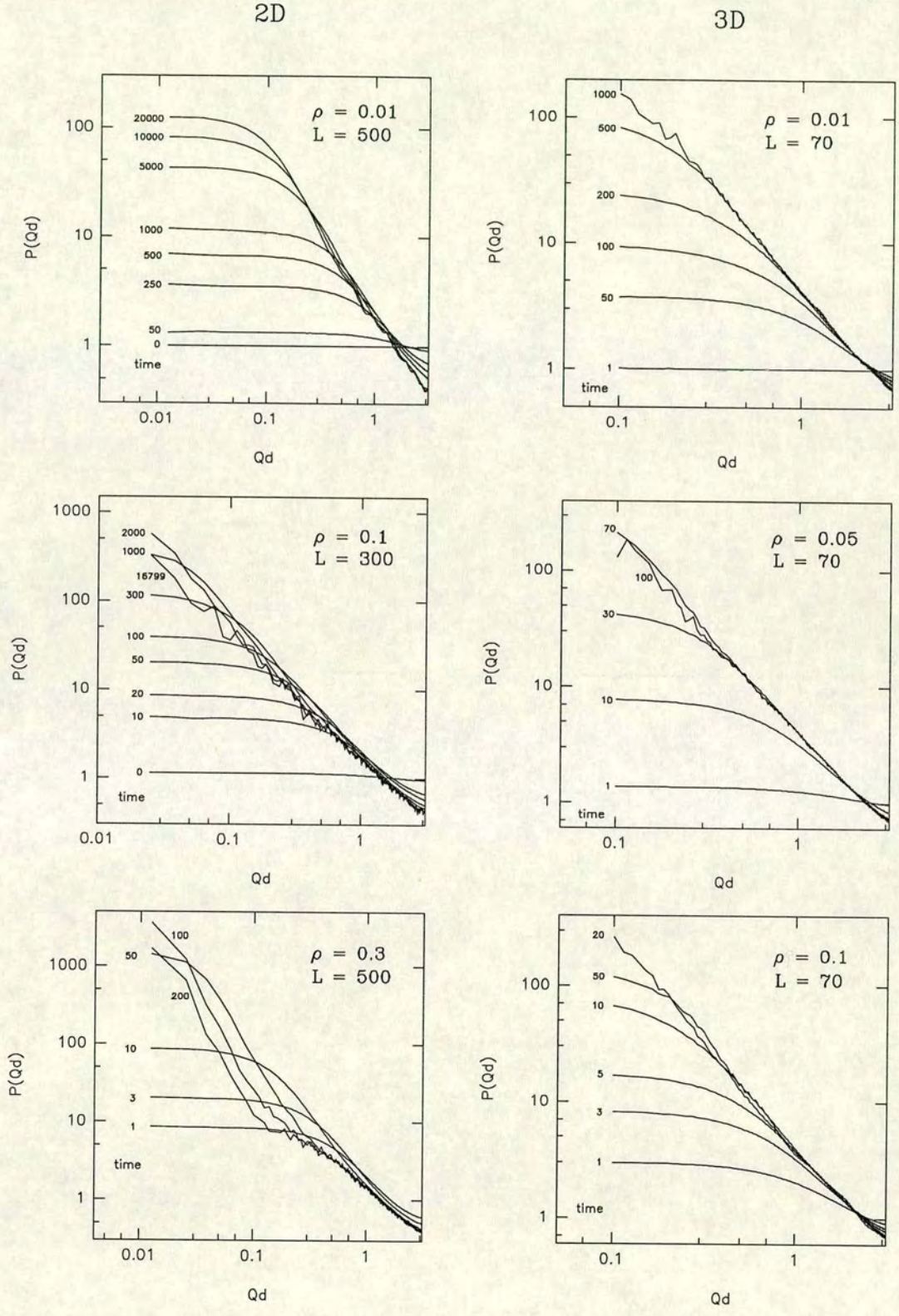

Figure 3.12. Circularly/spherically-averaged average form factors $P(Q,t)$ for lattice-based DLCA simulations in 2D (left column) and 3D (right column), calculated from equation (3.11). ρ is the number density of the system and L is the system size; times are indicated near each curve.

like, this curvature) gives $d_f \approx 1.6$, which actually compares reasonably with our own mass-radius estimates at high density (see Chapter 5 and Ref. [115]). However the significant and fast-increasing polydispersity of the high density system (Chapter 5) means the average form factor may include clusters with a wide range of structure, and 'blind' estimation of a single fractal dimension is not really advisable. Furthermore, as the aggregation proceeds a definite bend appears in the $P(Q)$ function (quite visible in Figure 3.12). For example, at time $t = 50$, estimating two slopes from below and above this bend (around $Qd \simeq 0.4$) we obtain a dimension $d_f = 2.08$ at long length scales (small Q) and a dimension $d_f = 1.40$ at short lengths. This may be evidence that even at this early time the largest clusters in the high density system have begun to assemble *homogeneously* (with long-length scale dimension $d_f \approx D$, the space dimension). However, the ranges of Qd over which we obtain these dimensions are very limited. The data do demonstrate at any rate that the structure of clusters at high density (or close to gelation) becomes far more complex and is not adequately described by simple fractal concepts.

Density	time	Qd range	d_f
0.01	2000	0.3–2.0	1.41
	5000	0.3–2.0	1.47
	10000	0.3–2.0	1.42
	20000	0.3–2.0	1.37
'Average' : 1.42 ± 0.05			
0.1	100	0.2–2.0	1.45
	300	0.3–2.0	1.43
	1000	0.2–2.0	1.38
	2000	0.2–2.0	1.39
'Average' : 1.42 ± 0.04			
0.3	10	0.3–2.0	1.58
	20	0.4–2.0	1.40
	20	0.1–0.4	2.08
	30	0.4–2.0	1.28
	30	0.07–0.4	2.16

Table 3.2. Power-law fits to the average form factor from lattice-based 2D simulations. The 'averages' give the 'typical' dimension d_f with an error bar estimated from the variation over the different times. At density $\rho = 0.3$ there is so much change in $P(Q)$ over time (see Figure 3.12) that it is not reasonable to measure an 'average' (see text).

Density	time	A	R_g	d_f	Maximum Qd
0.01	100	9.35	2.47	1.64	2.0
	200	25.2	4.16	1.85	1.5
	300	49.3	6.29	1.72	1.0
	500	102.6	8.32	2.19	0.8
0.05	5	3.62	1.43	1.33	2.0
	10	7.83	2.11	1.90	1.5
	20	22.87	3.72	2.04	1.6
	100	328.4	16.4	2.26	1.0
	100			1.63	$0.2 < Qd < 1.0$
0.1	1	3.0	1.25	1.31	1.5
	3	8.33	2.16	1.97	1.5
	10	78.90	7.21	2.10	1.0
	20	941.2	28.2	2.03	1.0
	20			1.89	$0.2 < Qd < 1.0$

Table 3.3. Parameters of fits of the 'Fisher-Burford' (FB) expression, equation (3.9), to cluster form factor data from 3D simulations (see Figure 3.13). 'Maximum Qd' is the maximum value of Qd for which $P(Qd)$ data was used in the fit; d is the particle diameter. For the last lines at the two higher densities, estimates of d_f from simple power-law fits to the $P(Qd)$ data are also shown.

For 3D simulations comparison of the DLCA average form factors with the Fisher-Burford expression equation (3.9) is given in Figure 3.13. Here a least-squares fitting procedure is used to fit the FB expression to the data and find the 'best fit' parameters, R_g, d_f and A (equation (3.9)). The fitted parameters are given in Table 3.3. Generally it is found that, at least at early times, the DLCA average form factors follow the FB form quite well, though there are variations in the fitted parameters (e.g. d_f). Given the small system sizes in the simulations and the always limited region of Q over which the function can be fitted, one would not expect a very precise determination of any of the parameters. If there is a trend, for instance in d_f, it is for d_f to increase with time; this is not surprising since at early time the presence of monomers and small non-fractal clusters will reduce the slope of the power-law region of the form factor. At the latest times the function does not really fit well enough for the parameters to be very meaningful. Table 3.3 and Figure 3.13 also include, for times $t = 100$ at $\rho = 0.05$ and $t = 20$ at $\rho = 0.1$, simple power-law fits to the $P(Qd)$ data.

As a broader check for changes in the 'average structure' of the clusters one can scale

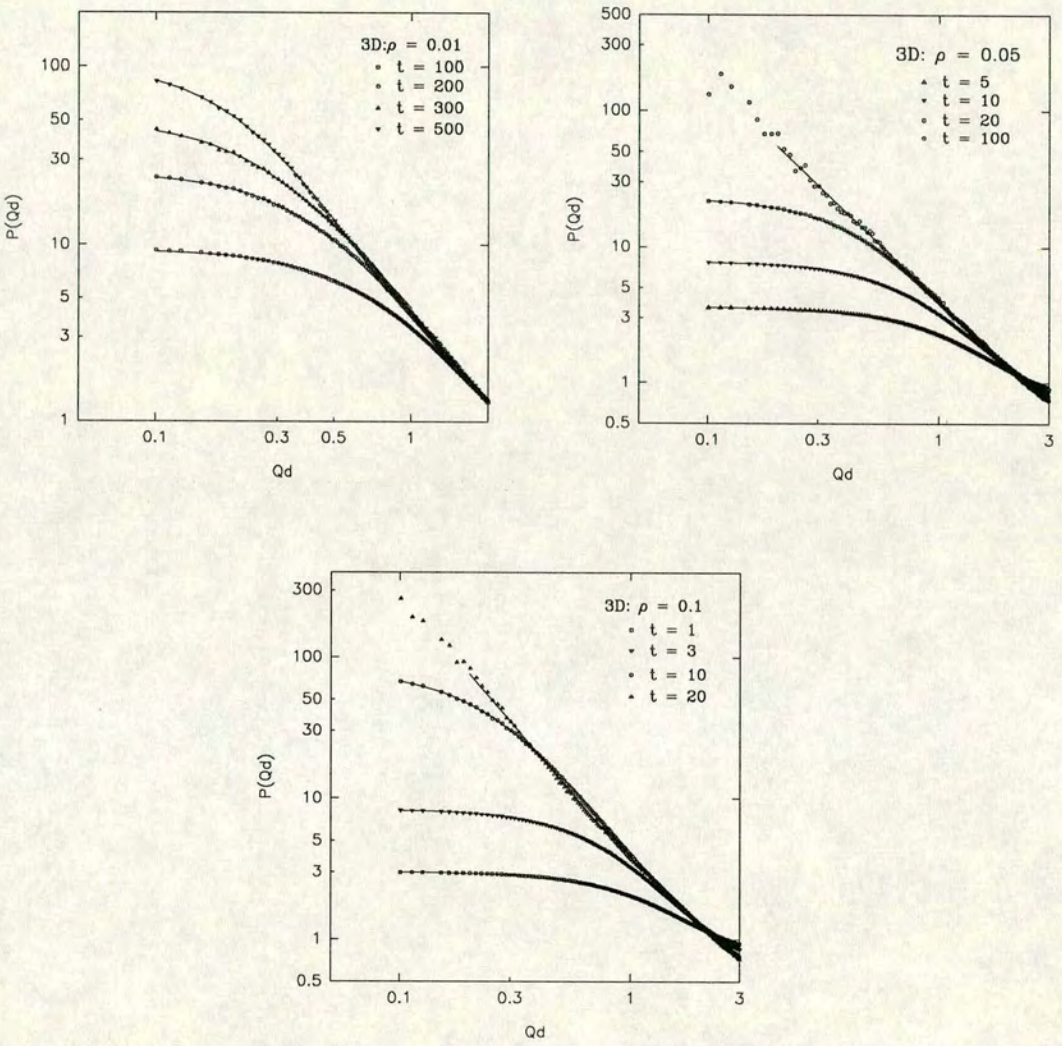

Figure 3.13. Fitting the Fisher-Burford equation (3.9) to average form factors $P(Q,t)$ for lattice-based DLCA simulations in 3D calculated from equation (3.11). ρ is the number density of the system. The lines drawn are the best fits estimated by least-squares; fit parameters are given in Table 3.3. For $t = 100, \rho = 0.05$ and $t = 20, \rho = 0.1$ the lines are simple power laws rather than the FB expression; see also Table 3.3.

the form factors from different times using the fitted FB parameters. In Figure 3.14 we plot $P(QR_g)/A$ *vs* QR_g for different times at each number density. The curves fall onto each other quite well, except at larger QR_g (where the FB form no longer applies–outside the fractal region of the form factor). These plots indicate that the apparent changes in the d_f parameter from the individual FB fits are not indicative of major changes in average cluster structure, but rather the fits simply cannot determine d_f to any better precision given the limited Q range.

The above Fisher-Burford analysis provides a good comparison with the experimental data in Ref. [6]. In that study Carpineti and co-workers fitted the Fisher-Burford form to scattering data from a low-concentration aggregating charged colloidal system. Similar agreement with the Fisher-Burford form was found, though the estimate of fractal dimension d_f for that system was quite low ($d_f \simeq 1.6$). We may conclude that while cluster structure is qualitatively similar in the DLCA model and such colloid experiments, details like the precise value of the fractal dimension may still depend on details of the experimental system.

Density	d_f (A *vs.* R_g)
0.01	1.92
0.05	1.84
0.1	1.85
all	1.85

Table 3.4. Estimates of average cluster fractal dimension d_f from Fisher-Burford fit parameters A and R_g for 3D simulations.

An 'average' fractal dimension d_f may also be estimated from the simulation form factor data by plotting the Fisher-Burford fit parameters A *vs* R_g. A is proportional to $P(Q \to 0)$ (equation (3.10)) which in turn is proportional to the weight average of the mass distribution (equations (3.11) and (3.12)); R_g is proportional to some characteristic radius of the clusters. Thus these parameters should be related according

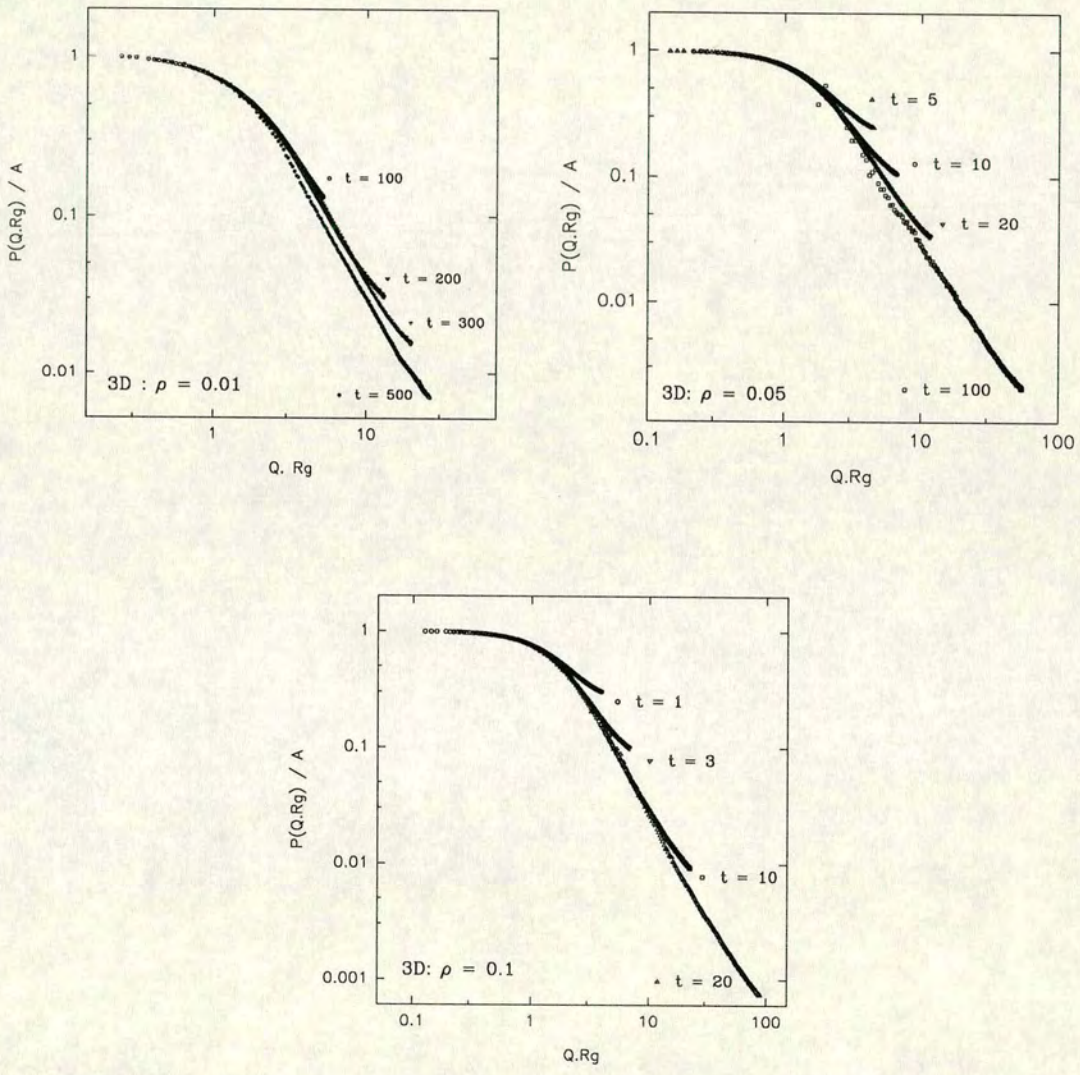

Figure 3.14. Scaled average form factors for lattice-based DLCA simulations in 3D calculated from equation (3.11). The x-axis is QR_g where R_g is the 'radius' parameter from the Fisher-Burford fit (equation (3.9) and Table 3.3). The y-axis gives the form factor amplitude $P(QR_g)$ scaled by the Fisher-Burford 'amplitude' parameter A.

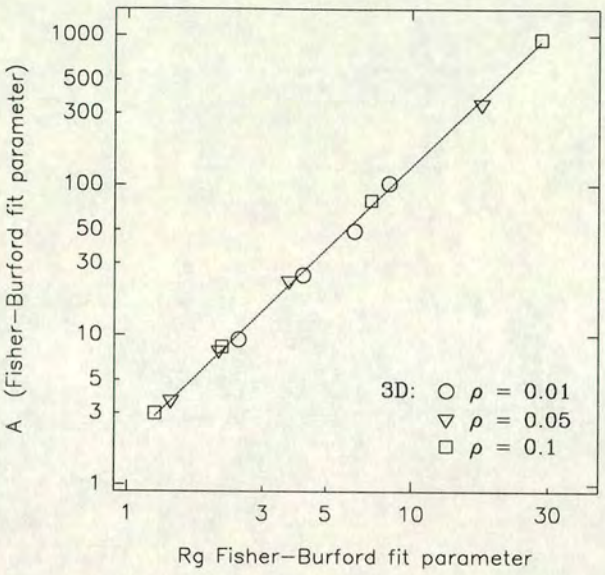

Figure 3.15. Fisher-Burford fit amplitude parameter A *vs.* 'radius' parameter R_g (equation (3.9)), for FB fits to 3D average form factor data from various example times during the aggregation. The line is a power-law fit to data from all densities; fitted exponents for this and for fits to each density separately are given in Table 3.4.

to the fractal mass-radius relation:

$$A \sim R_g^{d_f}. \tag{3.13}$$

The plot is shown in Figure 3.15, with estimates of d_f given in Table 3.4. A power-law relation is clearly observed over a good range in both R_g and A. For the lowest density where the clusters are smaller (at the times used for the fits), the estimate of d_f is slightly higher, possibly reflecting the fact that the underlying lattice structure affects the structure of smaller clusters more strongly. The two higher densities give estimates of d_f in good agreement with the 'expected' fractal dimension of 3D DLCA clusters [34].

Effects of finite size and gelation on $P(Q)$

Near the end of the aggregation two effects may be observed via the cluster average form factor $P(Q)$. In those cases where the system is smaller than the 'gel size' and therefore not large enough to include a number of 'gel clusters' in a homogeneous assembly, the

system becomes filled at late time by a single fractal cluster (see Chapters 1 and 2). The system is not large enough for further growth to be observed. The $P(Q = 0)$ limit becomes less and less obtainable in the small system. This can be seen in Figure 3.12 for the lower densities. $P(Q)$ no longer approaches a constant at some $Q_l > 0$; the typical cluster size R_l has reached the system size. This is a good demonstration that when the simulation is too small one cannot properly study late time behaviour (i.e. the onset of gelation) in the DLCA system.

A different behaviour of $P(Q)$ at late time is evident for the simulations at higher number density (e.g. 2D, $\rho = 0.3$, $L = 500$). In these cases $P(Q \to 0)$ *decreases* at the latest times and the $P(Q)$ function looks quite different from the expected single fractal form of equations (3.7). The structure of the 'typical' cluster whose form factor we are now calculating has changed. Fractal clusters have begun to assemble to form the *gel*; the 'typical' cluster is now a 'prototype piece' of the final gel. The decrease of the scattering intensity at small Q indicates that on long length scales the cluster is becoming more homogeneous. The fractal clusters are assembling near-homogeneously to make the gel. At the final 'gel time', when an *infinite* cluster spans the entire system, $P(Q)$ must of course be trivially equal to the complete scattering function $I(Q)$ of the final gel structure, since all particles then belong to this single cluster. Study of the 'transition' of $P(Q)$ from the single fractal form to the final gel form with a peak at $Q > 0$ and reduced scattering at $Q \to 0$ would provide direct information on the structural development of the gel. We discuss this further in the concluding paragraph of this subsection.

Form factors—conclusion

Calculation of the average form factor of clusters in the system as the aggregation proceeds provides a useful picture of how the structure of the 'typical' aggregate evolves. After an early time regime when the system contains a significant number of small, non-fractal clusters, the average form factor evolves into a power-law form as expected for scattering by a fractal structure. Estimates of the power-law exponent, both from power-law fits in the power-law region and from fitting the Fisher-Burford equation which extends to smaller Q, provide an alternative measure of the 'average' fractal

dimension which agrees reasonably with 'accepted' estimates from previous studies (which were obtained using mass-radius relations rather than scattering methods) and with experimental measures. The form factor also follows quite well the Fisher-Burford form predicted for a fractal cluster even though it is an average over a distribution of differently-sized clusters. Scaling of the form factors from different times indicates that at early and intermediate times the structure of the typical cluster is time-independent, involving only a change of scale as the growth proceeds. At the latest times however the average form factor begins to change, providing a good way both to check for finite size effects and, if the system is large enough to avoid finite size limits, to study the development of the gel structure as the fractal clusters assemble to form the system-filling gel.

Experimental study of the average form factor near to gelation would be a good way to 'watch' gelation, more useful than studying the complete scattering function $I(Q)$ since nothing very singular happens to $I(Q)$ at gelation. The $I(Q)$ peak 'freezes' [11, 53], but a proper study of this effect requires the examination of dynamics, for instance by dynamic light scattering, which is often more difficult, expecially in concentrated systems [11]. If instead the average form factor $P(Q)$ could be studied as the aggregation proceeds the *structural* changes during gelation (as $P(Q)$ goes from the single fractal form to the 'gel' $I(Q)$ with peak at $Q > 0$) could be observed directly. However the experimental problems are formidable. In order to measure the form factor, one would need to create a *dilute* system of clusters (so that there are no cross-cluster interference effects on the scattering pattern). This could probably only be done in systems where the aggregation is reasonably slow, and can be 'switched off' easily, and where the bonding between particles is rigid enough and strong enough that dilution of the system would not change the structure of the clusters. At any stage of the experiment one could then 'stop' the aggregation, dilute the system and measure the scattering function of the currently 'typical' cluster. In fact in charged colloidal systems one can 'stop' aggregation by dilution with water, which reduces the salt concentration and thus allows the particles' stabilising double layers to expand. Some such experiments have been carried out, though only in an attempt to measure cluster mass distributions by counting single clusters, and not using light-scattering [136]. Kallala and co-workers

[134], studying gelation of titanium alkoxide polymers, describe how dilution was used to show that the low-Q depression in their measured scattering was due to inter-cluster correlations. In this somewhat complicated system aggregation is apparently due to irreversible chemical reactions so that dilution is unlikely to distort the cluster structure; but it appears no more detailed study of the form factors of the diluted samples was carried out.

In simulation, the $P(Q)$ function can be directly studied at any time, without the technical problems of 'dilution'. However, large system sizes are required if one wants a very detailed picture of how the structure of the gel develops. In a smaller system gelation happens almost instantaneously, so development of the gel from assembling 'pieces' is difficult to study. From the data reported here we can begin to see how the gel structure develops; unfortunately constraints on computer power and memory mean we have been unable to study larger systems. The further study of gelation in the DLCA model would seem likely to be computationally demanding but potentially very interesting.

3.3.3 Cluster arrangement–the structure factor

We study the arrangement of the clusters in the system by calculation of the scattering function of the *centres of mass* of the clusters. We use equation (3.1), now assuming that the individual *cluster* scattering functions $P(Q) \equiv b_j = 1$, and inserting the set of centre of mass coordinates $\{\mathbf{r}_{ck}\}$ into the equation:

$$S_{CM}(\mathbf{Q},t) = \frac{1}{N_c}\left|\sum_{k}^{N_c} exp(i\mathbf{Q}.\mathbf{r}_{ck})\right|^2 \tag{3.14}$$

where N_c is the number of clusters at time t and $\mathbf{r}_{ck}$ is the centre of mass position of cluster k. Once again $S_{CM}(\mathbf{Q},t)$ is circularly/spherically averaged to obtain $S_{CM}(Q,t)$.

Plots of $S_{CM}(Q,t)$ are given in Figure 3.16 (lattice-based simulations) and Figure 3.17 (off-lattice simulations). Before the aggregation starts, at time $t = 0$, $S_{CM}(Q)$ should be equivalent to the structure factor of a hard spheres/disk fluid, since (in the off-lattice

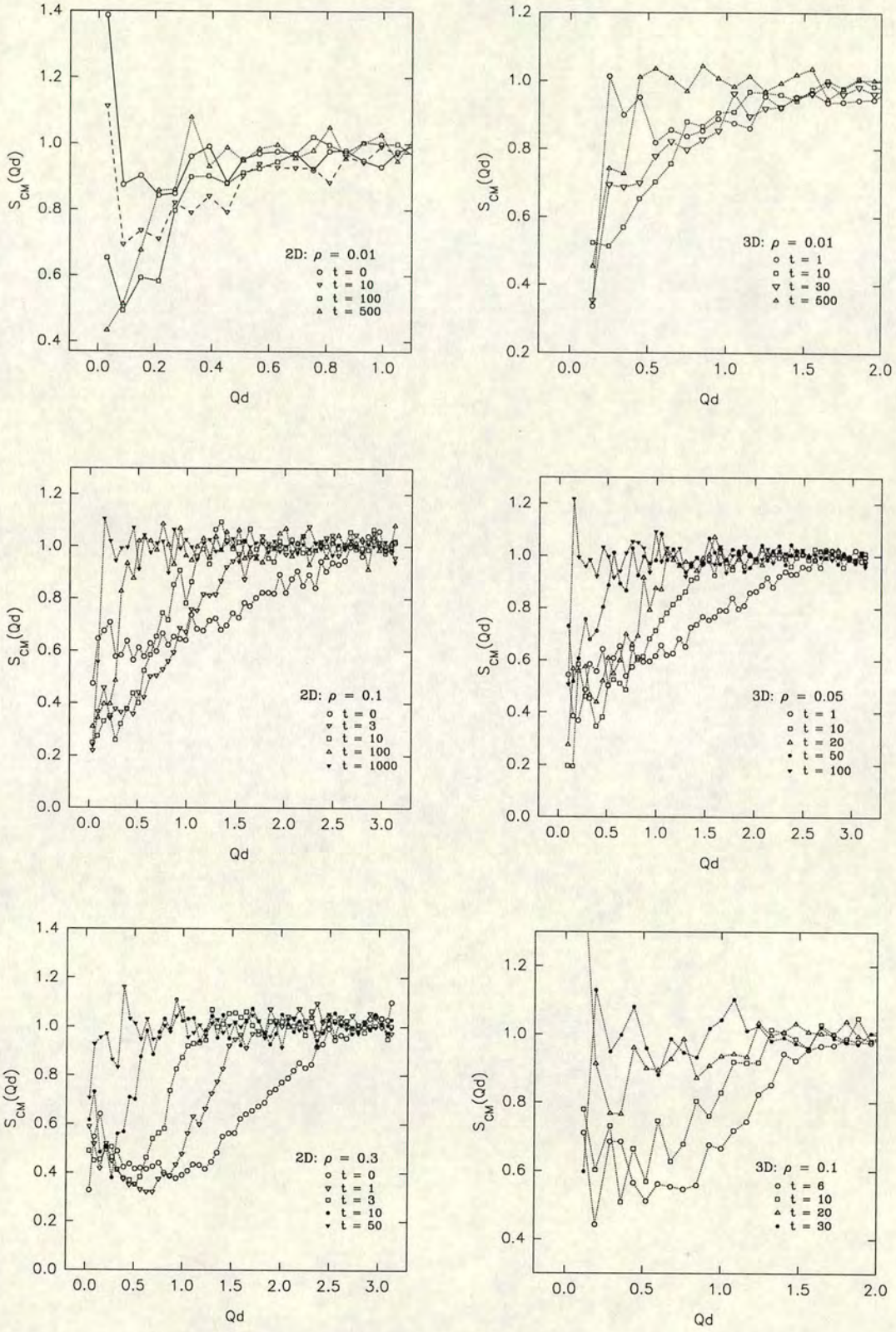

Figure 3.16. Structure factors of the centre of mass positions of clusters in lattice-based DLCA simulations in 2D and 3D. The simulation system sizes are $L = 500$ ($\rho = 0.01$, 2D), $L = 300$ ($\rho = 0.1$ and 0.3, 2D), and $L = 70$ (3D). The x-axis is $Q \times d$ where d is the particle diameter (lattice-spacing).

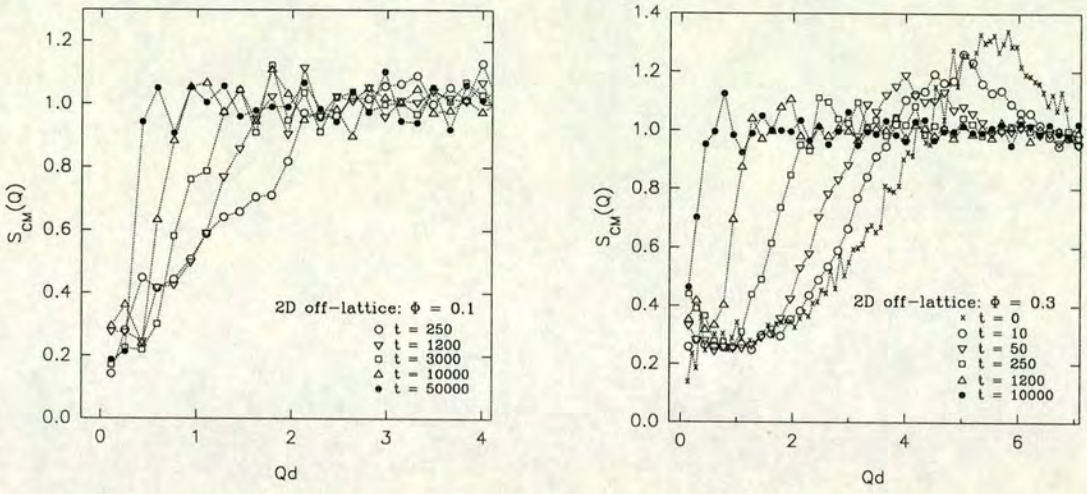

Figure 3.17. Structure factors of the centre of mass positions of clusters in off-lattice DLCA simulations in 2D. The system sizes are $L \approx 51.8$ for area fraction $\Phi = 0.3$ and $L \approx 89.9$ for $\Phi = 0.1$.

model at least) there are only monomers in the system. The initialisation routine which is applied to the monomers prior to commencing aggregation (see Chapter 2) is a standard Monte Carlo scheme in which the particles behave like hard spheres, so that if fully equilibrated the initial structure of the system will be that of a hard sphere fluid at the given density. The typical form of the hard sphere structure factor $S_{HS}(Q)$ is well-known, and for moderate volume fractions in 3D systems the Percus-Yevick approximation has been shown to give a good match to experimental data [2]. A Percus-Yevick approximation for the 2D system (of hard disks) has a similar shape [137]. $S_{HS}(Q)$ features a broad 'fluid' peak at some scattering vector Q_s and, for $Q < Q_s$, decreases to a value $S_{HS}(Q \to 0)$ which depends on the density. The broad 'fluid' peak corresponds roughly to a most common 'near-neighbour' separation. $S_{HS}(Q \to 0)$ decreases as density is increased, reflecting the increasing tendency as density increases for a typical particle to be more 'confined' by surrounding neighbours. These general features can be seen in the $S_{CM}(Q, t = 0)$ curve for the 2D *off-lattice* system at area fraction $\Phi = 0.3$, in Figure 3.17. Note that in the lattice-based systems the fluid peak is replaced by a strong *Bragg peak*; the short-range structure is imposed by the underlying lattice. In practice we do not calculate $S_{CM}(Q)$ for the lattice-based systems beyond $Qd \sim \pi$.

We consider now how the cluster positional structure factor changes as the aggregation proceeds. The broad 'near-neighbour' peak at $Q = Q_s(t)$ (visible in the off-lattice simulations) quite quickly disappears, such that for $Q > Q_s(t)$ $S_{CM}(Q)$ is approximately constant at $S_{CM}(Q) = 1$. This indicates the lack of significant *ordering* of cluster positions—some sort of semi-crystalline ordering, for instance, would give rise to a marked peak in $S_{CM}(Q)$. A semi-crystalline ordering of clusters in the aggregating system has occasionally been proposed [49] as a possible 'explanation' of the appearance of the small-angle scattering peak in the scattering function $I(Q)$. The structure factor of the cluster positions indicates that this is not the case. In fact as we have seen the presence of a typical cluster-depletion zone 'object' is enough to give the peak in $I(Q)$. It should be noted though that studies of the structure factor of a *polydisperse* system of hard spheres [128, 129, 130] have implied that polydispersity can strongly affect the broad fluid peak. The polydispersity of clusters in the DLCA simulation is examined in Chapter 5; the polydisperse hard-sphere scattering model is considered further below.

The scattering vector at which $S_{CM}(Q)$ begins to fall below 1.0, $Q_s(t)$, decreases with time, indicating the growth of structure. As clusters grow their *centres* on average necessarily get further apart. For $Q < Q_s(t)$ $S_{CM}(Q)$ falls below 1.0, to some value $S_{CM}(Q \to 0)$. The value $S_{CM}(Q \to 0)$ and the shape of the curve depend on time. For the lattice-based model the earliest times are only observable for the lowest-density systems. As the aggregation proceeds $S_{CM}(Q \to 0)$ first decreases. In intermediate time it remains approximately constant. At late time it increases again. At the end of the simulation $S_{CM}(Q) = 1$ trivially for all Q, since there is only one 'centre of mass' in the system; thus $S_{CM}(Q \to 0)$ must increase toward 1.0 as the system approaches gelation.

In the high density systems there is a clear minimum in $S_{CM}(Q)$ between Q_s and $Q \to 0$. At the smallest Q, $S_{CM}(Q)$ *rises* as Q approaches zero. We show in Chapter 4 that this rise is probably due to an effective association of small clusters (in the channels formed between larger clusters). That it is the arrangement of the small clusters which causes the rise in S_{CM} at small Q is supported by calculation of the *mass-weighted*

centre-of-mass structure factor, as shown in section 3.3.5.

Modelling the cluster structure factor

The question arises how the (instantaneous) structure of the set of clusters in the DLCA system compares with various 'model' systems for which there are analytical approximations or simulation results. Here we compare the structure factor of the DLCA cluster positions with structure factor approximations derived for monodisperse and polydisperse hard sphere systems.

The well-known Percus-Yevick (PY) expression for the structure factor of a system of monodisperse hard spheres, $S_{PY}(Q)$, has been shown to give a reasonably good approximation both to experimental data on near-hard sphere colloids [2] and to computer simulation results, for 3D systems at low volume fraction ($\Phi \leq 0.3$) [130]. An example of a calculated $S_{CM}(Q)$ curve from a 3D (lattice-based) DLCA simulation ($\rho = 0.05$, $t = 10$) is compared with the PY form in Figure 3.18. Rather than try to calculate the effective (cluster) volume fraction and (cluster) radius parameters for the PY expression from the simulation data we have simply varied the two parameters to find the 'best' comparison between S_{PY} and S_{CM}. For monodisperse hard sphere systems S_{PY} is usually calculated as a function of Qr, where r is the radius of the hard sphere. In this case we plot S_{CM} versus Qd where d is a particle diameter in the simulation. Therefore we express the Percus-Yevick radius parameter in terms of d. For the example shown, the 'best' comparison with the PY expression is found with the following parameters: volume fraction $\Phi_c \approx 0.1$; and cluster radius $d_c \approx 1.5d$.

The PY form and the calculated structure of the cluster centres can be seen from the plot to have some qualitatively similar features, but (as one might expect) they do not really agree in detail. A *peak* similar to that in $S_{PY}(Q)$ is seen at early time in the 2D off-lattice simulations, which is reasonable given that at $t = 0$ in the off-lattice model we do have a system of hard disks; however this peak clearly disappears as the aggregation proceeds. To reduce the strength of the peak in S_{PY} one must reduce Φ_c substantially, but this leads to a substantial increase in $S_{PY}(Q \to 0)$, which we do not observe in S_{CM} until the very latest times when there are very few clusters in the

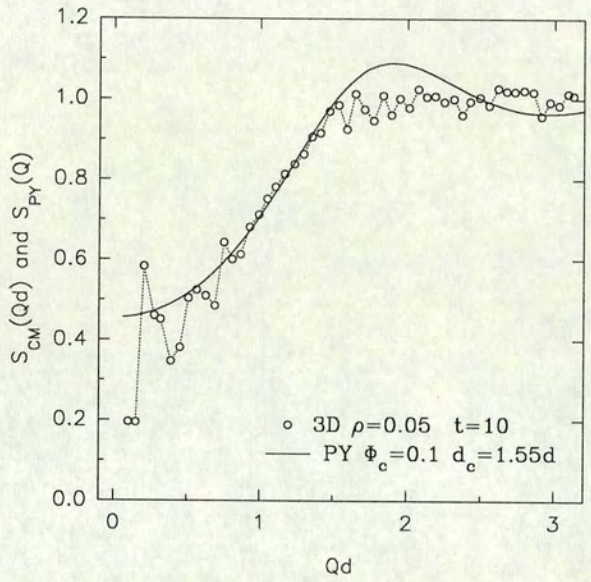

Figure 3.18. Comparison of the centre-of-mass structure factor $S_{CM}(Q)$ calculated from a 3D DLCA simulation at density $\rho = 0.05$, with the Percus-Yevick (PY) monodisperse hard sphere structure factor approximation, $S_{PY}(Q)$. Φ_c is the volume fraction parameter in the PY expression. S_{PY} is rescaled on the x-axis such that it gives the structure factor for hard spheres with diameter $d_c = 1.5 \times$ the simulation particle diameter; this volume fraction and sphere size give the best qualitative agreement with S_{CM} for this example.

system. Also S_{PY} cannot reproduce the rise in S_{CM} for $Q \rightarrow 0$ which we observe for the higher densities.

Given the polydisperse nature of the system of clusters (see Chapter 5) the simple hard-sphere model would not be expected to give results very comparable to the cluster structure factor from the DLCA simulations. Therefore rather than compare with S_{PY} in more detail we consider the effect of the polydispersity in cluster sizes. In attempts to study the effect of particle polydispersity in hard sphere systems, extensions to the PY monodisperse hard sphere approximation have been developed by Vrij and others [128, 129, 131]. Frenkel and co-workers [130] showed that the *polydisperse Percus-Yevick* approximation for the structure factor compared quite well to Monte Carlo simulation results. However it is important to understand that in the various work with the polydisperse hard sphere approximations, the structure factor derived is *not* the structure factor of the *centre of mass positions* of the spheres (as calculated here, for clusters rather than spheres). The 'polydisperse structure factor' studied in Refs. [128, 129, 130] is a derived quantity whose physical significance is not clear. Vrij's expression may be used to calculate the complete scattering function $I_{poly}(Q)$ of the polydisperse hard sphere fluid [128]. Vrij and Van Buerten [129] and Frenkel and co-workers [130] then calculate an average form factor $P_{poly}(Q)$ for the polydisperse system of spheres using a predetermined size distribution and an expression equivalent to the size-weighted averaging in equation (3.11), and simply derive a 'structure factor' given by $S_{poly}(Q) = I_{poly}(Q)/P_{poly}(Q)$. The relation between $S_{poly}(Q)$ and the *centre of mass* structure factor $S_{CM}(Q)$ is not discussed in any of the above References. A closing comment in Ref. [130] indicates that $S_{CM}(Q)$ for a Monte Carlo simulated polydisperse hard sphere system was calculated and then 'adjusted' for polydispersity effects according to the method of Kotlarchyk and Chen [132]; it is mentioned that $S_{CM}(Q)$ thus 'adjusted' does not match the derived $S_{poly}(Q)$ data from the simulation very well. It remains unclear whether an *unadjusted* $S_{CM}(Q)$ would match $S_{poly}(Q)$, though one might have expected the authors of Ref. [130] to have noticed if such a simple relation were applicable. It thus appears that $S_{CM}(Q)$ is not equal to the derived $S_{poly}(Q)$ for a polydisperse hard sphere system.

However, it is a simple matter to follow a similar method to obtain a 'new' cluster structure factor from the DLCA data, that is to calculate a *derived structure factor* $S_d(Q)$ from

$$S_d(Q) = I(Q)/P(Q), \tag{3.15}$$

using the calculated scattering function for the system $I(Q)$ and the average cluster form factor $P(Q)$. It is further possible to extract the radius distribution of clusters from the DLCA data and insert this directly into the Vrij expression for the polydisperse (complete) scattering function; then an effective polydisperse hard sphere structure factor $S_{poly}(Q)$ is obtained *as if one had a distribution of spheres with the DLCA radius distribution*, by dividing the Vrij expression $I_{poly}(Q)$ by the average form factor of such a distribution of spheres[5].

The only parameter required by Vrij's expression apart from the radius distribution is the volume fraction Φ. What is required is some estimate of the volume 'occupied' by the fractal clusters. There are various ways this can be measured. Most obviously one could simply take the total occupied cluster volume as equal to the sum of the radii of gyration cubed, giving a cluster volume fraction Φ_c:

$$\Phi_c(t) \simeq \sum_{j}^{N_c} R_{gk}^3/L^3 \tag{3.16}$$

where N_c is the number of clusters at time t, R_{gk} is the radius of gyration of the k^{th} cluster, and L^3 is the total volume of the simulation box. In general $\Phi_c(t)$ is a function of time; as the system approaches gelation $\Phi_c(t)$ should increase, because the clusters are filling the system.

The above measure of cluster volume fraction is expected to be no more than approximate, since the radius of gyration of the fractal cluster may not perfectly describe how much space the cluster effectively 'occupies'; branches of the fractal may extend substantially beyond R_g, especially for highly anisotropic clusters. Thus once again, rather than try precisely to determine a value of $\Phi_c(t)$ to insert into Vrij's expression

[5] A computer program to calculate $S_{poly}(Q)$ (a rather laborious and complicated expression) was kindly provided by T-T. Chui.

for the polydisperse structure factor, we instead try to find the 'best' match between Vrij's expression and the DLCA $S_{CM}(Q)$ calculation, by varying Φ_c as a 'fitting' parameter. Then if reasonable values of Φ_c can be found for which the Vrij expression and $S_{CM}(Q)$ match, we can begin to believe that the polydisperse hard sphere model does indeed describe the arrangement of the clusters in the DLCA simulation. This would imply that the cluster arrangement at any given time is determined mostly by the radius distribution and is not particularly dependent on the internal structure of the scattering objects; a system of hard spheres with the same radius distribution would be arranged in the same way.

Polydisperse structure factor—results

In Figure 3.19 we compare the 'derived structure factor' $S_d(Q)$ for a 3D simulation at number density $\rho = 0.05$ with the polydisperse hard sphere structure factor model. The Figure shows the 'best' fits of the model to the simulation data at four times during the aggregation; the 'fit' parameter in the polydisperse structure factor expression is the volume fraction Φ (shown on the plots). (Note that these 'best' fits were selected by eye rather than by any more quantitative fitting procedure.) It is clear that the model does not fit very successfully at early times, though the comparison is somewhat more reasonable for the later times. The noise in the simulation data is such that nothing more than an approximate comparison is possible, but at the very least we can say that the polydisperse PY model compares significantly better than the monodisperse PY approximation to the DLCA simulation cluster structure. It would probably not be wise however to claim that at a given instant the DLCA clusters are arranged in the system exactly as if they were particles in a system of polydisperse hard spheres, since it is not clear how 'sensitive' to exact structural details these structure factors are. Figure 3.19 does demonstrate how polydispersity as well as 'object' structure can strongly affect the scattering. The problem remains however that the polydisperse hard sphere structure factor $S_{poly}(Q)$ is not the same as the structure factor of the centres of mass of the 'particles', and it is not clear what information $S_{poly}(Q)$ or $S_d(Q)$ really provide concerning the physical arrangement or interaction of clusters in the system. A detailed modelling study of the relation between these functions and different spatial

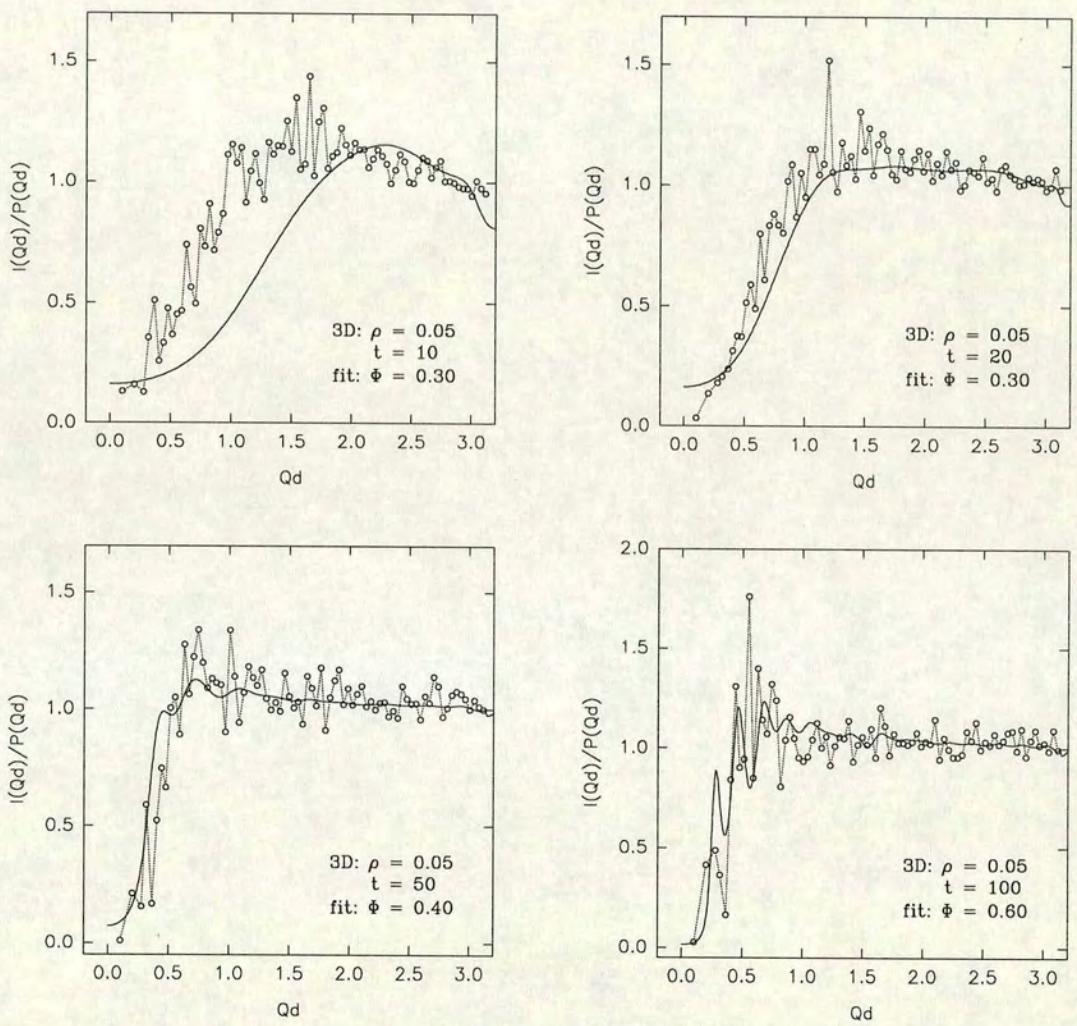

Figure 3.19. 'Derived structure factors' $S_d(Q) = I(Q)/P(Q)$ for a 3D lattice-based simulation at number density $\rho = 0.05$, at times $t = 10$, 20, 50 and 100 (the final 'gel' time being $t = 596$). The solid lines are calculated from the polydisperse hard sphere structure factor expression due to Vrij and co-workers [128, 129]; the lines are approximate 'best' fits selected by eye, varying the volume fraction parameter Φ.

structures would be of some use, but is rather beyond the scope of this work.

3.3.4 Time evolution of cluster arrangement

The curves in Figure 3.16 suggest that the arrangement of cluster centres in the aggregating system may have a similar *form* at different times. To test this idea the scaled cluster position structure factor may be examined. In Figure 3.20 (lattice model) and Figure 3.21 (off-lattice) we plot S_{CM} *vs.* the scaled scattering vector $Q/Q_m(t)$, where $Q_m(t)$ is the position of the peak in the scattering function $I(Q,t)$ at time t. We discuss the 2D results first. For all except the latest times the data from 2D simulations collapse reasonably onto a single scaled curve, indicating that the cluster arrangement can be characterised by the single time-dependent measure $Q_m(t)$. Physically this implies that the form of the cluster arrangement is constant as the aggregation proceeds, simply 'expanding' to a larger length scale as the clusters grow. Only as the system nears gelation (or as finite size effects mean the system no longer contains enough clusters for a proper measure of their arrangement to be obtained) does the cluster arrangement begin to take on a different form. This latter is as expected, since near gelation the character of the aggregation is changing from the aggregation of fractal clusters to the assembly of fractals into the near-homogeneous gel.

All the scaled curves begin to fall from $S_{CM}(Q/Q_m) = 1.0$ at the same value of the scaled scattering vector, $Q_c = Q/Q_m(t) \simeq 1.5$. This implies that the 'expansion' of the cluster position structure proceeds at the same rate as the expansion of the cluster-plus-depletion-zone object indicated by the decrease of Q_m in the scattering function. In other words, while these two length scales which characterise the cluster arrangement and the cluster-depletion zone are *not* equal ($Q_c \neq 1$), they do scale in the same way as the aggregation proceeds. Furthermore, if we interpret Q_c as the typical separation between cluster centres, $Q_c > 1$ implies that *typically there are neighbour clusters inside a given cluster's depletion zone.* In other words, the depletion zone around a cluster is not empty—as we might expect, as the depletion zone in the $g(r)$ functions does not reach zero. We discuss this point further in Chapter 5.

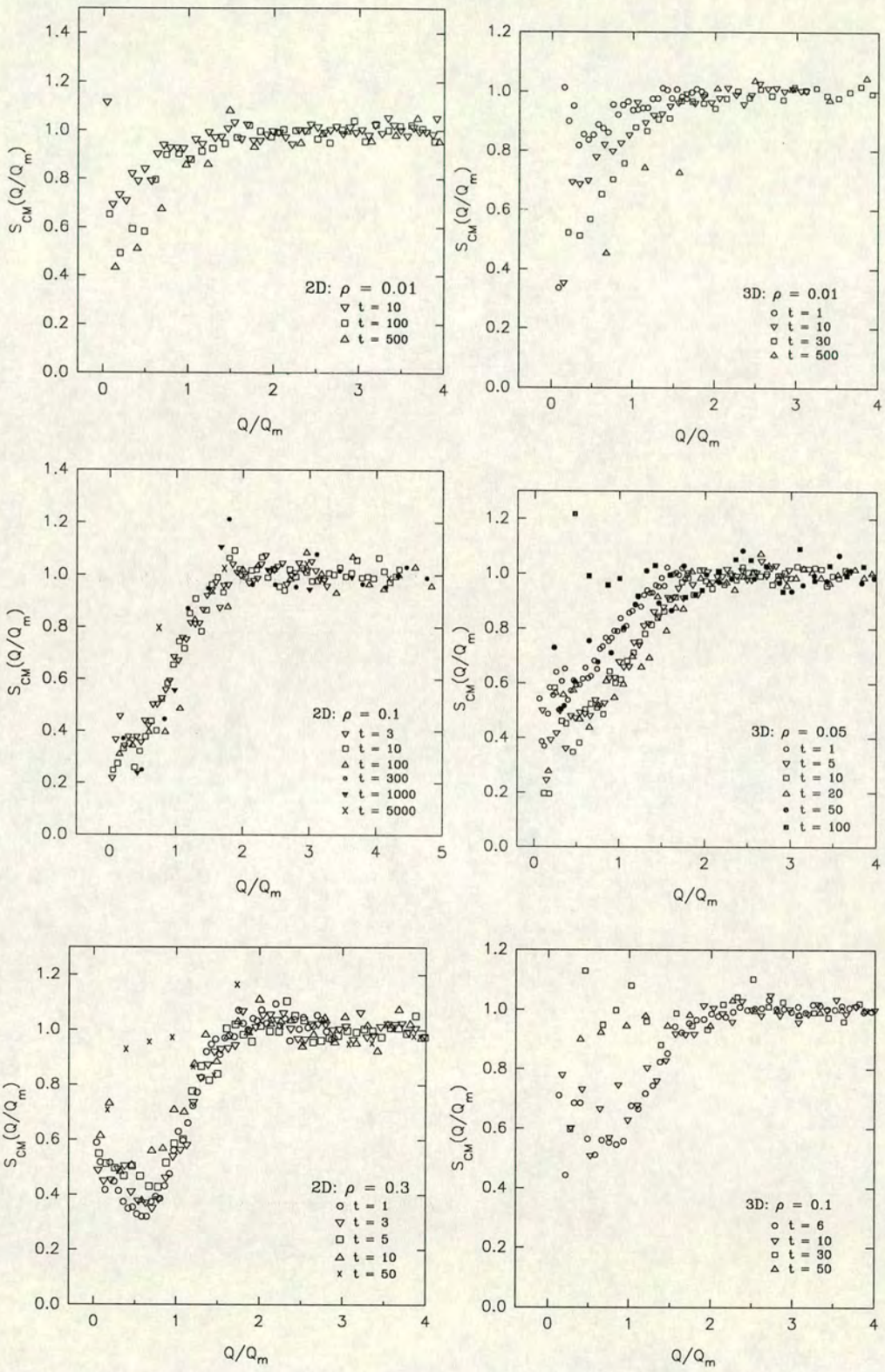

Figure 3.20. Scaled centre of mass position structure factors from lattice-based DLCA simulations in 2D and 3D. $S_{CM}(Q,t)$ is calculated from equation (3.14) and plotted versus the scaled x-coordinate, $Q/Q_m(t)$, where $Q_m(t)$ is the position of the peak in the scattering function $I(Q,t)$.

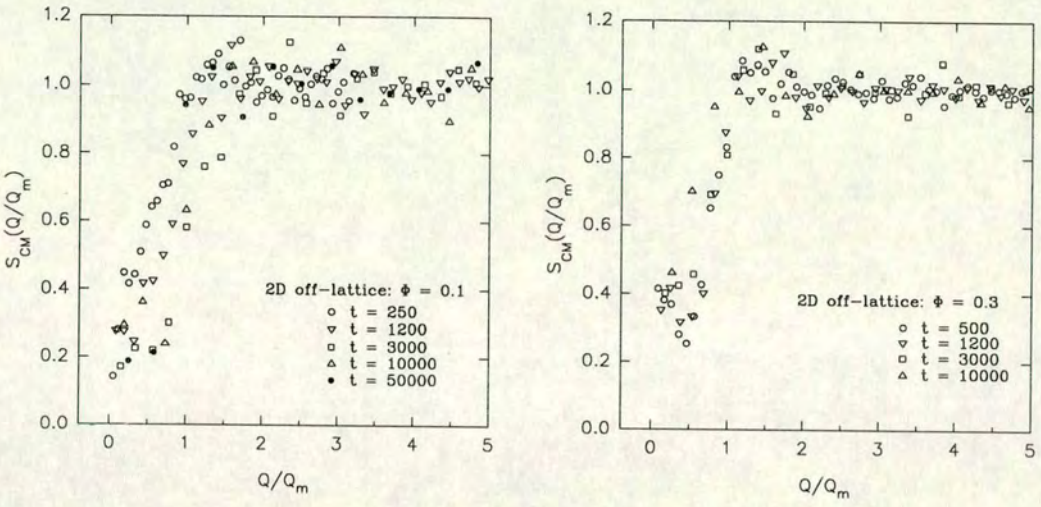

Figure 3.21. Scaled centre of mass position structure factors from off-lattice DLCA simulations in 2D. $S_{CM}(Q,t)$ is plotted versus the scaled x-coordinate, $Q/Q_m(t)$, where $Q_m(t)$ is the position of the peak in the scattering function $I(Q,t)$.

While time-independent scaling is less well-demonstrated for $Q/Q_m \to 0$ in the 3D simulations, still all the curves collapse reasonably well around $Q/Q_m = Q_c$. For the small 3D systems statistical noise in the data makes a confirmation of scaling more difficult at smaller Q. Consistent with the 2D results, the lowest density systems where earliest times are accessible show that scaling does not hold at early time. Then, $S_{CM}(Q)$ at small Q decreases with time (the dip in S_{CM} becomes deeper) and so simply scaling the Q axis by a characteristic length cannot lead to scaling collapse of the data.

The time-independent form for the cluster arrangement in the 2D DLCA simulations agrees with 2D experimental studies [98, 138], indicating that the DLCA model is a good model for these experimental systems.

3.3.5 Separation of scattering for the DLCA system

Finally we investigate whether the simple separation of the complete scattering function $I(Q)$ into form factor and structure factor, equation (3.5), works for the system of

aggregating clusters in the DLCA model. The product

$$A_{CM}(Q,t) = S_{CM}(Q,t)P(Q,t), \tag{3.17}$$

is calculated from the average form factor and cluster positional structure factor. In Figures 3.22 and 3.23 $A_{CM}(Q,t)$ is compared with the directly calculated complete scattering function $I(Q,t)$, for some example 2D and 3D systems. It is clear that the separation in equation (3.5) does *not* work for the DLCA system. Results for other densities are similar; the system structure cannot be completely described by imagining a 'typical' cluster with structure given by $P(Q)$, 'copies' of which are placed at the centre of mass positions whose arrangement is described by $S_{CM}(Q)$.

We are thus led to conclude that there is some 'element of structure' beyond the internal structure of the clusters and the arrangement of clusters in the DLCA system which is important in determining the complete scattering function $I(Q)$. If one considers the scattering function as measuring *correlations* between particle positions, then one can think of the complete scattering function $I(Q)$ as measuring the 'full set' of correlations between the positions of all particles. Each particle's contribution to this 'set' is made up of two parts: the correlations of the particle's position with the positions of other particles in *its own cluster*; and the correlations of the particle's position with the positions of particles in *other* clusters. 'Same cluster' correlations are accounted for by the form factor $P(Q)$[6]. For the separation in equation (3.17) to work, then, we require that all cross-cluster correlations are accounted for by the cluster position structure factor $S_{CM}(Q)$.

This will only be the case if two conditions are satisfied. Firstly, *every* particle in a given cluster must have essentially the *same* correlations with other clusters' particles. Then cross-cluster correlations for that cluster may be calculated by measuring the cross-cluster correlations for just one of the particles in the cluster—e.g. the central particle. Secondly, one set of these correlation terms must be included for every particle in the cluster–that is, the cluster's contribution should be *weighted* by the mass of the

[6]Though it should be kept in mind that for the DLCA system $P(Q)$ is an average over the polydisperse set of clusters.

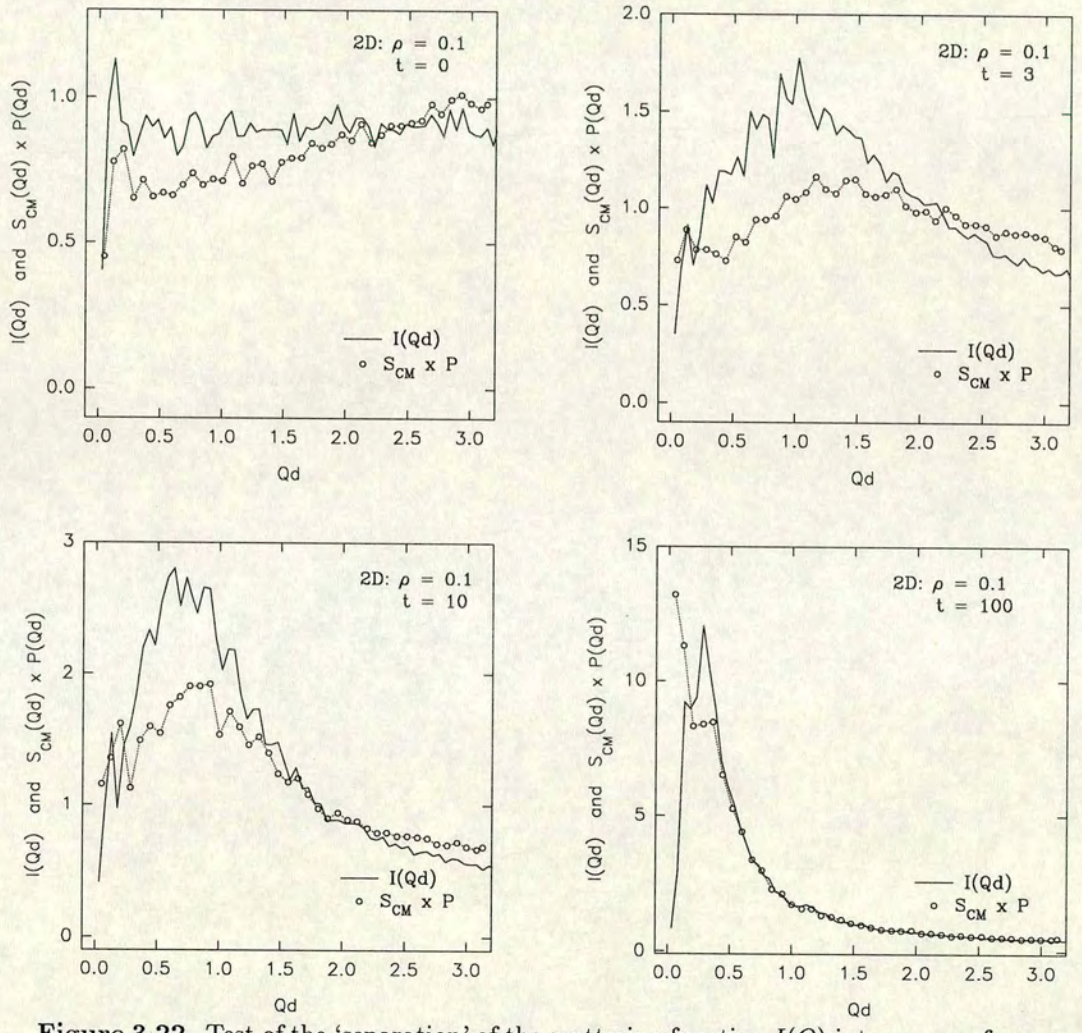

Figure 3.22. Test of the 'separation' of the scattering function $I(Q)$ into average form factor $P(Q)$ and cluster positional structure factor $S_{CM}(Q)$. $I(Q)$ is compared with the product $S_{CM}(Q) \times P(Q)$ for a 2D lattice-based simulation at $\rho = 0.1$, system size $L = 300$.

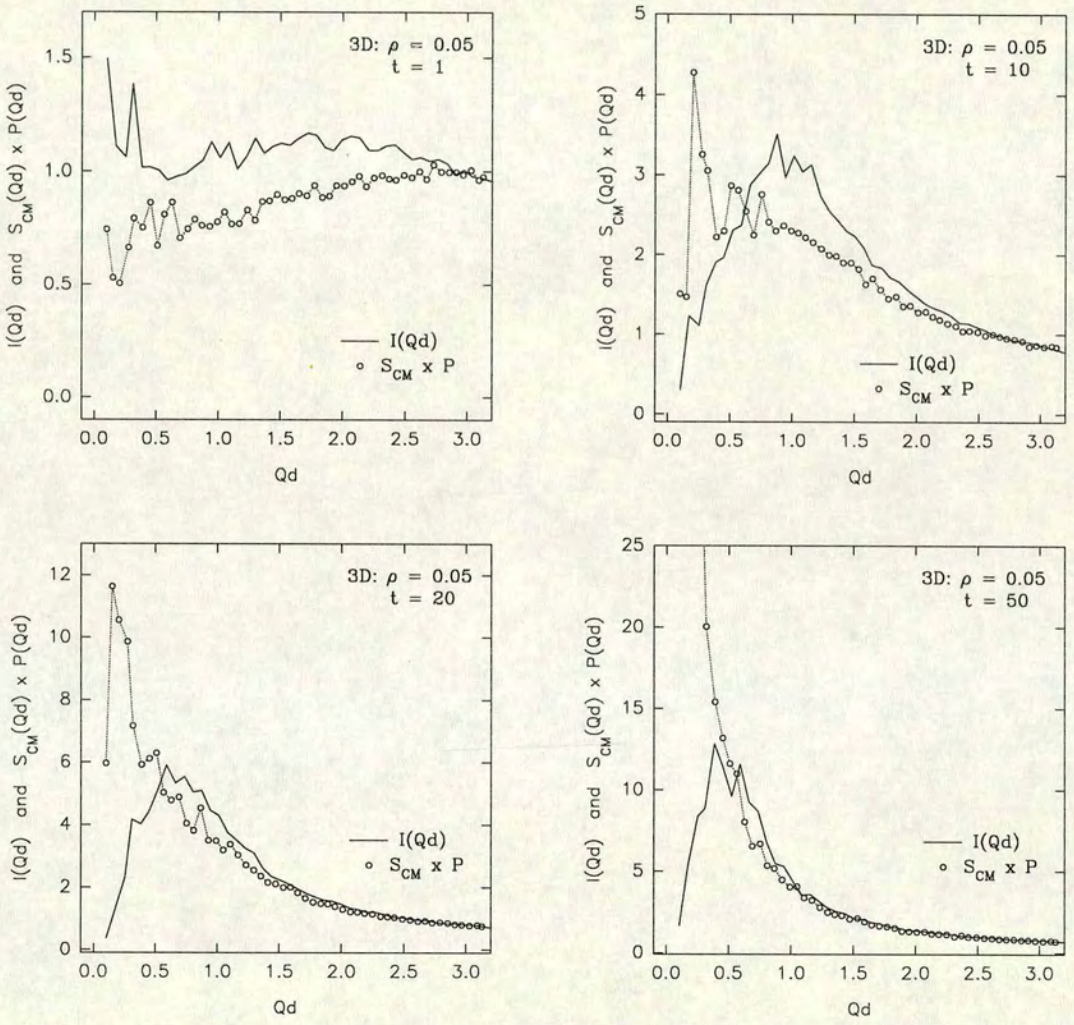

Figure 3.23. Test of the 'separation' of the scattering function $I(Q)$ into average form factor $P(Q)$ and cluster positional structure factor $S_{CM}(Q)$. $I(Q)$ is compared with the product $S_{CM}(Q) \times P(Q)$ for a 3D lattice-based simulation at $\rho = 0.05$, system size $L = 70$.

cluster. So the second assumption 'hidden' in equation (3.17) is that *all clusters have the same mass*, since each cluster-centre makes the same contribution to the structure factor S_{CM} (equation (3.14)).

Mass-weighted cluster structure factor

From the above discussion it is clear that a useful next step in trying to account for all the elements of structure in the DLCA system is to consider the effect of cluster mass. To do this we calculate a *mass-weighted cluster structure factor* $S_{MW}(Q)$:

$$S_{MW}(\mathbf{Q},t) = \left| \sum_{k}^{N_c} M_k exp(i\mathbf{Q}.\mathbf{r}_{ck}) \right|^2 / \sum_{k}^{N_c} M_k^2 \tag{3.18}$$

where once again N_c is the number of clusters at time t, $\mathbf{r}_{ck}$ is the centre of mass position of cluster k, and M_k is the mass of cluster k. $S_{MW}(\mathbf{Q},t)$ is circularly/spherically averaged to give $S_{MW}(Q,t)$. This equation therefore essentially includes an identical term $exp(i\mathbf{Q}.\mathbf{r}_{ck})$ for each particle in cluster k. To imagine the calculation physically, it is as if every particle were moved to the centre of its cluster. (Note that we are thus still assuming the first condition discussed in the previous paragraph, that all particles in the cluster have the *same* correlations with other clusters' particles.)

The normalisation factor $\sum_k^{N_c} M_k^2$ can be obtained by considering the 'self-term' in the equation. We can equivalently write equation (3.18) in the form

$$S_{MW}(\mathbf{Q}) = \sum_{j}^{N_c} \sum_{k}^{N_c} M_j M_k exp[i\mathbf{Q}.(\mathbf{r}_{cj} - \mathbf{r}_{ck})]. \tag{3.19}$$

For large Q, the terms for $j \neq k$ tend to cancel out; the sum of the complex exponentials comes out as the sum of cosines of randomly distributed angles. Therefore the only significant contribution to the sum at large Q comes from the sum of self-terms with $j = k$, where the exponential terms are all equal to 1. Therefore for large Q,

$$S_{MW}(Q) \rightarrow \sum_{k}^{N_c} M_k M_k.$$

Now we expect $S_{MW}(Q) \rightarrow 1.0$ at large Q, because at large Q the scattering vector is

probing inside the clusters, where there will be no inter-cluster structure. To obtain this condition $S_{MW}(Q)$ must be normalised by the sum of self-terms, $\sum_k^{N_c} M_k^2$.

Mass-position correlation

Mass-weighted cluster structure factors are plotted in Figures 3.24 and 3.25. It is immediately obvious that, at intermediate times at least, $S_{MW}(Q \to 0) < S_{CM}(Q \to 0)$. This can be understood by noting that large clusters contribute more to $S_{MW}(Q)$, and in a polydisperse system large clusters tend to be more 'confined' by each other (small clusters on the other hand can explore the narrow spaces between the large clusters). Such confinement tends to drive the structure factor down at small Q (large lengths). The rise in $S_{CM}(Q)$ as $Q \to 0$ for high density systems (section 3.3.3) is no longer visible in $S_{MW}(Q)$, suggesting that the rise is due to small clusters (which are strongly underweighted in S_{MW}); this is further discussed in the next Chapter.

That $S_{MW}(Q)$ differs markedly from $S_{CM}(Q)$ indicates that there are important cluster mass-position correlations in the system. The question arises whether it is simply the *mass 'number' distribution* (the number of clusters at each mass) or also the *mass spatial distribution* which is important. To check this we can eliminate the mass spatial distribution by 'shuffling' the masses about the clusters, that is randomly swapping the masses M_k of pairs of clusters and then recalculating $S_{MW}(Q)$ from equation (3.18). This procedure significantly alters the calculated structure factor, as shown for one example in Figure 3.26. Therefore the form of $S_{MW}(Q)$ depends not simply on the mass number distribution but also on the spatial distribution of the masses.

Similar ideas have been proposed for polydisperse systems in general [2]. While most models of the scattering of polydisperse systems are forced to make the assumption that particle size and particle position are uncorrelated (see e.g. Refs. [132, 133]), it is generally recognised that in strongly polydisperse systems size and position are correlated. At a very simple level, consider a system of large and small particles; the small particles will be able to explore areas from which the large particles tend to be excluded. Structure in polydisperse systems [128, 132, 133, 139] would seem a

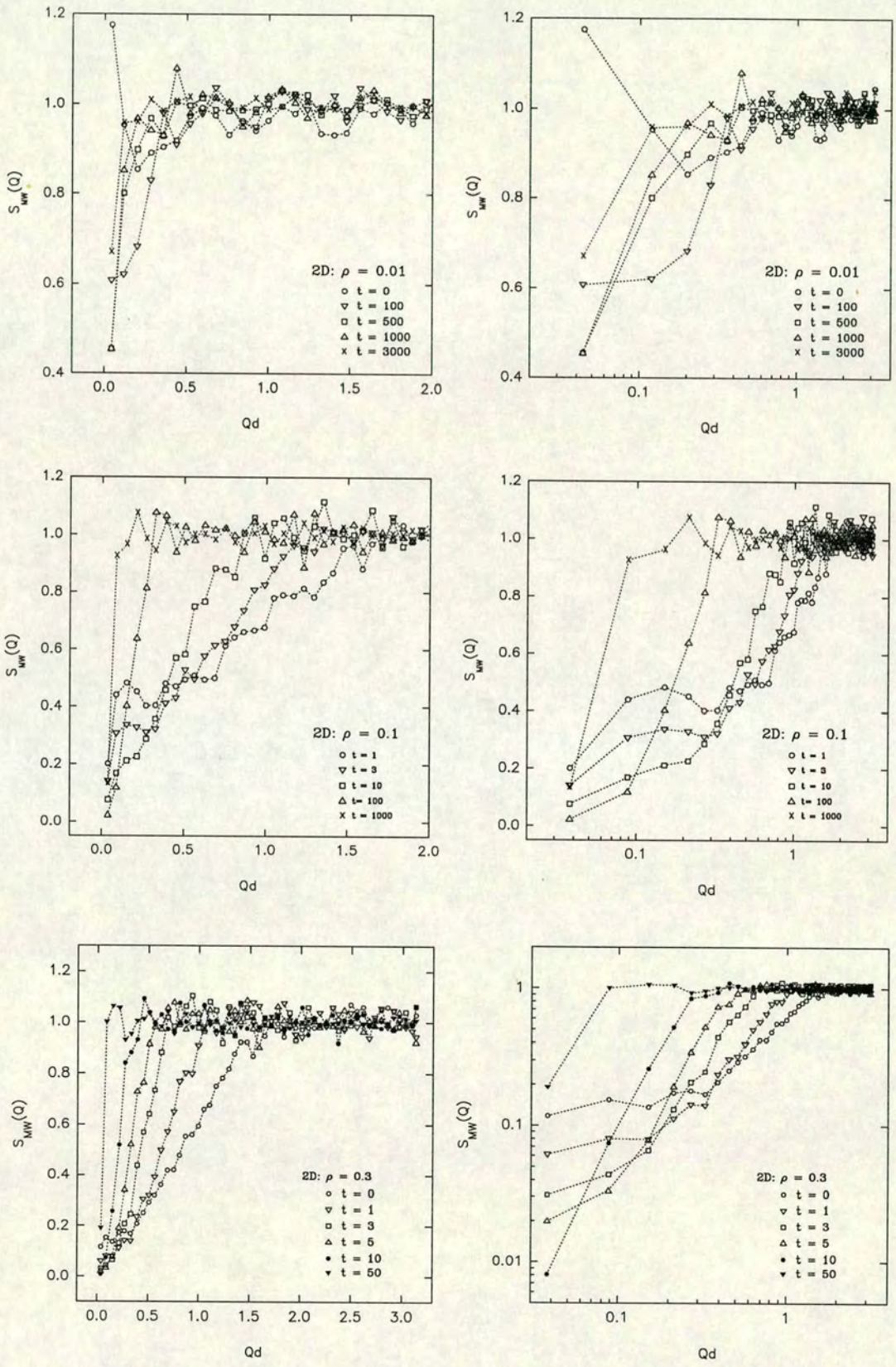

Figure 3.24. Mass-weighted structure factors of the centre of mass positions of clusters in lattice-based DLCA simulations in 2D. $S_{MW}(Q,t)$ is calculated from equation (3.18). The x-axis is $Q \times d$ where d is the particle diameter (lattice-spacing).

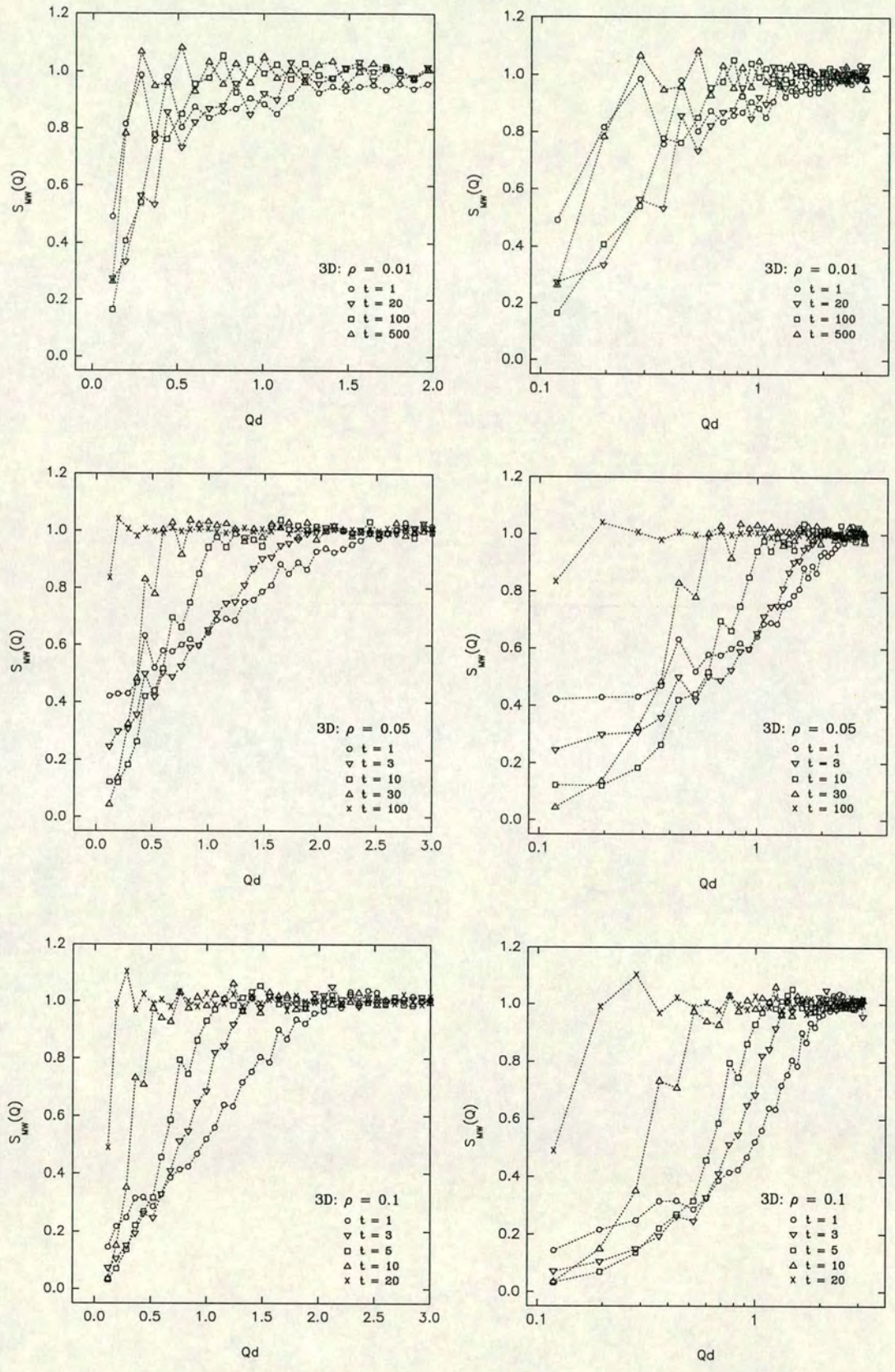

Figure 3.25. Mass-weighted structure factors of the centre of mass positions of clusters in lattice-based DLCA simulations in 3D.

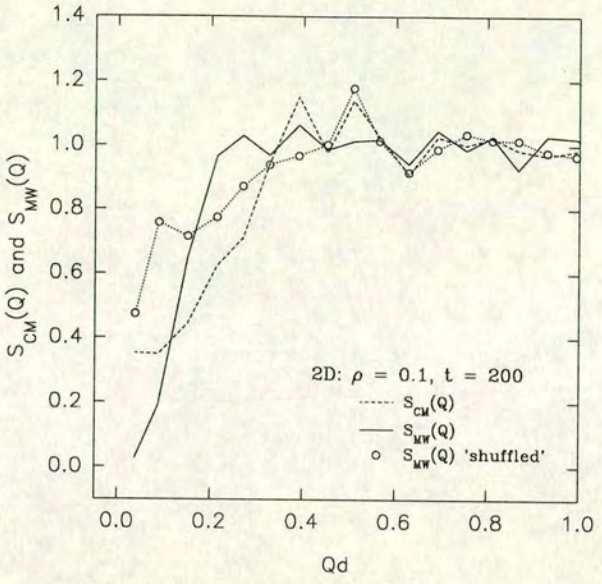

Figure 3.26. The effect of spatial mass distribution on the centre of mass structure factor. Comparison of unweighted and mass-weighted centre of mass structure factors $S_{CM}(Q)$ and $S_{MW}(Q)$, and the mass-weighted structure factor recalculated after 'shuffling', i.e. random swapping of pairs of cluster masses. In this example the system is a 2D lattice-based simulation at number density $\rho = 0.1$, at time $t = 200$ steps.

potentially very interesting and important area for future research, given its relevance to industrial systems. We return to the discussion of mass-position correlations in the next Chapter.

Cross-cluster correlations

We try once again the separation in equation (3.5), this time computing

$$A_{MW}(Q,t) = S_{MW}(Q,t)P(Q,t). \tag{3.20}$$

$A_{MW}(Q,t)$ is compared with $I(Q,t)$ in Figures 3.27 to 3.30. While once again the separation fails in general, there is one case ($\rho = 0.1$ in 2D) where for a limited time region ($50 \leq t < 500$) the separation works remarkably well. The trend is for A_{MW} to underestimate $I(Q)$ at early time and overestimate $I(Q)$ at late time. Only in the case of $\rho = 0.1$ in 2D is there an appreciable region of time when $A_{MW}(Q) \simeq I(Q)$.

That the separation in equation (3.5) works with the mass-weighted structure factor

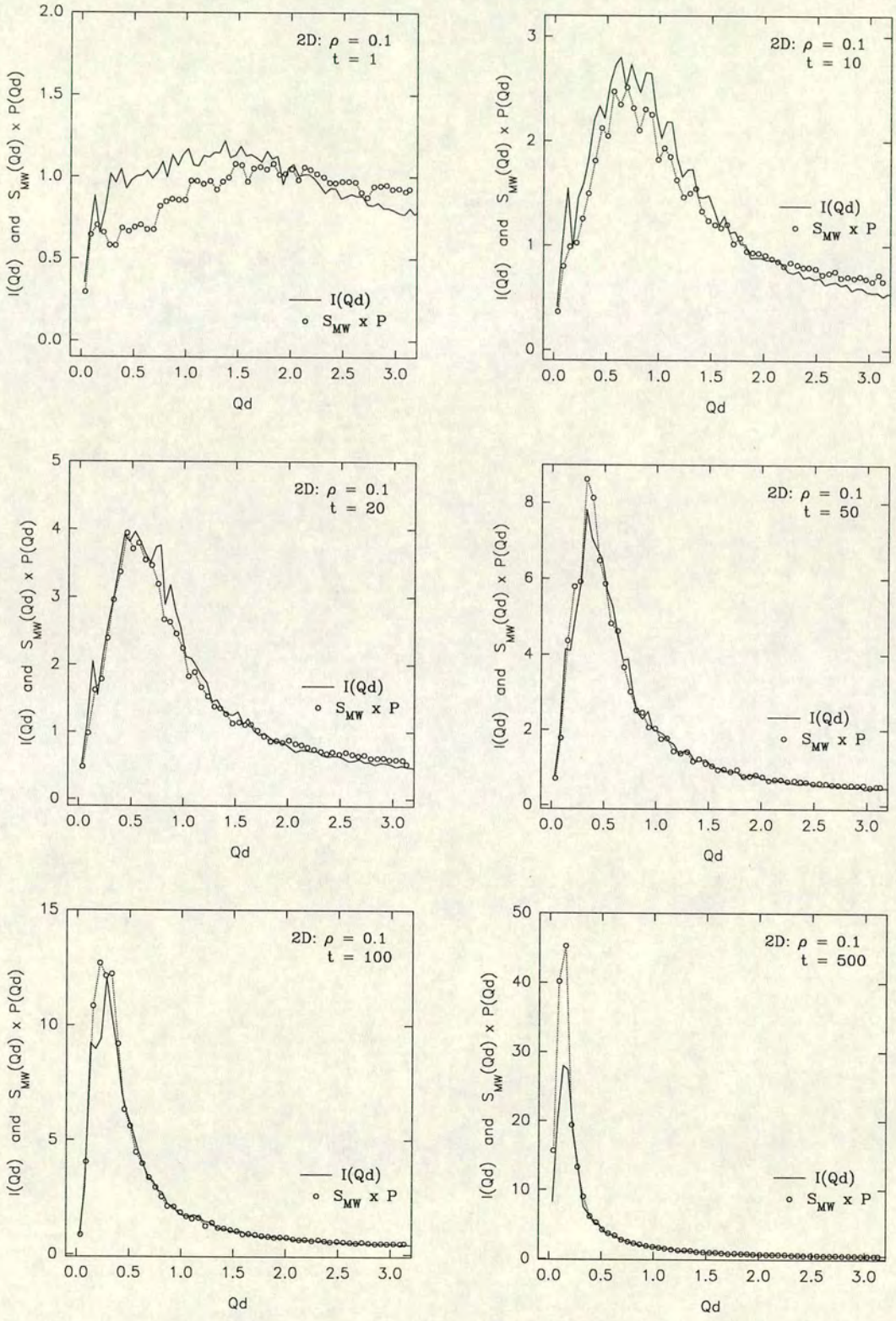

Figure 3.27. Comparison of $I(Q)$ and $S_{MW}(Q) \times P(Q)$ for a 2D simulation with $\rho = 0.1$, $L = 300$. S_{MW} is the mass-weighted centre-of-mass structure factor, $P(Q)$ is the average form factor.

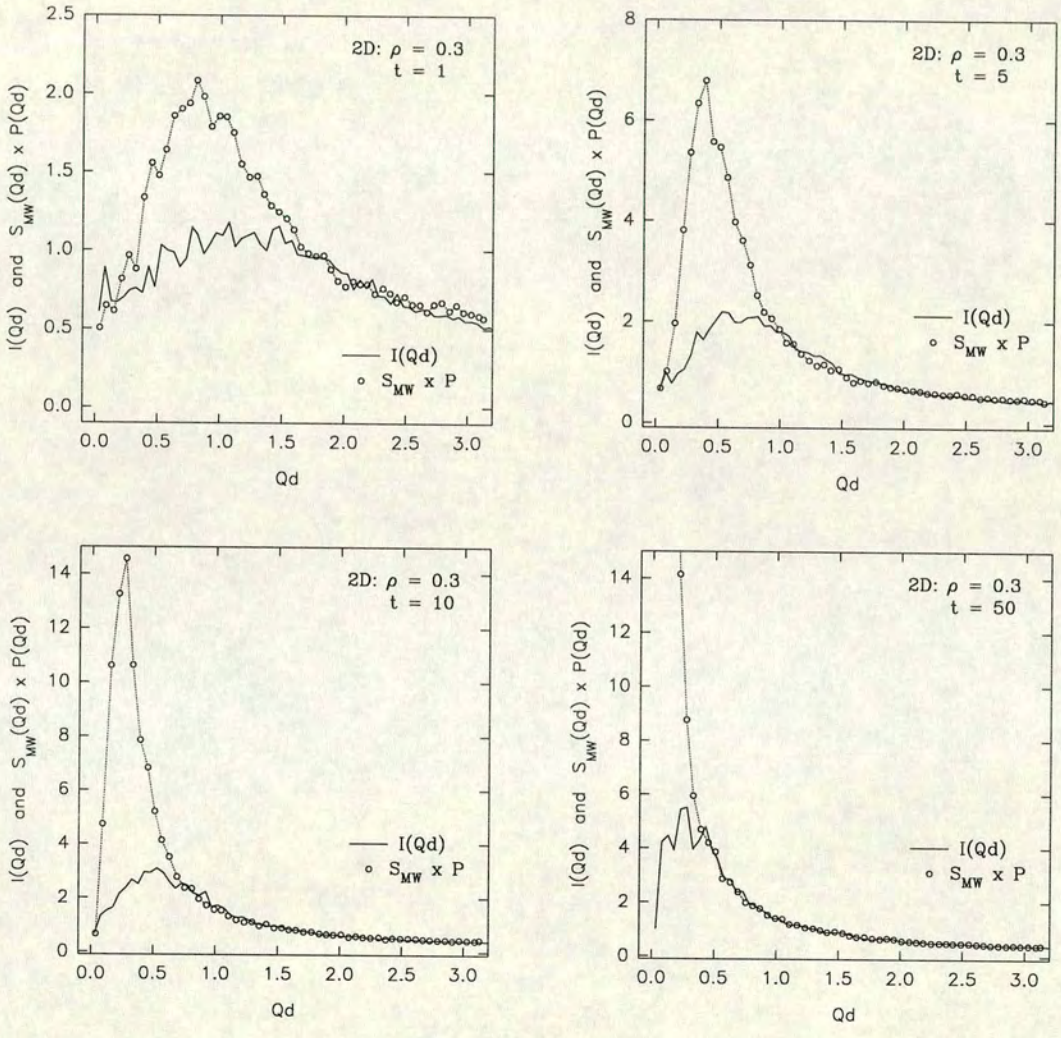

Figure 3.28. Comparison of $I(Q)$ and $S_{MW}(Q) \times P(Q)$ for a 2D simulation with $\rho = 0.3$, $L = 300$. S_{MW} is the mass-weighted centre-of-mass structure factor, $P(Q)$ is the average form factor.

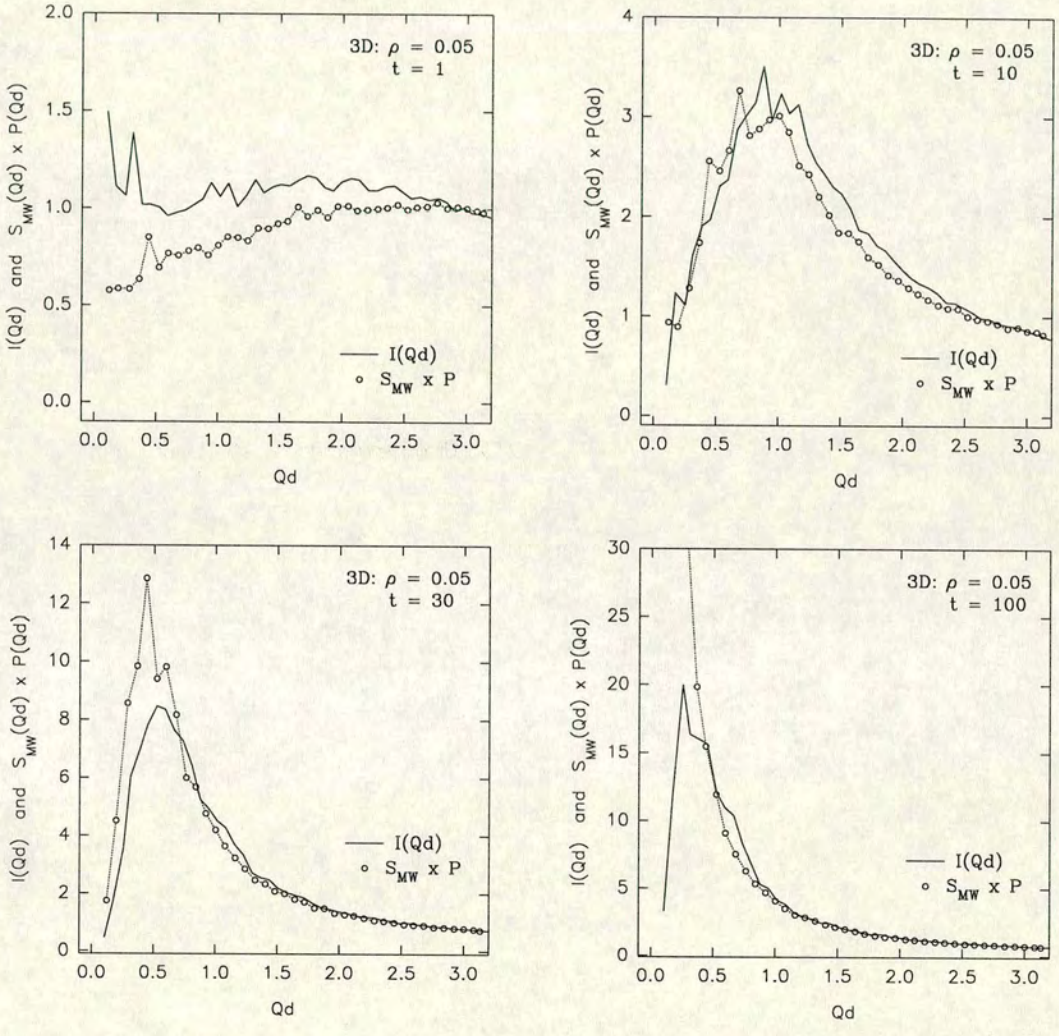

Figure 3.29. Comparison of $I(Q)$ and $S_{MW}(Q) \times P(Q)$ for a 3D simulation with $\rho = 0.05$, $L = 70$. S_{MW} is the mass-weighted centre-of-mass structure factor, $P(Q)$ is the average form factor.

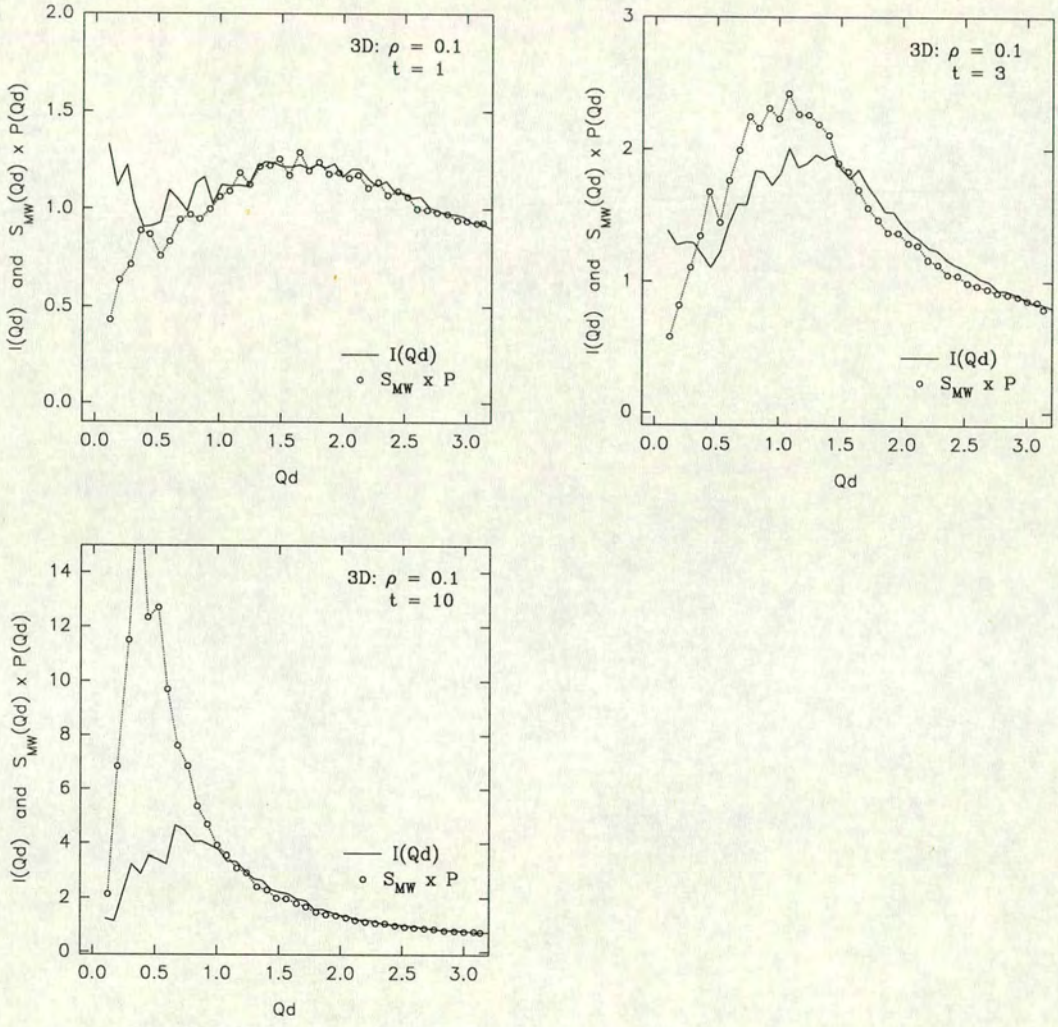

Figure 3.30. Comparison of $I(Q)$ and $S_{MW}(Q) \times P(Q)$ for a 3D simulation with $\rho = 0.1$, $L = 70$. S_{MW} is the mass-weighted centre-of-mass structure factor, $P(Q)$ is the average form factor.

only in a limited time regime indicates then that the addition of mass-position correlations still is not sufficient to completely describe the structure of the DLCA aggregating system at all times. Recall that use of equation (3.18) in equation (3.5) still involves our first condition, that *every* particle in a given cluster has the *same* correlations with other clusters' particles. Therefore breakdown of the separation implies that there remain in the DLCA system important positional correlations between particles in different clusters. The most probable source of these correlations is the *shape correlation* of the surfaces of neighbouring clusters. Visual examination of the aggregating systems (section 3.1.1) demonstrates quite convincingly that, especially at higher densities, the neighbouring surfaces of neighbouring clusters do have some degree of *shape correlation.* The formation of quite well-defined 'channels' between clusters is clear [99], and a little thought demonstrates what a 'channel' is: where there is a 'bay' in the surface of one cluster, there is a corresponding 'promontory' in the surface of its facing neighbour. But only particles near the surface will 'feel' this neighbour-cluster correlation strongly, and then only with the nearest neighbour clusters; these particles will have weaker correlations (if any) with more distant clusters; and particles further into the body of a cluster will tend not to feel any strong correlations with other clusters.

The degree of neighbour-surface correlations must depend on how strongly the growth of clusters is affected by the presence of other clusters. The strength of this effect will in turn clearly depend on the *effective density* of the system. As space is filled by the growing fractals (see Chapter 1) the effective density increases, consistent with the observation that the separation of scattering using S_{MW} fails at later times. At the highest particle concentrations a situation of near-'isolated' growth of clusters is never realised, so that we would expect cross-cluster correlations to have a substantial effect at almost all times in systems at high concentration. Because with the lattice model we cannot observe very early times, we never see $A_{MW}(Q) = I(Q)$ in high density systems (e.g. Figure 3.28).

The failure of the separation of scattering using S_{MW} at early times is more difficult to understand. It may be that the problem then lies with $P(Q)$; the average form factor at early time combines larger near-fractal clusters with small non-fractal clusters

(monomers, dimers, trimers). Furthermore on the lattice there are pre-existing 'percolation clusters' (see Chapter 2) whose structure and structural correlations presumably differ from DLCA clusters; it may take some time for the 'memory' of these percolation clusters to be lost.

Elements of structure—Conclusions

The analysis of this subsection gives a somewhat clearer picture of the elements of structure and correlation which go together to determine the structure of the DLCA system. We conclude that the DLCA scattering function depends on a number of important factors: internal cluster structure; cluster arrangement; cluster mass number distribution; cluster mass *spatial* distribution; and cross-correlations of particles in different clusters, themselves probably a very complicated set of terms derived from the shape correlations of neighbouring surfaces. It is clear then that the detailed structural description of the DLCA system is a far from simple problem.

3.4 Evolution of the scattering function

We go on now to consider the time-evolution of structure in the DLCA system. A useful way to study the evolution of the scattering function and thus the evolution of structure in the aggregating system is to examine how the position Q_m and amplitude $I(Q_m)$ of the small-angle peak in $I(Q)$ change as the aggregation proceeds. This sort of analysis has been carried out for other simulation models (e.g. of phase separation, Ising model simulations, and so on) as well as for experiments and theoretical models [53, 55, 57, 58, 59, 140, 141], and so offers a good opportunity for comparison between the DLCA model and related systems.

Power-law approximations for the dependence of peak amplitude and position have been extensively used in previous work. While it is often the case that data for Q_m and $I(Q_m)$ from simulations and experiments do not exhibit perfect power-law relations [142], and indeed sometimes fail to show any extended region of power-law behaviour, it is still worth following previous analyses of simulations, theory and experiments. This,

at the least, enables us to compare results from the DLCA simulation model with other models and related phenomena. It should be kept in mind however that, as discussed in Ref. [142], these power-law models remain *approximations*. There are however various more or less 'phenomenological' models of growth in phase separating systems [143, 144], discussion of and comparison with which are included in the following subsections.

3.4.1 Peak position Q_m

Plots of Q_m versus simulation time for a range of number densities ρ in both 2D and 3D are given in Figure 3.31. Q_m is estimated carefully 'by eye' from the circularly-averaged plots of $I(Q)$, after selecting an optimum 'bin width' δQ for the circular average. (In practice 'optimum' means the best compromise between resolution of the peak position in Q and averaging over enough reciprocal lattice points to give a reasonably noise-free estimate of $I(Q_m)$.) Error bars in the plots are estimated again by eye, from the maximum spread of the $I(Q)$ data about the peak[7].

Approximate power-law dependence of the peak position Q_m on time

$$Q_m \sim t^{-\alpha}, \tag{3.21}$$

at least over some time regime, is observed in all simulations. Estimates of the exponent α are given in Table 3.5. Exponents are estimated using a linear least-squares fit to the logarithms of the Q_m *vs* t data [145]. Because of the relatively small simulation sizes L, error bars on Q_m are rather large, expecially at the latest times when Q_m approaches $2\pi/L$. Thus the uncertainty on the exponent in the relation (3.21) is quite high. Error bars and Q_m ranges for the fits are also given in Table 3.5.

[7] Attempts were made to estimate peak positions, amplitudes and error bars more 'objectively' by fitting n-degree polynomials to the $I(Q)$ data. However it was found that this method did not generally give reliable estimates of Q_m or $I(Q_m)$ and careful direct measurement turned out to be less prone to error.

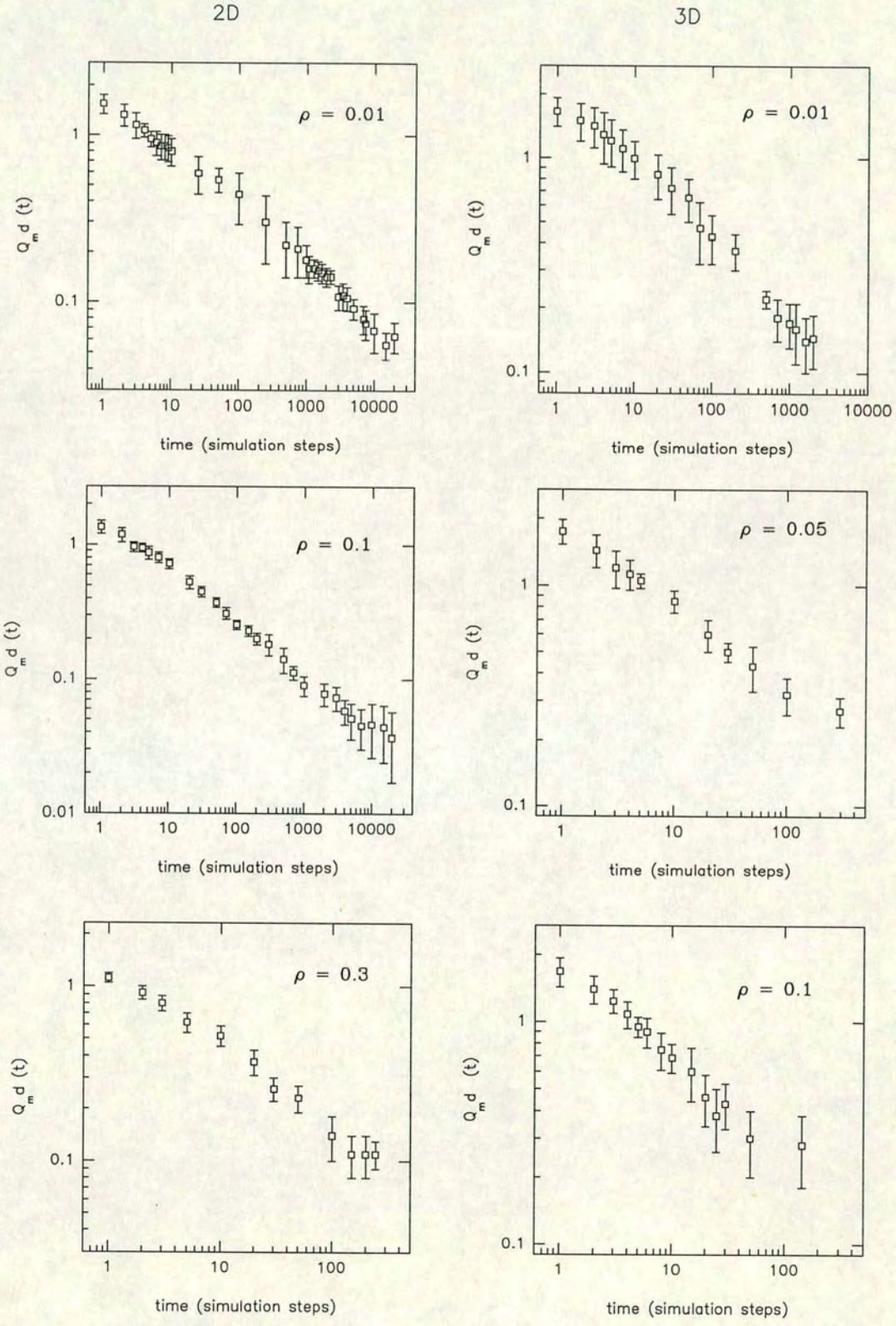

Figure 3.31. Scattering function small-Q peak position, Q_m, *vs.* time, for lattice-based simulations in 2D (left column) and 3D (right column). Systems sizes are $L = 500$ ($\rho = 0.01$, 2D), $L = 300$ ($\rho = 0.1$ and 0.3, 2D) and $L = 70$ (3D).

Density	α	(range)	β	(range)	γ	(range)	$d_{f,P(Q)}$
(a) 2D							
0.01	0.33 (0.01)	1-15000	0.79 (0.02)	1000-15000	1.77 (0.14)	0.06-0.6	1.37–1.47
0.1	0.42 (0.02)	10-20000	0.61 (0.01)	10-5000	1.48 (0.06)	0.07-1.0	1.38–1.45
0.3	0.42 (0.03)	1-200	0.39 (0.02)	1-30	1.17 (0.21)	0.4-1.2	1.25–1.58
(b) 3D							
0.01	0.39 (0.03)	5-5500	1.05 (0.07)	100-1000	2.5 (0.39)	0.1-0.7	1.92
0.05	0.38 (0.03)	1-100	0.85 (0.07)	10-50	1.72 (0.13)	0.2-2.0	1.84
0.1	0.44 (0.05)	1-50	0.70 (0.07)	4-10	1.44 (0.05)	0.5-2.0	1.85

Table 3.5. Exponents for power-law fits to $Q_m(t) \sim t^{-\alpha}$ and $I(Q_m, t) \sim t^{\beta}$. γ is the exponent in the fit of $I(Q_m) \sim Q_m^{-\gamma}$. 'range' is the ($t$ or Q_m) range over which the fit is estimated. Figures in brackets are error-bars for the exponents. $d_{f,P(Q)}$ is the fractal dimension as estimated from the average cluster form factor $P(Q)$ (section 3.3.2), either from a power-law fit (2D) or from fitting the Fisher-Burford formula (3D).

The approximate power-law behaviour of the peak position (equivalently of the 'characteristic' length scale) invites the comparison with other phase-separating systems [53, 55, 57, 59, 60, 140]. The Lifshitz-Slyozov-Wagner (LSW) theory for the growth and coarsening of droplets in liquid phase separation [143], for instance, considers a 'mean field' situation of a single growing cluster embedded in a uniform, spherically-symmetric background far from any other growing cluster; it is assumed there are no 'interactions' (e.g. competition for particles) between growing clusters and any possible effects of inter-cluster structure are ignored. All growth is assumed due to capture of monomers by the growing cluster[8]. This model applies best to a system of well-separated, well-defined droplets. The Binder-Stauffer (BS) model [144] on the other hand derives a growth exponent by considering the diffusion of clusters. In the DLCA case we would expect these models to apply, if at all, to a low-density system of large

[8]The Lifshitz-Slyozov-Wagner theory is often called a *coagulation* theory, which is misleading: growth does not occur by coagulation of growing clusters, but rather large clusters grow 'at the expense of' small clusters. The implied mechanism is that the small clusters 'evaporate' into monomers, and the monomers then join the large cluster. There is no co-diffusion and collision of clusters.

clusters, where growing clusters are very far apart and diffuse slowly. For the lowest density simulations our exponents are in reasonable agreement with the predictions of the LSW theory and the BS theory, both of which models predict a growth exponent in separating fluids $\alpha = 1/3$.

Even in low-density systems however, the eventual onset of gelation where fractal clusters progressively fill more space and approach closer to each other, is likely to render the LSW model incorrect, even if estimated exponents show no change. A simple estimate of the growth exponent is not necessarily a very precise test of whether the *physical processes* of a model are indeed close to the real system. This is demonstrated by the fact that the LSW and BS models, based on apparently different premises, give the same predictions for the growth exponent.

There may be some trend for the exponent α to increase with increasing density in the DLCA simulations (though it is important to note that curvature in the data or lack of power-law dependence, as often seen in experiments [146], is difficult to rule out given the error bars in the data). It is certainly the case that at the higher densities (e.g. $\rho = 0.3$ in 2D, see Figure 3.3) a situation of separate well-defined clusters is never realised even at the earliest accessible times; it would not seem reasonable to apply the LSW model here.

Effect of cluster diffusion scaling

In a recent simulation of a 2D DLCA system at area fraction $\Phi = 0.1$ [81] an estimate of the growth exponent $\alpha \sim 0.7$ is reported. In Ref. [81] α is estimated from an examination of the scaling of the 'first zero of $g(r,t)$' with simulation time. However the simulations of Ref. [81] were implemented with a constant, *size independent* cluster diffusion coefficient D_{cl} (Chapter 2) [147]. It appears that using different exponents δ in equation (2.4) (Chapter 2) has a substantial effect on the behaviour of $I(Q)$. Assuming *constant* diffusion for all clusters regardless of their size ($\delta = 0$ in equation (2.4), as used in Ref. [81]) leads to a faster aggregation, and from a 2D simulation at number density $\rho = 0.1$, we obtain an exponent $\alpha = 0.65 \pm 0.06$ (Figure 3.32). This is in good agreement with the results reported in Ref. [81] though the importance of the cluster

diffusion scaling prescription does not seem to have been considered in that paper.

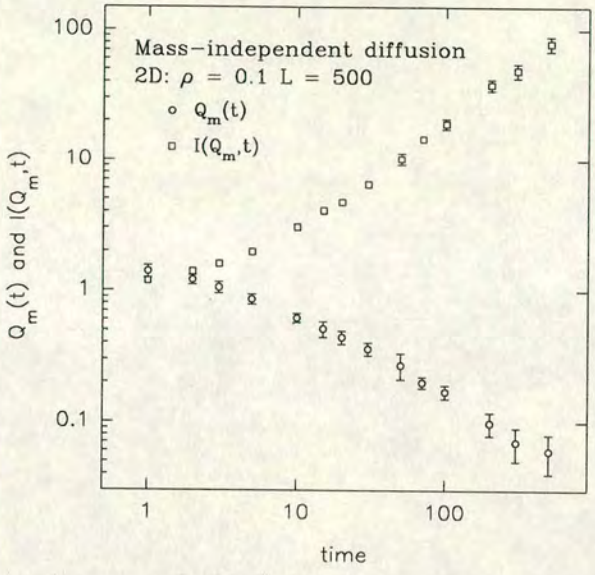

Figure 3.32. The time-evolution of $I(Q)$ peak position Q_m and peak intensity $I(Q_m)$ for a 2D simulation at $\rho = 0.1$, where the diffusion rates of clusters are independent of the cluster sizes.

Gelation and 'pinning'

In some experiments [11, 53] and simulations of other models (e.g. [148, 149]) a 'pinning' effect is observed, where further growth of the characteristic length scale is frustrated by the onset of *gelation*. The effect on the scattering peak is to 'freeze' the peak at some near-constant $Q_m = Q_g$. (Striking dynamic effects have also been observed by dynamic light scattering in a gelling colloid-polymer mixture [11], where diffusion in the system on a wide range of length scales slows down dramatically. This can be observed directly simply by watching the speckle pattern of light scattered by the experimental sample; the remarkable slow-down of the intensity fluctuations of the speckles is easily visible.) In our DLCA simulations, at the higher densities ($\rho = 0.3$ in 2D and $\rho = 0.05$ and 0.1 in 3D) in those systems where a proper gel forms (as opposed to a single large fractal cluster) Q_m is similarly observed to approach a constant. Unfortunately the large error bars again make determination of Q_g rather inaccurate. The gel peak position Q_g has been considered as an estimate of the 'gel size', that is the size of fractal clusters in the gel assembly, $R_{gel} \simeq 2\pi/Q_g$ (Chapter 1), by some authors [46, 49, 65].

However equation (1.30) of Chapter 1 gives estimates substantially lower than implied by our measured Q_g. It is not clear that the lengths R_{gel} and $2\pi/Q_g$ are equivalent, since the simple model of gelation from which R_{gel} is derived essentially assumes the cluster grows *until its average density reaches the average system density*, i.e. it does not take account of the depletion zone which persists into the gel structure ($Q_g > 0$). The *scaling* of Q_g with system density Φ has been examined in experiments [46, 49] and recently in simulation [65]. In experiments the scaling appears to agree quite well with equation (1.30) *up to a maximum density* $\Phi \approx 0.01$. Similarly in the DLCA simulations of Gonzalez and Ramirez-Santiago the scaling of Q_g and Φ agrees well with equation (1.30), *but now works at least up to* $\rho = 0.08$. Given the limited number of different number densities we have studied we cannot hope to similarly study the scaling of our Q_g with ρ. However it is worth pointing out that in our 3D simulations at $\rho = 0.05$ and $\rho = 0.1$ we find $Q_{gel} \approx 0.3$ (particle diameters)$^{-1}$, i.e. our simulations are consistent with the experiments, in that Q_{gel} approaches a constant independent of density for densities higher than $\rho \approx 0.01$.

3.4.2 Peak intensity $I(Q_m)$

Analysis of $I(Q_m)$ in terms of power-law approximations has been widely used in studies of first-order phase transitions [55]. $I(Q_m)$ and error bars are estimated from the plots of $I(Q)$ 'by eye' as described above, and plotted against simulation time t in Figure 3.33. A first examination leads to the identification of three regimes in time from the data. (The lattice effect on the 'start time' as discussed in Chapter 2 means that for the lattice model the early time region is accessible only at the low densities, $\rho = 0.01$ in both 2D and 3D). In this early time region $I(Q_m)$ clearly does not follow a power law. During these early times, in fact, the data better fit an *exponential* relation, $I(Q_m, t) \sim e^{\beta t}$, as shown in Figure 3.34. The time regime for this behaviour is rather short, and the fit may be no more than coincidental. A linear model for the evolution of structure in an unstable mixture (i.e. phase separation by spinodal decomposition) [55, 60] predicts a similar exponential growth of scattering peak amplitude at very early time; however the same theory also predicts that the peak position Q_m or characteristic

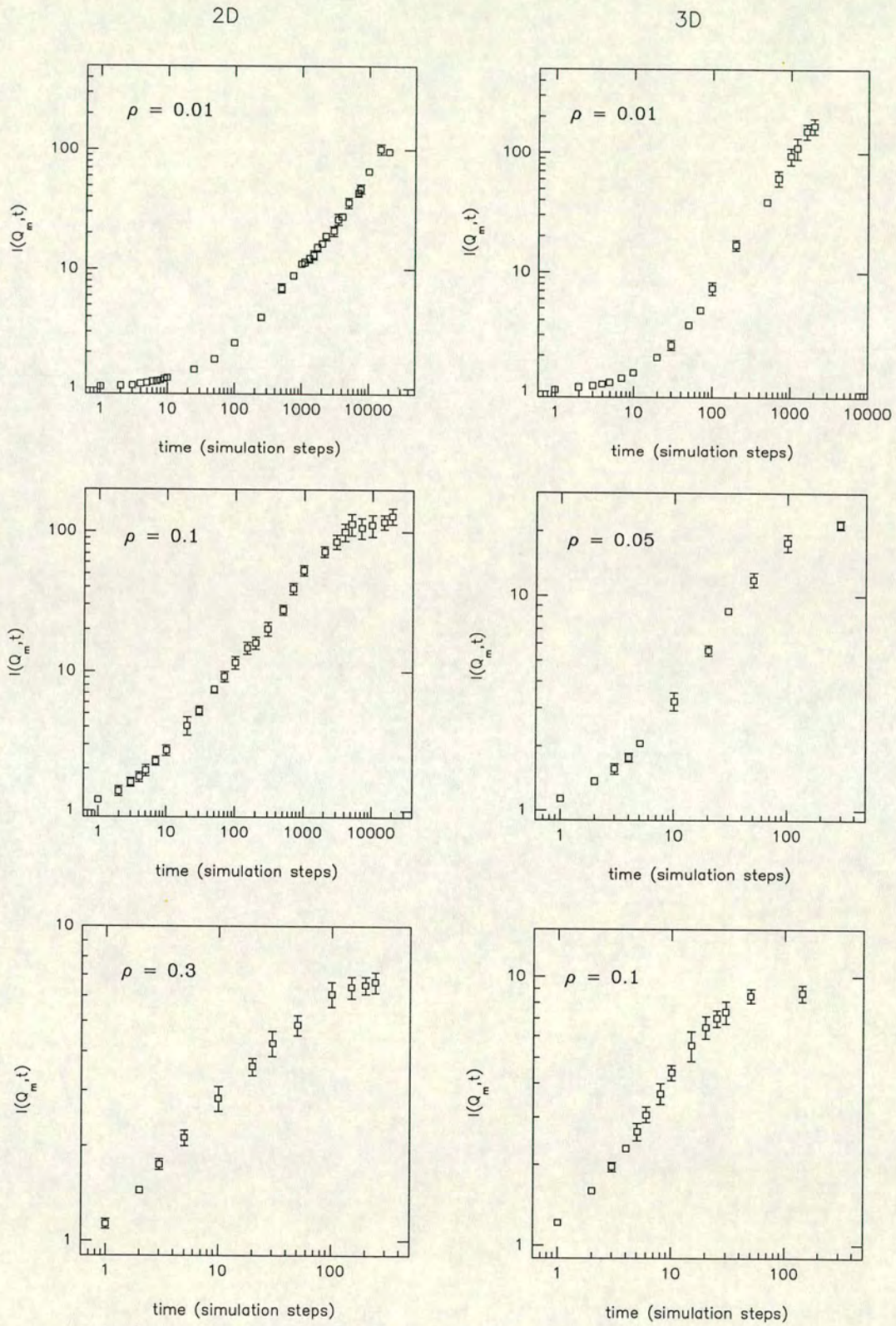

Figure 3.33. Scattering function small-Q peak intensity, $I(Q_m)$ *vs.* time, for lattice-based simulations in 2D (left column) and 3D (right column). Systems sizes are $L = 500$ ($\rho = 0.01$, 2D), $L = 300$ ($\rho = 0.1$ and 0.3, 2D) and $L = 70$ (3D).

length scale should be a constant in this time regime, which is not evident from the DLCA data. In fact this exponential regime has rarely been convincingly confirmed in previous simulation or experiment [150], and the DLCA data here are similarly unconvincing.

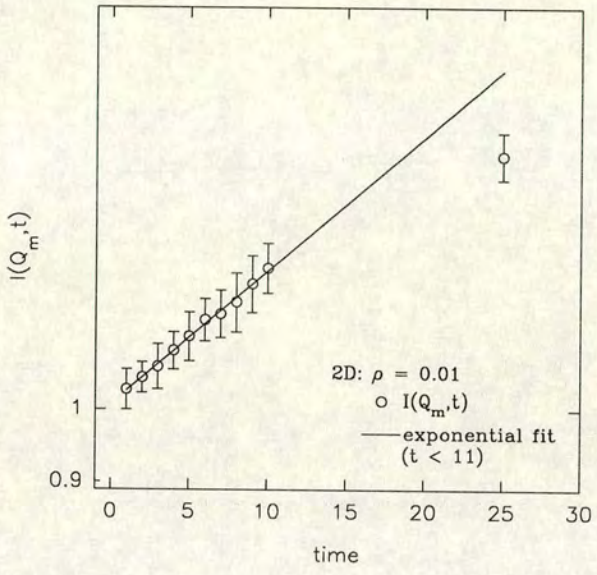

Figure 3.34. Log-linear plot of scattering function peak intensity $I(Q_m, t)$ *vs.* time t, for a low density ($\rho = 0.01$) 2D DLCA simulation. The straight line is an exponential function, $I(Q_m, t) = Kexp(\beta t)$ fitted to the data between times $t = 1$ and $t = 10$.

In an intermediate time regime, approximate power law behaviour,

$$I(Q_m, t) \sim t^{\beta}, \tag{3.22}$$

develops. Estimates of the exponent β for the different densities in 2D and 3D are given in Table 3.5. (The power-law exponents and error bars are determined from least-squares linear regression fits to the logarithms of the data [145].) In both 2D and 3D simulations, there is a definite trend for the power-law exponent β to decrease with increasing density.

At late times at the higher densities the amplitude $I(Q_m)$ 'saturates' and approaches a constant I_{gel}. Now of course trivially $I(Q_m)$ must become constant at gelation, when

growth stops. As the growth changes character from fractal aggregation to the 'close-packed' assembly of clusters near gelation one might expect the behaviour of $I(Q_m)$ to change. Similar near-gelation saturation effects on $I(Q_m)$ have been observed in experiments with polymer mixtures [53] and with colloid-polymer aggregates [11, 16]. We show in Chapter 4 that under conditions where clusters grow more compactly and gelation is 'avoided', such an intensity saturation is not observed, indicating that the saturation we see in the simulations is indeed due to gelation. Consistent with this we only convincingly observe saturation at the higher densities where the system is large enough to properly simulate the onset of gelation.

Finite size effects and lattice effects on $I(Q_m)$ and Q_m

For the 2D simulation at $\rho = 0.3$ Figure 3.35 presents $I(Q_m, t)$ and $Q_m(t)$ data from two lattice-based simulations with different system sizes, $L = 500$ and $L = 300$. It can be seen from the $I(Q_m, t)$ plot that the estimates are not affected by the finite size of the system at the system sizes and density considered. However there is evidence that the saturation behaviour in $I(Q_m)$ may be affected by system size in smaller systems (see Figure 3.36). A significant problem is that estimates of Q_m and $I(Q_m)$ are subject to greater uncertainty at late times since as Q_m approaches $2\pi/L$ there are fewer and fewer points in the reciprocal lattice for the circular or spherical average. With systems as large as $L = 300$ and $L = 500$ it seems that the system is large enough that the late-time saturation is unaffected within the error bars. This is in the highest density system; it is certainly the case that at lower densities, where the gel cluster size will be much larger, we cannot properly observe the late-time gelation behaviour of $I(Q_m)$. This is consistent with the results from the calculation of average form factors $P(Q)$.

Q_m and $I(Q_m)$ data from lattice-based simulations and off-lattice simulations in 2D are compared in Figure 3.36. The lattice-model number densities are $\rho = 0.1$ and $\rho = 0.3$, and the continuum-model area fractions are $\Phi = 0.1$ and $\Phi = 0.3$. (The $\Phi = 0.3$ off-lattice results are obtained from an average over 9 repeat runs of the off-lattice simulation; the $\Phi = 0.1$ results come from a single run.)

In the plots off-lattice simulation time is rescaled to agree approximately with on-lattice

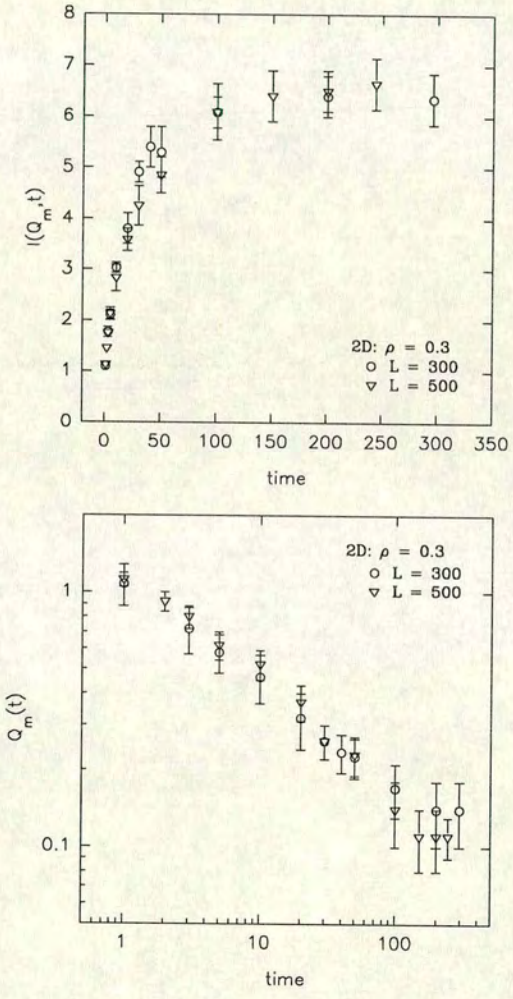

Figure 3.35. Comparison of the scaling with time of scattering function peak amplitude $I(Q_m, t)$ and peak position $Q_m(t)$, for different-sized 2D lattice systems. The number density is $\rho = 0.3$; the system sizes are $L = 300$ and $L = 500$ particle diameters.

time. The time step in the off-lattice simulations is much shorter than that in the lattice-based model, because the off-lattice average random-walk step length is 3.3% of the particle diameter, whereas the equivalent step length on-lattice is of course a whole lattice spacing or particle diameter. A diffusing monomer in the off-lattice simulation would have on average a displacement of one particle diameter after approximately $1/(0.033^2) \simeq 919$ random-walk steps. Therefore off-lattice time is rescaled by dividing by 919, and the plots give Q_m and $I(Q_m)$ against time in lattice-time units. The lattice effect on the 'start time' as discussed in Chapter 2 is well-demonstrated in the Figure. The off-lattice model has the advantage that much earlier times are accessible compared to the lattice model; there is no effect of density on the 'start' time.

The data in the early-time regions and the power-law regions do not differ substantially, indicating the absence of significant effects due to the use of the lattice (and also the absence in early time, as noted above, of significant effects due to the smaller size of the off-lattice systems). This is encouraging because it is at early time when the characteristic length is small (closer to the lattice parameter) that we might expect the most important structural effects of the use of the lattice. For instance there are undoubtedly effects of the lattice on $I(Q)$ at short length scales as indicated by the speckle plots in Figure 3.6, but $I(Q_m)$ does not seem to be sensitive to these effects.

However the *late-time* behaviour of both Q_m and $I(Q_m)$ differs. The effects of the lattice and of the smaller size of the off-lattice systems are compounded here. Since at late time (small Q_m) Q_m and $I(Q_m)$ are measuring *large* structural details, one would expect that lattice effects on the structural data would be less important at late time (certainly less important than at early time when the characteristic length is much more comparable to the lattice parameter). Thus the late-time differences in Figure 3.36 seem more likely due to the small sizes of the off-lattice systems. Certainly the effects of system size must be more important at late time when the system contains large structures. Unfortunately due to computational constraints it has not been possible to carry out off-lattice simulations with larger systems.

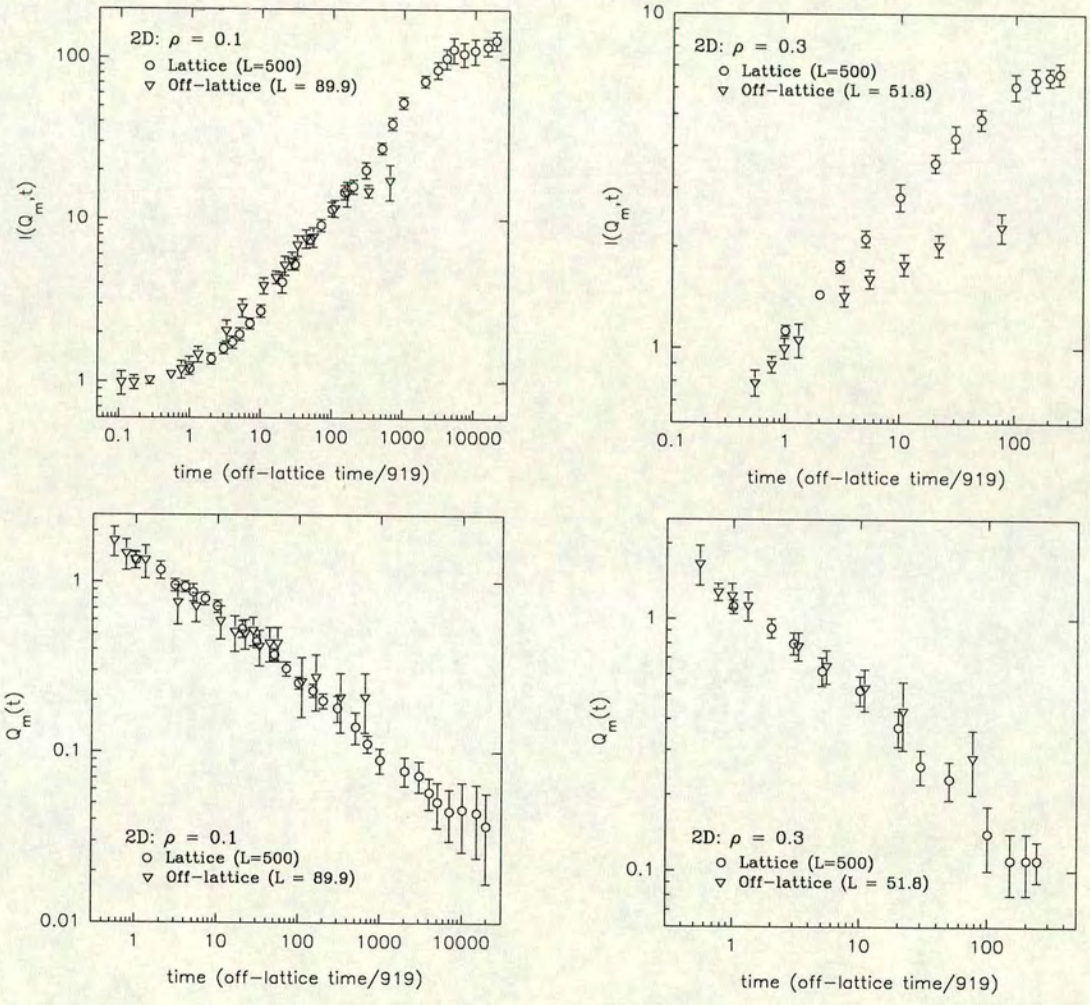

Figure 3.36. Comparison of scattering function peak amplitude $I(Q_m, t)$ and peak position $Q_m(t)$ from 2D lattice-based and off-lattice models. Lattice-based system sizes are $L = 500$ with number densities $\rho = 0.1$ and $\rho = 0.3$. The off-lattice systems are at area fractions $\Phi = 0.1$ (system size $L \approx 89.9$) and $\Phi = 0.3$ ($L \approx 51.8$). Off-lattice time is rescaled as described in the text.

3.5 Scaling of the scattering function

Perhaps one of the more remarkable phenomena demonstrated in recent colloidal aggregation experiments is that the scattering function has a *time independent form.* In analogy to the *dynamic scaling hypothesis* for the scattering function of a spinodally decomposing system first introduced by Marro and co-workers [58] and later examined extensively by Furukawa [151], it has been demonstrated [16, 45, 52] that $I(Q,t)$ for the aggregating colloidal system obeys a scaling relation:

$$I(Q/Q_m,t) \sim Q_m^{-\gamma}(t)F(Q/Q_m) \tag{3.23}$$

where $Q_m(t)$ is the position of the small-Q peak in $I(Q,t)$ at time t, $F(Q/Q_m)$ is a *time-independent* scaling function and γ is the *scaling exponent.* In colloidal aggregation experiments γ has been shown to be approximately equal to the fractal dimension d_f of the clusters of colloidal particles. In many systems undergoing unstable (i.e. spinodal) phase separation or first order phase transitions, from simple liquids to mixtures of polymers, the scattering function is found to scale as in equation (3.23), but with a scaling exponent $\gamma = D$, the space dimension.

Presumably the difference between colloidal particle aggregation and phase separation in these other systems is that colloidal aggregates are fractal objects rather than compact droplets or phases[9]. It has been suggested that the intensity of the small-Q peak $I(Q_m)$ should be approximately proportional to the mass of a typical 'scattering object' (e.g. [64]). If the length scale of the typical scatterer is given by $l \sim Q_m^{-1}$, then $I(Q_m)$ should be given by

$$I(Q_m) \sim m_t \sim l^\gamma \sim Q_m^{-\gamma}. \tag{3.24}$$

Now $\gamma \equiv D$, the space dimension, for a compact object, giving $I(Q_m) \sim Q_m^{-D}$. For a fractal, $\gamma \equiv d_f$, the fractal dimension, giving $I(Q_m) \sim Q_m^{-d_f}$. However it is not clear that the observed intensity $I(Q_m)$ is easily related to the 'mass' of a typical scatterer:

[9] There is some evidence that fractal 'clusters' are formed in the very earliest stages of spinodal decomposition, before compactifying [152]; see also Chapter 4.

as we have shown, Q_m corresponds more to the radius of the depletion zone or the typical separation of clusters than to a cluster size. $I(Q \to 0) \to M$ for an *isolated* cluster of mass M (see section 3.3.2), but of course the clusters in the DLCA system are not isolated and we have already shown how the cluster arrangement has important effects on the scattering function.

The scaling equation (3.23) implies that the system may be characterised by a 'typical structure' whose form does not change; the $1/Q_m$ scaling on the x-axis and the $Q_m^{-\gamma}$ scaling on the y-axis imply a simple enlargement of the *scale* of the structure but no change in its 'shape'. For time-independent scaling of $I(Q)$ to hold in a given range of Q requires that all structure or correlations in the system over the equivalent range of length scales *must change at the same rate.* In other words, any important length scales the system may contain (e.g. the cluster size, the cluster separation) *which determine the scattering function* must evolve in time in the same way. All these length scales will be simply proportional, each related only by a constant.

In the following subsections we test the scaling equation (3.23) as applied to the scattering function for data from DLCA simulations at various densities in 2D and 3D. In Chapter 5 and Ref. [117] a more general investigation of the scaling hypothesis is carried out by directly examining various length scales in the DLCA simulation to determine whether a single length scale can be said to characterise the aggregating system.

3.5.1 Scaling at the small-Q scattering peak

Considering only the value of the scattering function at the small-Q peak, $I(Q_m)$, equation (3.23) implies that the peak amplitude $I(Q_m, t)$ and the peak position $Q_m(t)$ are related by

$$I(Q_m, t) \sim Q_m^{-\gamma}(t). \tag{3.25}$$

This relation was directly tested for an experimental aggregating colloidal system in

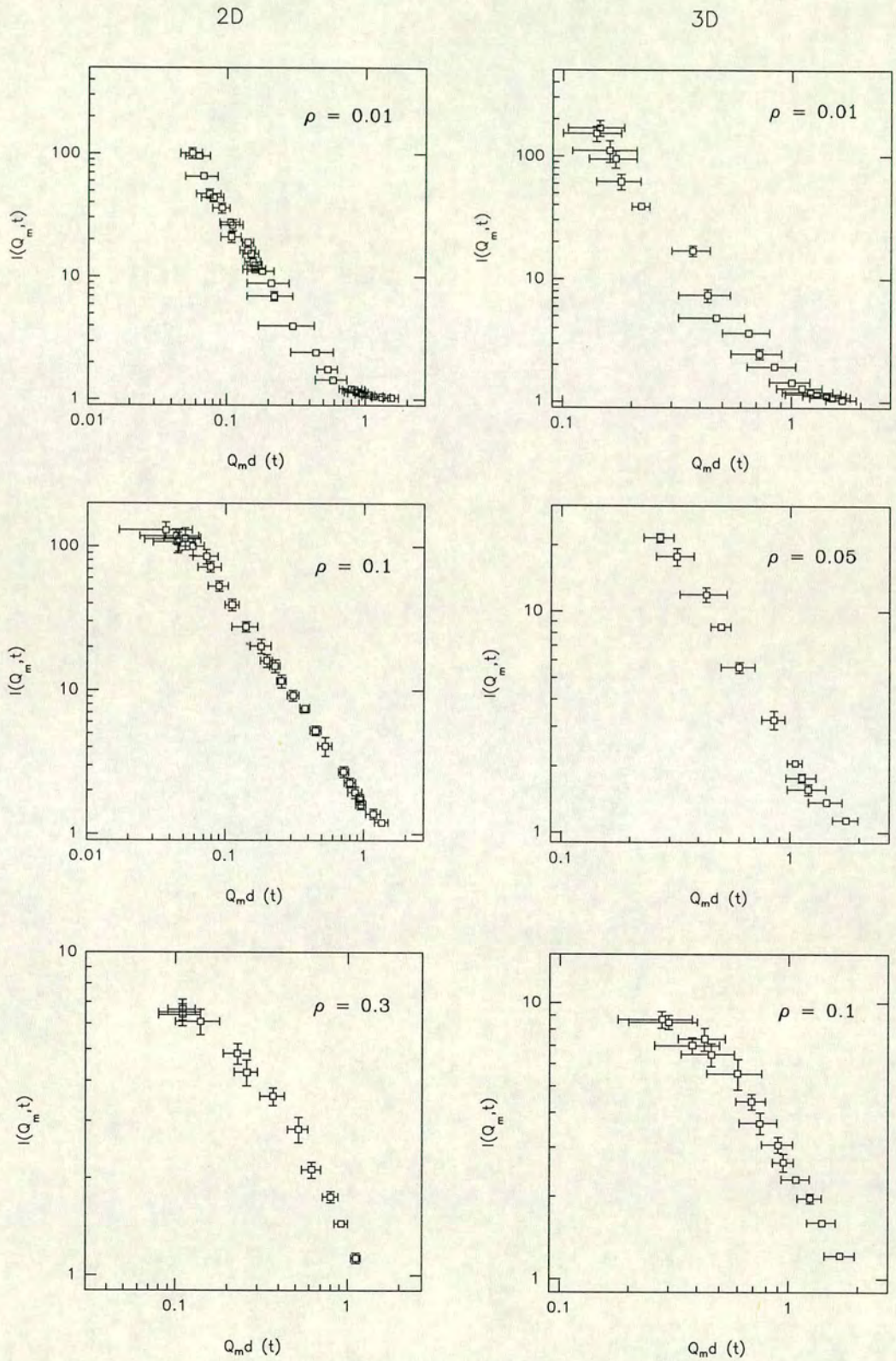

Figure 3.37. Scattering function small-Q peak intensity $I(Q_m, t)$ *vs.* peak position $Q_m(t)$, for lattice-based simulations in 2D (left column) and 3D (right column). Systems sizes are $L = 500$ ($\rho = 0.01$, 2D), $L = 300$ ($\rho = 0.1$ and 0.3, 2D) and $L = 70$ (3D).

Ref. [45], for which system an estimate $\gamma = 1.41 \equiv d_{f,DLCA}$ was obtained. In Figure 3.37 $I(Q_m, t)$ is plotted against Q_m on log-log scales. Fitted exponents γ and ranges for the fits are given in Table 3.5. As in other cases, fits are linear least-squares regression fits to the logarithms of the data, taking into account the estimated error bars for both $I(Q_m)$ and Q_m.

At the lower densities a power-law relation between $I(Q_m)$ and Q_m is certainly only reasonably indicated for later times; for the earliest times (smallest $I(Q_m)$) at the lower densities there is noticeable curvature in the $I(Q_m)$ *vs* Q_m plots. We fit power laws to estimate γ excluding this early-time region. It is seen that for the lowest densities γ is somewhat higher than the cluster fractal dimension d_f as estimated from the average form factor data (section 3.3.2) and the 'accepted' fractal dimension $d_{f,DLCA}$ as obtained from previous (low density) DLCA simulations [30, 31, 34]. This may be because the smaller clusters at the lower density are more strongly affected by the underlying structure of the lattice; it may also be that, given the earlier 'start time' at the lower density we have not reached very far into the 'scaling' region beyond the early time curvature. Indeed at intermediate density ($\rho = 0.1$ in 2D and $\rho = 0.05$ in 3D) γ agrees well with the cluster form factor fractal dimension d_f and with the 'accepted' fractal dimension.

For the high density systems ($\rho = 0.3$ in 2D and $\rho = 0.1$ in 3D) we find γ somewhat less than d_f (we compare with d_f as measured from the average form factor). Certainly γ is much less than the 'dilute' fractal dimension $d_{f,DLCA}$. $\gamma << d_{f,DLCA}$ is in contrast to estimates of d_f from the mass-radius relation (Chapter 5, and e.g. Ref. [120]), where for high density systems the fractal dimension seems to increase. However d_f is less clearly defined at high density as we have already discussed. We have seen evidence from the form factor data that due to the onset of gelation clusters may have different structure on different length scales. It is clear that any power-law region in the $I(Q_m)$ *vs.* Q_m plot becomes very limited as we increase the system density. We return to the scaling of the high-density scattering functions using *low* exponents γ below.

In the higher densities the late-time curvature in the $I(Q_m)$ *vs.* Q_m plots is associated with the gelation 'saturation' effect on $I(Q_m)$ (section 3.4.2). While Q_m continues

to decrease somewhat (the characteristic length continues to grow), the scattering intensity saturates. At late time the system does not consist of growing fractals but rather near-touching fractal clusters 'assembling' or gelling near-homogeneously, and again this change in the type of growth is expected to lead to substantial changes in the scattering behaviour.

Clearly if $Q_m \sim t^{-\alpha}$ and $I(Q_m) \sim t^{\beta}$ then relation (3.25) implies $\gamma = \beta/\alpha$. However this equality does not necessarily exactly hold unless the peak intensity and peak position follow power-laws *over the same time regimes.* This is certainly not always the case for the DLCA data. Interestingly, in their experiment on aggregating charged colloids at low volume fraction [45], while Carpineti and co-workers found an estimate $\gamma \approx d_{f,DLCA}$, their estimates of α and β were rather different to those given here and also to anything expected from theories for phase-separating systems. There are other differences between these experiments and the DLCA simulations, as is discussed further in Chapter 6.

3.5.2 Full Q_m^{γ} scaling of $I(Q,t)$

Full scaled plots $Q_m^{\gamma} I(Q/Q_m, t)$ *vs.* Q/Q_m are given in Figure 3.38 (lattice-based) and Figure 3.39 (off-lattice). These are essentially plots of the scaling function $F(Q/Q_m, t)$ in equation (3.23), so that if fractal scaling 'works' and the scaling function is independent of time, all the curves from different times should 'collapse' onto a single curve. In the plots we show the γ value which gives the 'best' data collapse *near to the expected fractal dimension* $d_{f,DLCA}$ [30, 31, 34]. Thus these plots are a test of the 'fractal scaling hypothesis' with $\gamma \approx d_{f,DLCA}$. For the simulations at intermediate densities where the data collapse is best ($\rho = 0.1$ in 2D and $\rho = 0.05$ in 3D), we find respectively $\gamma = 1.47$ (2D) and $\gamma = 1.78$ (3D). Thus reasonable scaling collapse is found with $\gamma \approx d_{f,DLCA}$. However once again the early time regime when fractal scaling does not work is clearly visible, especially for the lower densities ($\rho = 0.01$ in both 2D and 3D) where the early time regime is more accessible. Even at intermediate densities the early non-scaling regime is clearly demonstrated, before at later times the curves collapse quite well.

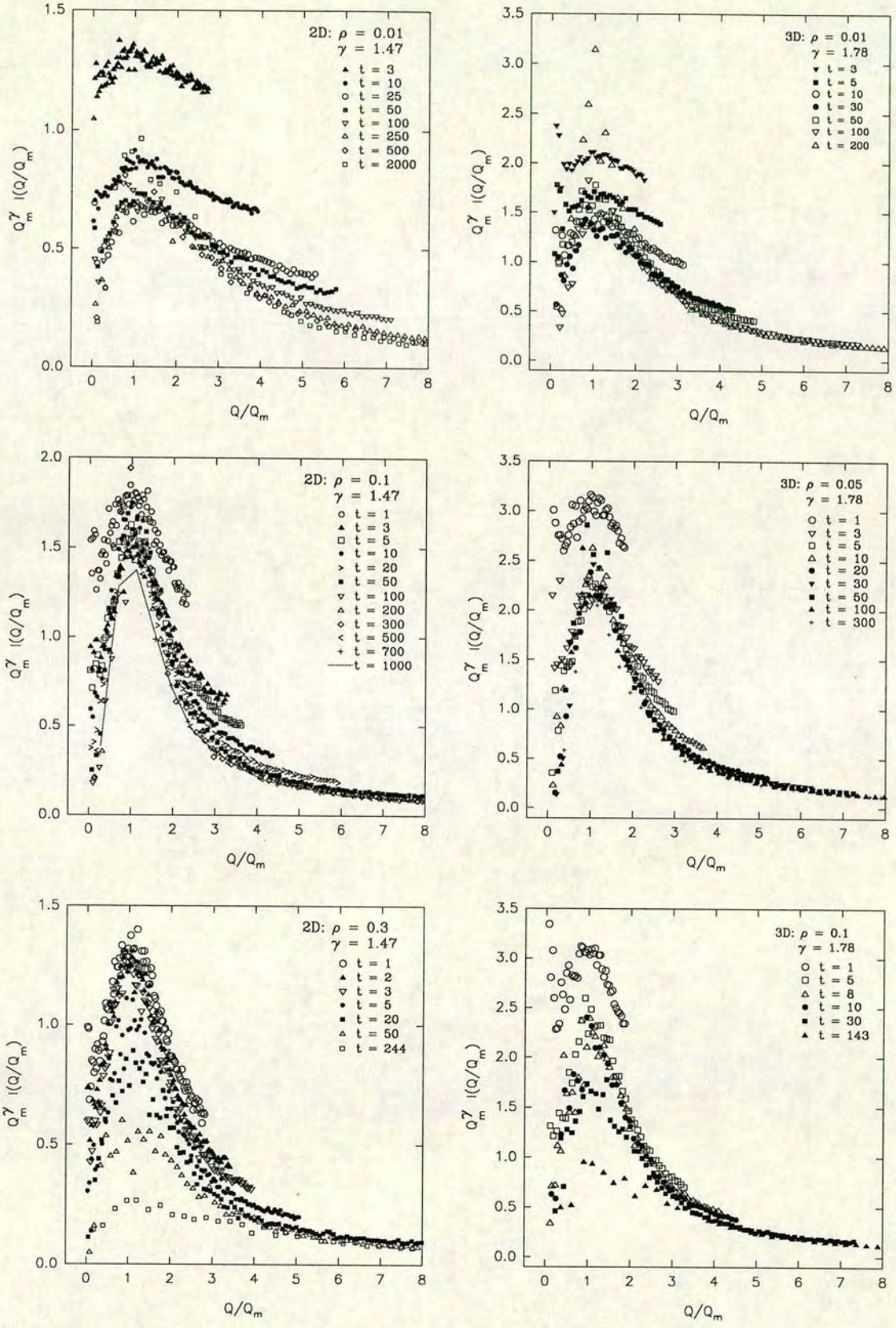

Figure 3.38. Scaled scattering functions $I(Q/Q_m)Q_m^{\gamma}$ *vs.* Q/Q_m, where $Q_m(t)$ is the small-Q peak position and γ is the scaling exponent in equation (3.23). These plots are the 'best attempt' to scale the scattering function data using $\gamma \simeq d_{f,DLCA}$, the 'expected' DLCA fractal dimension of the clusters.

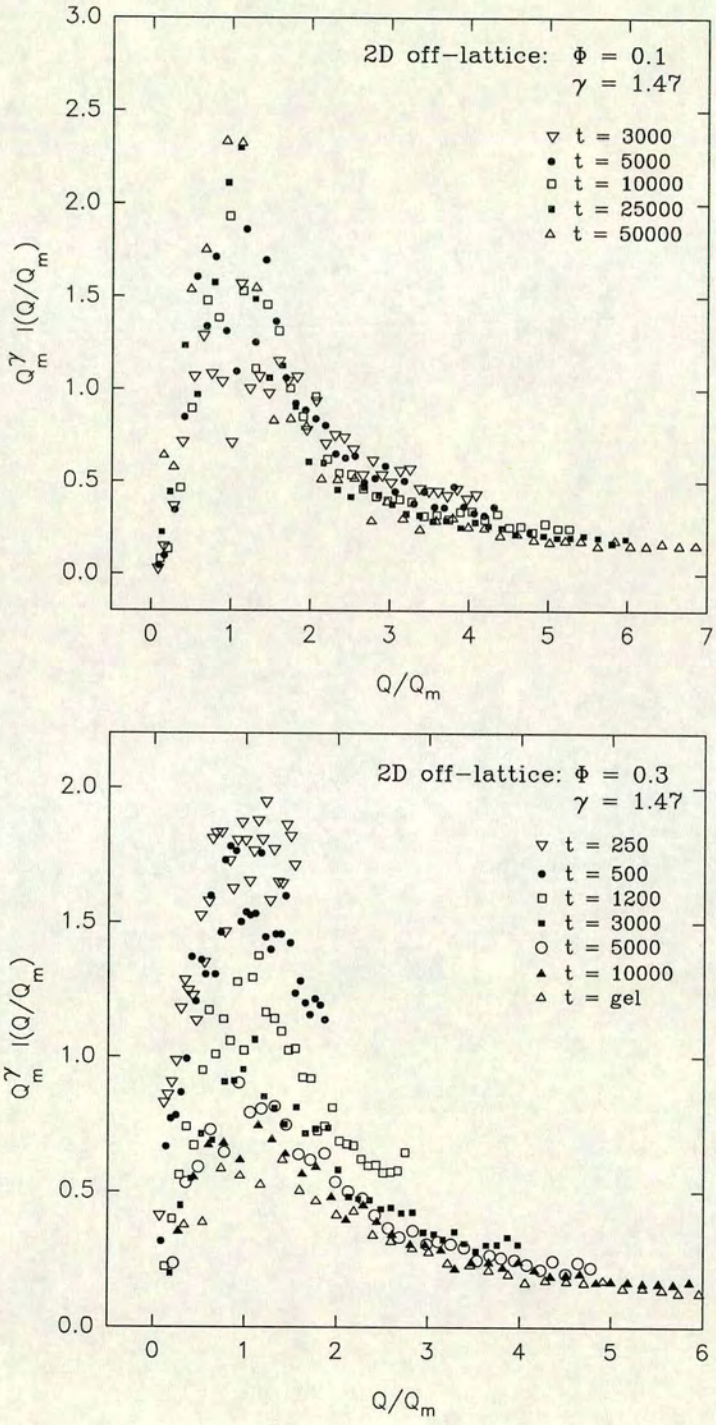

Figure 3.39. Scaled scattering functions $I(Q/Q_m)Q_m^\gamma$ *vs.* Q/Q_m for off-lattice 2D simulations, where $Q_m(t)$ is the small-Q peak position and γ is the scaling exponent in equation (3.23). These plots are the 'best attempt' to scale the scattering function data using $\gamma \simeq d_{f,DLCA}$, the 'expected' fractal dimension of the clusters for DLCA.

At the latest times for the low and intermediate densities the scaling collapse again fails (for clarity very late times are not shown on the plots; we find in late times that the scaled peak rises substantially higher than the peaks for earlier times). By such late time the effect of the small size of the simulation box becomes important (at these lower densities, as discussed, the simulation boxes are not large enough to give a 'proper' gel at late time). Therefore this late-time breakdown of scaling is quite probably a finite-size effect. Nonetheless, as mentioned in the previous section one would expect a change in the character of the growth in the system as gelation is approached, since the clusters begin to aggregate not fractally but more compactly. Unfortunately to obtain a proper view of gelation at the lower densities requires larger systems than it has been possible to simulate. It remains unclear from experiments whether scaling holds all the way to gelation. No detailed experimental investigations of an aggregating colloidal system very close to gelation have been reported; it is difficult of course to distinguish time-independent scaling from the 'freezing' of growth in the gelled system, when $I(Q)$ is approximately independent of time anyway.

For the simulations at higher density ($\rho = 0.3$ in 2D and $\rho = 0.1$ in 3D) this 'fractal' scaling of $I(Q,t)$ does not work at all with $\gamma \approx d_{f,DLCA}$. Throughout the aggregation the amplitude of the scaling function $F(Q/Q_m,t)$ falls continuously. (In the Figures the 'fractal scaling collapse' is shown with $\gamma = 1.47$ in 2D and $\gamma = 1.78$ in 3D, but see below for a more successful attempt to scale the data with $\gamma = 1.0$.) Note that the finite-size effect at the lower densities drives the scaled $I(Q/Q_m)Q_m^{-\gamma}$ *higher* as scaling begins to break down at late time, whereas in the high density case the scaled amplitude decreases substantially, indicating that the breakdown of scaling at high density is not a finite size effect.

Early-time scaling with $\gamma = 1.0$

Figure 3.40 shows the effect on the scaling function when an exponent $\gamma = 1.0$ is used in equation (3.23), for data from the early-time regimes. In two dimensions collapse of the early-time data to a time-independent $F(Q/Q_m)$ is much better compared to the scaling with $\gamma \approx d_{f,DLCA}$, especially for the high density simulation. The reason for this is not clear. In high density one would certainly expect the fractal dimension to be

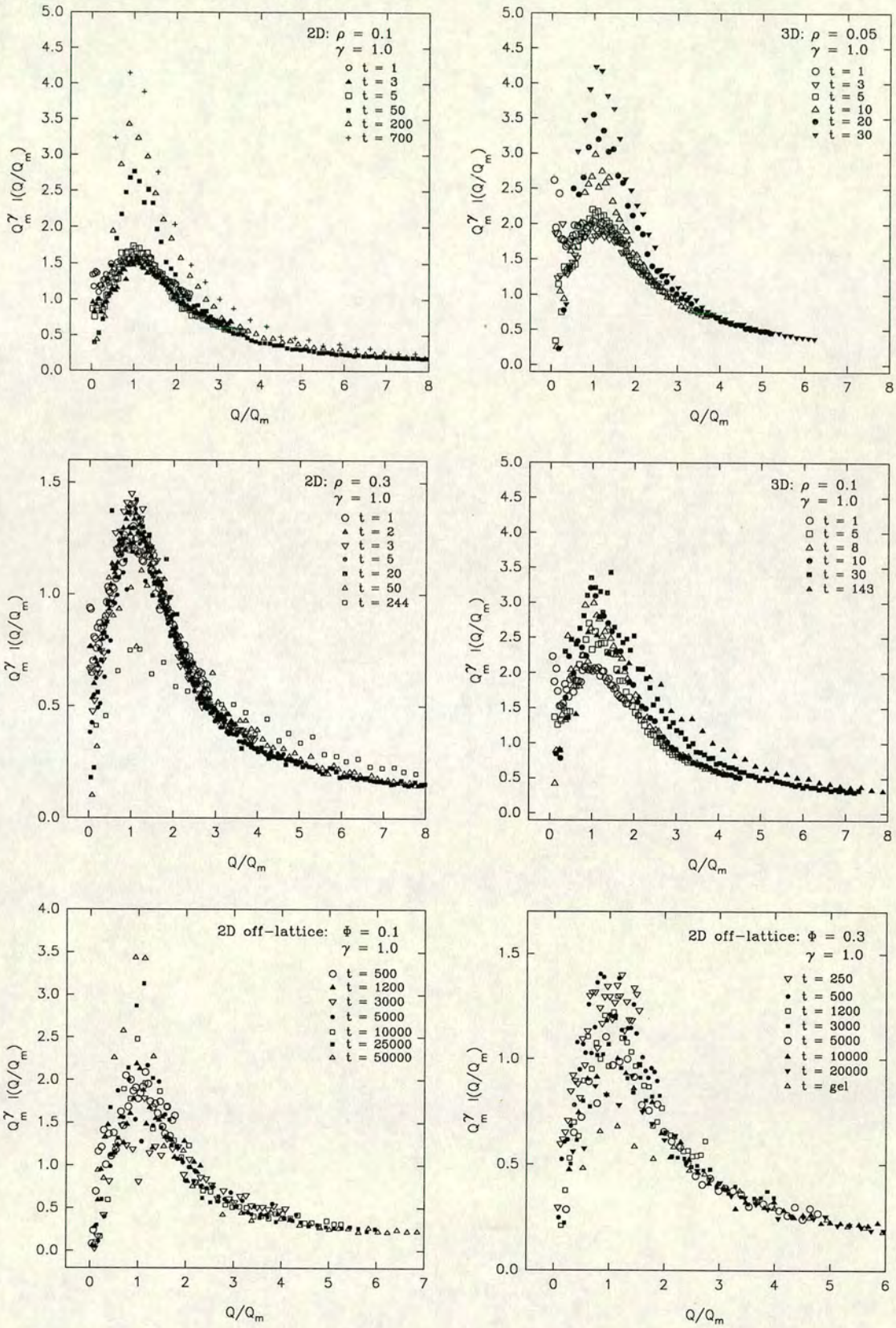

Figure 3.40. Scaled scattering functions $I(Q/Q_m)Q_m^\gamma$ *vs.* Q/Q_m, where $Q_m(t)$ is the small-Q peak position and the scaling exponent (equation (3.23)) is $\gamma = 1.0$. The upper four plots are from lattice-based simulations (2D in the left column, 3D in the right), the lower two plots are from 2D off-lattice simulations.

less well defined, because the fractal clusters cannot grow very large before gelation. It may be that the very earliest clusters tend to be near-linear. (The scattering function for a rod [153], at large Q, has the form

$$I_{rod}(Q) \sim Q^{-1}. \tag{3.26}$$

Thus to collapse the data at least at large Q would require $\gamma = 1.0$ in equation (3.23).) At high density the initial small parts of the 'pre-fractal' clusters will not be large enough to feature much branching, but are more likely to be very short chains. Imagine taking a *small* cut from a large 2D fractal cluster with $d_f = 1.4$. At such a low fractal dimension the cluster is not very dense at short length scales, thus at length scales close to the 'monomer' size it tends to be made of short chains with no branches. The effective fractal dimension of such a small cut-out would be quite small, close to that of a linear chain, i.e. $d_f \approx 1$. Because gelation interferes with the growth of the fractals very quickly at high density, this 'pre-fractal' structure is all that can be formed before space is filled. We discuss these ideas further in Chapter 4.

Simple time-independent form of the scattering functions

The investigations above tend to point to the conclusion that the *fractal* scaling hypothesis with scaling exponent $\gamma = d_{f,DLCA}$, while approximately satisfied in low density systems, is not satisfied in high density systems. However, this may be mostly due to the difficulty of defining a fractal dimension at high density. The question remains whether the scattering functions at high density do still have a time-independent form—that is, whether the scattering functions do scale under some other scaling hypothesis. In Figures 3.41, 3.42 and 3.43, we show an attempt to *directly* scale the scattering function data simply by scaling Q and $I(Q)$ by their characteristic values, Q_m and $I(Q_m)$:

$$I(Q/Q_m) \sim I(Q_m)F'(Q/Q_m). \tag{3.27}$$

This scaling *forces the data at the peaks* to collapse to a single point. If the data over the remaining range of Q still collapse to a single curve, we can say that the scattering function does have a time-independent form $F'(Q/Q_m)$, whose characteristic scales are

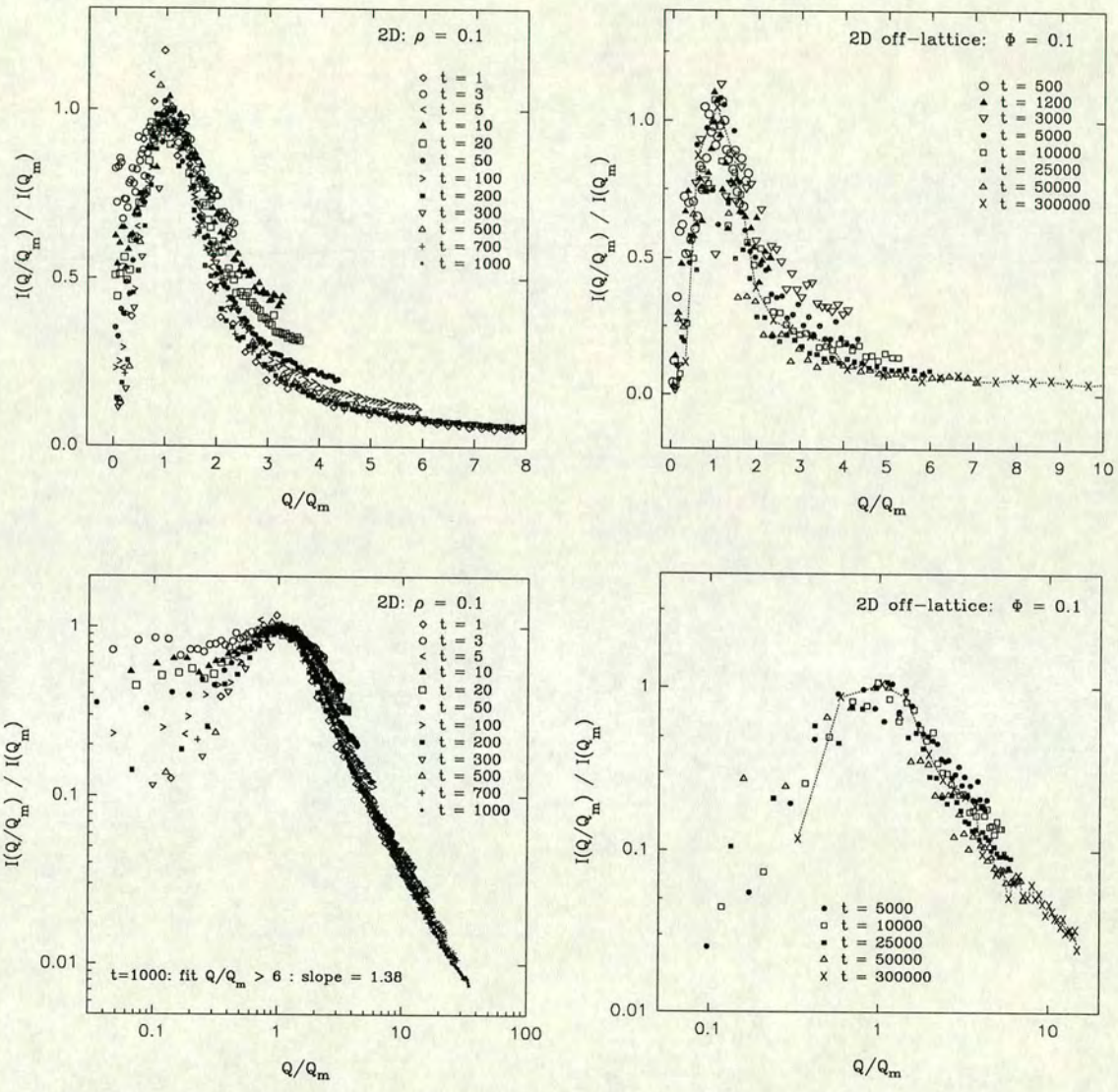

Figure 3.41. Scaled scattering functions $I(Q/Q_m)/I(Q_m)$ *vs.* Q/Q_m, where $Q_m(t)$ is the small-Q peak position, for simulations in 2D at number density/area fraction ρ / $\Phi = 0.1$. The left-hand column is for lattice-based simulations, the right-hand column for off-lattice simulations.

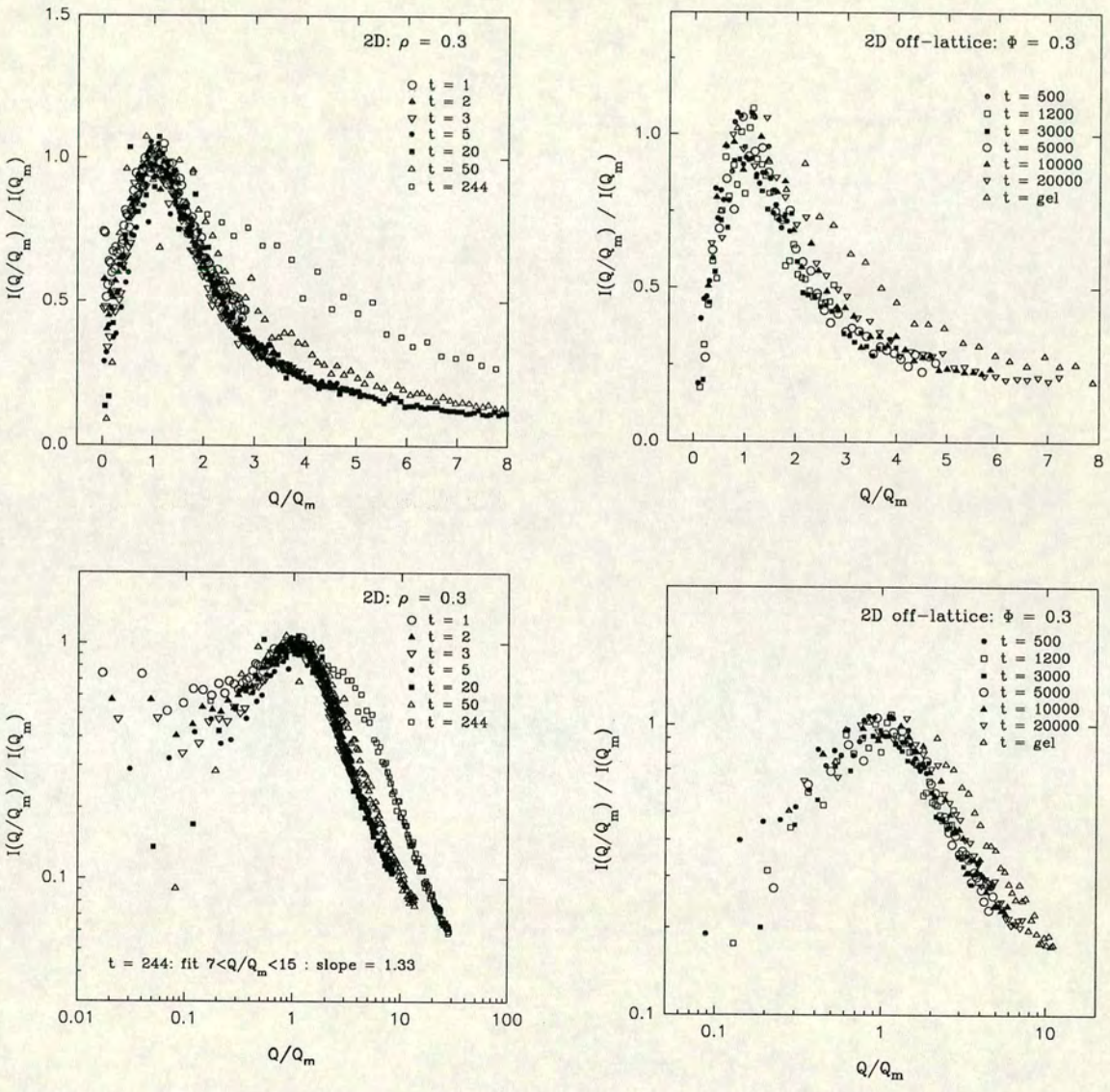

Figure 3.42. Scaled scattering functions $I(Q/Q_m)/I(Q_m)$ *vs.* Q/Q_m, where $Q_m(t)$ is the small-Q peak position, for simulations in 2D at number density/area fraction ρ / $\Phi = 0.3$. The left-hand column is for lattice-based simulations, the right-hand column for off-lattice simulations.

given by the peak position and peak amplitude.

The scaling collapse around the peak and for $Q > Q_m$ is rather good, especially for the high density systems (we include lower density systems for comparison). Only at $Q << Q_m$ and at late time (near gelation) does the time-independent scaling form not apply. In other words in the high density systems, while the fractal scaling hypothesis does not seem to work (at least not with $\gamma \approx d_{f,DLCA}$) the scattering functions do have a time-independent shape for times well before gelation. Given the form $F'(Q/Q_m)$, only the characteristic time-dependent values Q_m and $I(Q_m)$ are required to give $I(Q)$ at any time.

The *fractal* scaling hypothesis can be seen to be a specific case of this general scaling: in the systems which show fractal scaling with exponent γ, we have $I(Q_m) \sim Q_m^{-\gamma}$, and equations (3.27) and (3.23) become equivalent.

Comparison of DLCA scaling and experimental results

The scaling hypothesis equation (3.23) has been applied to data from a variety of experimental and simulation systems. Notable colloid experiments include the two-dimensional aggregation experiment of Robinson and Earnshaw [52] and, in three-dimensions, the charged colloid experiments of Carpineti and co-workers [45, 47] and the colloid-polymer mixture experiments of Pirie and co-workers [11, 16]. In the case of the 2D experiment in Refs. [7, 52], an area fraction of colloidal particles close to $\Phi = 0.1$ was studied, matching quite well with the 2D lattice-based simulation runs here at number density $\rho = 0.1$ and the single small-scale off-lattice simulation at $\Phi = 0.1$. The scaling collapse of scattering functions from the DLCA simulations is certainly at least as good as the scaling of the data in Ref. [52]. The system size used to calculate the scattering functions in the experiment was comparable to the DLCA system size here ($L \approx 700$ compared to $L = 500$ in the DLCA simulation). The 'best' scaling exponent found in the experiment was $\gamma = 1.43 \pm 7\%$, agreeing well with $\gamma = 1.47$ from the DLCA simulation. Furthermore scaling of $I(Q)$ was only observed after an early-time non-scaling region[10]. Unfortunately no similar 2D experiments have been

[10]Note however that the experiment may involve an RLCA-DLCA 'crossover' at early time, an

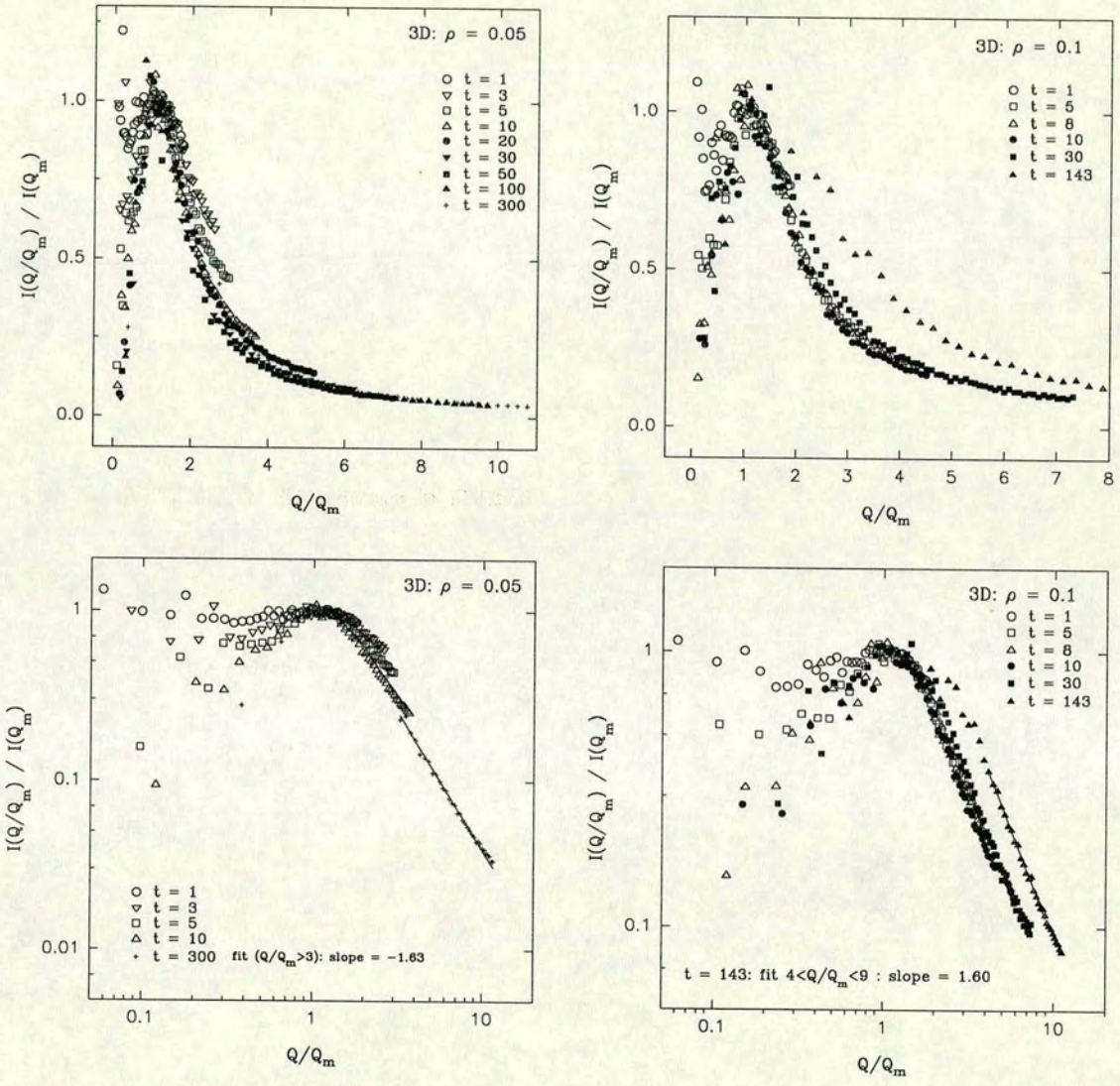

Figure 3.43. Scaled scattering functions $I(Q/Q_m)/I(Q_m)$ *vs.* Q/Q_m, where $Q_m(t)$ is the small-Q peak position, for lattice-based simulations in 3D at number densities $\rho = 0.05$ (left column) and $\rho = 0.1$ (left column).

reported for higher area fractions, which would serve as a useful comparison with the breakdown of 'DLCA fractal' scaling we find in the high-density DLCA simulations.

In the 3D experiments similar $I(Q)$ scaling is observed, with $\gamma \approx d_f$, the measured fractal dimension. The experiments of Carpineti and co-workers [45] involved aggregation of charged colloids at low volume fraction (typically $\Phi \approx 0.003$). Aggregating colloid-polymer mixtures have been studied at higher volume fractions, $\Phi \approx 0.2$. Light-scattering data for this system scale quite well [16] even at such a high density, with an exponent $\gamma = 1.7 \pm 0.2$, comparable with the 'accepted' fractal dimension for the 3D DLCA model and with the fractal dimensions as measured by various methods in our simulations. The scaling collapse of the DLCA simulation data in 3D at higher densities is not so convincing, implying that the simulation may not perfectly model this experiment; however the system sizes for the 3D simulations are not large, and this may have a substantial effect on the appearance of scaling. In fact given the noise in the calculated scattering functions for the simulation, one cannot rule out scaling.

Comparison of DLCA scaling and results from other systems

Scaling of scattering functions of DLCA simulations has also recently been studied for a few densities in 2D by Sintes and co-workers [81] and in 3D by Gonzalez and Ramirez-Santiago [65]. Similar conclusions, that at intermediate density fractal scaling holds after an early-time non-scaling region, were drawn by these authors. Note that the simulations of Ref. [81] used a size-independent cluster diffusion coefficient, whose effect on the kinetics of the scattering function has already been demonstrated in section 3.4.1 to be rather important. It is not clear how the scaling of cluster diffusion affects the fractal scaling hypothesis, though it appears from a comparison of the results reported here and those in Ref. [81] that scaling holds regardless. As mentioned, in studies of charged-colloid aggregation [45] while scaling was found with a value for the scaling exponent $\gamma \simeq d_{f,DLCA}$, estimates of the peak position exponent (α, equation (3.21)) and the peak intensity exponent (β, equation (3.22)) do not agree with those found here (Table 3.5). In other words the fractal dimension of the clusters and the fractal

explanation for the lack of scaling in the experiment which cannot apply to the simulation.

scaling of the scattering function do not appear to be sensitive to the individual values of α and β. This is a rather interesting result which may warrant further investigation.

In a recent paper [64] the scaling of scattering functions is studied by molecular dynamics simulation of a low-temperature quenched 2D fluid of particles interacting through a potential of the Lennard-Jones (LJ) form. For shallow quenches, the LJ system characteristically phase-separates by forming compact droplets of a high-density phase, which grow by a Lifshitz-Slyozov-Wagner mechanism. For the deep quench in Ref. [64], 'fractal-like' structures are formed instead, and 'pinning' of the growth by a system-spanning gel is observed. Good scaling collapse of the scattering functions is demonstrated for this system, using $\gamma = 1.85$, at a number density of $\rho = 0.325$. Once again an early non-scaling regime is observed. However the structure of the system and of the (irreversible) DLCA system studied here is visibly different (compare Figure 3.3 and Figure 1 of Ref. [64]). In fact the 2D LJ system, which allows thermal restructuring, is visually more comparable to the *reversible* DLCA model which we study in Chapter 4, and the comparison of the two systems will be returned to in that Chapter.

3.5.3 Scaling of $I(Q)$ for DLCA—Conclusions

If the *form* of the scattering function can be shown to be constant through the aggregation, one may conclude that structural changes are limited to an expansion of length scales and an expansion of scattering by some 'characteristic' structure. In such a time-independent scaling region, given the time-independent scaling form of the scattering function, one would need only two measures to characterise the scattering function of the system at any time; Q_m and $I(Q_m)$. Figures 3.41 to 3.43 demonstrate that, at least around the peak Q_m and for $Q >> Q_m$, the scattering function for the aggregating system does indeed have an approximately time-independent form. Data from high-density simulations show that this scaling breaks down however near gelation.

In experiments this simple time-independent scaling approach has been taken further, and a *fractal* scaling hypothesis has been proposed and tested. In this case, it is

proposed that the scattering function peak amplitude $I(Q_m)$ is given by

$$I(Q_m) \equiv Q_m^{-\gamma}. \tag{3.28}$$

with the scaling exponent $\gamma = d_{f,DLCA}$, the DLCA fractal dimension. Inserting this relation into the scaling equation (3.27) one obtains the fractal scaling form of equation (3.23). The power-law relation (3.28) describes the expected scattering by a (single) fractal *in the fractal range of wave-vectors* Q. Fractal scaling of the scattering function using relation (3.28) over the *entire* range of Q would seem to imply that the system has a self-similar structure described by dimension $d_{f,DLCA}$ over *all* length scales. This is an idea which has not been fully explained; as discussed by Earnshaw and Robinson [154] it implies an inter-cluster interaction over scales much greater than the typical cluster size.

Data from the DLCA simulations reported in this section demonstrates that at low and intermediate density the fractal scaling form for the scattering function does apply reasonably well, after an early-time non-scaling region. However at higher system density, it becomes more difficult to define an exponent γ (e.g. from the peak scaling, $I(Q_m)$ *vs.* Q_m) in the same way as it becomes more difficult to define a cluster fractal dimension. While the scattering function at high density *does have a time-independent scaling form* (see the previous paragraphs) it is not given by the fractal form of relation (3.28) with $\gamma \approx d_{f,DLCA}$. This is perhaps not surprising, because at high density gelation interferes with the growth of fractal clusters before the fractals can grow to anything like a reasonable size. That we find much better scaling with $\gamma \approx 1.0$ is consistent with the idea that the high-density system cannot 'escape' from an early-time, unbranched cluster structure to reach the 'classical' DLCA system of well-defined, large fractal clusters.

Chapter 4

Structure of the reversible DLCA system

Abstract

An extension of the basic DLCA simulation model is investigated, where bonding between particles is no longer permanent but a finite bond energy E is defined, such that thermal fluctuations may cause clusters to break apart and restructure. 'Weak' bond energies are considered, where E is of the same order as the average thermal energy k_BT. The effect of different bond energy on the structure of the simulated aggregating system is studied, using methods analogous to scattering experiments as in Chapter 3. Bond energy E is shown both to affect the rate of growth of clusters and to allow restructuring of aggregates on different length scales, leading to a wide range of possible morphologies in the aggregating system.

4.1 DLCA with finite bond energy

4.1.1 Thermal energy and interparticle potentials

In Chapter 3 the structure of the *irreversible* DLCA aggregating system is investigated, where the attractive potential between particles is so strong that, once 'bonded', particles cannot escape each other again. This is likely to be a good model under certain conditions, for example for aggregation due to strong van der Waals' forces. However many systems involve weaker attractive potentials, such that 'thermal' (i.e. random, Brownian) fluctuations in the kinetic energy of particles are sufficient to enable particles to escape their neighbours' attractive potentials.

Though it may be 'bonded' in an aggregate, a colloidal particle remains subject to the Brownian 'bombardment' of solvent molecules. Thus the kinetic energy of the particle fluctuates as it collides continuously with solvent molecules coming from all directions. The average *thermal kinetic energy* of such a particle K_{av} is proportional to the temperature T:

$$K_{av} \sim k_B T, \tag{4.1}$$

where k_B is Boltzmann's constant.

The probability that a particle at any moment has thermal kinetic energy *greater than* some energy e is given by an integral over the Boltzmann distribution:

$$P(e) \sim exp(-e/k_B T). \tag{4.2}$$

Consider a particle in an aggregate such that it lies in an attractive potential (from neighbour particles) V ($V < 0$ for attractive potentials). If the fluctuating kinetic energy of a particle momentarily becomes greater that $|V|$, the particle can *escape* the attractive potential of its neighbours. From equation (4.2) the probability that the particle has kinetic energy $|e| > |V|$, the probability that the particle escapes the

aggregate due to thermal fluctuations, is therefore

$$P_b \sim exp(V/k_BT). \tag{4.3}$$

This is the basis of the *reversible* DLCA simulation model.

4.1.2 Weak potentials

Particular attention is paid in this Chapter to *weak* interparticle potentials, that is to systems with bond strengths E of at most a few times the thermal energy k_BT. The rich kinetic and phase behaviour (and presumably therefore the corresponding rich range of structure) found in experiments on colloid-polymer mixtures [11, 12, 16] (see Chapter 1) provides particular experimental motivation for the study of weak potentials. In the colloid-polymer experiments the effective interparticle potential can be varied easily by changing the polymer concentration. Typically bond strengths of $|E| \simeq 1 - 5k_BT$ have been studied [16]. The equilibrium phase diagram [11, 12] of such a system includes a single-phase stable fluid and two- and three-phase coexistence of fluids and solids[1]. At the highest bond strengths and narrow potentials a *transient gel phase* is found. In the gel phase growth of separate phases appears to be frustrated by the formation of large system-spanning structures. These interpretations of the experimental data are however not fully confirmed since direct observation in the colloidal systems is difficult. In Chapter 3 aggregation has been studied for the case of very strong (irreversible) interparticle bonding, and the space-filling *gelation* effect has been shown to be a natural consequence of such irreversible growth of fractal structures. However it seems that a model incorporating weaker interparticle potentials ought to be able to demonstrate the different phase behaviour as seen in the experiments. For instance gelation should only occur at high interparticle bond strength; at lower bond strength, structural measurements in the colloid-polymer system have indicated that the 'fractal aggregating system' becomes instead more comparable to a typical *phase*

[1] An important variable besides the interparticle potential in the colloid-polymer system is the *range* of the potential. The DLCA model is essentially restricted to very short range 'touching' attractions; effects of differently-ranged potentials will not be considered here.

separating system [16].

4.1.3 Implementing reversible bonding

In general the reversible DLCA algorithm is very similar to the standard irreversible algorithm as described in Chapter 2. First implementations of the 'bond-breaking' reversible DLCA model were reported by Shih and co-workers [107] (see below). As in those studies we have implemented the reversible-bonding DLCA model only as a *lattice-based* algorithm.

Bond energy E

In the simulations a *bond energy* parameter E is defined, which is the 'depth' of the attractive potential of a single particle. E may be most conveniently specified in units of the average thermal energy k_BT.

On the lattice a particle has a number of near neighbours n_b ($0 \leq n_b \leq 4$ in 2D simulations, $0 \leq n_b \leq 6$ in 3D). As in the 'standard' lattice-based DLCA model we assume that only nearest neighbour particles are bonded (equivalently the potential is very short-ranged). The total potential in which a particle lies depends on the number of nearest neighbours it has:

$$V = n_b E \tag{4.4}$$

A particle bonded to two nearest neighbours is therefore in a potential well with depth $V = 2E$, and so on. So from (4.3) the probability P_b that the particle will escape, that is break *all* its bonds, in terms of the single bond strength E, is then

$$P_b \sim exp(n_b E/k_B T). \tag{4.5}$$

($E < 0$ for attractive interparticle potentials.)

The standard DLCA model where interparticle bonds are permanent corresponds to a bond breaking probability $P_b \to 0$, or an interparticle potential $E \to -\infty$. Thus the standard DLCA model can be considered the very strong bond limit of the reversible

model[2].

Bond-breaking

Thermal 'breaking' of interparticle bonds is implemented as follows. After the cluster diffusion step (see Chapter 2), each particle makes an 'attempt' to escape from its bonds. For each particle in turn, the number of nearest neighbour bonds, n_b, is counted. Now the particle is in a potential $V = n_b E$ ($E < 0$), so that the probability that the particle escapes (breaks *all* its bonds with its neighbours) is

$$P_b = exp(n_b E / k_B T). \tag{4.6}$$

A random number r is generated from a uniform distribution in the range zero to one. If the random number r satisfies

$$r < exp(n_b E) \tag{4.7}$$

the particle escapes. (The parameter E is expressed in *units* of $k_B T$, so that no actual temperature need be specified.) The escaping particle is immediately moved to a nearest-neighbour site randomly selected from all its *free* nearest-neighbour sites. (If all the particle's nearest-neighbour sites are occupied, that is the particle is 'fully bonded' with $n_b = 4$ in 2D or $n_b = 6$ in 3D, it *cannot* escape.)

Following each escape event, the fragments of clusters left behind are reidentified. Various fragmentation and restructuring processes are possible after the escape of a single particle (Figure 4.1). After all particles have attempted to escape, the radii of gyration and masses of all new clusters are recalculated. Then the simulation time is incremented and the next diffusion step commences.

Previous simulations of the DLCA model with bond breaking (see below) have implemented a second parameter in addition to the bond energy E, the 'break frequency' f [107]. In this variant, particles attempt to escape only every $s = 1/f$ simulation

[2] Assuming rigid bonding and non-deformable particles. In some systems very strong interparticle potentials may actually deform the particles [50].

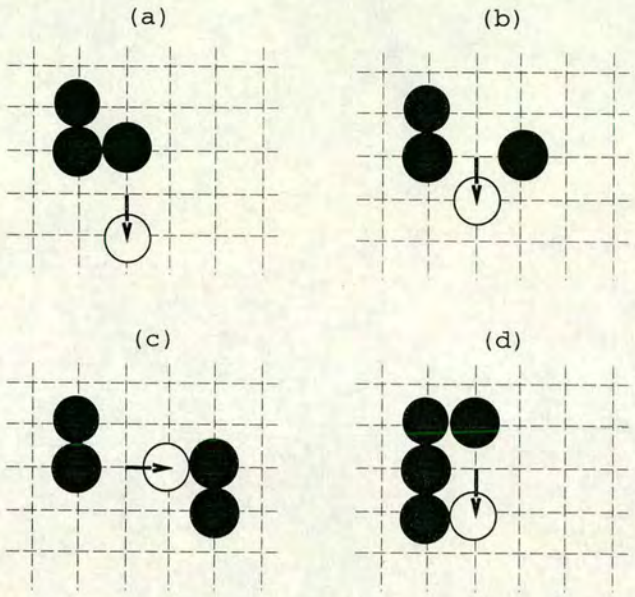

Figure 4.1. Various 'fragmentation' events which can occur when a particle 'escapes' its bonds to its near-neighbours. In (a) a particle breaks away to become a monomer, leaving a single smaller cluster behind. In (b) a particle breaks two bonds to fragment a cluster into a total of three new parts. In (c) the escaping particle collides immediately with another cluster. In (d) the 'escaping' particle only moves along the surface of its cluster, changing the cluster structure but not fragmenting the cluster.

steps (*all* particles still attempt to escape at the same step). However the physical justification of $s \neq 1$ is not clear. In equation (4.5) f presumably appears as a constant of proportionality. Changing f changes the effective time-scale of bond-breaking or restructuring *without changing the time-scale of diffusion/aggregation.* Physical situations in which this could occur do not readily spring to mind. In any case for simplicity we have dispensed with the parameter f and implement the bond-breaking routine after every cluster diffusion step, i.e. we assume $s = f = 1$.

Additionally, in some of the previous simulations of Shih and co-workers [107] (see below), the system was allowed to aggregate for an initial time before the bond-breaking was 'switched on'. Physically this would correspond to a change in interparticle potential with time. But as we will show, the bond energy E not only affects the *restructuring* of clusters after their growth, but also has substantial effects on the growth itself, from the earliest times. Thus in these simulations bond-breaking is always implemented from the start of the simulation.

With the introduction of reversibility, there is no longer any well-defined *finish time* of the simulation. Even if a single cluster containing all particles in the system does appear, it can always begin to break apart again. In practice one might expect a dynamic equilibrium to be reached if one could run the simulation for long enough, in which the cluster structure and cluster size distribution are constant within small statistical fluctuations. Even in this state bonds continue to be broken and remade, however, so that the simulation could in principle continue forever in dynamic equilibrium. In practice, with the computational power available, this situation is not reached anyway. Given the limitations on computational power and cpu time, in this thesis we have concentrated not on trying to reach the equilibrium state of the weak aggregation system, but rather on studying the structures which are formed in and the kinetics which are obeyed by the systems when they are far from, and as they begin to move toward, equilibrium.

4.1.4 Limitations of the restructuring algorithm

Some points should be made about the method of implementing 'bond-breaking' which has been adopted here. First, a particle always breaks *all* its bonds or none; a three-bonded particle cannot just break one of its bonds. This restriction is forced upon us by the use of the simple square or cubic lattice with nearest-neighbour bonding. When a particle escapes it must be moved away from the neighbours it was previously bonded to; if it remained nearest-neighbours with its previous partners it would by definition remain bonded to them. In an *off-lattice* model more complex restructuring could be implemented (with, for instance, a small finite range of the potential so that a particle may shift out of bonding with one neighbour while remaining bonded to another [108]), but only at great cost in necessary computation.

Another alternative restructuring method would be to break *clusters* apart rather than just unbonding single particles. Once again such a procedure would be more computationally demanding. To some extent it can occur anyway with the single-particle escape method. This is illustrated in Figure 4.1; the escaping single particle can break the 'bridge' between two pieces of cluster, thus fragmenting a cluster.

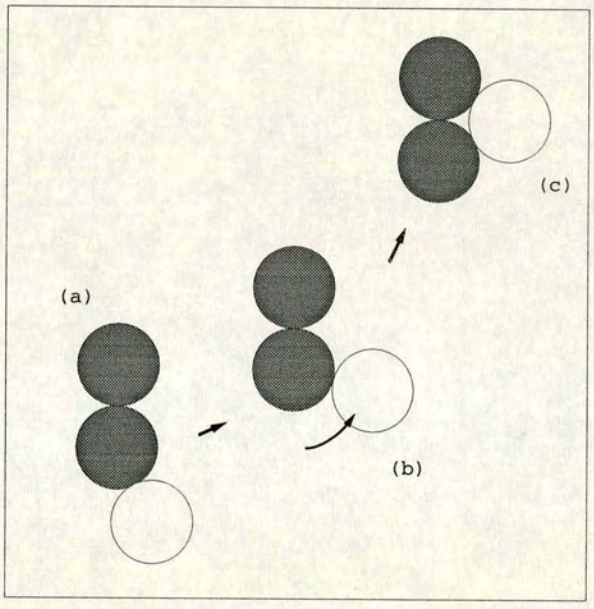

Figure 4.2. Compactification by 'rolling' rather than bond-breaking. The near-linear trimer in (a) can restructure and compactify if its particles 'roll' around each others' surfaces until, in (c), all the particles are in contact with two neighbours, a more stable arrangement. In 'rolling' the particle does not require kinetic energy to *escape* the attractive potential.

Lastly, an important limitation of this restructuring method is that clusters remain *rigid*. In some experimental systems it is quite conceivable that compactification of clusters might occur not by cluster fracture events but rather by a process involving the rotation and 'rolling' of particles about neighbours (see e.g. [111]). For two particles in a relatively weak potential there would presumably be very little energy cost in one (singly-bonded) particle 'rolling' around the surface of its neighbour. Thus linear structures could compactify as shown in Figure 4.2; for instance a linear trimer might restructure to a more stable compact equilateral trimer. Larger rotations of pieces of cluster about mutual bonds might also occur (though the hydrodynamic drag involved would mean these processes would be very much slower and less important). All these processes are once again difficult to simulate using the lattice-based model, and no attempt has been made to implement them here. They should be kept in mind as being possible reasons for differences between the simulation results and particular experimental systems. However before any great effort in simulation is undertaken, direct investigation of the importance of these more complex restructuring 'modes' in given experimental systems, for instance by direct microscopic imaging or by careful analysis of (dynamic) scattering measurements, would be of substantial use. As an example, the 'restricted' Brownian motion of particles within the attractive potential of nearby neighbours has been measured for colloid-polymer aggregates using dynamic light scattering [16]. On the other hand, in this particular system structural measurements still imply that 'bond breaking' is a more important process than 'rotational restructuring' [16].

4.1.5 Simulations of reversible aggregation

First implementations of the 'bond-breaking' reversible DLCA model were reported by Shih and co-workers [107, 155], who studied the effect of the interparticle 'bond energy' on the fractal dimension of clusters via the fractal mass-radius relation. We will compare some of our results in detail in following sections. Here we briefly mention some other methods of simulating reversibility in aggregation which have been implemented.

Sorensen and co-workers [109] use an Ising-like model in which some particles are

labelled as 'solid' and do not diffuse, while 'fluid' particles may diffuse and 'transform' into solid particles according to some probabilities. The effect of temperature and system density on cluster structure is studied; the model reduces to the particle-cluster DLA model as density $\rightarrow 0$. Meakin and Jullien [111] consider the effect of restructuring immediately after collision by allowing two colliding clusters to rotate about their mutual bond until another bond is formed, leading to stabilisation. In this model clusters tend to be more compact at short length scales, but measurements of the cluster fractal dimension show little sensitivity to the restructuring. Kolb [112] and Meakin [113] have both studied the structural effects of breaking random bonds within aggregates, finding a short length scale compactification though again little effect on the fractal dimension on longer length scales. In general all these analyses of the effect of reversible bonding have concentrated simply on the structure of individual clusters, chiefly studied via estimation of the fractal dimension.

In Brownian dynamics (BD) simulations Dickinson and co-workers [108, 110] have studied the effect of finite depth, finite range potentials on the structure of aggregates. Particles may still diffuse within the attractive potentials of their neighbours so that 'bonds' are effectively more flexible. Interestingly, there seems a contradiction between the results of *bond-breaking* style simulations (e.g. Shih and co-workers [107] and the simulations described here) and 'flexible bond' style BD simulations. In the BD simulations deeper potentials lead to more compact structures, as if the stronger bonds tend to 'suck' the aggregate in. In contrast, as we shall see, stronger bonds in DLCA generate more ramified structures, as might be expected as the bond energy E tends to the irreversible DLCA limit, $E \rightarrow -\infty$. These contradictions will be discussed further below.

There are similarities between the reversible DLCA model and the lattice-gas conserved order-parameter Ising model (see e.g. [156]). The interparticle potential in the reversible DLCA model implies that the two models have effectively the same Hamiltonian (a nearest-neighbour only interaction). Therefore there is reason to believe the *equilibrium* phase diagram of the two systems should be the same. The kinetics of the lattice-gas Ising model, and in particular the percolation behaviour of the system, have

been studied in some detail by Hayward, Heermann and Binder [157]. Hayward and co-workers find a 'correlated percolation' line such that, in the percolation region, large clusters appear which span the system. Lironis, Heermann and Binder [158] consider a 'transient percolation' phenomenon where, in the correlated percolation region, the system-spanning cluster exists for a finite time before thermal restructuring leads to its disappearance. An important difference between the spin-exchange Ising model simulations of Refs. [157, 158] and the reversible DLCA model appears in the dynamics: in DLCA clusters diffuse, whereas in the Ising simulations clusters 'move' only by the exchange of spins (which tend to move the centres of mass of connected clusters). The diffusion of clusters in DLCA may even imply an extra interaction beyond the nearest-neighbour sticking potential, in that particles distant from each other in the same large cluster diffuse together, and thus effectively interact. While we draw attention to the clear similarities between phase separation models such as the Ising model and DLCA in this Chapter, still a detailed comparison of the two models is rather beyond the scope of this work.

4.2 Visual study of system structure

Table 4.1 gives details of those simulations which have been carried out and whose results are analysed in this Chapter. Simulations in 2D and 3D have been run at various number densities and various values of the interparticle potential parameter E. Real cpu runtime tends to increase substantially as number density is increased, as for the irreversible DLCA simulations. But runtime also increases as $|E|$ is *decreased*, because at the lower bond energies the system contains more separate clusters. At *very* low bond energies where there is little significant aggregation, runtime decreases again because less time is spent trying to break bonds.

We begin the analysis of the structure of the reversible DLCA system by studying some pictorial snapshots of the 2D simulations at various times during aggregation. This provides an initial picture of the structural effects of the interparticle potential or

Density	E (k_BT)	System size L	No. particles	total run time
(a) 2D				
0.01	-1.0	500	2500	2000
	-1.5	500	2500	18000
	-2.3	500	2500	1000
0.1	-1.5	300	9000	2000
	-2.3	500	25000	2000
0.3	-1.5	300	27000	2200
	-2.3	500	75000	1000
	-2.5	300	27000	2300
	-3.0	300	27000	13000
	-4.0	300	27000	1000
(b) 3D				
0.01	-1.5	70	3430	100
0.05	-1.5	70	17150	100
	-3.0	70	17150	500
	-4.0	70	17150	500
0.1	-2.0	70	34300	150
	-4.0	70	34300	200

Table 4.1. Details of lattice-based reversible DLCA simulations including number densities ρ and interparticle potential E. In some cases especially at the lowest density, a few (typically 3-5) independent repeat runs have also been carried out to improve statistics in the scattering functions, etc..

bond energy E. Figures 4.3, 4.4 and 4.6 to 4.9 show snapshots of 2D systems at number densities $\rho = 0.1$ and $\rho = 0.3$. These snapshots may also be compared with pictures of the *irreversible* ($E \to -\infty$) system at the same number densities (Chapter 3).

The morphological effects of reversible bonding are quite striking. At $\rho = 0.1$ (Figures 4.3 and 4.4), the system changes from a typical 'DLCA' system of finely ramified fractal clusters at $E \to -\infty$ to, at low bond energy, something more reminiscent of the typical 'coarsening droplet' pattern familiar from phase-separation studies. The low bond energy system contains quite compact clusters in a 'sea' of monomers and dimers. Because the system density is quite low the clusters are well-separated (compare with the higher density system in Figures 4.6 and 4.7). At the bond energies studied ($E = -1.5k_BT$ and $E = -2.3k_BT$) the internally compact clusters retain, however, somewhat ramified shapes on longer length scales. At the stronger potential, the 'unaggregated phase', the sea of monomers and small clusters in which the

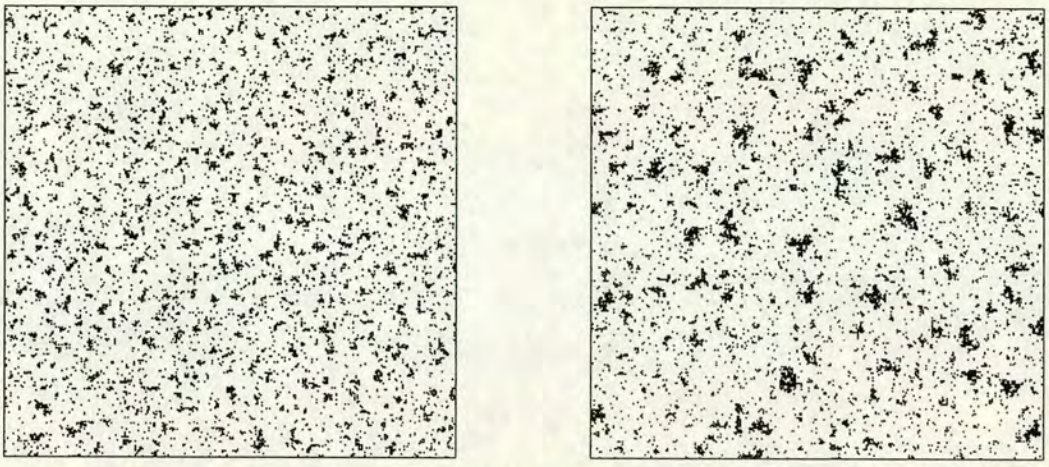

Figure 4.3. Reversible DLCA in a 2D system with system size $L = 300$, number density $\rho = 0.1$ and bond energy $E = -1.5k_BT$. Times shown are $t = 100$ and $t = 2000$ simulation steps.

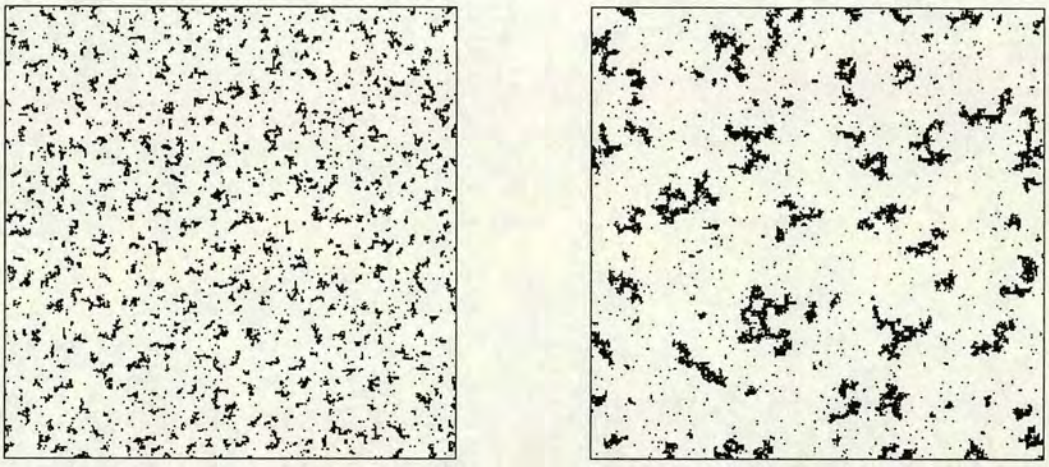

Figure 4.4. Reversible DLCA in a 2D system with number density $\rho = 0.1$ and bond energy $E = -2.3k_BT$. While the system size for this simulation is $L = 500$, for comparison with other snapshots a 300×300 cut-out is shown here. Times are $t = 100$ and $t = 2000$ simulation steps.

near-compact larger aggregates are embedded, is at considerably lower density. This is consistent with the simple picture of a widening 'two-phase region' in the generic binodal phase diagram (see Figure 4.5). As the system is 'quenched' deeper (stronger interparticle potential) the densities of the two final coexisting equilibrium phases get further apart; the low density phase decreases in density, the high-density phase increases. While our simulations have certainly not been run to long enough times to enable study of the equilibrium phase diagram, as we have mentioned above the definition of the interparticle interaction in the reversible DLCA model implies that we might expect the equilibrium phase diagram of the model to be equivalent to that of the Ising model, itself a reasonable model for many phase-separating systems (see e.g. [60]).

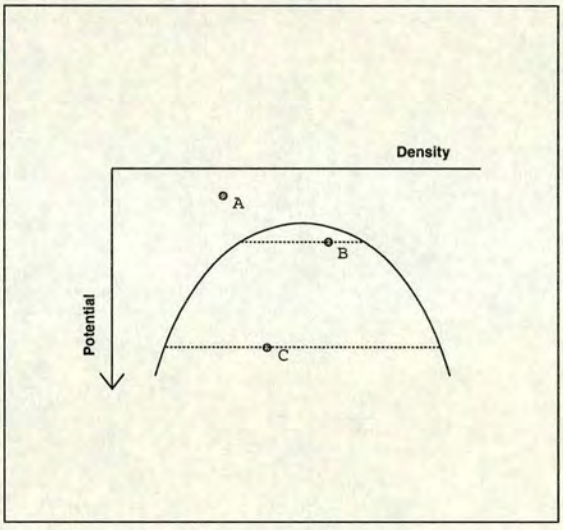

Figure 4.5. Generic 'binodal' phase diagram. The y-axis is increasing (negative) attractive interparticle potential (equivalent in the more familiar variable to *decreasing* temperature). A system at point A is in the single-phase (stable) region, and no phase-separation occurs; systems quenched beneath the binodal curve, within the two-phase region, separate into two coexisting phases at equilibrium. The equilibrium densities of the two phases are given by the points where the lines meet the binodal curve; for the deeper quench C, the low-density phase has a lower density and the high-density phase a higher density than for the shallow quench B.

At higher density, $\rho = 0.3$, we have also carried out simulations at stronger potentials, $E = -3.0k_BT$ and $E = -4.0k_BT$. At $E = -1.5k_BT$ the system contains reasonably separate clusters which look internally near-compact (with a few holes) but have quite

significantly ramified shapes. At $E = -2.3k_BT$ the irregularity of the shapes is quite striking. The clusters are larger and *almost* contact each other across the whole system. At $E = -3.0k_BT$ there is another significant development in morphology; at the latest times a large cluster does span the whole system. But it is not like the spanning 'fine filament' gel cluster of the irreversible simulations (Chapter 3). Instead it is made up of 'fat' filaments; at short length scales the structure has compactified so that most of the particles are in very stable multiply-bonded configurations. The compactification process does not simply result in separate compact droplets, as is sometimes assumed to be the only effect of reversibility in the bonding. Instead at this bond energy and density the long-length scale ramification remains, and very large structures are still able to grow and span the macroscopic system.

Presumably if the simulation were run for long enough, even the very ramified structure at the high bond energy would eventually fully compactify into a state of maximum stability, with all particles multiply-bonded into one or more compact droplets. However it is clear that such a process would take a very long time, because the restructuring must necessarily take place on short length scales (the restructuring consists only of single particles breaking bonds with their nearest neighbours). And on short length scales the structure is already very strong, because of the local compactification into fat filaments. The possibility of simulating such a long-term process with the current algorithm and available computational power seems very remote, though the collapse of such large near-gel structures is a subject of some interest [157, 158]. Such long-lived *but metastable* structures are common in industrial and commercial applications (e.g. cosmetic products, food products, and so on). In such applications external effects like gravity will probably be important in determining the long-term evolution of the system, another element which it would be interesting to investigate via simulation.

Visual study—Preliminary conclusions

Visual study of the aggregating reversible systems generates a number of useful qualitative observations. It is clear that the two cases of DLCA-type fine fractals and spinodal-type compact droplets are only two limits of the morphology of the system.

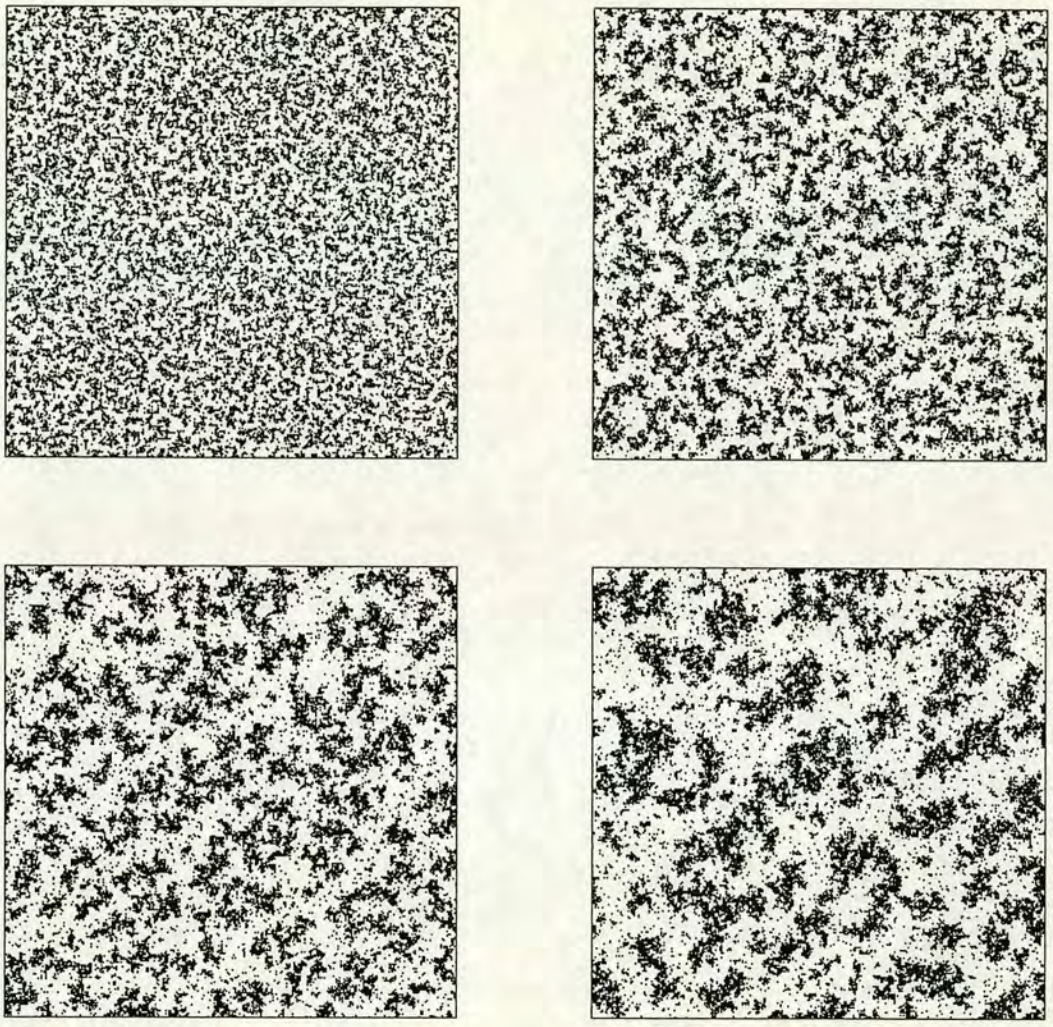

Figure 4.6. Reversible DLCA in a 2D system with system size $L = 300$, number density $\rho = 0.3$ and bond energy $E = -1.5k_BT$. Times shown are $t = 10$, $t = 100$, $t = 500$ and $t = 2000$ simulation steps.

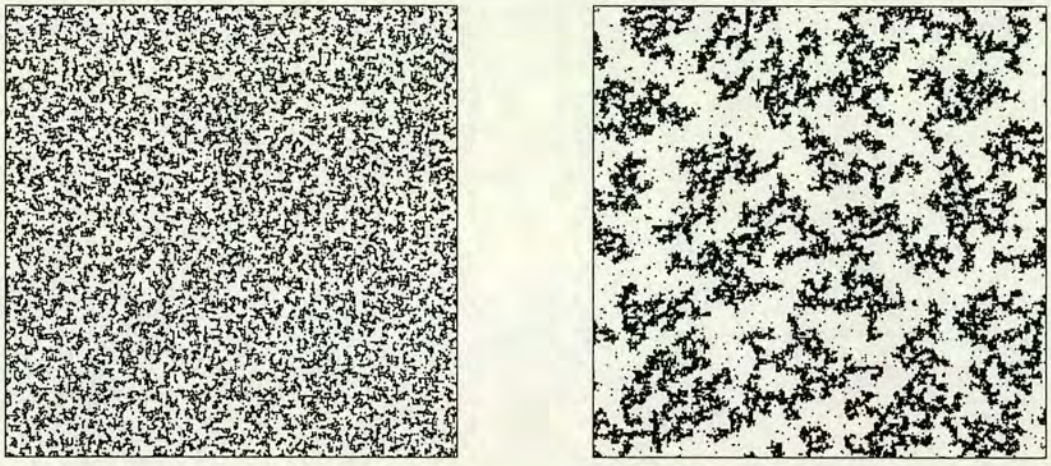

Figure 4.7. Reversible DLCA in a 2D system with number density $\rho = 0.3$ and bond energy $E = -2.3k_BT$. Times shown are $t = 10$ and $t = 1000$ simulation steps. While the system size is $L = 500$, for comparison with other systems the Figure shows a 300×300 cut-out.

In fact there is a wide range of morphologies which the system can exhibit, depending on the bond energy and the density. With increasing bond energy E the model generates aggregates with structures from droplets, to droplets with ramified shapes, to near-compact aggregates with very ramified shapes, to large filamentary structures whose 'fat' filaments are quite compact on short length scales but which still fill space, through to the uncompacted very fine filamentary 'gel' of the very strong bonding limit.

More direct experimental observations of well-characterised 'weakly aggregating' colloidal systems would be of great interest. Two-dimensional experimental systems offer probably the best hope of such direct observation. In the existing literature there are some pictures of 2D aggregating systems with some suggestive similarities to the simulations [36, 37, 38, 159]. Skjeltorp [38] has observed short-range compactification and hexagonal ordering of particles within long-length scale ramified clusters in a 2D system; the pictures in Refs. [36, 159] suggest some small-length scale compactification and large-scale structures similar to the fat-filament gels observed here, though the details are not always clear. A careful systematic study within an easily-imaged system where the interparticle potential may also be easily controlled (and expressed

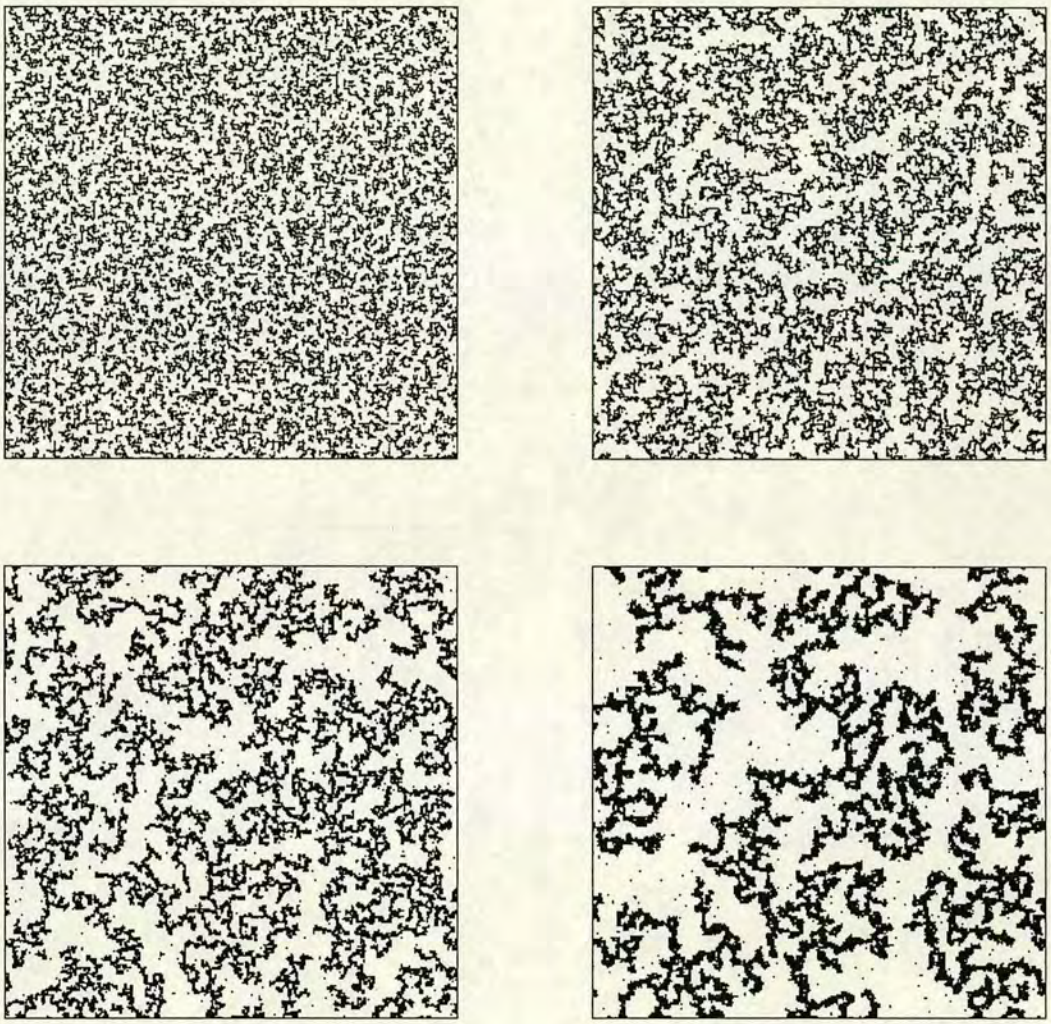

Figure 4.8. Reversible DLCA in a 2D system with system size $L = 300$, number density $\rho = 0.3$ and bond energy $E = -3.0k_BT$. Times shown are $t = 10$, $t = 100$, $t = 1000$ and $t = 10000$ simulation steps.

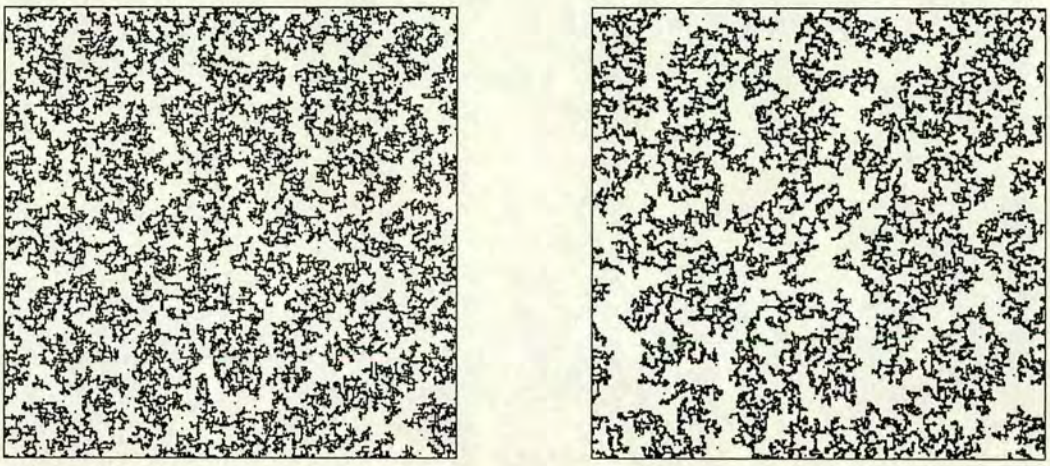

Figure 4.9. Reversible DLCA in a 2D system with number density $\rho = 0.3$ and bond energy $E = -4.0k_BT$. Times shown are $t = 100$ and $t = 1000$ simulation steps. While the system size is $L = 500$, for comparison with other systems the Figure shows a 300×300 cut-out.

in the simple terms of k_BT) would be of enormous interest.

4.3 Scattering functions and system structure

In this section we study the effect of the finite bond energy on the scattering behaviour of the reversible DLCA system. Figures 4.10 to 4.13 show circularly/spherically averaged scattering functions $I(Q)$ for reversible DLCA simulations at various number densities ρ and bond energies E. All the simulations use the lattice-based model, so that $I(Q)$ may be calculated as described in Chapter 2 using the FFT algorithm. The 'bin' widths for the circular/spherical averaging are selected to obtain the best compromise between resolution of features and reduction of statistical noise, and are typically $\delta Qd = 0.06$ for the higher number density systems to $\delta Qd = 0.1$ for the lower density systems (d is the particle diameter). In some cases (the lower density systems where the number of particles is small) results from up to five independent repeat runs of the simulation have been averaged in order to further reduce statistical fluctuations. Even

then the problem of small system size, which means that there are only a few scattering components in the 'bins' at the smallest scattering vector magnitudes, means that some of the data exhibit strong fluctuations at small Q.

4.3.1 Low bond energy

Effect on gelation—'compact' growth

Figure 4.10 shows scattering functions for 2D simulations at quite low bond energy, $E = -2.3k_BT$. As in the irreversible model we see the appearance of a strong peak in the scattering at small Q, in qualitative agreement with scattering experiments [11, 16, 13, 51]. At this lower energy (at the densities studied) aggregation still occurs. However it is immediately apparent that the small-Q peak grows much stronger at late time compared to the irreversible model. For the high-density system, $\rho = 0.3$, while in the irreversible simulations the small-Q peak 'freezes' (space-filling occurs) at $I(Q_m) \simeq 10$, at $E = -2.3k_BT$ $I(Q_m) \simeq 30$ at the latest time shown. (The differing kinetics of the growth process, as evidenced by the time-evolution of the scattering function, are studied in more detail in section 4.3.3.) The scattering data therefore suggest that the 'freezing' of the peak at higher energy is due to the space-filling effect of gelation. At the lower energies, as can be seen in the snapshots in Figures 4.3, 4.4 and 4.6, space-filling does not occur, and the small-Q peak does not 'saturate' but continues to grow and to move to smaller Q. This is in qualitative agreement with experimental observations in the colloid-polymer system [16] where freezing of the $I(Q)$ peak (and extreme slowing of the dynamics of the system) was observed for high bond energies but not for low bond energies.

Compactification on different length scales can also be observed in the scattering functions. In the log-log plots an increase in the slope of $I(Q)$ on the high-Q side of the peak as time increases is visible. This implies that the aggregates become more dense *at short length scales* (high Q). The snapshots in Figures 4.3, 4.4, 4.6 and 4.7 show that on longer length scales the clusters are still somewhat 'ramified'; they have irregular shapes and surfaces. For the higher density the increase in slope in $I(Q)$ is more of

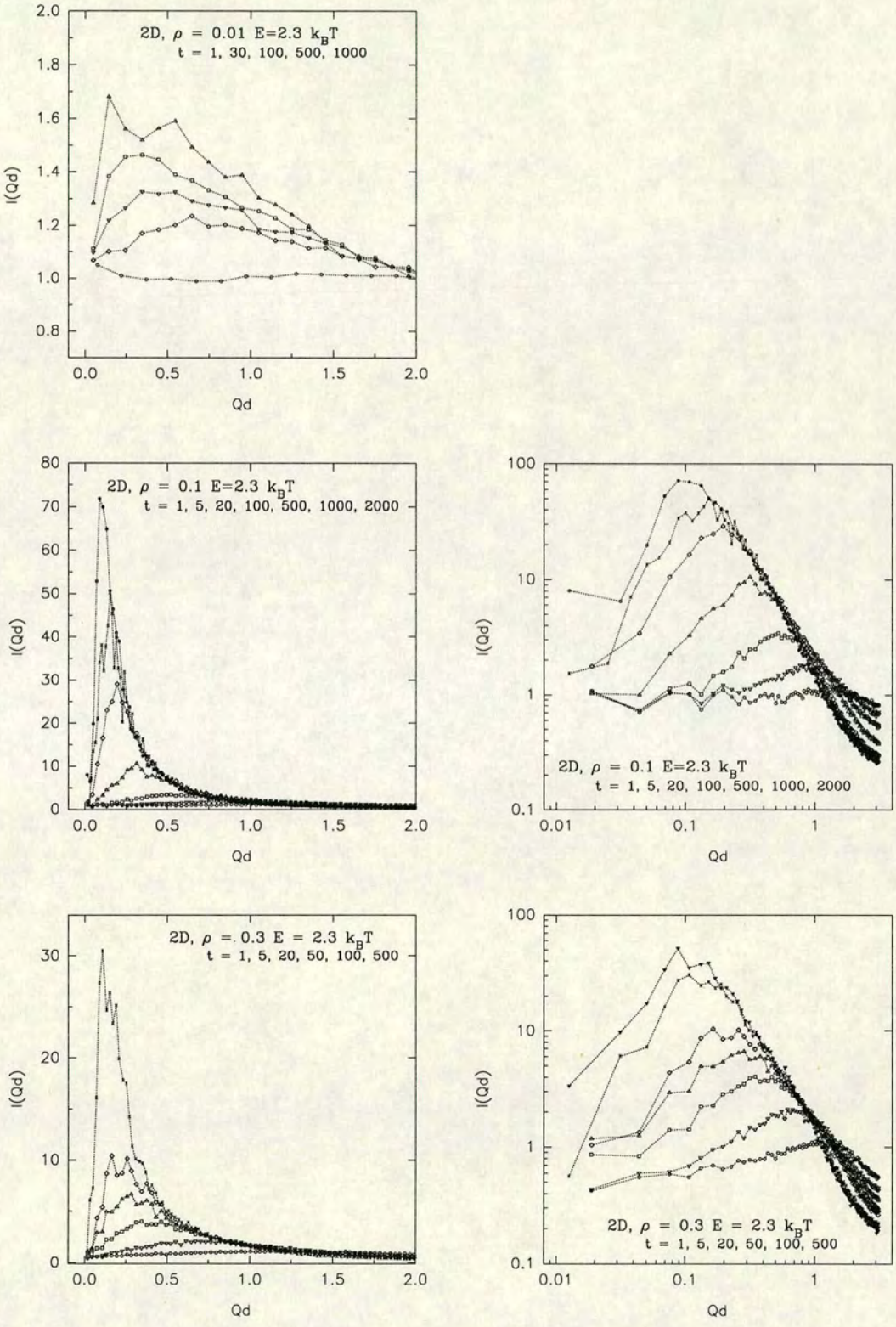

Figure 4.10. Scattering functions $I(Q)$ for the 2D reversible DLCA simulation model. In this Figure we compare results for a single bond energy, $E = -2.3k_BT$, for three number densities ρ. The system sizes are $L = 500$ for all ρ.

a noticeable *bend* in the function, implying that at longer length scales the aggregates are still substantially ramified, consistent with the pictures of the aggregating systems.

Effect on growth–approach to a 'nucleation' model

At the lowest density ($\rho = 0.01$, $E = -2.3k_BT$, Figure 4.10) it is seen that growth of the scattering function peak is very slow. By 1000 steps the small-Q peak has reached an intensity of only $I(Q_m) \simeq 1.6$. Thus the effect of a finite, low bond energy is not limited to compactification of clusters after growth, there is also a substantial effect on growth itself. In fact if the bond energy is sufficiently low, very little growth occurs at all: we observed that in a simulation at $\rho = 0.01$ and energy $E = -1.0k_BT$, no cluster larger than 6 particles had appeared in the system after 50000 time steps. At such a low bond energy any singly-bonded particle has a high probability of escaping, so that one must await the chance appearance of multiply bonded clusters which can 'live' long enough to begin to grow. This situation is then reminiscent of the *nucleation and growth* scenario in phase separation, in which only sufficiently large aggregates can grow [55], smaller aggregates on average tending to 'evaporate' before they can grow larger. That the low-density, low bond-energy systems are possibly in a nucleation region of the 'phase diagram' rather than the region of fast, immediate growth, is also suggested by analysis of the cluster structure, as described in section 4.5. However, as discussed more fully below it is difficult to make definite statements about nucleation given the small system sizes and short run-times within our computational capacity. In a nucleating system *before nucleation* one expects [55] to see a peak in the scattering at $Q \to 0$, due to the loose association of particles, followed by the appearance of a peak at $Q > 0$ *after* nucleation has occurred. We have been unable to run our system for long enough to observe nucleation; the problems associated with observing nucleation are discussed further in section 4.5.

4.3.2 High bond energy

At higher bond energy growth is faster (because clusters are not likely to collapse even when small) but now the effects of the *frustration of growth* by space-filling or gelation

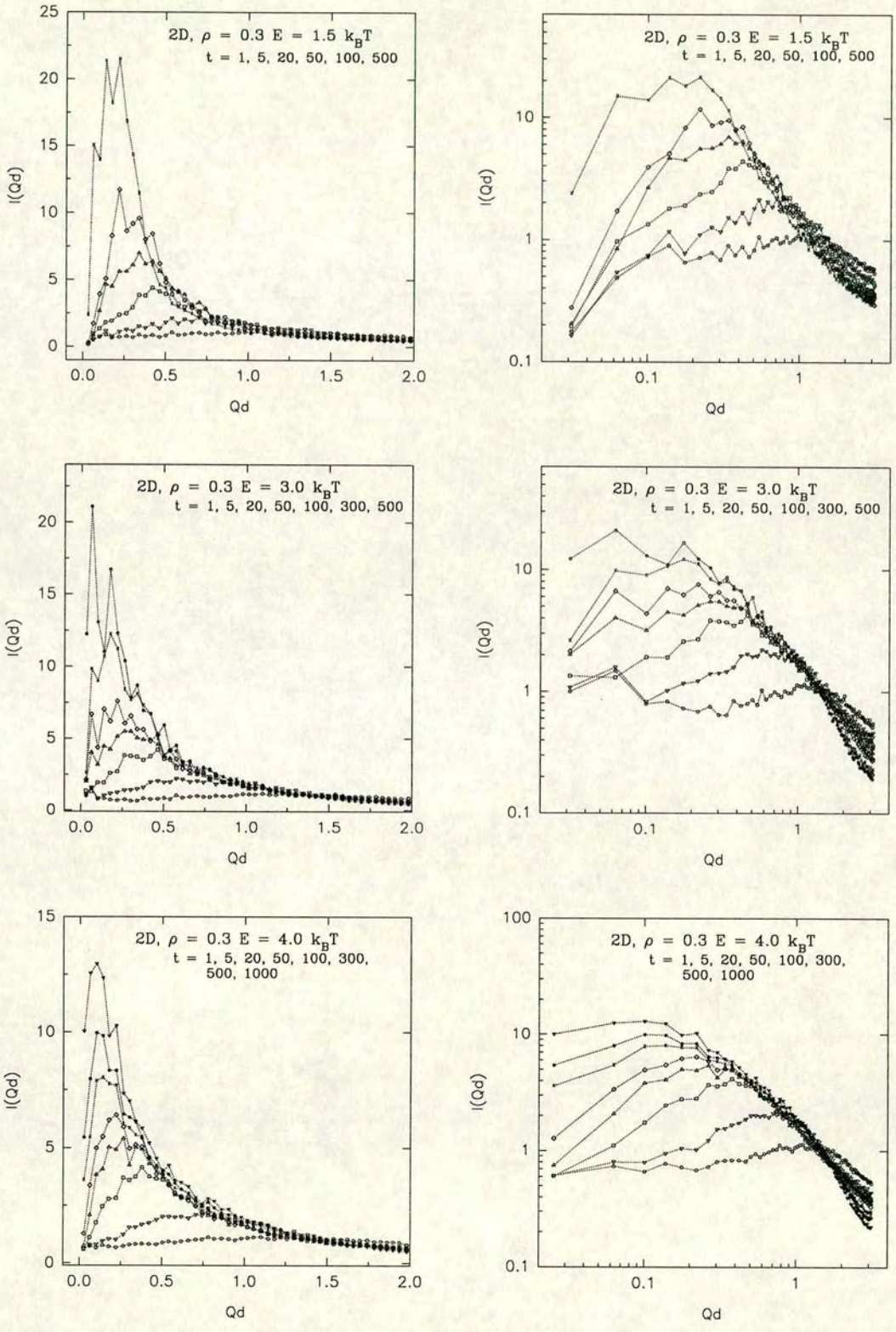

Figure 4.11. Scattering functions $I(Q)$ for the 2D reversible DLCA simulation model. In this Figure we compare results for the high-density 2D simulations ($\rho = 0.3$) at increasing bond energies, $E = -1.5k_BT$ to $E = -4.0k_BT$. The system sizes are $L = 500$ for $E = -4.0k_BT$, $L = 300$ for the other energies.

become evident. Figures 4.11, 4.12 and 4.13 include results from simulations at higher bond energies, $E = -3.0k_BT$ and $E = -4.0k_BT$. Above very low energies the initial growth rate (in the intensity of the small-Q peak) appears to be nearly independent of energy (see the logarithmic plots of $I(Q)$ for the 2D simulation at $\rho = 0.3$ in Figure 4.11, showing $E = -1.5, -3.0$ and $-4.0k_BT$). However the stronger bonds begin to affect continued growth at later time. By $t = 500$ simulation steps growth of $I(Q)$ for the two higher-energy systems has clearly slowed.

In the 2D case the long-length scale ramification plus the short-length scale compactification can be clearly seen in the scattering functions for the higher energies, where there are noticeable bends in $I(Q)$ near $Qd \simeq 1.0$. Interestingly, at the same energies ($E = -3.0$ and $-4.0k_BT$) in the 3D simulations at $\rho = 0.05$ (Figure 4.12) such bends are not really apparent. This may be because, with a greater coordination number in 3D (a greater number of possible nearest neighbours), stability of structure is achieved with less apparent compactification. A 3-bonded particle configuration in 3D is not very compact compared to a 3-bonded configuration in 2D, and yet (at the same bond energy) is equally stable.

Consistent with this point, the 3D systems at $\rho = 0.05$ and $E = -3.0$ or $-4.0k_BT$ are also more strongly affected by gelation or frustration of growth. The $I(Q)$ plots demonstrate well the effect of increasing bond energy. The effect of increasing *density* can also be seen in Figure 4.13 ($\rho = 0.1$). Here growth frustration is evident even at $E = -2.0k_BT$, and rather striking at $E = -4.0k_BT$.

4.3.3 Time evolution of peak intensity and position

We go on to study the effect of the bond energy on 'rates of growth' in more detail by examining the time evolution of the intensity and position of the small-Q peak in the scattering function $I(Q)$.

Peak position Q_m

The rate of decrease of the scattering function peak position, $Q_m(t)$, is plotted for 2D

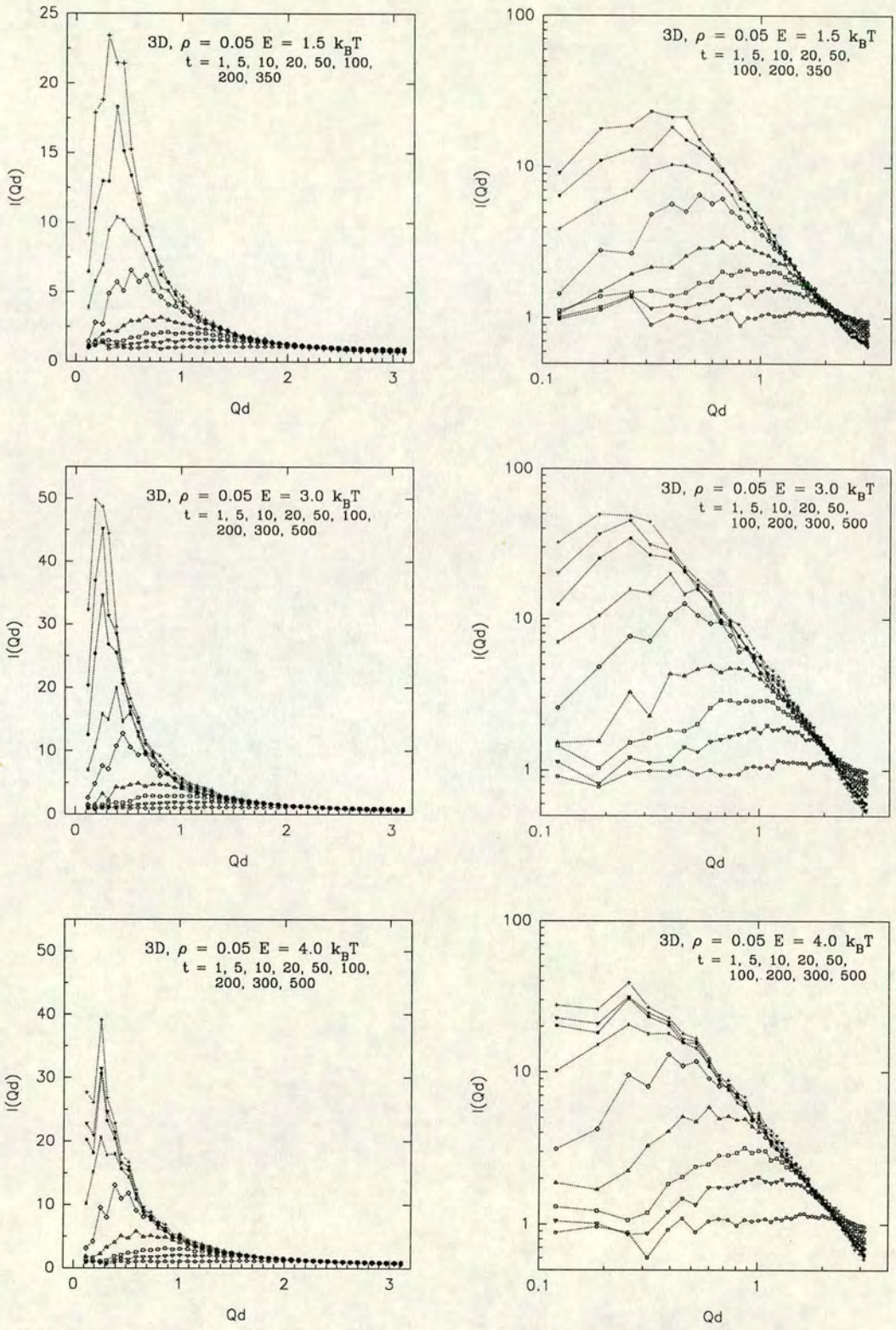

Figure 4.12. Scattering functions $I(Q)$ for the 3D reversible DLCA simulation model. In this Figure we compare results for the 3D simulations at number density $\rho = 0.05$, at increasing bond energies, $E = -1.5k_BT$ to $E = -4.0k_BT$. The system sizes are $L = 70$ for all runs.

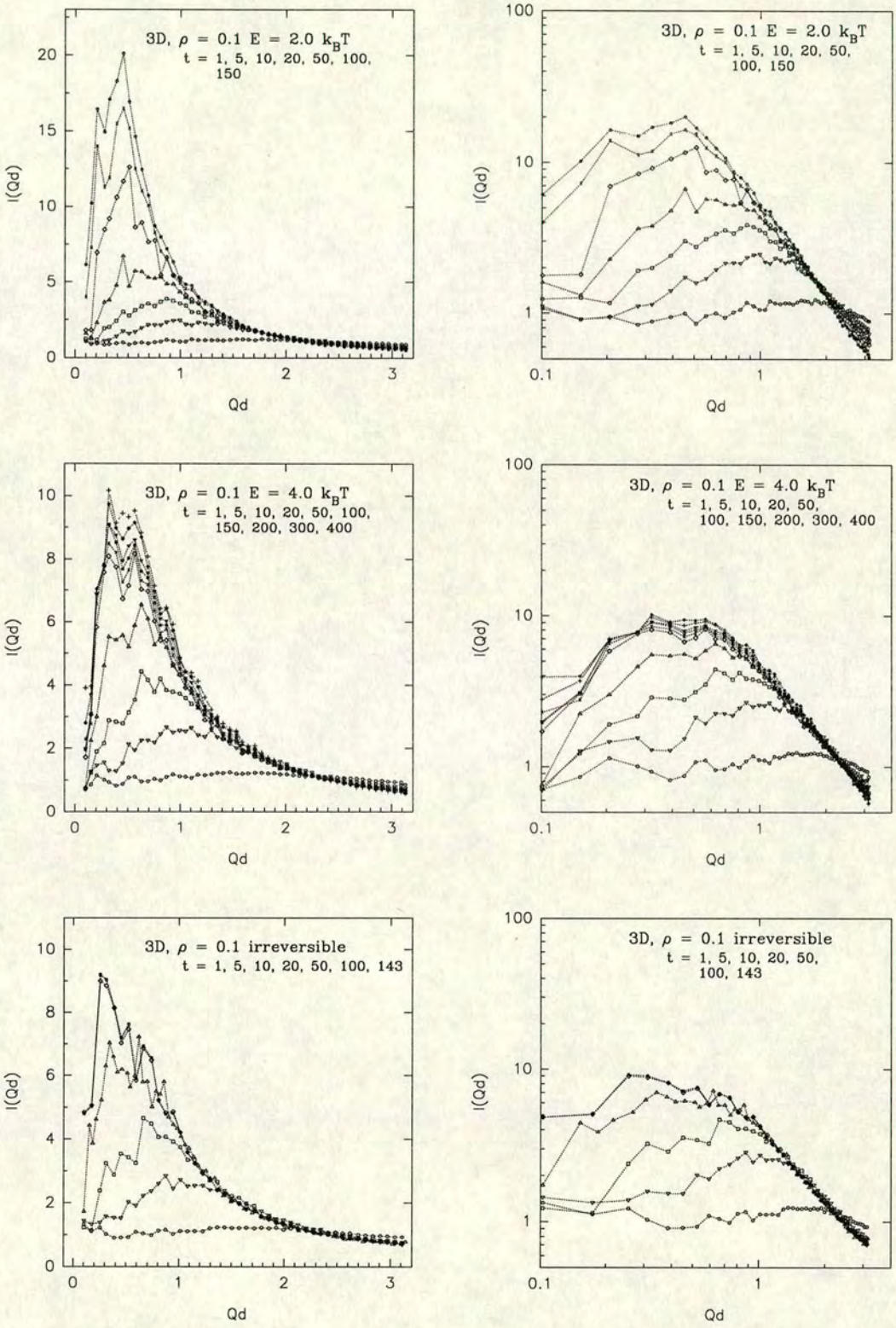

Figure 4.13. Scattering functions $I(Q)$ for the 3D reversible DLCA simulation model. In this Figure we compare results for the high-density 3D simulations (number density $\rho = 0.1$), at bond energies $E = -2.0k_BT$ and $E = -4.0k_BT$, with the *irreversible* model ($E \to -\infty$). The system sizes are $L = 70$ for all runs.

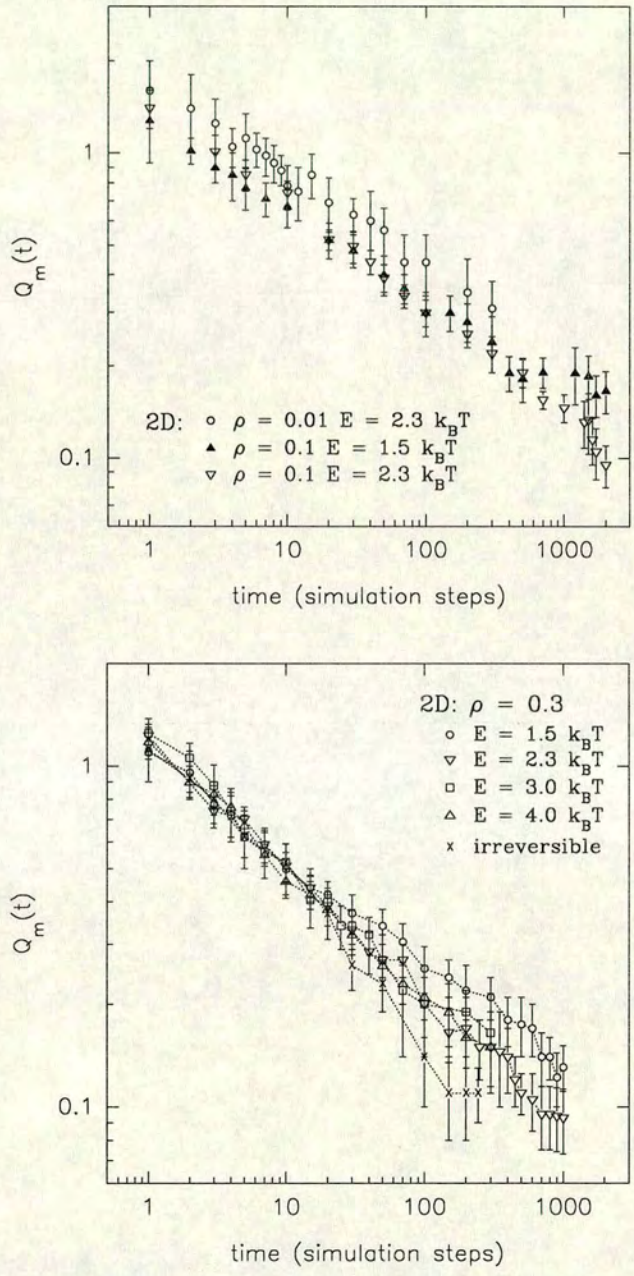

Figure 4.14. Evolution of the position of the scattering function peak Q_m as the aggregation proceeds, for 2D simulations. The upper plot shows results for low-density simulations ($\rho = 0.01, L = 500$ and $\rho = 0.1, L = 300$ for $E = -1.5k_BT$ and $L = 500$ for $E = -2.3k_BT$). The lower plot shows results from simulations at $\rho = 0.3$.

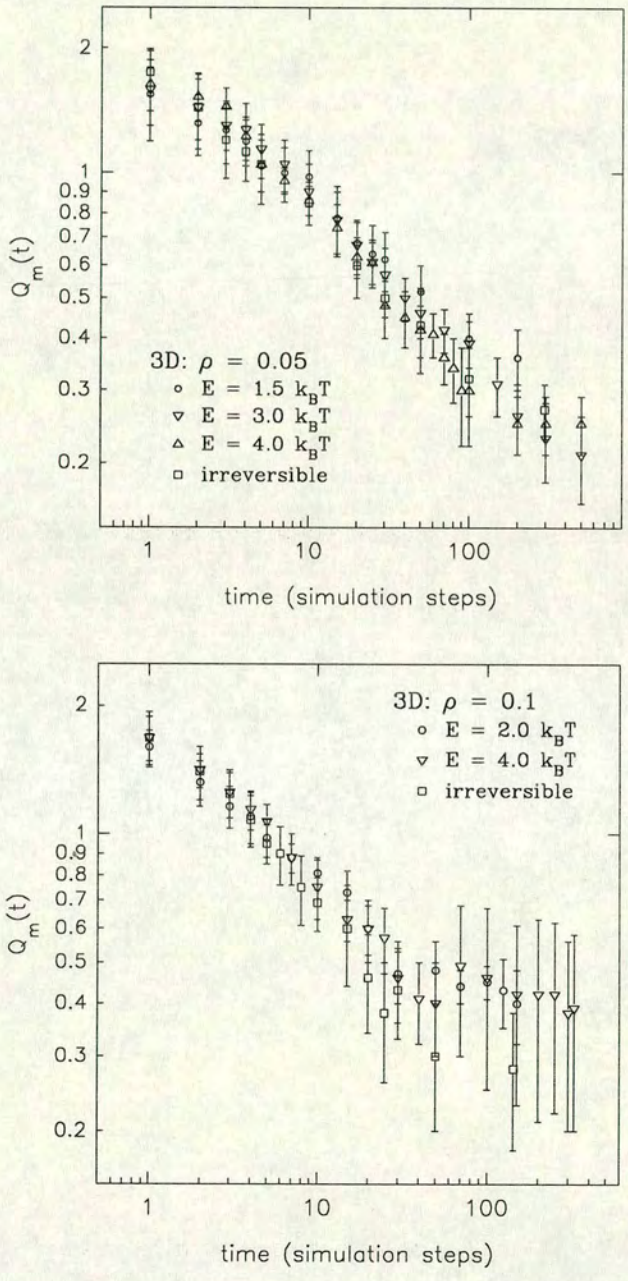

Figure 4.15. Evolution of the position of the scattering function peak Q_m as the aggregation proceeds, for 3D simulations. The upper plot shows results for simulations at $\rho = 0.05$, the lower plot $\rho = 0.1$. All systems have size $L = 70$.

and 3D systems at various densities and bond energies in Figures 4.14 and 4.15. As for the irreversible model, we analyse the $Q_m(t)$ data in terms of power-law approximations, assuming that Q_m and time t are approximately related by a power law:

$$Q_m(t) \sim t^{-\alpha} \tag{4.8}$$

Least-squares estimates of the exponent α are given in Table 4.2 together with time ranges for the fits, and error-bars. (Error-bars for Q_m are estimated by eye from the $I(Q)$ plots.)

Given the error bars in Q_m, the data follow the power-law relation (4.8) quite well. Any curvature is not really detectable with the accuracy of the data collected here. While little bond-energy dependence is apparent on the plots, the fitted exponents do seem to show a trend for α to increase with increasing E. At the lowest bond energies we find $\alpha \simeq 0.3$. This is reasonably consistent with what we might expect when the low-bond energy DLCA system approaches a system of compact clusters or droplets; the system then might be expected to compare well with 'standard' phase-separation models [55, 60]. In simulations of droplet growth in spinodal decomposition a range of exponents $\alpha \simeq 0.2$ to 0.33 has been found [57, 59, 68, 126, 160, 161, 162], while theoretical treatments, as mentioned in Chapter 3, predict $\alpha \simeq 1/3$ [143, 144]. It seems then that higher bond energies, for which the DLCA system tends to generate more fractal or ramified clusters rather than droplets, lead to a *faster* increase in the characteristic length scale. We can make some rough arguments in support of this. Since the growing objects are fractals, the 'addition' of a given mass of particles results in an increase of radius greater than that for compact objects. Furthermore as the growing fractals fill more space their 'collision cross-sections' must increase relative to that of compact objects.

Peak intensity $I(Q_m)$

The rate growth of the scattering function peak intensity, $I(Q_m, t)$, is plotted for 2D and 3D systems at various densities and bond energies in Figures 4.16 and 4.17. Again

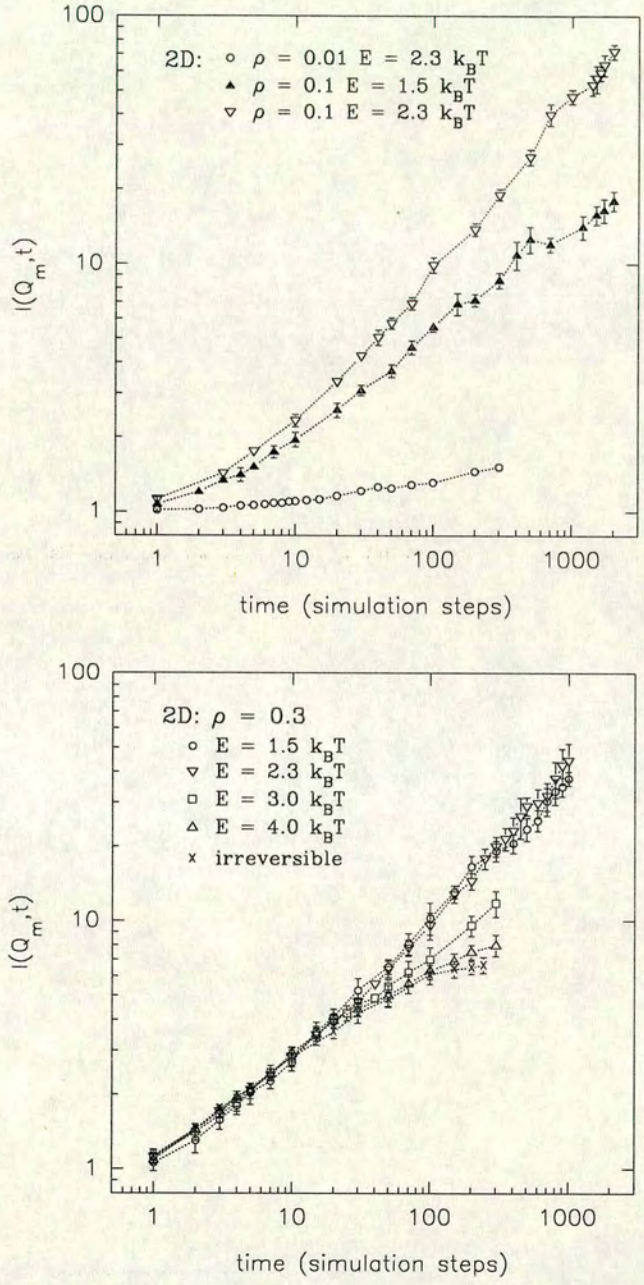

Figure 4.16. Evolution of the scattering function peak intensity $I(Q_m)$ as the aggregation proceeds, for 2D simulations. The upper plot shows results for low-density simulations ($\rho = 0.01, L = 500$ and $\rho = 0.1, L = 300$ for $E = -1.5k_BT$ and $L = 500$ for $E = -2.3k_BT$). The lower plot shows results from simulations at $\rho = 0.3$.

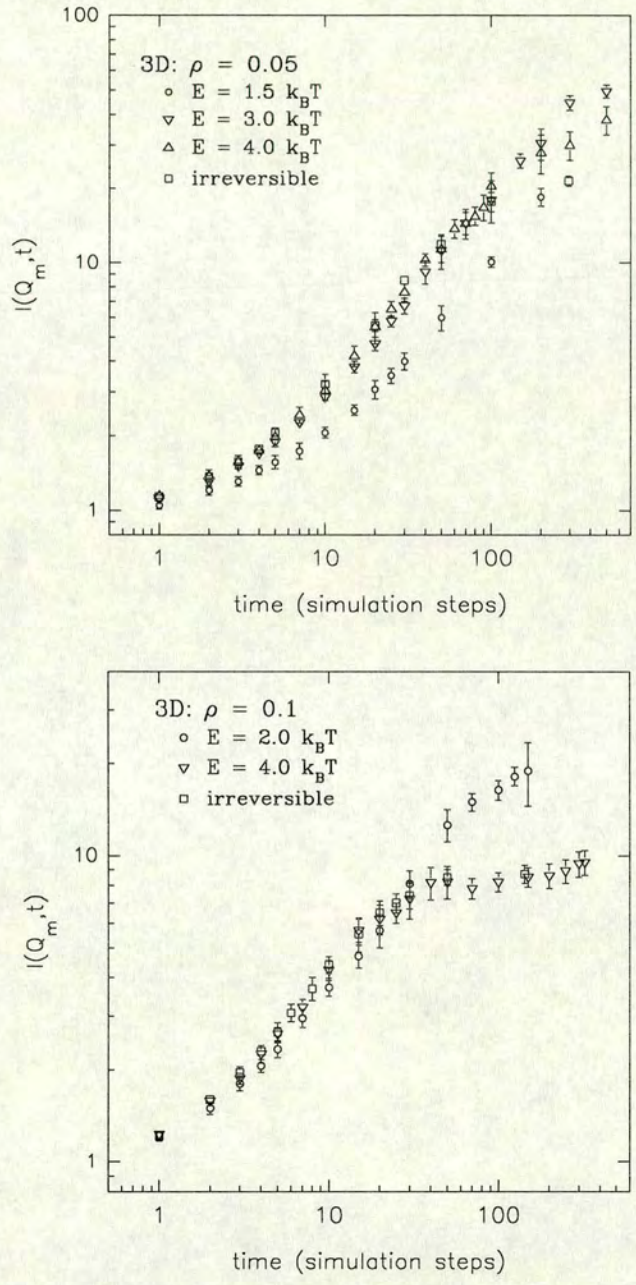

Figure 4.17. Evolution of the scattering function peak intensity $I(Q_m)$ as the aggregation proceeds, for 3D simulations. The upper plot shows results for simulations at $\rho = 0.05$, the lower plot $\rho = 0.1$, all with system size $L = 70$.

we analyse according to the power-law approximation:

$$I(Q_m, t) \sim t^{\beta}. \tag{4.9}$$

Exponents β for least-squares fits are given in Table 4.2.

Some of the effects of bond energy on growth of the peak intensity have already been discussed. At low bond energies initial growth of $I(Q_m)$ is slowed (e.g. 2D, $\rho = 0.1$, compare $E = -1.5k_BT$ and $E = -2.3k_BT$). At still higher bond energy the space-filling effect slows down the growth of $I(Q_m)$ so that (e.g. 2D, $\rho = 0.3$) we see a 'crossover' where by later time $I(Q_m)$ is substantially higher at low bond energy. The plots for $\rho = 0.3$ in 2D and $\rho = 0.05$ in 3D suggest that we find a near-continuous range of late-time growth from complete 'freezing' for very strong bonding to continuing power-law growth for low bond energy. The results for $\rho = 0.1$ in 3D show that in terms of the onset of space-filling and freezing of $I(Q_m)$ energy $E = -4.0k_BT$ is almost indistinguishable from the irreversible model.

Scaling of peak intensity with peak position

Figures 4.18 and 4.19 show the scaling of the peak intensity $I(Q_m, t)$ with the peak position Q_m for 2D and 3D reversible DLCA simulations. Lines of slopes equal to the space dimension, the (approximate) 'accepted' irreversible DLCA fractal dimension, and slope 1.0, are drawn near the data to aid a comparison. The data have been analysed in terms of a power-law relation

$$I(Q_m) \sim Q_m^{-\gamma}. \tag{4.10}$$

Fitted estimates of γ, with the Q_m ranges over which the power-law has been fitted, are given in Table 4.2.

From the 2D simulation results in Figure 4.18 some effects of finite bond energy E are immediately apparent. In the lower-density simulations we can see that the peak

Density	$E(k_BT)$	α	(range)	β	(range)	γ	(range)
(a) 2D							
0.01	2.3	0.29 (0.03)	1-300	—		—	
0.1	1.5	0.30 (0.02)	1-500	0.45 (0.02)	10-3000	1.61 (0.19)	0.1-0.5
	2.3	0.34 (0.02)	1-1000	0.67 (0.01)	20-3000	2.05 (0.14)	0.14-0.6
0.3	1.5	0.30 (0.02)	1-1000	0.56 (0.02)	20-1000	1.91 (0.14)	0.1-0.6
	2.3	0.38 (0.02)	1-1000	0.62 (0.02)	20-1000	1.54 (0.09)	0.09-0.6
	3.0	0.38 (0.03)	1-1000	0.39 (0.04)	20-1000	1.09 (0.08)	0.16-1.3
	4.0	0.39 (0.02)	1-1000	0.42 (0.02)	1-30	1.00 (0.06)	0.15-1.2
(b) 3D							
0.05	1.5	0.30 (0.03)	1-350	0.79 (0.04)	25-200	2.23 (0.30)	0.3-1.1
	3.0	0.38 (0.03)	2-500	0.84 (0.04)	20-500	2.12 (0.31)	0.2-0.9
	4.0	0.43 (0.03)	3-100	0.80 (0.04)	10-500	1.87 (0.18)	0.2-1.1
0.10	2.0	0.32 (0.03)	1-50	0.87 (0.19)	20-50	2.40 (0.27)	0.3-1.0
	4.0	0.38 (0.04)	1-50	0.76 (0.14)	7-15	1.57 (0.19)	0.5-1.7

Table 4.2. Exponents for power-law fits to $Q_m(t) \sim t^{-\alpha}$ and $I(Q_m, t) \sim t^{\beta}$. γ is the exponent in the fit of $I(Q_m) \sim Q_m^{-\gamma}$. 'range' is the ($t$ or Q_m) range over which the fit is estimated. Figures in brackets are error-bars for the exponents.

intensity $I(Q_m)$ grows more slowly with the increase in characteristic length (decrease in Q_m) for lower energy. The fitted γ estimate for $\rho = 0.1$, $E = -2.3k_BT$, when compared with the γ estimate for the irreversible model (Chapter 3, $\gamma = 1.42$) is consistent with *compactification* of the 'typical' growing object; instead of fractal clusters with $\gamma \simeq d_{f,DLCA}$ the system now contains near-compact objects with $\gamma \simeq D$, the space dimension (see Figure 4.4). At still lower energy (and density) it takes more time for the system to reach the 'compact' region of the $I(Q_m)$ *vs.* Q_m relation. Thus we cannot simply describe the system as 'fractal or compact', since there is a distinct time-dependence of structure, which in turn is itself bond energy-dependent.

At the higher density ($\rho = 0.3$) we see similar effects. As the aggregation proceeds there is a remarkable divergence in the development of the $I(Q_m)$ *vs.* Q_m relation for different bond energies. At the lowest energy studied, $E = -1.5k_BT$, an approach to a compact system is observed ($\gamma = 1.91$). As bond energy is increased we find the onset of the late-time/small-Q_m 'saturation' in $I(Q_m)$ indicative of space-filling by the increasingly ramified objects. γ (Table 4.2) also decreases, down to $\gamma \simeq 1.0$ at the highest energy. Thus at high energy we recover the high-density scaling behaviour as demonstrated for the irreversible model, where the scaling exponent $\gamma \simeq 1.0$. As before we interpret this tentatively in terms of early-time near-linear objects becoming quickly 'pinned' into the structure at the higher bond energies and densities, such that more branched objects with higher dimensions cannot develop. But when the bond strength is decreased this effect is less marked since these linear objects are inherently less 'stable' than more compact objects, more of whose particles are multiply-bonded. Further discussion is deferred until we examine the full scaling of the $I(Q)$ function in section 4.7.

Results from 3D simulations are similar. Here because of the small system sizes error bars on γ are large, but the trend for increasing compactness as bond energy decreases remains clear, especially for the set of data at $\rho = 0.05$. In this case (Table 4.2) we find $\gamma \simeq 2.2$ at $E = -1.5k_BT$, going to $\gamma = 1.87 \simeq d_{f,DLCA}$ (Chapter 3) at $E = -4.0k_BT$. This result at $E = -4.0k_BT$ agrees rather well with measurements in colloid-polymer experiments [16], where it was found that the effective dimension as

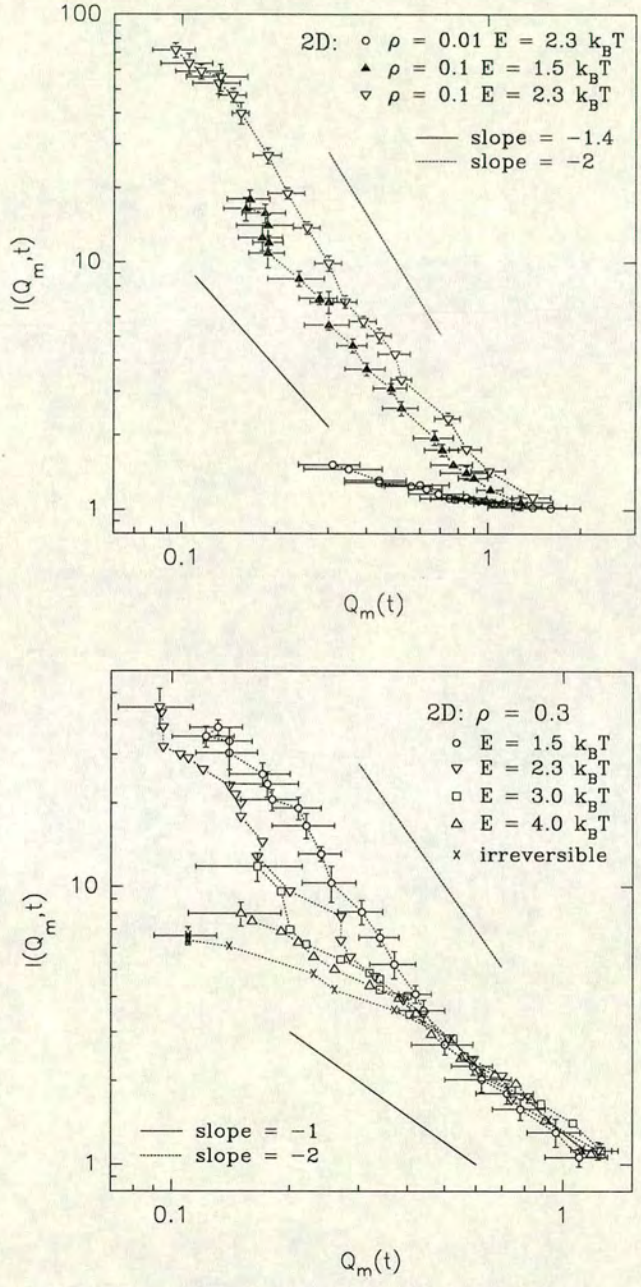

Figure 4.18. Scaling of peak intensity $I(Q_m, t)$ with peak position $Q_m(t)$ in 2D reversible DLCA. The upper plot shows results for low-density simulations ($\rho = 0.01, L = 500$ and $\rho = 0.1, L = 300$ for $E = -1.5k_BT$ and $L = 500$ for $E = -2.3k_BT$). The lower plot shows results from simulations at $\rho = 0.3$. For clarity only some symbols have been drawn with error bars; the error ranges shown are typical of all the data.

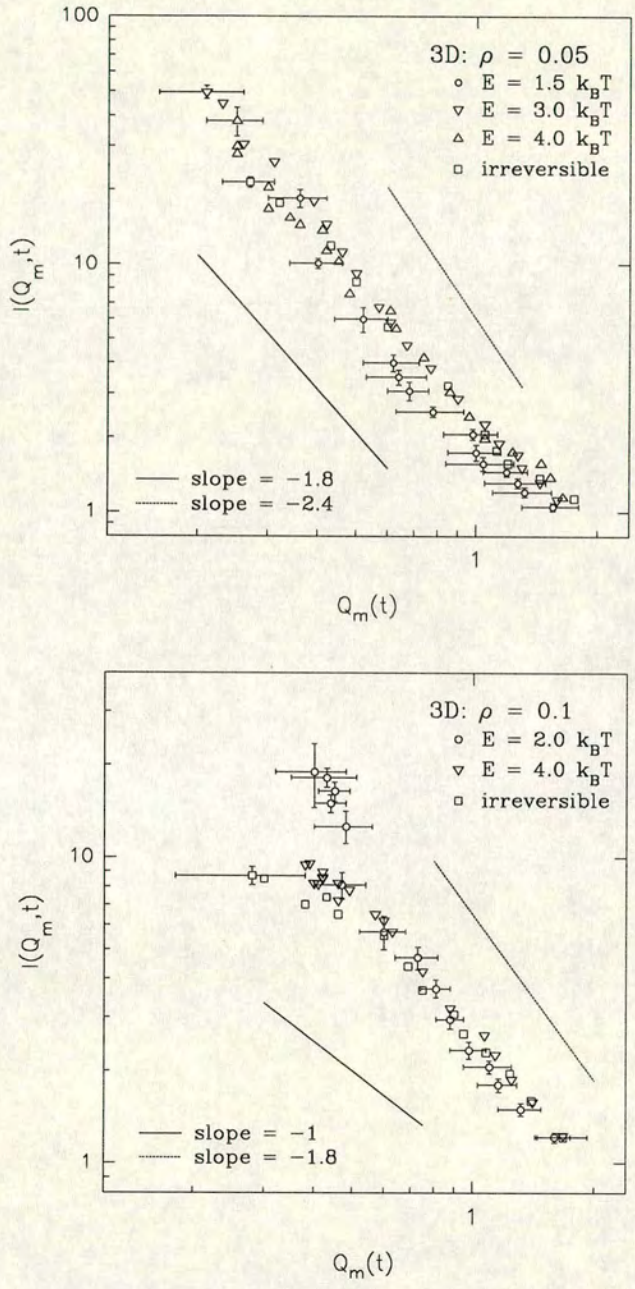

Figure 4.19. Scaling of peak intensity $I(Q_m, t)$ with peak position $Q_m(t)$ for 3D reversible DLCA. The upper plot shows results for simulations at $\rho = 0.05$, the lower plot $\rho = 0.1$, all with system size $L = 70$. For clarity only some symbols have been drawn with error bars; the error ranges shown are typical of all the data.

measured from light-scattering experiments remained close to $d_{f,DLCA}$ until the 'bond' energy was decreased below $E = -4.0k_BT$, at which point increasing compactification was observed as E was decreased. (Additionally in previous *two-dimensional* reversible DLCA simulations where the *fractal dimension of individual clusters* was measured via the mass-radius relation [107], an 'upper critical' value $E = -4.0k_BT$ was measured near which the fractal dimension reached the irreversible DLCA dimension. No changes in d_f were observed for larger E, while an increase in d_f toward the space dimension D was found for smaller E. The form of the bond-energy dependence of d_f was similar to that measured in the 3D experiments.) Thus our scattering-based methods give results quite consistent with other simulation and with experiments.

4.3.4 Growth and frustration

The scattering results from the reversible DLCA simulations at different bond energies indicate that, for a given density, we may divide the systems roughly into two regimes on the basis of the bond energy E. At lower energies, growth of structures (at least growth as measured by the scattering function $I(Q)$) is slowed, due to the collapse or evaporation of clusters. At low enough energy we might expect to find nucleation-like behaviour, where growth is initially very slow, until 'critical' nuclei appear by chance which are large enough to be stable and grow further without collapsing (see section 4.5). At very low bond energies we might further find a 'single-phase equilibrium' system where significant long-lived aggregation never occurs.

At high energies the *initial* rate of growth seems approximately independent of the bond energy. If the system is above the bond energy where the smallest clusters—single-bonded dimers—are themselves quite stable (for the time it takes such small clusters to grow further) then increasing bond energy further would not increase the *initial* rate of growth. But at later times *frustration of growth* becomes an important phenomenon. At later time at the *highest* energies growth is slowed because large near-system-spanning structures are formed, leaving no more room for further diffusion and aggregation. These large structures can still compactify (because the bond energies are still finite) but this will be a much slower process, and furthermore *will happen only*

at short length scales. Long-length scale structural changes will have to 'wait' until many small-scale compactifications begin to fragment the large structure. Therefore the 'collapse' of the large system-spanning gel-like structures will be very slow.

The above arguments imply that for a given density we might imagine a 'critical' bond energy for *maximum sustained growth* of the scattering function. At this energy the early-time effects of the collapse of small clusters are minimised, while late-time frustration due to space-filling by large clusters is avoided by just sufficient compactification. For example, our simulation data suggest that, in 2D at $\rho = 0.3$, the critical energy E_c is somewhere between $1.5k_BT$ and $3.0k_BT$. The pictures of the system at $E = -2.3k_BT$ (Figure 4.7) suggest that E_c is probably slightly higher than $2.3k_BT$. In this thesis we have carried out these 'preliminary' investigations of the reversible DLCA model without being able to be more exhaustive; from a more detailed investigation one could presumably obtain a 'kinetic phase diagram' and measure E_c and its dependence on system density ρ more precisely.

4.4 Real-space structure—pair correlation functions

We consider now the real-space structure of the reversible DLCA system by calculating the pair correlation functions $g(r)$. Figures 4.20 and 4.21 show $g(r)$ for 2D and 3D reversible DLCA simulations at various number densities and bond energies. The pair correlation function is calculated as described in Chapter 3. Also indicated on the plots are length scales $l_q(t)$ corresponding to the scattering function small-Q peak positions $Q_m(t)$, $l_q(t) = 2\pi/Q_m(t)$. It is clear that in the reversible DLCA system, as was the case for the irreversible model, the scattering function peak position corresponds to a length scale of the *outer radius of the 'depletion zone'* in $g(r)$.

There appears a difference in the time evolution of the depth of the depletion zone in low bond energy and high bond energy systems. In the 2D systems at low bond energy ($E = -1.5k_BT$ and $E = -2.3k_BT$ for $\rho = 0.1$, $E = -1.5k_BT$ for $\rho = 0.3$) the depth of the depletion zone does not decrease so substantially as at higher bond energies, in fact is approximately constant in time, especially for $\rho = 0.1$ at $E = -2.3k_BT$. This

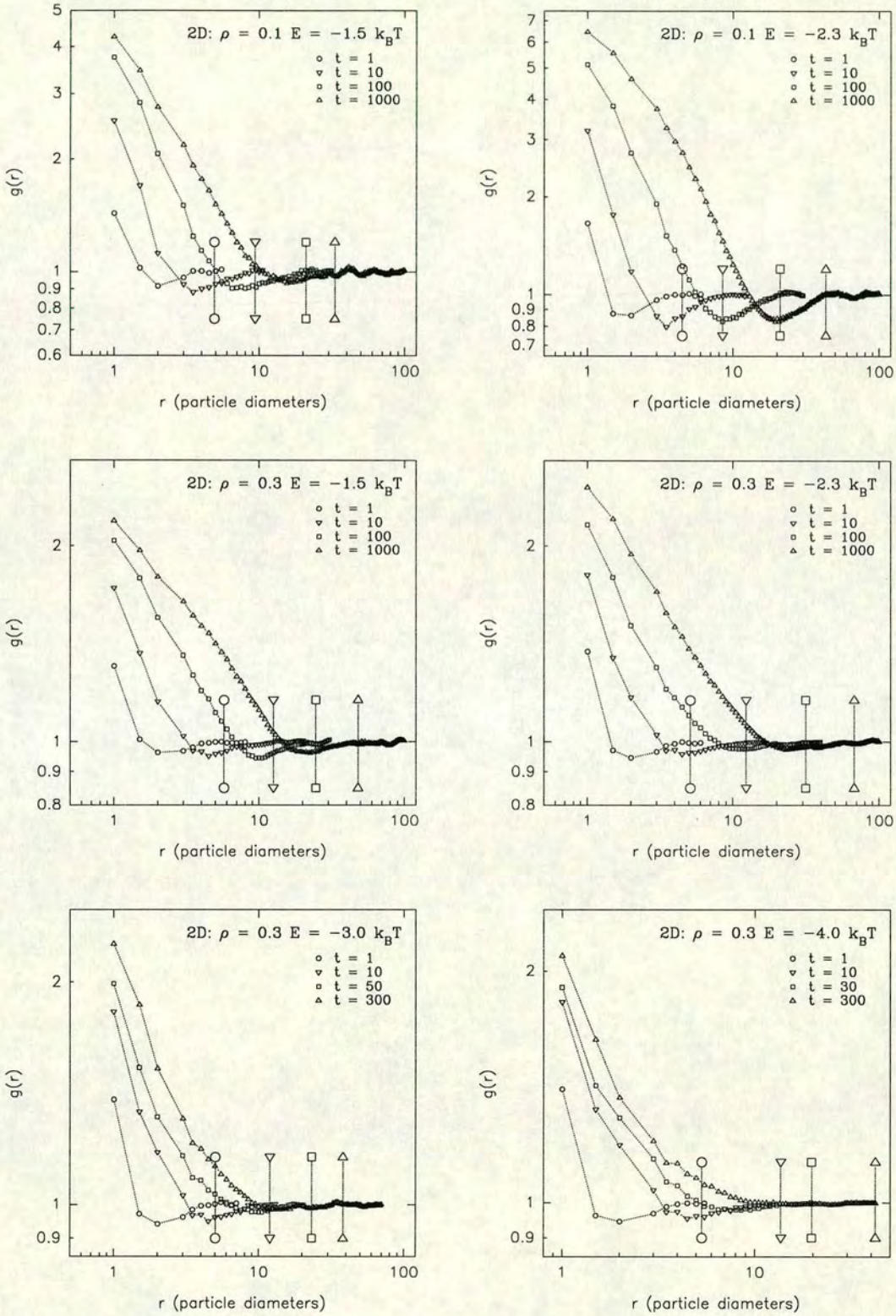

Figure 4.20. Pair correlation functions $g(r)$ from 2D reversible DLCA simulations. The large symbols with vertical dashes indicate the length scale $l_q(t)$ corresponding to the small-Q peak position in the scattering function, $l_q(t) = 2\pi/Q_m(t)$. For clarity points are plotted only to r just beyond the depleton zone; at larger r $g(r) \approx 1$, i.e. the system is homogeneous.

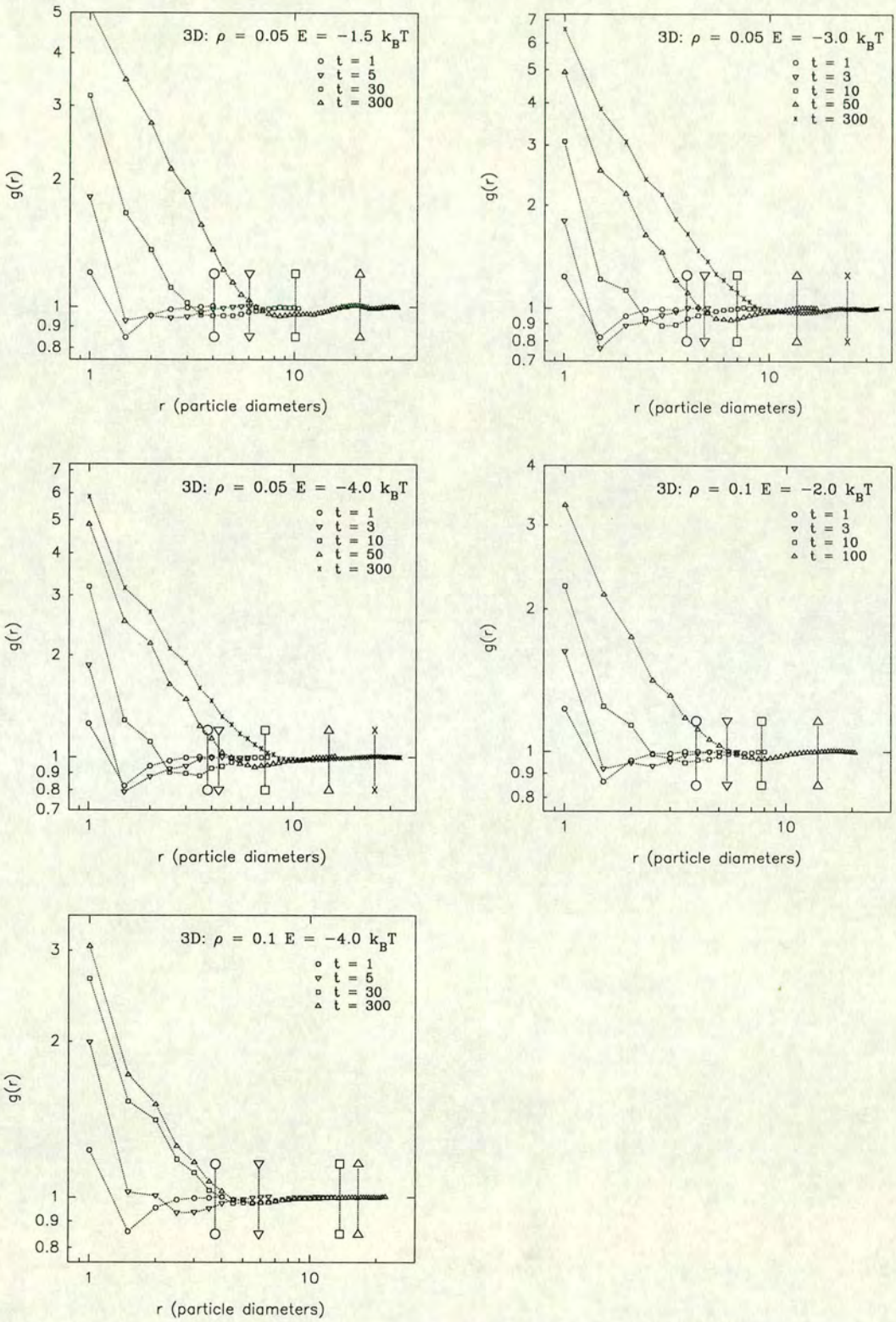

Figure 4.21. Pair correlation functions $g(r)$ from 3D reversible DLCA simulations. The large symbols with vertical dashes indicate the length scale $l_q(t)$ corresponding to the small-Q peak position in the scattering function, $l_q(t) = 2\pi/Q_m(t)$. For clarity points are plotted only to r just beyond the depleton zone; at larger r $g(r) \approx 1$, i.e. the system is homogeneous.

is perhaps consistent with simulations of phase-separating systems in which a similar depletion zone in $g(r)$ was found [68]. Those simulations involved a *shallow* quench into the two-phase region of the system (see Figure 4.5) for which the effective interparticle interaction was quite low (the temperature was quite high), corresponding to our low bond energy case.

The difference in the time-behaviour of the depletion zone depth for high and low bond energies is further consistent with the idea (Chapter 3) that it is the space-filling effect or the approach of the system to gelation which affects the depth of the depletion zone. In the low bond energy systems near-compact clusters form which do not fill space. At higher bond energies the growing fractals extend further and further toward the edge of their depletion zones (the fractal cluster grows faster than the region originally occupied by its constituent particles, as described in Chapter 1) thus tending to 'fill in' the depletion zones to some extent. However the scattering functions retain a finite-Q peak at gelation (both in these simulations and in experiments) indicating that in the gel structure *there is still a depletion zone.* This is clear from the simulations of the irreversible model in Chapter 3.

At very low bond energy where little aggregation takes place one would expect no depletion zone (or a very shallow dip), and for higher energies (initially) deeper depletions. The 2D $\rho = 0.1$ $g(r)$ plots ($E = -1.5k_BT$ and $E = -2.3k_BT$) are consistent with this, the higher bond energy showing a deeper depletion (the 'unaggregated phase' is at lower density, see Figure 4.5). The same *system density* effect as observed with the irreversible model, that of higher densities having a shallower depletion zone, is observed in the reversible simulations.

4.5 Structure of aggregates

In this section we study the effect of bond energy on the structure of individual aggregates in the reversible DLCA systems. Average form factors $P(Q)$ are calculated in exactly the same way as in Chapter 3. Figures 4.22 and 4.23 show results from 2D simulations; Figure 4.24 results from 3D simulations.

As has already been mentioned, the effect of the introduction of reversible bonding on the structure of DLCA aggregates has been studied to some extent by Shih and co-workers [107]. In their 2D simulations they measured the fractal dimension of clusters at different E via the mass-radius relation, and compared estimates of d_f with experiments. It was found that for potentials weaker than a certain bond energy $E \simeq -4.0k_BT$, d_f was increased compared to the irreversible DLCA value; indeed d_f seemed to approach the space dimension for the weakest potentials. For potentials stronger than $E \simeq -4.0k_BT$ d_f was found to 'saturate' at the irreversible DLCA value. These measurements compare rather well to experiments. A very similar form of the dependence of the effective d_f on interparticle potential was also found for the colloid-polymer system[3] [16]. In the colloid-polymer experiments the 'effective fractal dimension' was actually estimated using the scaling properties of the scattering function as measured by light-scattering.

In this work we also use methods analogous to scattering to study the structure of aggregates. Going beyond a simple estimate of the effective fractal dimension, the advantage of calculating the average form factor for the system is that we can study the structure of aggregates on various length scales. As is described below, this enables us to demonstrate that the apparent change in the single statistic d_f is not enough to fully describe the effects of reversible bonding in the DLCA model.

4.5.1 Low density and low bond energy

We first consider the $P(Q)$ results from low density/low bond energy systems. The top-left plots in Figures 4.22 and 4.24 show $P(Q)$ for 2D and 3D simulations at $\rho = 0.01$, $E = -1.5k_BT$. After a period of initial growth, the $P(Q)$ functions stop rising with time at small Q. In the 2D case where we have been able to run to much longer time this is particularly striking; the magnitude of $P(Q \to 0)$ is almost unchanged between times $t = 100$ and $t = 18000$ simulation steps. Therefore growth at these low densities/bond energies is certainly extremely slow, and it is possible that the system

[3] Even though the experimental system is 3D while the simulations are 2D.

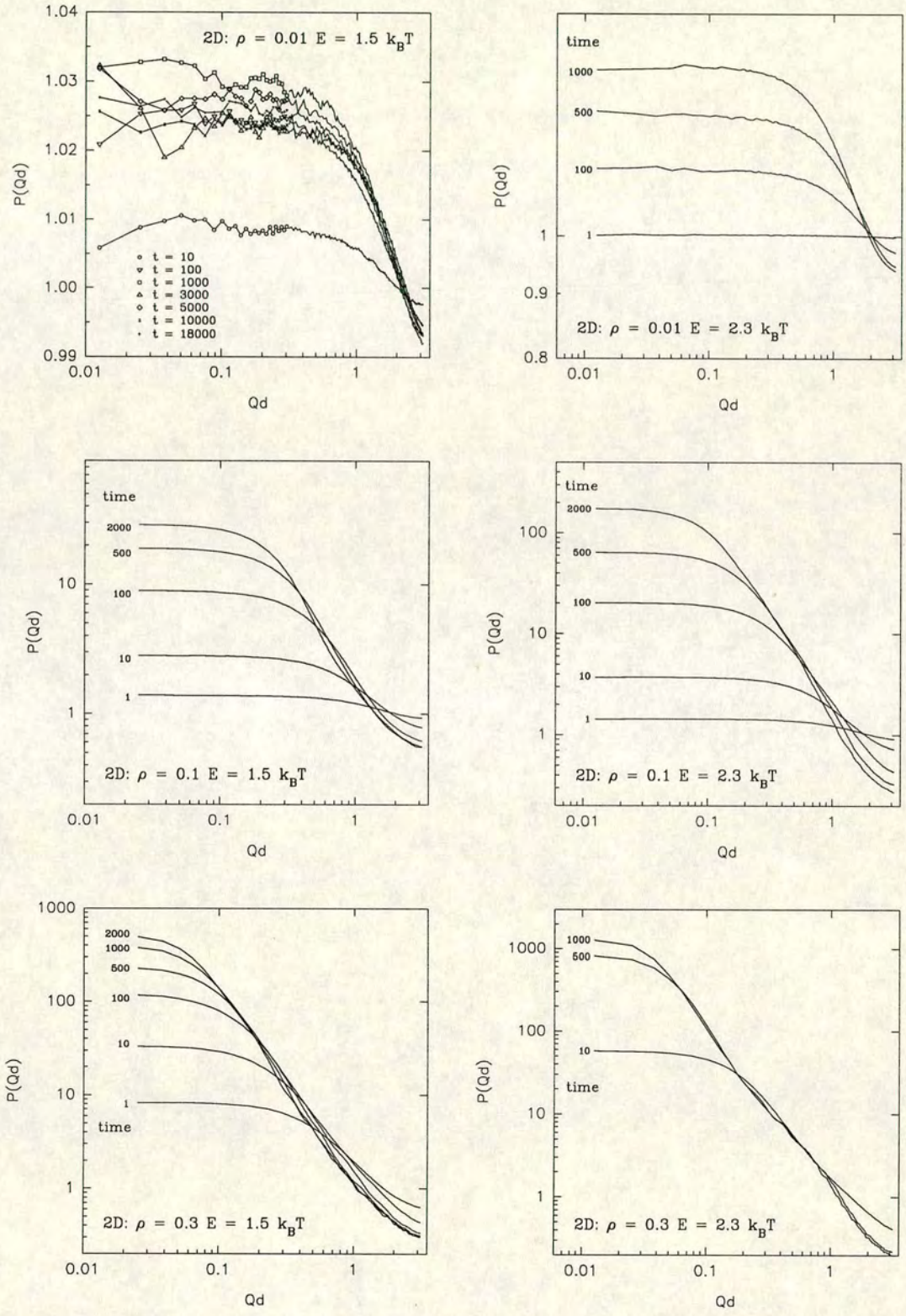

Figure 4.22. Average form factors $P(Q)$ for the 2D reversible DLCA simulation model, at bond energies $E = -1.5k_BT$ and $E = -2.3k_BT$ and three number densities, $\rho = 0.01, 0.1$ and 0.3. The system sizes are $L = 500$ for $\rho = 0.01$, $L = 500$ for $\rho = 0.1$ and 0.3 at $E = -2.3k_BT$, and $L = 300$ for $\rho = 0.1$ and 0.3 at $E = -1.5k_BT$.

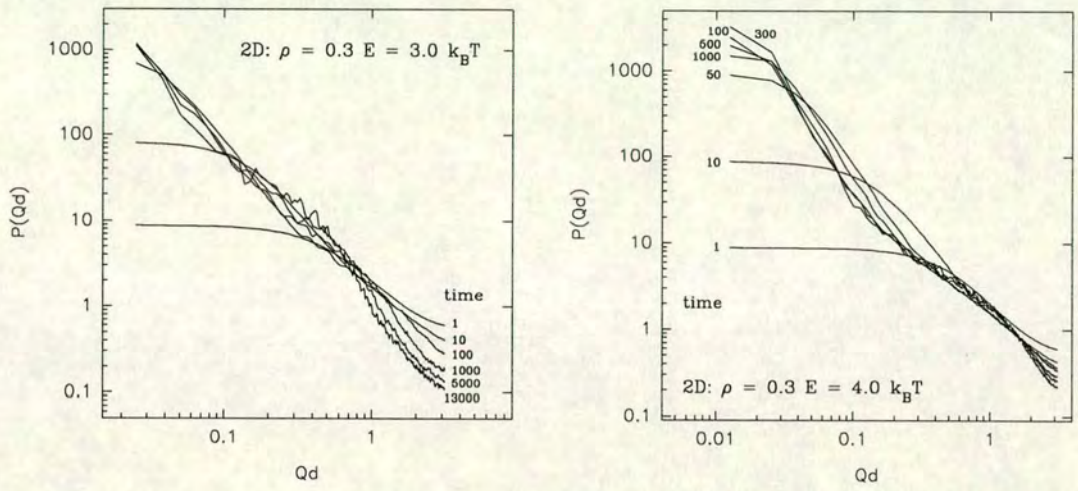

Figure 4.23. Average form factors $P(Q)$ for the 2D reversible DLCA simulation model, at number density $\rho = 0.3$, for 'high' bond energies $E = -3.0k_BT$ and $E = -4.0k_BT$. The system sizes are $L = 300$ for $E = -3.0k_BT$ and $L = 500$ for $E = -4.0k_BT$.

has reached a *dynamic equilibrium*. Small aggregates are still forming and collapsing, but there is no growth in the 'average' aggregate size.

However it is difficult, as often in simulations, to be certain that the system is really in equilibrium. It remains possible that at later time a 'nucleation' event may occur in the system and faster growth begin. Nucleation processes, where only for aggregates above a certain critical size can growth dominate evaporation or collapse [55, 60], are notoriously difficult to detect, especially in small-scale simulations. The nucleation rate (the mass incorporated into growing nuclei per unit volume and unit time) is likely to be a very sensitive function of temperature or interparticle potential; conventional nucleation theory predicts an exponential dependence [60]. In such a model the probability of observing a nucleation event goes from very low to very high in a narrow range of temperature/bond energy. Thus at slightly too low a bond energy we might never see a nucleation event in our small simulation system. At slightly too high a bond energy nucleation and subsequent growth would occur so quickly that, with the time-resolution limitations of the lattice-based model, we would not be able to distinguish it from immediate fast aggregation. We would therefore have to rely on

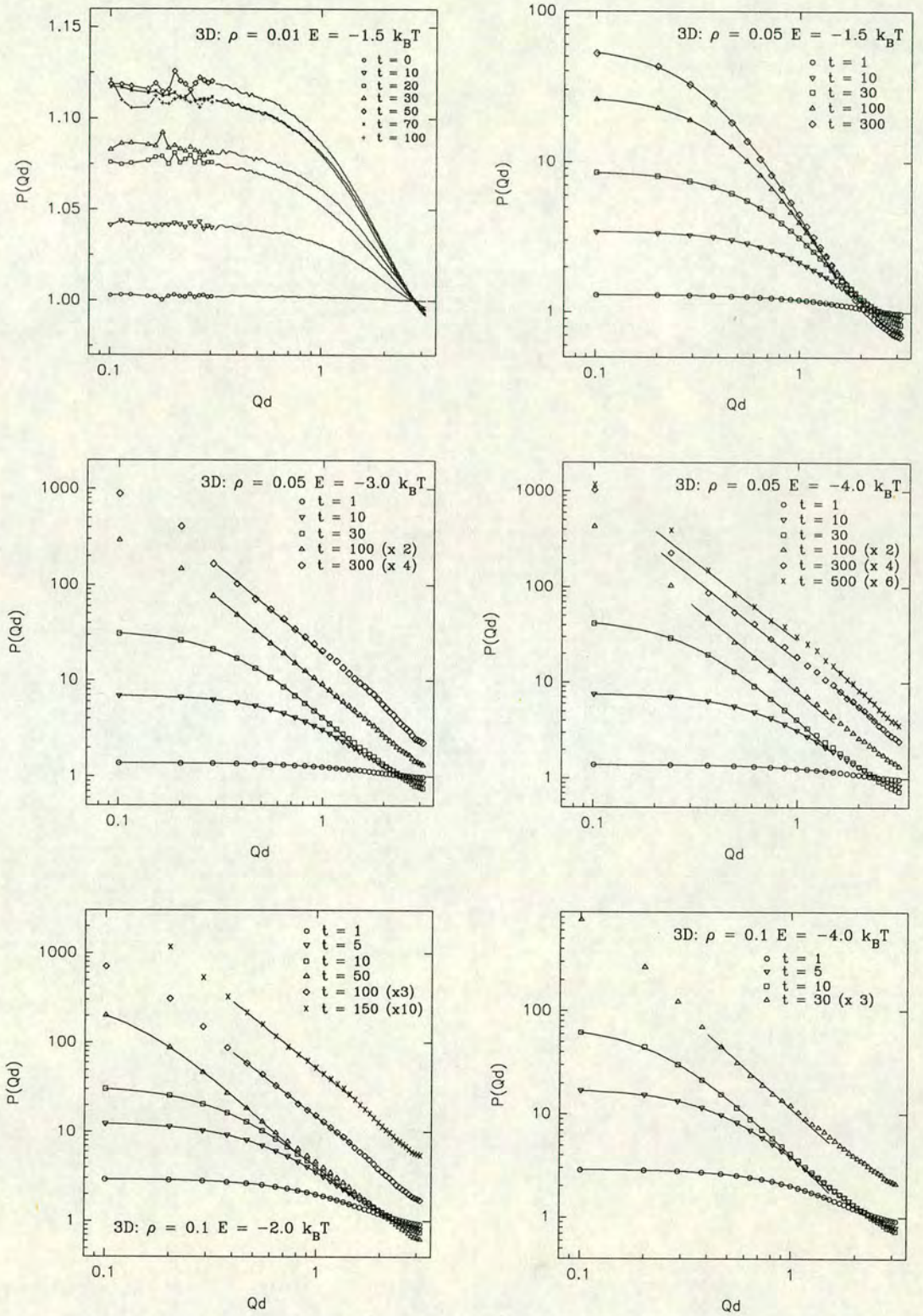

Figure 4.24. Average form factors $P(Q)$ for 3D reversible DLCA simulations. In some cases fits to the data of the Fisher-Burford expression, or (at later times) of a simple power-law, are shown. Exponents and parameter estimates are given in Table 4.3. For clarity symbols are plotted only every 7 or 10 $P(Q)$ data points. Later-time $P(Q)$ data and fits are shown shifted vertically so that different times may be distinguished; the shift-factors are given in the Legend.

making a good guess as to the 'best' bond energy at which to observe nucleation. A more complete mapping of the 'phase diagram' via collection of results from a much larger number of simulations at many densities and bond energies is probably the only way to estimate the 'phase boundaries' between the one-phase equilibrium system, the nucleating system and the fast-growth 'unstable' system. Nevertheless, the form factor data for the low bond energy/low density systems here indicate that these systems are in a different region of the 'phase diagram' of the reversible DLCA model compared to the higher density/energy simulations.

4.5.2 Analysis of structure from $P(Q)$

The *Fisher-Burford* functional form for the scattering by a fractal,

$$P(Q) \simeq \frac{A}{[1 + 2Q^2R_g^2/3d_f]^{d_f/2}}, \tag{4.11}$$

was used in Chapter 3 to fit to the form factor results from the irreversible simulations and obtain estimates of the fractal dimension of the 'typical' cluster. In this subsection we discuss attempts to quantify the structure of aggregates in the reversible simulations using similar methods. In those cases where the functional form appears reasonable, the Fisher-Burford expression has been fitted to the 3D reversible simulation results. Parameter estimates A, R_g and d_f for the reversible simulations are given in Table 4.3.

By a 'reasonable' Fisher-Burford functional form we mean at least that the 'rolloff' of the $P(Q)$ data at small Q should be visible in the Q-range available. At the lowest densities and earliest times, even though this condition is satisfied, the fitting is probably not valid. The parameter estimates obtained are unrealistic; for instance we consistently find very low estimates of the exponent or fractal dimension d_f. This is probably to be expected, since at early time (and always at low density/bond energy, where growth is very slow) the form factor is calculated from an average which includes many monomers and very small clusters. It is not surprising that the Fisher-Burford expression is not robust to the inclusion into the average $P(Q)$ of a large number of

Density	E (k_BT)	time	A	R_g	d_f
0.05	-1.5	1	1.30	0.51	0.40
		10	3.45	1.43	1.35
		30	8.64	2.37	1.83
		100	27.5	3.94	2.26
		300	57.4	5.04	2.54
	-3.0	1	1.38	0.60	0.41
		10	7.01	2.03	1.81
		30	33.0	4.43	2.11
	-4.0	1	1.38	0.57	0.5
		10	7.64	2.12	1.82
		30	45.8	5.51	2.03
0.1	-2.0	1	2.94	1.30	1.15
		5	12.6	2.82	1.94
		10	32.5	4.56	2.03
		50	336.1	14.0	2.21
	-4.0	1	2.90	1.22	1.29
		5	17.6	3.56	1.93
		10	71.9	6.92	2.08

Table 4.3. Parameters of fits of the 'Fisher-Burford' expression, equation (4.11), to cluster form factor data from 3D reversible DLCA simulations (see Figure 4.24). The fits are to $P(Qd)$ data for $Qd < 1.5$; d is the particle diameter.

monomers (for which $P(Q) = 1$) and dimers, etc..

At intermediate times, once sufficient growth has occurred that the system contains larger aggregates, the Fisher-Burford form fits quite well to the data, and gives reasonable parameter estimates. The parameters R_g and A increase with time as expected for growing objects. There is also a clear trend for the exponent d_f to increase. While we might expect the estimated d_f exponent to reflect the compactification of clusters as particles move into more stable configurations, it is not clear that the d_f results really show this. The exponent d_f is probably not estimated with much accuracy (there is not a very extended Q region beyond the 'rolloff' where the power-law scattering should dominate, see also the next section). Furthermore there are clear indications from looking more carefully at the plots of $P(Q)$ that a description of the effect of the finite bond energy simply in terms of compactification and increase in the 'dimension' of objects is not really adequate. Instead there appear to be *different structural changes on different length scales.* The Fisher-Burford form by definition assumes a single fractal structure (or that the averaging procedure for $P(Q)$ generates a 'typical' single fractal

structure) so that the Fisher-Burford form is not likely to describe properly structures which are changing in different ways at different length scales.

At later times the Fisher-Burford form cannot be fitted to the data in any case, instead $P(Q)$ continues to rise in an approximate power-law as $Q \to 2\pi/L$. In these cases we have tried to fit simple power-laws to the data instead; estimates of exponents are given in Table 4.3. It can be seen clearly from the plots though that the data rarely support *single* power-laws (see below). The reversible bonding and restructuring have different effects on aggregate structure at different length scales. The study of $P(Q)$ demonstrates that the simple picture, where even at low bond energy the only effect of the finite bond energy is to increase the fractal dimension of otherwise still DLCA-like fractal clusters, is *not* adequate to fully describe the structural effects of the bond energy E. A simple estimation of a 'fractal dimension' from a scatter plot of mass *vs* radius, for example, as carried out by Shih and co-workers [107], is unlikely to give information on changes in structure at different length scales. While a 'fractal dimension' might be estimated, the *meaning* of this dimension becomes very unclear. It certainly does not fully describe the structure of aggregates under conditions of 'weak' attraction.

4.5.3 Restructuring

The $P(Q)$ data demonstrate that the finite bond energy allows *restructuring* of aggregates with time. The slopes of the $P(Q)$ curves at large Q generally show a steepening over time, indicating that at small length scales the aggregates are becoming more compact. The same steepening or bend is visible in the scattering function $I(Q)$ and is consistent with visual observation of the simulation systems. At lower energies this restructuring is effective on longer and longer length scales as time increases; behind the 'growth front' there is a 'restructuring front' expanding through the system. It is then the relative rates of expansion of these 'fronts' which determines the structure of the aggregates on different length scales.

The above-mentioned steepening of $P(Q)$ at large Q is well demonstrated in the $P(Q)$ functions from the 2D simulations. We might fit power law relations, $P(Q) \sim Q^{-d_r}$,

to the $P(Q)$ data separately at smaller Q and larger Q to obtain estimates of the nominal 'dimension' d_r in each Q-region. Typically for the 2D systems we find $d_r > 2$ in the large-Q (steepening) region. This might seem to imply an unphysically high 'dimension', $d_f > D$, the space dimension. One possible explanation is that the 2D, low bond energy clusters are both volume fractals and *surface* fractals (Chapter 1). In this case a 'scattering exponent' $d_r = 2d_f - d_s$ is expected [24], where d_f is the familiar volume fractal dimension and d_s is the surface fractal dimension. Thus it is possible to obtain $d_r > D$, the space dimension ($d_f < D$ while $D - 1 < d_s < D$). Visual observation shows that the 2D low-energy clusters certainly have ramified surfaces. However another possible explanation is that as the surfaces of the clusters become 'smoother' at short length scales due to restructuring the scattering function approaches the *Porod* form, $P(Q) \sim Q^{-(D+1)}$ [27, 134]. It is difficult given the data available to distinguish between these two alternatives, and indeed there may not be any real distinction between them. In any case, it is most important to note that at the relatively high number densities and small clusters which we are considering, the range of Q over which we may look for power-law relations and estimate exponents is quite limited; in the reversible model we are even more limited since now we are trying to distinguish between volume fractality, surface fractality and smooth local surfaces all within a rather small range of length scales. The separation of $P(Q)$ into just two regimes is itself rather arbitrary, and it is probably more likely that there is a near-continuous change in structure over the complete scale of the aggregates. Simple estimation of multiple fractal dimensions is not really a reliable way to describe the structure.

In the 2D systems at the higher density/higher bond energies (Figure 4.23) the situation is more complex still. The steepening in $P(Q)$ at large Q is still visible (more so here in 2D than in 3D, as already discussed). However, at long length scales we observe a similar effect to that in the irrereversible model, such that $P(Q)$ also rises more steeply at long length scales. In Chapter 3 we interpreted this as possibly being due to the onset of homogeneous packing of clusters at the largest length scales, i.e. to gelation. Thus in the reversible model the effects of restructuring and the effects of gelation are both observable in the average form factor. The evolution of the cluster structure at high density is thus rather complex, and without doubt more detailed study of the

growth process in the high density system is required before we can take these ideas any further. The $P(Q)$ functions may also be subject to statistical fluctuations given the small number of separate clusters especially at later times.

Our conclusions must remain then largely qualitative. There is no doubt that the effects of the finite bond energy on the structure of aggregates are substantial, and are well demonstrated by the scattering functions. Our results are consistent with a restructuring of clusters on a growing length scale, indicating that the important variable for determining the evolution of the cluster structure is the rate of restructuring relative to the rate of growth. Thus at low bond energies and low densities, restructuring 'keeps pace' with growth and the growing aggregates are compact; at higher densities and bond energies growth is faster while restructuring is slower, producing clusters partly fractal, partly compact. Ultimately at high enough energy or high enough system density, the fractal growth is fast enough that the part-fractal clusters fill space to form a gel, as in the irreversible model[4]. Further growth is then frustrated, while restructuring continues; presumably eventually this gel will restructure enough to break up back into separate clusters, leading in turn to the sort of collapse of gels observed in some experiments [11, 16].

Our results appear to be in contradiction to Brownian dynamics (BD) simulations of reversible aggregation [108, 110] in which *increase* in the interparticle potential 'depth' leads to more compact aggregates (as measured—actually for rather small aggregates with masses $\leq$ 30 particles—via the mass-radius fractal dimension). Probably the most likely cause of this disagreement is the 'flexibility' of bonding in the BD model and the non-zero range of the interparticle potential. More detailed structural studies of the BD model would be useful. The 'rigid bond' DLCA model gives results more consistent with certain experimental systems [16, 155], suggesting that in these systems the dominant restructuring 'event' is the thermal breaking of bonds rather than thermal 'flexing'. In any event direct observation of the experimental systems would help to identify the relative importance of these processes.

[4] See Ref. [89] for a discussion of the possible influence of cluster surface dimension on gelation.

4.6 Cluster arrangement

We go on to study the effect of the finite bond energy E on the *arrangement of aggregates* in the reversible aggregating system. We calculate the *structure factor of the centres of mass* of aggregates, $S_{CM}(Q)$, in the same way as for the irreversible simulations in Chapter 3. Results are shown in Figures 4.25 and 4.26.

4.6.1 Size-position correlation and $S_{CM}(Q)$

The form of $S_{CM}(Q)$ is generally similar to that for the irreversible simulations. At large Q, $S_{CM}(Q) \approx 1.0$, showing no strong oscillations and no peak, indicating that there is no significant ordering of cluster positions even in high density systems. Below some time-dependent value of Q, $Q = Q_s$, $S_{CM}(Q)$ falls. Similarly to the simple hard sphere system, this can be interpreted as being due to the exclusion of cluster centres by the 'steric' interaction of the clusters[5]. This does not just mean that a given pair of clusters cannot approach each other closely; because they have other neighbours all around them, they also cannot easily get much further away from each other ! A cluster is *confined* by its neighbours.

However at the smallest Q values, as for the irreversible simulations (especially at high density), $S_{CM}(Q)$ begins to *rise* again. In fact the rise in $S_{CM}(Q)$ as $Q \to 2\pi/L$ for the reversible simulations is rather more marked than for irreversible DLCA. We have already discussed this effect to some extent in Chapter 3. To understand the rise at small Q, it is helpful to look directly at the spatial distribution of the cluster centres of mass. In Figures 4.27, 4.28 and 4.29 we plot points at each centre of mass position in the $\rho = 0.3$ 2D system at different bond energies and compare the structure of the set of points as the aggregation proceeds. In the plots one observes both *holes* in the distribution of cluster centres, and a tendency for *grouping* of centres. As $S_{CM}(Q)$ shows, the distribution is clearly not completely random, nor is it that of a simple hard-sphere fluid. The holes appear at the positions of large clusters of particles;

[5] Or the steric interaction of the cluster-plus-depletion zone 'object'; as pointed out by Cahn [66], when particles are attracted to each other into high density regions they can also be thought of as being 'repelled' from areas of low density, i.e. repelled by depletion zones.

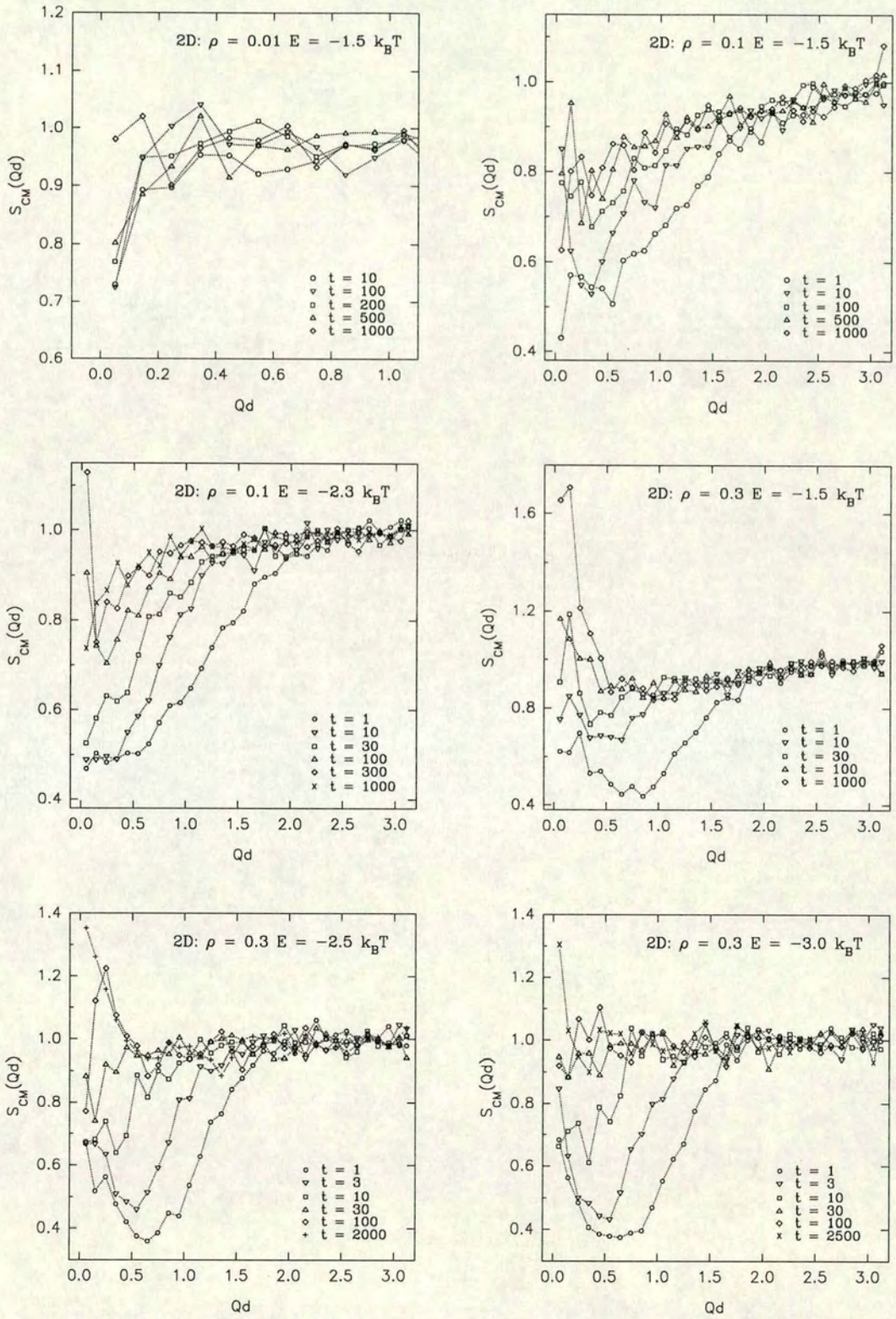

Figure 4.25. Cluster centre-of-mass position structure factors for reversible DLCA simulations in 2D.

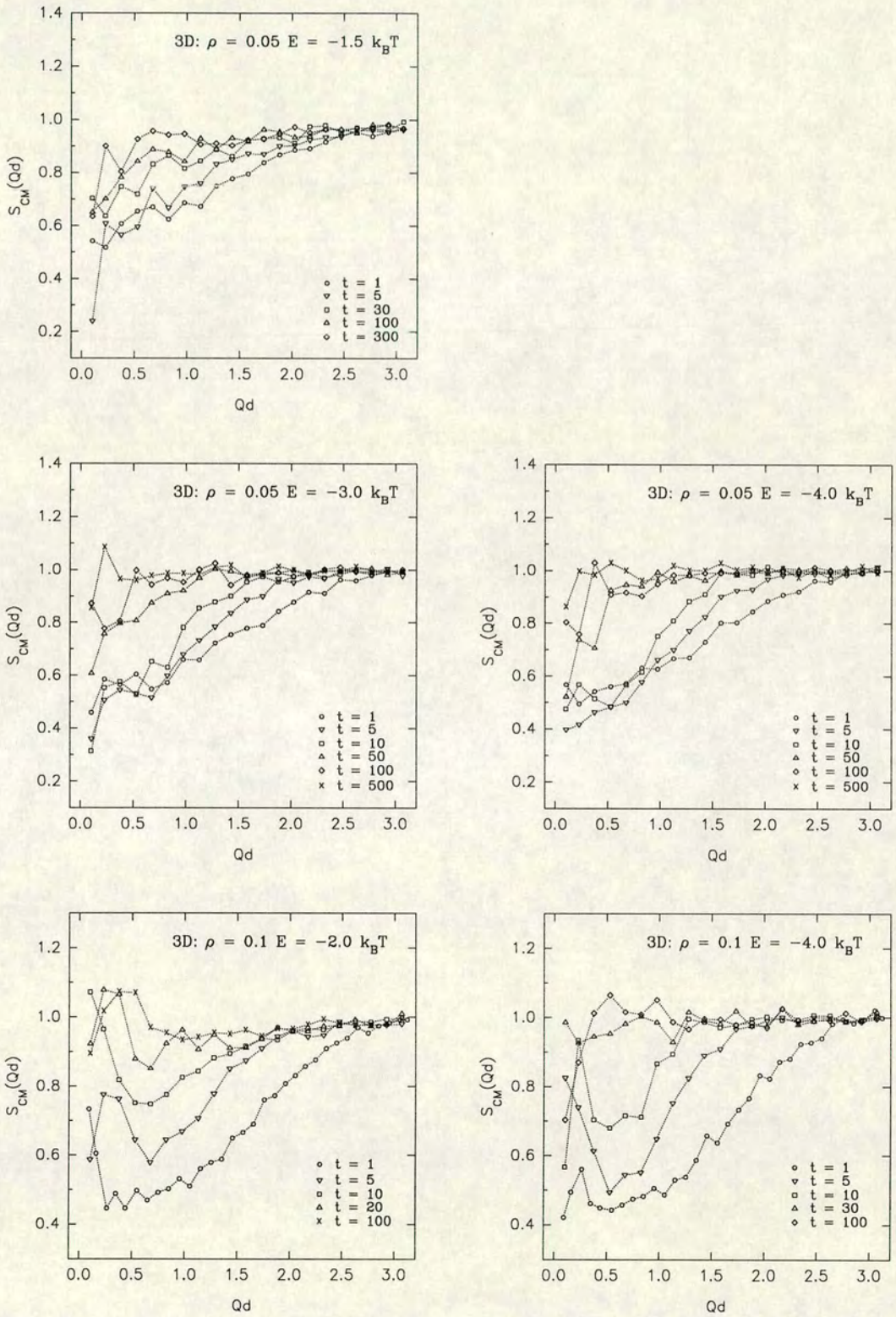

Figure 4.26. Cluster centre-of-mass position structure factors for reversible DLCA simulations in 3D.

centres grouped quite closely must be those of small clusters and monomers. *Thus the cluster polydispersity is important in determining the cluster arrangement.* Small clusters tend to be grouped together in the spaces between the large clusters. In both the reversible (Figures 4.27 and 4.28) and irreversible (Figure 4.29) models there is therefore a *correlation between cluster size and position.*

This is consistent with our findings in Chapter 3 where the separation of the scattering function into structure factor and form factor failed. It is clear that a correlation between particle size and position will lead to the failure of the separation of scattering, because in equation (3.1) in Chapter 3, the particle scattering amplitude $b_j \times b_i$ is now correlated with the separation $\mathbf{r}_j - \mathbf{r}_i$. In some previous attempts made by various authors to take account of polydispersity in experimental scattering measurements [132, 133], it has been assumed that particle size and position are not correlated. But for polydisperse systems with significant (short range) steric interactions (e.g. the simple hard sphere system) a size-position correlation is expected [2, 133].

The generation of a size-position correlation in the polydisperse system of clusters is strightforward to understand. Large clusters cannot get close to each other, nor can they penetrate small spaces between other clusters. Small clusters on the other hand can clearly move into the smaller spaces between large clusters. Hence the development of groups and 'channels' of small-cluster centres around and between the holes created by the large clusters.

To understand the form of $S_{CM}(Q)$ at small Q we must consider the association or grouping of the positions of the small clusters. How does such a grouping of positions affect the scattering function ? We can compare for example with the *adhesive hard sphere* model. In this model the interparticle potential is infinitely short-ranged but defined such that its depth remains finite; particles which behave otherwise as hard spheres tend to stick to each other with some 'stickiness' when they approach very closely. Baxter [163] first developed an approximation for the structure factor (of the centres of mass) $S_{SHS}(Q)$ of such a system of monodisperse sticky hard spheres, based on the Percus-Yevick approximation. Kranendonk and Frenkel [164] compare Baxter's approximation with Monte Carlo simulations. The important result for us is that

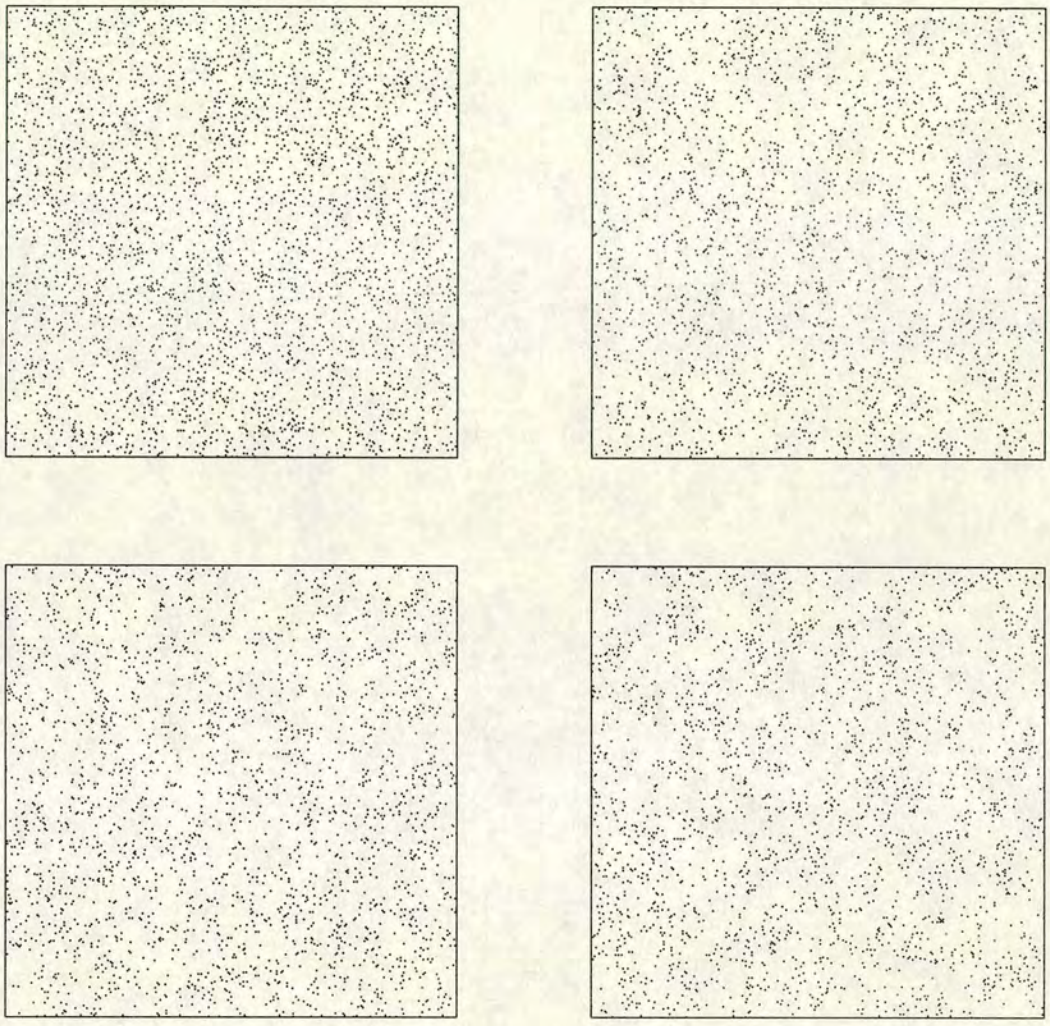

Figure 4.27. The spatial distribution of the centres of clusters, in a 2D reversible DLCA simulation with system size $L = 300$, number density $\rho = 0.3$ and bond energy $E = -1.5k_BT$. A single point is plotted at each centre of mass position. Times shown are $t = 10$, $t = 100$, $t = 500$ and $t = 2000$ simulation steps.

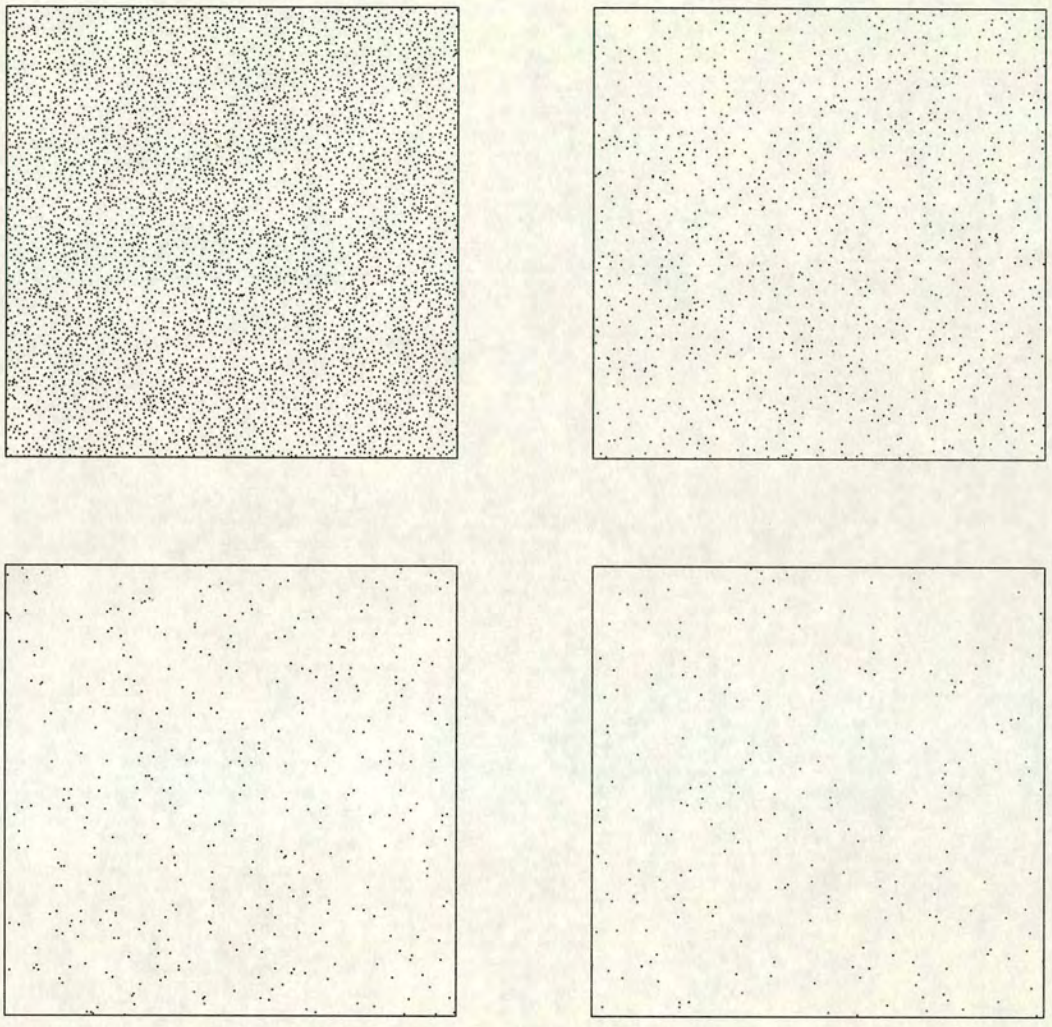

Figure 4.28. The spatial distribution of the centres of clusters in 2D reversible DLCA simulation, with system size $L = 300$, number density $\rho = 0.3$ and bond energy $E = -3.0k_BT$. Times shown are $t = 1$, $t = 10$, $t = 100$ and $t = 10000$ simulation steps.

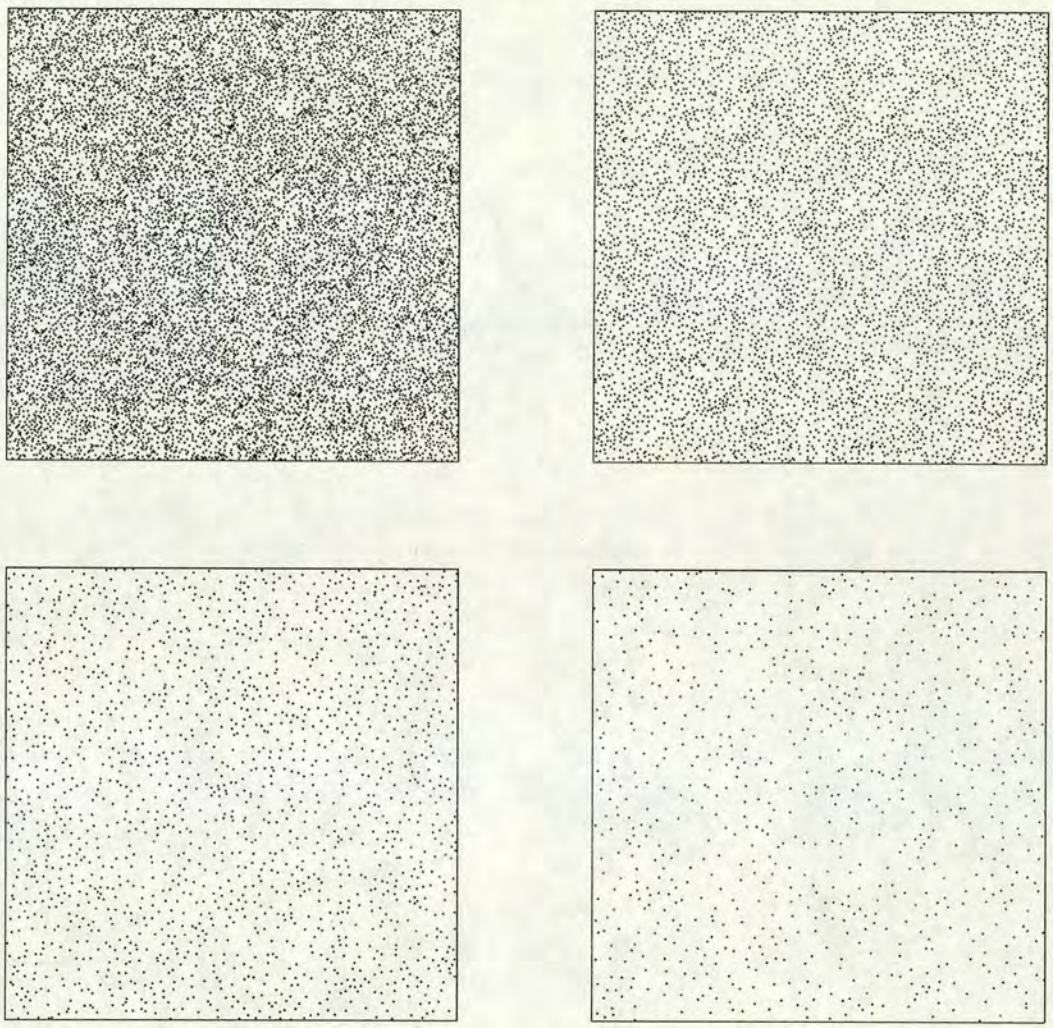

Figure 4.29. The spatial distribution of the centres of clusters, in a 2D *irreversible* DLCA simulation with system size $L = 300$ and number density $\rho = 0.3$. A single point is plotted at each centre of mass position. Times shown are $t = 0$, $t = 1$, $t = 5$ and $t = 10$ simulation steps.

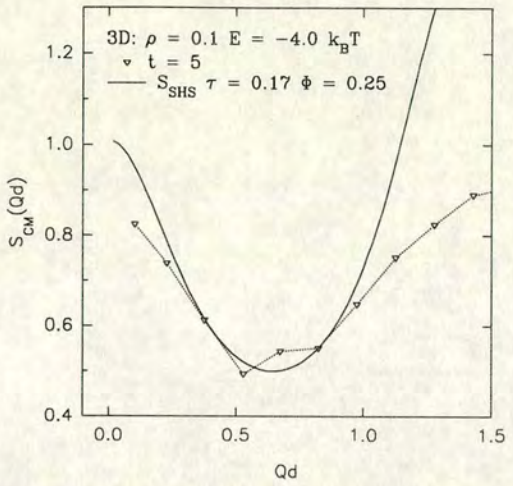

Figure 4.30. Comparison of S_{CM} with the form of the structure factor from the sticky hard sphere model, $S_{SHS}(Q)$. S_{CM} is from a 3D simulation. The stickiness parameter τ and the volume fraction parameter Φ in the sticky hard sphere model are selected for the best comparison with S_{CM}.

$S_{SHS}(Q)$ develops a peak for $Q \to 0$ as the particles become sticky. In other words, 'associating' particles generate a structure factor peaked at $Q \to 0$. In the DLCA cluster centre of mass distribution we have seen that there is a clear association of the centres of small clusters, due to the interaction of the steric (cluster shape) constraints and the polydispersity. In Figure 4.30 we compare an example $S_{CM}(Q)$ curve from a 3D simulation with the form of $S_{SHS}(Q)$. (In the plot we select the sticky hard sphere model parameters τ–stickiness–and volume fraction which give best comparison with the example $S_{CM}(Q)$.) While we make no proper quantitative comparison nor draw any direct link between the systems, the similarity of the effect on the structure factor is clear. Therefore it seems reasonable to explain the observed rise in $S_{CM}(Q)$ as due to this grouping of the positions of small clusters. The centre of mass plots demonstrate that the grouping effect is also more significant in the reversible model, consistent with the S_{CM} results. In the next subsection we demonstrate that when the effect of the small clusters is reduced, the structure factor is changed quite substantially, and the rise at small Q is no longer observed.

Mass-weighted structure factor

The above interpretation of the cause of the small-Q rise in $S_{CM}(Q)$ is supported

by calculation of the *mass-weighted* centre of mass structure factor, $S_{MW}(Q)$. Once again this same quantity has already been calculated and discussed for the irreversible DLCA simulations (Chapter 3). The expression for $S_{MW}(Q)$ is reproduced here for convenience:

$$S_{MW}(\mathbf{Q},t) = \left| \sum_{k}^{N_c} M_k exp(i\mathbf{Q}.\mathbf{r}_{ck}) \right|^2 / \sum_{k}^{N_c} M_k^2 \qquad (4.12)$$

N_c is the number of clusters in the system at time t, M_k is the mass of cluster k. Results for the reversible model are shown in Figures 4.31 and 4.32.

Small clusters are strongly underweighted in $S_{MW}(Q)$ compared to the large clusters, so that mass-weighting the calculation of the cluster structure factor tends to remove the effects of the presence of small clusters and monomers. $S_{MW}(Q)$ does not dip and rise at small Q, supporting the idea that it is the grouped structure of the small clusters which leads to the rise in the centre of mass structure factor at small Q.

The form of $S_{MW}(Q)$ at large Q, where the function is very flat, indicates that there is no significant ordering in the positions of the large clusters in the system. This is consistent with the results from the irreversible simulations.

Interestingly, an identical mass-weighting of the structure factor has been employed recently by Sciortino and co-workers in their theoretical and simulation analysis of (irreversible) cluster aggregation [67, 69]. The authors state that this is an attempt to counter the effects of polydispersity, though no further details are given. There is no doubt from our analysis that 'removing' small clusters by underweighting will tend to lessen the structural effects of size-position correlation.

4.7 Scaling of the scattering function

In Chapter 3 the *scaling hypothesis* concerning the time-independent form of the scattering functions for the aggregating system was discussed and investigated for the irreversible simulations. In this section we examine the scaling properties of the scattering functions from the reversible DLCA simulations. This leads us to a more detailed picture of the evolution of the system structure and of the validity of the scaling hypothesis

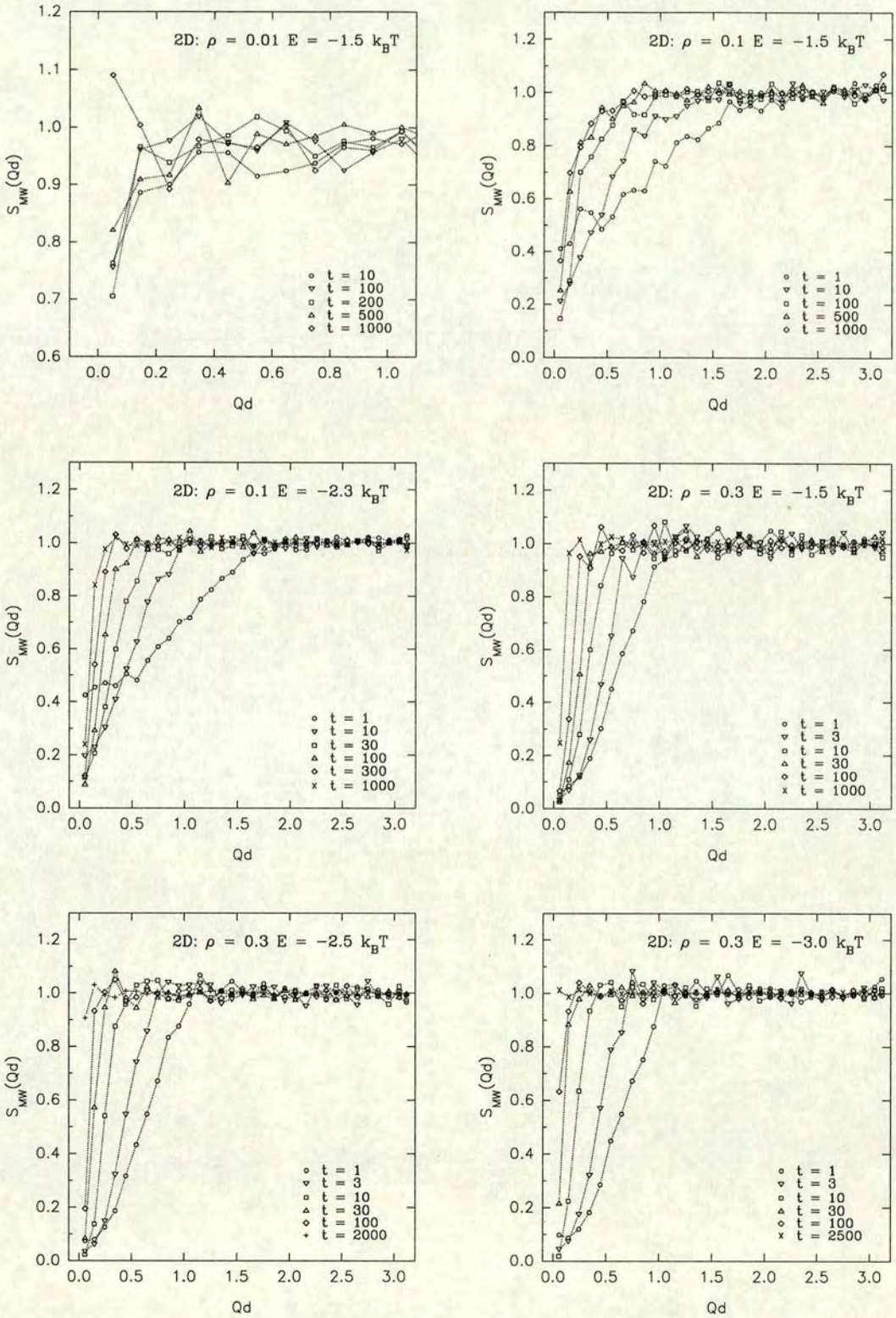

Figure 4.31. Mass-weighted cluster centre-of-mass position structure factors for reversible DLCA simulations in 2D.

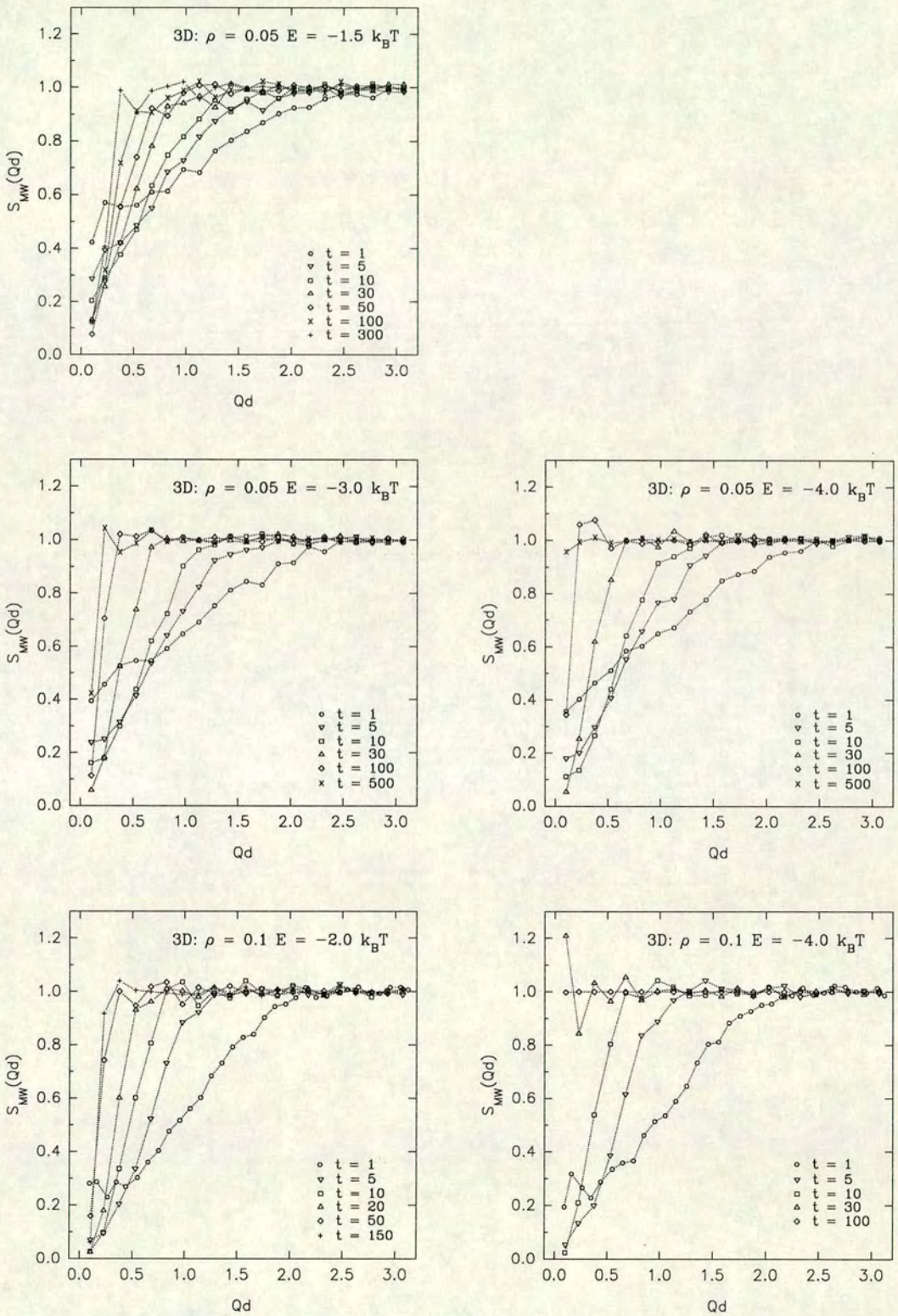

Figure 4.32. Mass-weighted cluster centre-of-mass position structure factors for reversible DLCA simulations in 3D.

itself.

4.7.1 Scaling exponent and bond energy

Figures 4.33 to 4.37 show the 'best' collapse of the $I(Q)$ data from 2D and 3D simulations, when scaled according to equation (4.13):

$$I(Q/Q_m, t) \sim Q_m^{-\gamma}(t) F(Q/Q_m). \tag{4.13}$$

Because cluster structure in the reversible DLCA simulations depends on the bond strength E, rather than trying to scale the scattering functions with the exponent $\gamma = d_{f,DLCA}$, we select the 'best' scaling collapse (by eye) by varying the exponent γ. The time-independent scaling hypothesis (see Chapter 3) predicts that $F(Q/Q_m)$ is a time-independent function. As with the irreversible model, scaling does not usually work very well for the early time data. *Approximate* scaling is found for later times, though in many cases the collapse is not very good, and does not extend very far about the peak at $Q/Q_m = 1$. In particular scaling does not hold very well for $Q << Q_m$ as demonstrated by the log-log plots. Furthermore, *the 'best' effective scaling exponent γ depends on the bond energy.* At low bond energy (e.g. 2D, $E = -2.3k_BT$ and $E = -1.5k_BT$ at number densities $\rho = 0.1$ and $\rho = 0.3$ respectively) the best scaling is obtained with a high value of γ; we find for the lower density $\gamma \approx D$, the space dimension, and $\gamma = 1.8$ for $\rho = 0.3$. (It should be noted that because the scaling collapse is not always very good, the effective 'error bars' on these γ estimates are probably at least ± 0.1–± 0.2. Given the compactification of clusters due to the finite, low bond energy, we expect a higher scaling exponent. (Compare the irreversible model for $\rho = 0.1$ in 2D where we find $\gamma = 1.47 \approx d_{f,DLCA}$.) However it is clearly not a simple case, especially at higher number density, of the two alternatives, either 'compact' scaling ($\gamma = D$) or fractal scaling ($\gamma = d_{f,DLCA}$). Rather there seems to be a continuous range of possible scaling exponents. This again might be expected given that, as discussed above, we find a continuous range of different morphologies in the reversible system, and not just a compact morphology at low bond energy and an

irreversible DLCA fractal morphology at high bond energy.

At low density then the scaling exponent reaches a minimum at high bond energy of the irreversible DLCA fractal dimension. But at high density we once again observe that the 'best' scaling exponent approaches not $\gamma = d_{f,DLCA}$ at high bond energy, but rather decreases all the way to $\gamma \approx 1.0$. For $\rho = 0.3$ in 2D, with $E = -1.5k_BT$ we find $\gamma = 1.8 \approx D$, the space dimension. As bond strength increases γ decreases, but does not 'stick' at $d_{f,DLCA}$; we find $\gamma = 1.2$ for $E = -3.0k_BT$ and, at still higher bond energy, $\gamma = 1.0$ for $E = -4.0k_BT$ (compare $\gamma = 1.0$ for the irreversible model). So at the high density it seems there is a complete range of scaling exponents from $\gamma = 1.0$ to $\gamma \simeq 2.0$ in 2D.

4.7.2 Scaling with $\gamma = 1.0$, 'time-dependent scaling'

As already noted for the irreversible model, at *early times* in all densities good scaling is obtained with exponent $\gamma = 1.0$, especially in 2D. Figure 4.38 demonstrates this for the 2D reversible system at $\rho = 0.3$, for various bond energies. It is clear that the $\gamma = 1.0$ scaling fails at later times, and the failure is worse for the lower bond energies. This is consistent with the picture developed for the irreversible model: at early time near-linear (unbranched) objects first form; at low density and/or low bond energy, these objects grow into branched or compact clusters, thus the effective scaling exponent rises; but at high density/high bond energy, the near-linear unbranched structure in the system is 'frozen in' by the onset of space-filling or gelation, so that the early-time scaling exponent $\gamma \approx 1.0$ is retained. At lower density, or at lower bond energies at high density, *where clusters do not grow large, ramified and fast enough to fill space*, the system can 'escape' the early-time $\gamma \approx 1.0$ scaling region. Thus at the highest bond energy and density in 2D, the $\gamma = 1.0$ scaling works until close to gelation; at the lowest energy, the scaling fails completely as the more compact clusters develop, and the scaling exponent becomes at later time $\gamma = 1.8$.

This time-dependence of γ of course strictly means that the *time independent* scaling

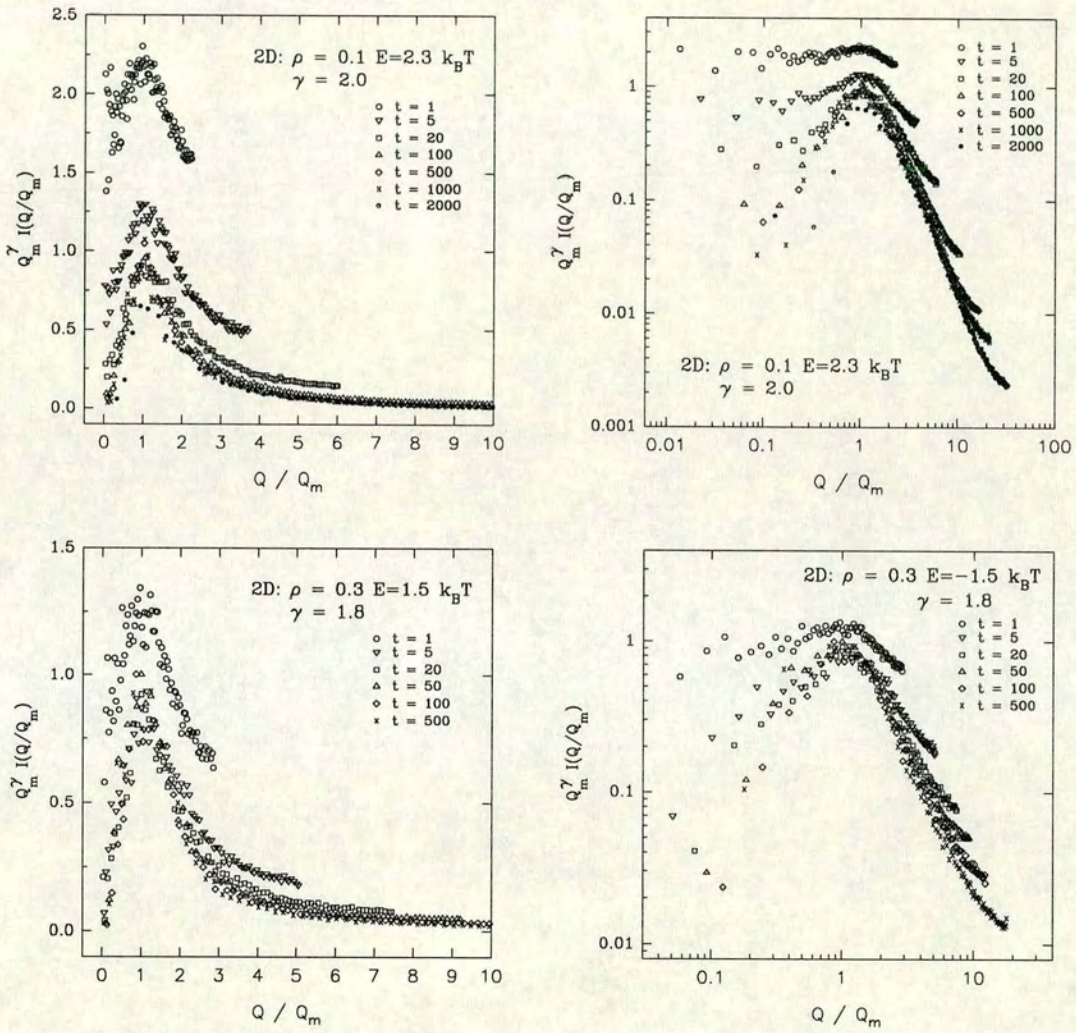

Figure 4.33. 'Best' scaling of scattering functions from 2D reversible DLCA at low bond energies, $E = -2.3k_BT$ (number density $\rho = 0.1$) and $E = -1.5k_BT$ ($\rho = 0.3$).

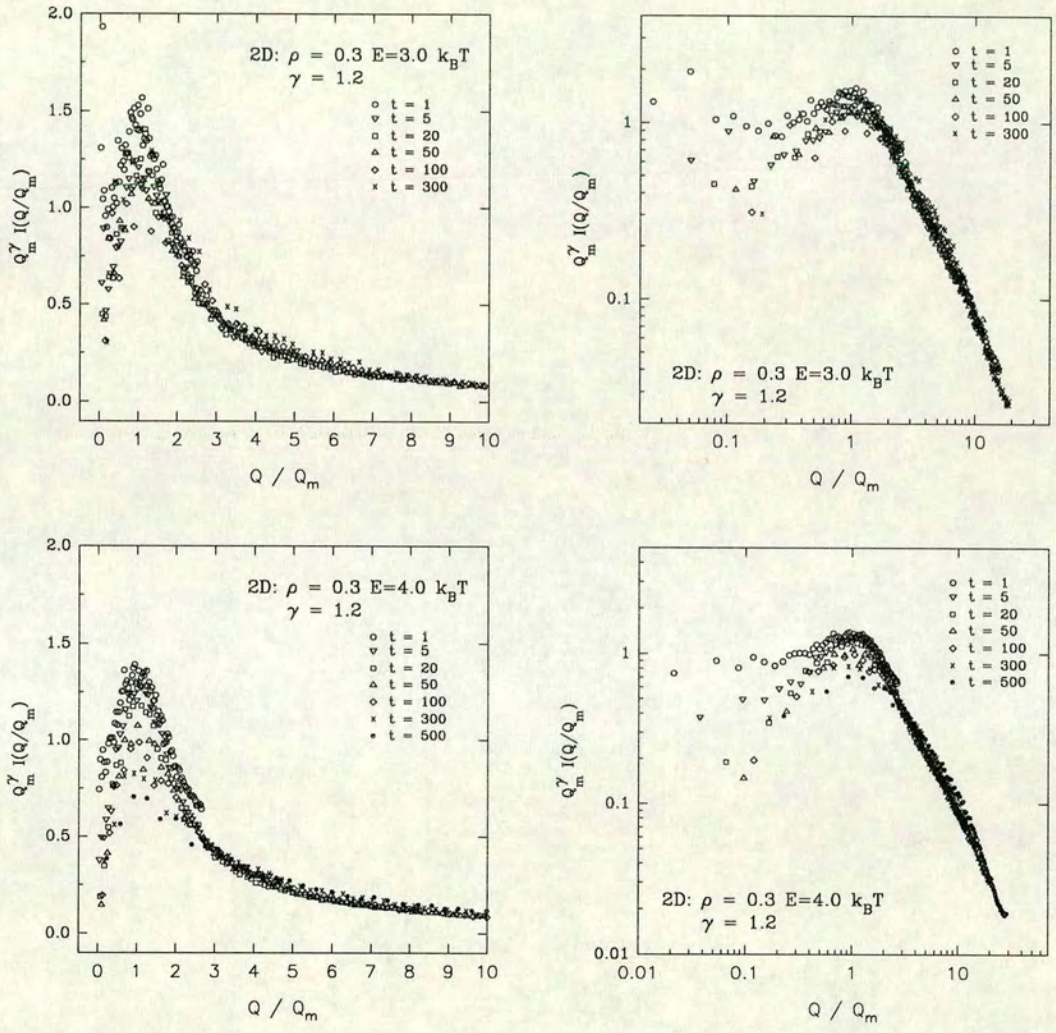

Figure 4.34. 'Best' scaling of scattering functions from 2D reversible DLCA at high number density ($\rho = 0.3$) and high bond energies.

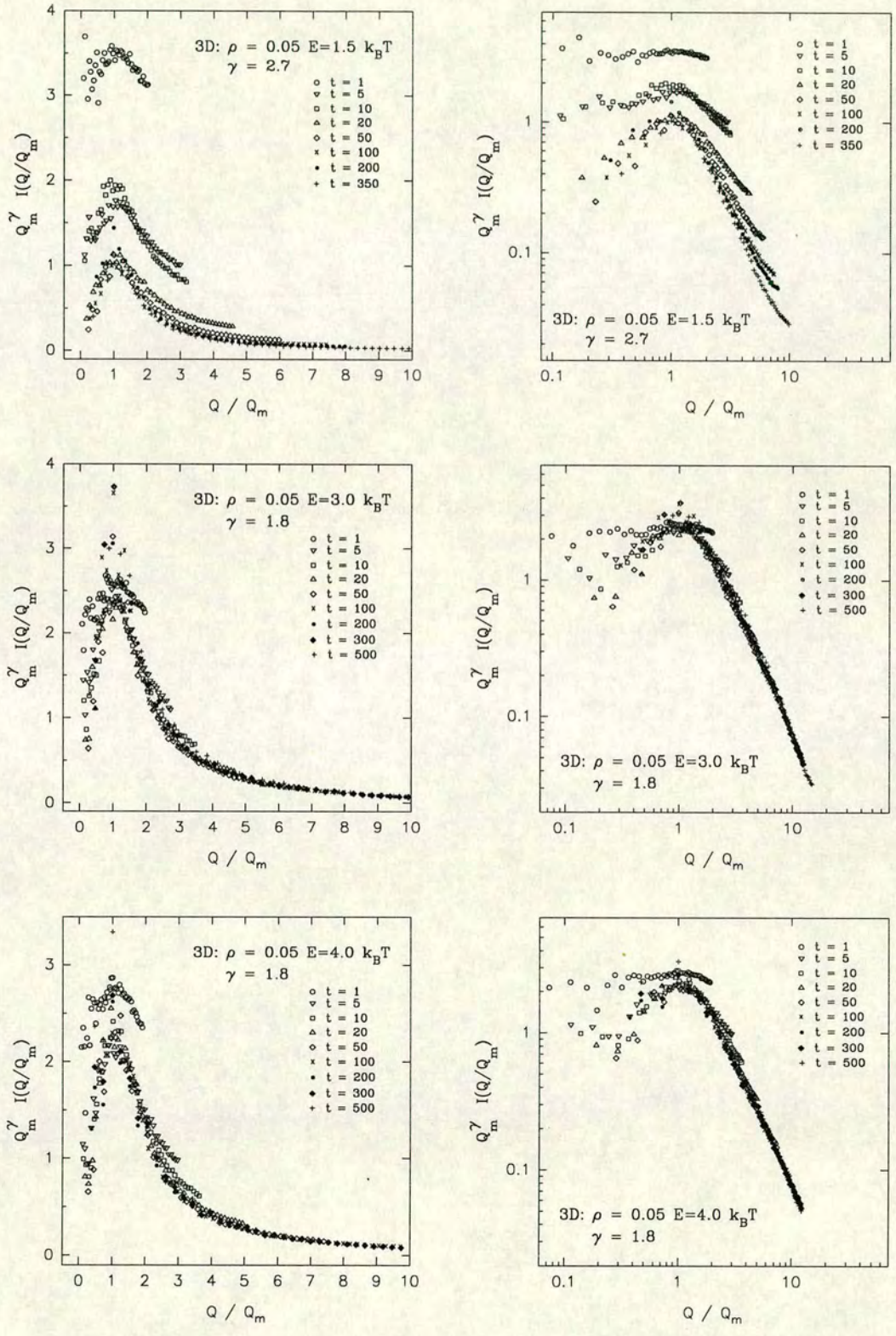

Figure 4.35. Scaling of scattering functions from 3D reversible DLCA at number density $\rho = 0.05$.

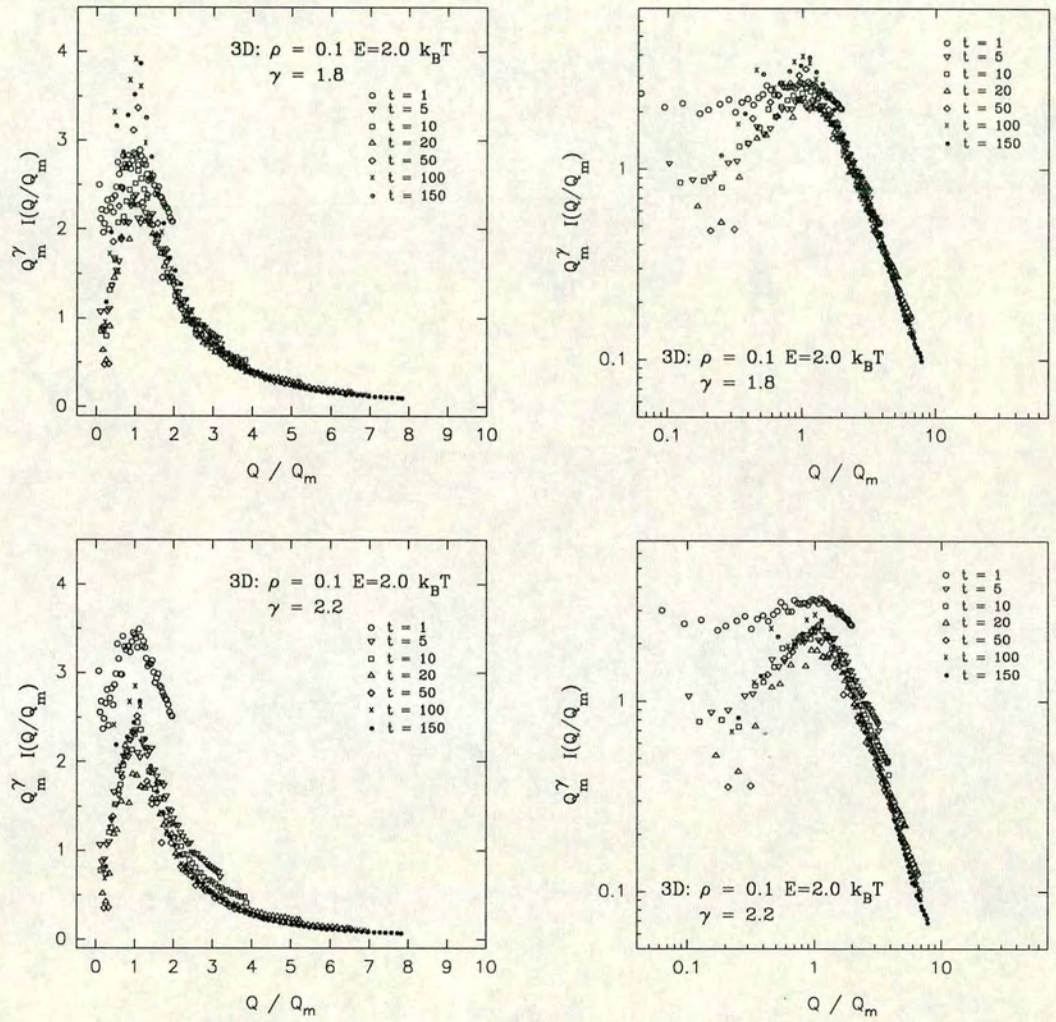

Figure 4.36. Scaling of scattering functions from 3D reversible DLCA at high number density ($\rho = 0.1$) and bond energy $E = -2.0k_BT$. Two scaling exponents are shown, $\gamma = 1.8$ and $\gamma = 2.2$. At early times the data scale better with $\gamma = 1.8$, at late times with $\gamma = 2.2$, indicating a possible time-dependence of the scaling exponent.

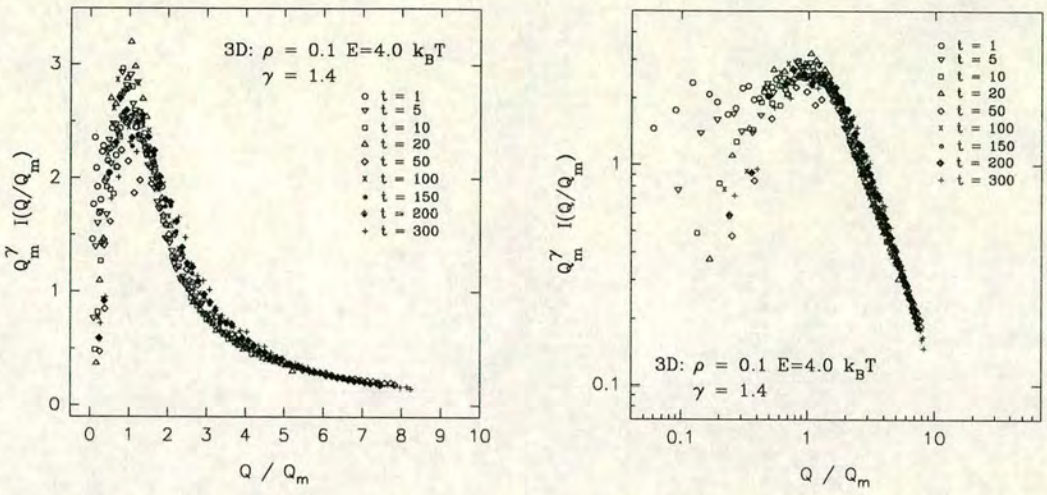

Figure 4.37. Scaling of scattering functions from 3D reversible DLCA at high number density ($\rho = 0.1$) and bond energy $E = -4.0k_BT$. At higher bond energy the 'best' exponent remains low, compare with Figure 4.36.

hypothesis is violated. Indeed, it is possible that, as the clusters in the system compactify (assuming space-filling doesn't occur to interfere with the growth), γ will make a continuous transition from $\gamma \approx 1.0$ to $\gamma \to D$, the space dimension. For instance in 3D at $\rho = 0.1, E = -2.0k_BT$ (Figure 4.36) we find that the best scaling is found with $\gamma = 1.8 \simeq d_{f,DLCA}$ at early times, but later the data scale better with $\gamma = 2.2$. Since it is not clear what such a time-dependent 'scaling exponent' means, we have not investigated the possible time-dependence of γ any further in this work. Similar experimental investigations of restructuring systems with weak potentials would be of great interest. It is worth noting that a similar time-dependent γ (or early-time $\gamma \approx 1.0$ scaling) was *not* reported in colloid-polymer experiments [16] and to our knowledge has not been observed in other experiments, though in all experiments [45, 52] and other simulations of aggregating colloidal systems [65, 81], an early-time 'non-scaling' region *is* found. Whether using $\gamma \approx 1.0$ would scale these early-time 'non-scaling' data is not known. In experiments it may be that it is not possible to observe the system early enough after the onset of aggregation to see an early $\gamma = 1.0$ region. In experimental systems other effects such as gravity may become more important at weaker bond energies.

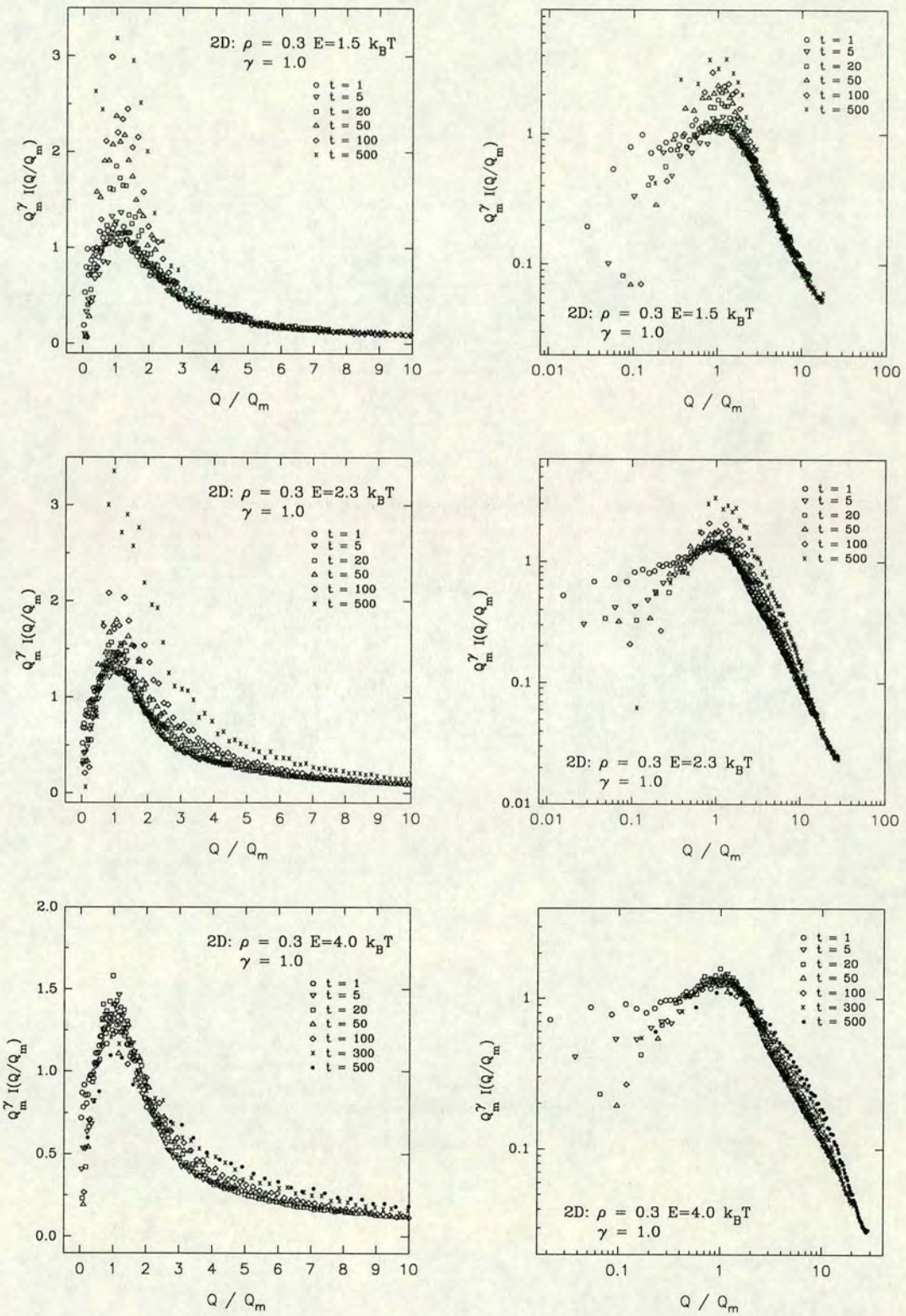

Figure 4.38. Scaled scattering functions from 2D reversible DLCA at number density $\rho = 0.3$, with scaling exponent $\gamma = 1.0$. The right-hand column shows log-log plots of the same scaled data to show more clearly the scaling at small Q/Q_m.

4.7.3 Scaling of $I(Q)$—Conclusions

In this subsection we summarise the findings of the previous subsections. First it should be stated that all 'scaling' observed in the scattering functions is at best *approximate*. The scaling plots in the log-log representation indicate that at small Q or large lengths the scaling breaks down somewhat. The simple picture of the aggregating system as composed of growing objects with dimension $d < D$, the space dimension, implies that scaling should not hold; the cluster size and the depletion zone radius (equivalent to $2\pi/Q_m$) should scale differently in time (see Chapter 1). More complex modelling [67, 69] leads to the same conclusion. Sciortino and co-workers [69] make a strong case for scaling to be simply 'apparent' rather than theoretically justified, in the case of fractal aggregation. On the other hand, the data presented here and simulation and experimental results in the literature [16, 45, 51, 64, 65, 81, 117] do show an often rather convincing data collapse, albeit usually in a limited time regime.

There is a *low* effective scaling exponent at early time. In 2D the data show that this early exponent, $\gamma_e \approx 1.0$. In 3D the data are not so conclusive but a low early-time exponent is still indicated. Our picture is that at early time the first objects to grow are near-linear or unbranched 'prefractal' clusters, which tend to have a scattering function $I(Q) \sim Q^{-1}$ like a rod (see Chapter 3).

As aggregation continues, these small unbranched structures themselves begin to aggregate, forming branched structures. In irreversible-bonding low density systems the growing structures branch out eventually to form classical DLCA fractal clusters, with well determined, 'universal' fractal dimensions. The late-time effective scaling exponent then matches the 'universal' DLCA fractal dimension, $\gamma_l \approx d_f \approx 1.45$ (in 2D) or ≈ 1.8 (in 3D). This is the 'fractal scaling regime' as seen in experiments and other simulations [16, 45, 52, 65, 81, 117].

But this transition to the DLCA fractal scaling regime requires that there is enough space for significant branching to occur. At high density and high bond energy this is not the case. Space is jammed up and filled very quickly by the small structures,

before the significantly branched DLCA-type fractal clusters can appear. The early-time structure is frozen into the system, and the late-time effective scaling exponent is held low near $\gamma_l \equiv \gamma_e \approx 1.0$.

The addition of reversibility in the aggregation allows the clusters to simultaneously grow and change their structure, compactifying into more stable structures. In the scaling behaviour of $I(Q)$ this manifests itself as follows. At low bond energies (and low enough densities) near-compact clusters form—compactification takes place on a time scale comparable to that of growth, and stable DLCA-like fractal clusters do not form. In the limit of fast compactification (compared to growth) we recover a coarsening droplet scenario similar to that found in spinodal decomposition, and, as found in that system, the effective scaling exponent $\gamma \approx D$, the space dimension.

At higher bond energy restructuring is slowed relative to growth. Clusters are internally near-compact but can have very ramified surfaces. The validity of the time-independent scaling hypothesis comes under stronger pressure, because now we have structures which are changing in different ways at different length scales. Compactification dominates at short length scales, but growth still dominates at large scales where quite ramified clusters are still colliding and connecting. The scaling analysis of $I(Q)$ indicates that in a certain time regime we can identify a reasonably time-independent form for $F(Q/Q_m)$, with an effective exponent γ which is somewhere between the space dimension and $d_{f,DLCA}$. However there are also indications especially from 3D data that as the aggregation proceeds the 'best' scaling is obtained with an increasing exponent γ. In other words the time-dependent parameter Q_m alone is no longer enough to characterise the scattering function, we also now have a time-dependent scaling exponent $\gamma(t)$.

At high density and higher bond energy, the situation approaches the irreversible model, where the effective scaling exponent is always *lower* than $d_{f,DLCA}$. Because of the limited space available for growth, the fully-branched fractals of the low-density irreversible model cannot form. As bond strength increases the scaling exponent decreases (c.f. $\gamma = 1.2$ for $\rho = 0.3, E = -3.0k_BT$ and $\gamma = 1.0$ for $E = -4.0k_BT$ and for the irreversible model). Presumably stronger bonding reduces the amount of compactification

of small clusters such that the early-time structures have less and less room to branch before space is filled.

When weak, reversible bonding is introduced into the aggregation model, the *effective scaling exponent* is no longer a single well-defined 'universal' number, but is rather a function of the bond energy E and the system density ρ. With the two variables density ρ and bond energy E we obtain a near-continuous range of possible scaling exponents. Furthermore there are indications, though the analyses here are far from exhaustive, that the scaling exponent γ may also be time-dependent. This does not necessarily mean that the scaling function $F(Q/Q_m)$ becomes time-dependent; rather one now has two time-dependent 'characteristic measures', $Q_m(t)$ and $\gamma(t)$. Exactly what form the time-dependence of γ may take, and further how it depends on ρ and E, remain unclear. Further simulations and experiments may provide substantially more information, but it remains the case that no clear theoretical understanding of the scaling of the scattering function in fractal aggregation yet exists. The examination of the transition from the irreversible fractal system to the compact spinodal-like system may be a useful direction for study in the future.

4.8 Structure of reversible DLCA–Conclusions

In this Chapter it has been demonstrated that, with the addition of a finite interparticle bond energy the DLCA model becomes a much more general kinetic model of growth phenomena. It seems that the model can generate familiar growth modes such as 'unstable' spontaneous compact growth (spinodal decomposition), and also demonstrates fractal growth and frustration of growth due to space-filling or gelation. These phenomena are observed in a very wide range of experimental systems (sometimes [16] all in the same system), from simple fluids and alloys through colloidal systems to phase-separating mixtures of polymers [53]. Thus one would expect that a general model should exhibit these features, that they are not qualitatively dependent upon specific system details.

The extension of the 'standard' DLCA model to reversible DLCA also provides a clearer

understanding of the kinetic and scaling properties of the standard model. It appears that there is a more or less *continuous* change with bond energy in the 'scaling exponent' of the scattering functions. At high energies and low enough density the 'fractal scaling' of the scattering function is demonstrated, with a scaling exponent $\gamma \simeq d_f$, the fractal dimension of clusters as measured by the mass-radius relation. However at high density and high energy the early-time regime of 'linear structures', with a scaling exponent $\gamma \simeq 1.0$, cannot be escaped since space is quickly filled. As the bond energy is reduced the effective scaling exponent seems to increase continuously, until near-compact structures are formed with $\gamma \simeq D$, the space dimension. The approach to this low-energy limit is consistent then with the scaling of the scattering function observed in spinodal decomposition, where the system is occupied by growing, compact droplets.

The effects of polydispersity in generating a cluster size-cluster position correlation are enhanced with the reversible model, since there are generally more small clusters in the system at lower bond energies (see Chapter 5). Under steric constraints the small clusters tend to associate in the channels and spaces between the large clusters.

Previous studies of the effect of reversibility in the DLCA model have concentrated solely on estimation of the fractal dimension of individual clusters (from the mass-radius relation). It is clear from the analyses reported here that the morphology of the system depends on the energy in ways too complicated to describe solely with one parameter. And it is the morphology of the system on many length scales which determines its kinetic evolution as well as its behaviour. An interesting future direction would be to investigate the effect of the different system structures on the response of the system to external stress and fields, such as shear, oscillation, and gravity [165]-[169].

Chapter 5

Polydispersity, surface and length scales in DLCA

Abstract

We calculate the cluster radius polydispersity in the DLCA system and consider the effects of gelation and of finite bond energy. In the irreversible model we find a 'DLCA' regime during which the radius polydispersity of clusters is approximately constant, while near to gelation the polydispersity rises steeply. In high density systems the constant regime is very short or not present at all. Examination of the total cluster perimeter/ surface in the evolving system indicates that irreversible DLCA is characterised by a late-time fractal regime wherein total perimeter/surface is nearly constant; in the reversible model restructuring allows perimeter/surface to continue to decrease. A direct examination of various length scales in the DLCA system indicates that the 'cluster size' and 'cluster separation' do not scale in the same way with time throughout the aggregation, but that an extended intermediate-time regime of 'apparent' proportionality may be observed.

5.1 Cluster polydispersity in DLCA

On various occasions it has been assumed in the literature that the DLCA system is essentially *monodisperse*; that is all the clusters in the system at a given time have approximately the same size (see for example [26, 33, 49]). This idea has been used in various theoretical models in which the distribution of cluster sizes is replaced by a single dominant cluster size (e.g. [170]). However to our knowledge the size polydispersity of the clusters in the DLCA system has rarely been directly studied. Griffin and Griffin use predictions for the mass distribution and scattering of the DLCA system to examine the 'polydispersity index' of DLCA [171] (the results are compared with dynamic light scattering measurements, hence this particular measure of polydispersity); however their analysis assumes that the scattering of the DLCA system is given by the scattering of single clusters, and so is at best a very low density (no inter-cluster correlation) approximation. It is therefore of considerable interest to obtain results directly from simulation data.

5.1.1 Irreversible DLCA

We define the *radius polydispersity* $\sigma_R(t)$ of the clusters in the DLCA simulation system at time t by

$$\sigma_R(t) = \frac{\sqrt{\frac{1}{N_c(t)} \sum_i^{N_c(t)} [r_i - R_m(t)]^2}}{R_m(t)} \tag{5.1}$$

where r_i is the radius of gyration of cluster i, $N_c(t)$ is the number of clusters in the system at time t, and $R_m(t) = \sum_i^{N_c(t)} r_i / N_c(t)$ is the average radius of gyration. (Note that the exact calculated values of σ_R may be affected by the use of the 'arbitrary' radius of gyration for a monomer, $r_g = a$, the monomer radius. However, the effective r_g of a monomer is certainly not expected to be lower than the monomer radius a, and we do not expect the effects to be severe. It is unclear anyway what alternative prescription might be employed.)

The polydispersity $\sigma_R(t)$ is thus easily calculated from the DLCA simulation data. In some cases data are averaged over a small number of repeat runs of the simulation to

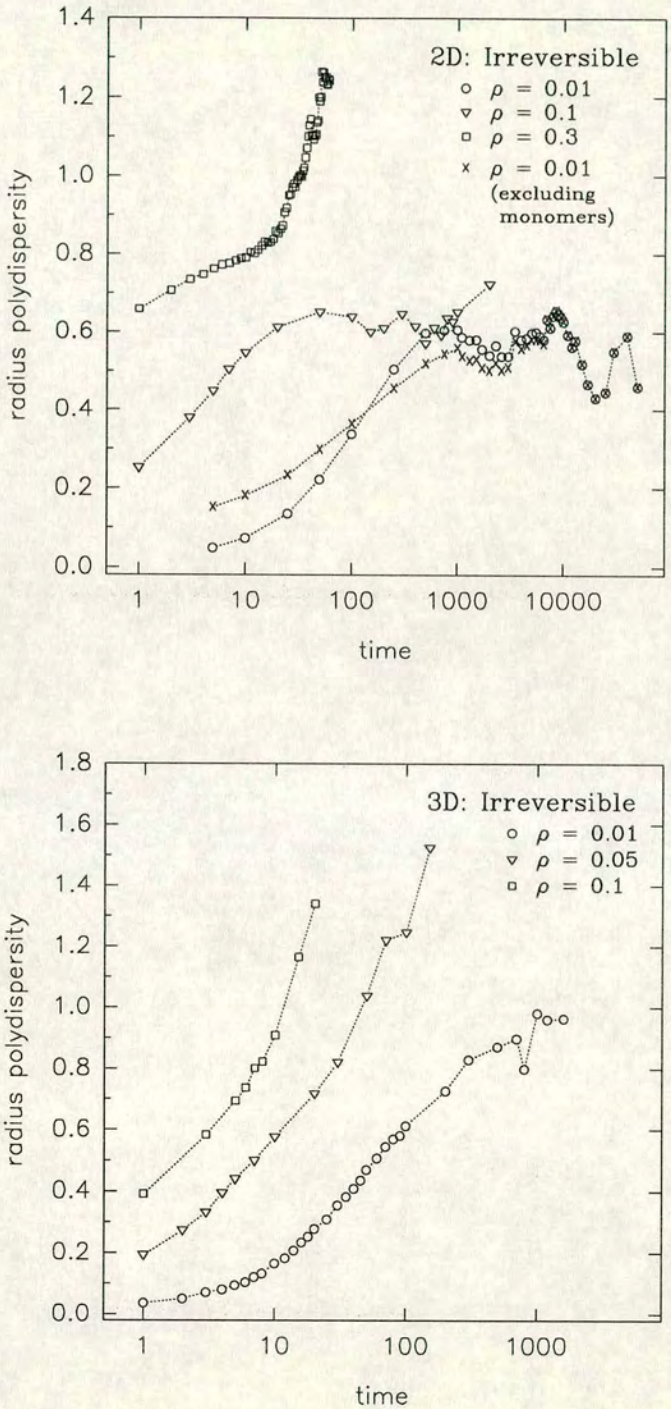

Figure 5.1. Time evolution of radius polydispersity in irreversible DLCA.

reduce statistical fluctuations. Results for various densities in 2D and 3D are shown in Figure 5.1.

The polydispersity curves demonstrate a number of interesting effects. Firstly, in an early-time period the radius polydispersity increases quickly; at $t \to 0$ we have a system of monodisperse monomers[1], so as growth starts clearly one expects an increase in σ_R. In the irreversible DLCA simulations in 2D at low and intermediate density the polydispersity does not simply continue to increase, however. At some intermediate time σ_R becomes nearly constant. (There are quite large fluctuations especially at late time as the number of clusters becomes small, but there is no *trend* in σ_R). So in an intermediate time period of the aggregation the polydispersity does not change. In terms of the *cluster mass distribution* this would imply that the shape and relative width of the distribution are more or less constant, which is consistent with the studies of the scaling of the mass distributions in Appendix A. The shape of the curves is also consistent with that derived by Griffin and Griffin [171] though it is not clear that the two measurements are exactly comparable; at least Griffin and Griffin find that the 'polydispersity index', after an initial steep rise, becomes more or less constant as the clusters grow.

At high density ($\rho = 0.3$ in 2D) an extended region of constant polydispersity is not observed. After going through a slight inflection the σ_R curve starts to rise again very steeply. This rise is probably caused by *gelation*. A very large cluster appears (the 'gel fraction') while there is still a significant number of smaller clusters in the system, so that the width of the radius distribution increases substantially. (Note that the steep rise begins well before the time at which a *system spanning* cluster appears, at which point the curves in Figure 5.1 stop. It is difficult to calculate the radius of the system-spanning cluster; if it percolates then its radius is nominally infinite anyway.)

Results from the 3D simulations are not so clear as those from the 2D systems, but may be interpreted in much the same way. At the lowest density ($\rho = 0.01$) we see the early rise in σ_R and the beginning of a curve into the 'DLCA' constant polydispersity region.

[1] Except that in the lattice model we always have some clusters at 'time zero'; how many depends on the number density.

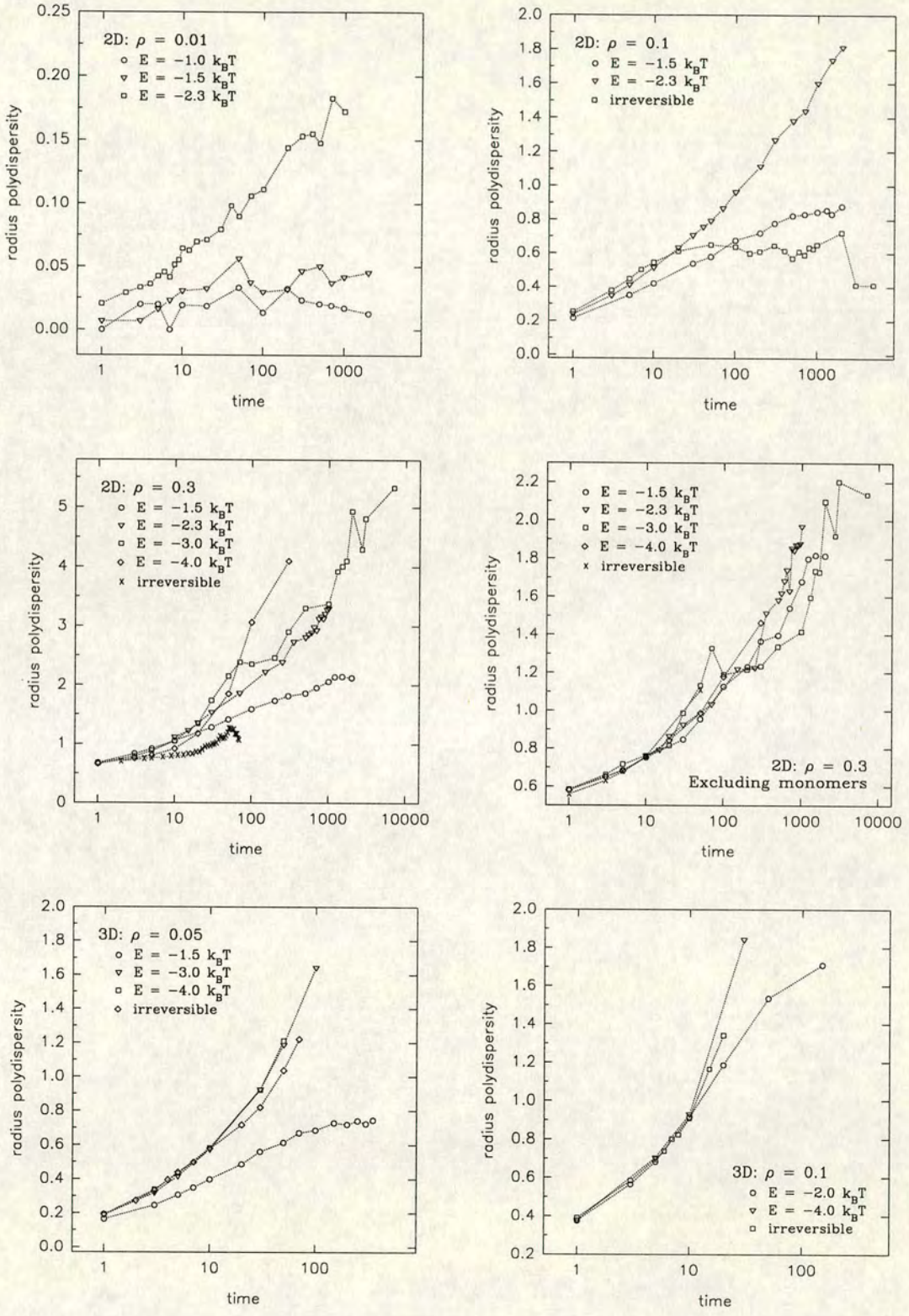

Figure 5.2. Time evolution of radius polydispersity in *reversible* DLCA at various bond energies E. For comparison some of the plots also contain the results from irreversible simulations (see Figure 5.1). Also shown for $\rho = 0.3$ in 2D (middle right plot) are the results when monomers are excluded from the polydispersity calculation.

Unfortunately due to the smaller system sizes in the 3D simulations a single spanning cluster appears in the low density system before a substantial region of constant σ_R can be observed. It is clear though that σ_R in this case does not rise steeply even though a system-spanning cluster is formed; in other words the polydispersity data can distinguish between the formation of a 'proper' gel and a single system-spanning fractal.

At $\rho = 0.05$ and $\rho = 0.1$ in 3D no region of constant polydispersity is observed, rather at these high densities we see σ_R rising steeply almost immediately the aggregation commences. Because of the small system sizes and the higher densities relative to the static percolation density ($\rho_p \approx 0.31$ in 3D, $\rho_p \approx 0.59$ in 2D on cubic/square lattices [77]) the effects of the initial clustering on the lattice are more significant in 3D; the 'effective start times' of the simulations are later in 3D than for the 2D simulations, therefore we are probably already 'too late' to see the inflection in the σ_R curve which is quite clear in the high density 2D results. Thus larger 3D simulations would be useful in order to further investigate the behaviour of σ_R, however the system sizes used here were once again at the limit of our computational capacity.

The polydispersity results from the irreversible model therefore provide another demonstration of the effect of system density ρ on the aggregation. The duration of the time regime in which polydispersity is constant is very sensitive to the system density. At high densities the constant-polydispersity regime is essentially not observed at all, consistent with the absence of a 'classical DLCA' scenario of well-separated clusters growing self-similarly; in high density space is already almost filled and gelation occurs very quickly.

5.1.2 Effect of reversibility

Figure 5.2 compares the time evolution of the radius polydispersity in reversible DLCA simulations at various bond energies E. For comparison some of the plots also repeat the results from the irreversible model. From the lower density simulations ($\rho = 0.1$ in 2D and $\rho = 0.05$ in 3D) we can see that the finite bond energy has two general

effects, much as was observed in the scattering analysis of Chapter 4. At low enough energy the initial rise in σ_R is slowed because large clusters do not grow so quickly with the lower bond energy. However, at later time the low-bond energy polydispersity can increase above the irreversible value. The $E = -1.5k_BT$ results for $\rho = 0.1$ in 2D imply that σ_R may be approaching a constant value similarly as in the irreversible DLCA; however this constant σ_R is higher and the constant regime is reached later. At $E = -1.5k_BT$, $\rho = 0.05$ in 3D, σ_R seems to approach a constant regime while the irreversible model σ_R simply continues to rise.

Thus the effects of bond energy on σ_R may be summed up as follows. At early time and low energy σ_R grows more slowly because large clusters take longer to appear. At low enough energy at later time σ_R approaches a constant, even at those high densities where σ_R diverged in the irreversible model. The value of σ_R in the reversible model may rise substantially higher than σ_R in the irreversible constant-polydispersity regime; see for example the results for $\rho = 0.1$, $E = -2.3k_BT$ in 2D, where σ_R is still rising at the latest times. These results imply that the irreversible 'classical' fractal DLCA growth imposes a limit on the cluster polydispersity. When growth is more compact a substantially more polydisperse system of clusters may appear. This observation lends some support to the often invoked 'monodispersity' of DLCA, in that irreversible DLCA is therefore inherently less polydisperse than compact growth systems; but still it is not the case that the system of clusters *is monodisperse.* At $\rho = 0.1$ in 2D we see in irreversible DLCA $\sigma_R \approx 0.6$, which in fact is quite a substantial polydispersity. Furthermore it is clear that at high density the idea of monodispersity cannot really be supported at all; the polydispersity is not even constant in time.

At high bond energy, σ_R rises at early time at much the same rate as in the irreversible model; however as gelation does not occur so quickly with the reversible bonding (due to local compactification of clusters) σ_R can continue to grow. There seems to be a continuous change in the rate of rise of σ_R with bond energy (see e.g. $\rho = 0.3$ in 2D). However, much of this difference may be accounted for by considering the role of monomers in the system. As has been demonstrated, even at the highest bond energy studied, $E = -4.0k_BT$, there remains a substantial number of monomers and

small clusters in the reversible DLCA system. In one case in Figure 5.2 we include results for σ_R when monomers are excluded from the calculation ($\rho = 0.3$ in 2D). The curves for different bond energies now overlap quite well. Therefore from the point of view of radius polydispersity, the only significant difference in the systems at different bond energy is the presence of monomers. This is consistent with the analysis of mass distributions in Appendix A where the distribution of larger clusters (around the weight-average mass) is observed hardly to be affected by the different bond energies in the reversible simulations.

5.2 Surface

Surface and perimeter properties are of considerable importance in many situations, for example in chemical and physical reactions, in preparation of micro-smooth surfaces, and in substrate-mediated reactions like chemical and enzyme catalysis. In some sense fractals may be considered as virtually 'all surface' [172] in that they are very ramified or tenuous objects, so that in applications where fractals or near-fractals appear surface properties will be important. In this section we consider the total surface area or perimeter length, and its evolution in time, in the DLCA aggregation model.

The *surface* (in 3D) or *perimeter* (in 2D) of a cluster on a lattice can be defined as the number of empty lattice sites which are nearest neighbours of any particle in the cluster[2]. In a system of many clusters we can define the total surface or perimeter as the sum of surfaces/perimeters of all the clusters (*excluding overlapping surface sites*). While some analyses of perimeter length and structure, including quite complex considerations of the structure of holes and 'lagoons', have been carried out for diffusion-limited aggregation models [172], to our knowledge surfaces/perimeters in DLCA have not been investigated in any detail.

Calculation of total surface area/perimeter length by counting empty neighbour sites in the lattice is essentially one case of a more general problem. Because only free

[2]This then includes 'internal holes' in the structure as well as 'external' surfaces.

lattice spaces are counted, the total surface we arrive at is in fact the total surface *accessible to particles of the size of the monomers in the system.* In an *off-lattice* model one could conceivably have holes and openings and 'pieces of surface' on many smaller scales. In fact in the extreme limit of clusters made up of perfect spherical particles which touch and bond *at an infinitesimal point*, no surface is 'used up' at all in the aggregation ! To *infinitesimal* 'test' particles the entire surfaces of all the monomers would remain accessible. Thus it is necessary in any case to define what 'scale' of surface we are considering. The lattice model imposes on us the scale of single lattice sites or monomers.

The total system perimeter length (2D) or surface area (3D) P is calculated by adding (without double-counting any shared perimeter sites) the perimeters of all the clusters in the aggregating system. In Figures 5.3 and 5.4 we plot P against time (in simulation steps) for irreversible and reversible DLCA simulations. P is scaled by the square (2D) or cube (3D) of the simulation system size L in order to compare directly results from simulations in different-sized systems. (The plots thus show 'total perimeter/surface' per unit 'volume'. It might appear then that dividing P further by the system number density would give the *average 'free' perimeter/surface per particle* and would indicate the average coordination number of aggregated particles in the system. But care must be taken to note that what we have calculated is not exactly the free perimeter/surface per particle. This is because overlapping perimeters are not double-counted; a free perimeter site shared between more than one particle is counted only once.)

First let us consider the results from the irreversible simulations. On the basis of the total perimeter/surface curves the irreversible aggregation can be divided into three stages: an early slow decrease, an intermediate fast decrease and a late-time regime where P is almost constant. We can explain the shape of the curve as follows, with the help of Figure 5.5, in which for an example simulation we replot P together with the time evolution of the numbers of monomers, dimers, and trimers. In the early-time regime, the total perimeter/surface P decreases quite slowly. (This time regime is only accessible for the lowest densities, $\rho = 0.01$.) Most monomers and small clusters must diffuse a long distance before they collide, and in fact little clustering is taking place as

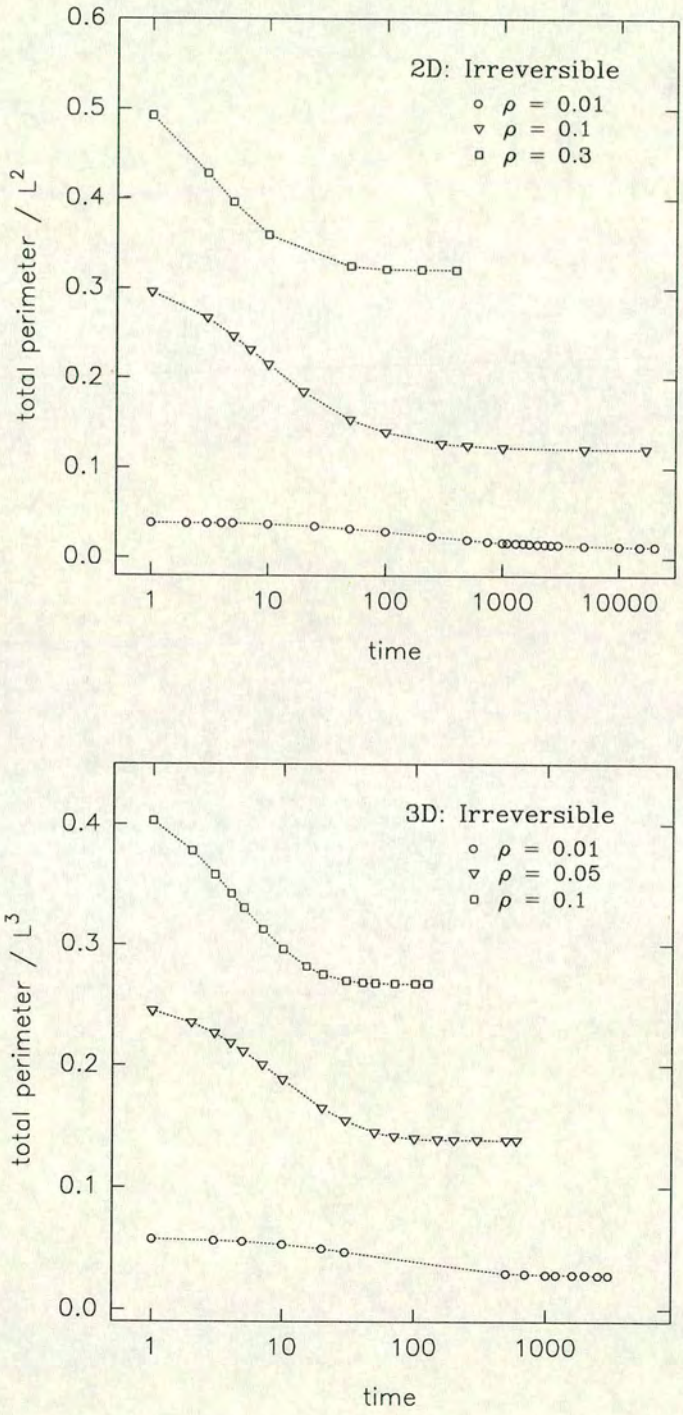

Figure 5.3. Time evolution of the total perimeter (2D) or surface (3D) in the irreversible DLCA systems. The perimeter/surface is scaled by the area/volume L^D of the simulation system.

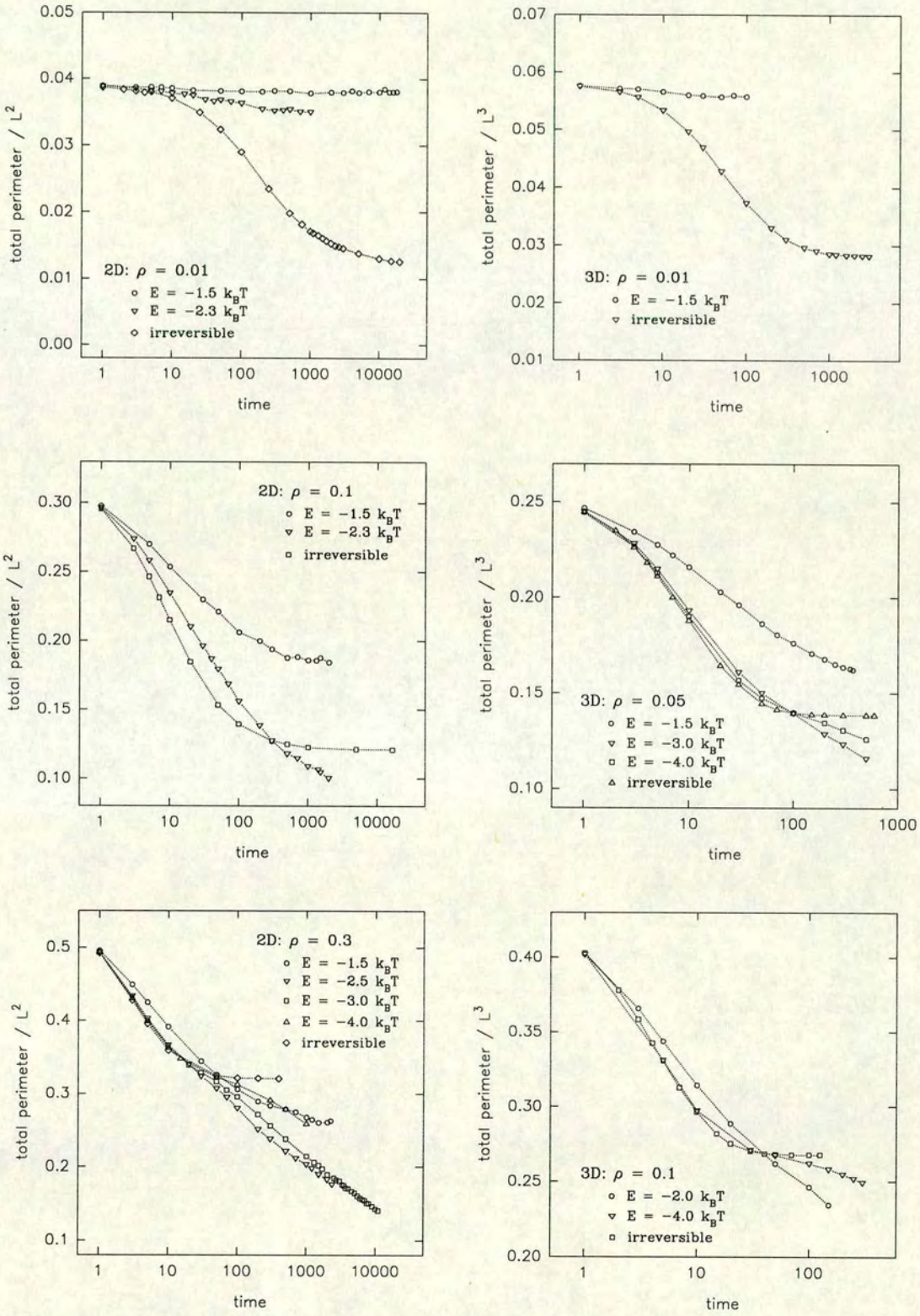

Figure 5.4. Time evolution of the total perimeter (2D) or surface (3D) in *reversible* DLCA simulations. The perimeter/surface is scaled by the area/volume L^D of the simulation system. The plots include the irreversible DLCA results for direct comparison.

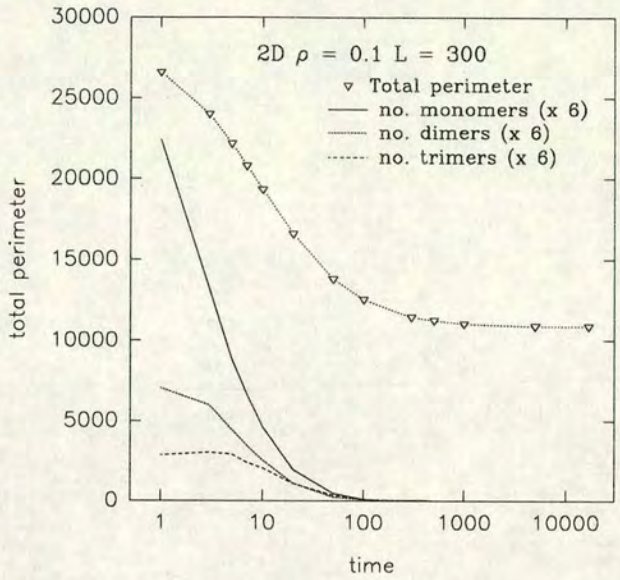

Figure 5.5. The number of monomers, dimers and trimers compared with the evolution of the total perimeter length, for a 2D irreversible DLCA simulation at $\rho = 0.1$. The numbers of monomers etc. are scaled upward (multiplied by 6) to aid visual comparison of time scales.

yet. In the intermediate time regime the total perimeter/surface decreases substantially because monomers and small near-compact clusters are most numerous in the system and most collisions involve these. When two monomers collide to form a dimer, the total perimeter/surface decreases (in 2D) by one quarter from 8 to 6 and (in 3D) by one sixth from 12 to 10. In other words, when compact objects collide the loss of perimeter/surface is quite substantial. In the late-time regime the decrease in P slows and almost completely stops. By this third time regime all the small clusters have disappeared (Figure 5.5) and the system consists almost entirely of fractal clusters. A collision between two fractals usually involves loss of only a single perimeter site (a single bonding site), insignificant compared to the surface area of a large fractal object, so that the total perimeter/surface remains almost constant even though the aggregation continues.

Note that, because the fractals cannot easily 'penetrate' each other, in the irreversible DLCA model large parts of the perimeters of the clusters actually become inaccessible to other clusters in the system, and will never be lost. This kind of effect may have some importance in real systems where different surface reactions proceed at different

rates. For example, consider a system of two types of particle A and B, such that type A particles aggregate with other A particles under *diffusion limited* conditions (i.e. sticking probability $P_s = 1$) while type B particles aggegate with type A (or indeed with other B) under *reaction limited* conditions ($P_s << 1$). Then 'internal' surfaces of growing A clusters may become inaccessible to B particles *before many B particles have bonded to them.* With appropriate 'tuning' of timescales, one could imagine a structure where external surfaces of A clusters are coated with B, but internally the clusters are free of B. Aggregation in such two-monomer systems has been modelled only rarely [173, 174] and conceivably has wide technological possibilities.

Effect of reversibility on perimeter/surface

Figure 5.4 shows how the total perimeter/surface P evolves with time in the reversible simulations. As in many previous instances, we can separate the effects of the finite bond energy into two parts, the effect on growth rates and the effect of compactification.

At the low bond energies P does not show such a substantial decrease from the early-time value, indicating that there is not sufficient clustering for substantial perimeter/surface to be lost. After a shallow curve downwards P again approaches a constant at the low bond energies, indicating that further clustering and growth is very slow. While some particles and clusters continue to aggregate, thus removing perimeter/surface, still the low bond energy means monomers are always detaching from clusters, thus *adding* perimeter/surface. Ultimately a dynamic equilibrium would be reached where the loss of perimeter due to collisions is equal to the regained perimeter from evaporation and fragmentation of clusters. One must again be careful however about claiming that our systems have reached any such equilibrium. In the long term the very much slower growth process of diffusion and *coagulation* of clusters (as opposed to evaporation and condensation of monomers from and onto clusters) may still lead to a decrease in P. (When the more compact low-bond energy clusters do collide, there will be substantially more loss of total perimeter/surface than in the case of colliding fractals). To study this long-term coagulation process however would require far longer simulation runs, currently beyond our capacity. Therefore we make no detailed claims

here about the behaviour of P all the way to equilibrium, but rather concentrate on the evolution of the perimeter/surface in the early stages, far from equilibrium.

At higher bond energies P shows a similar strong decrease to that in the irreversible simulations. However at later time the difference between the high-bond energy reversible simulations and the irreversible simulations is quite striking. When no bond breaking is allowed and the system consists of the 'classical' fine fractals of DLCA, P approaches a constant in the regime of fractal-fractal aggregation, as described above. However when the finite bond energy is introduced, P continues to decrease, sometimes for a very extended time (e.g. $\rho = 0.3, E = -3.0k_BT$ in 2D). In the reversible DLCA systems the clusters are able to compactify, thus continuing to decrease their surfaces/perimeters. Because multiply-bonded configurations are much more stable, there is a 'driving force' toward smooth surfaces. This surface smoothing is also a quicker process than longer-length scale restructuring, because it requires only local restructuring. Thus even when the clusters retain fractal structures on long length scales, there can be substantial continuing reduction in total perimeter/surface due to local surface restructuring. One would expect eventually all surfaces to be 'locally' nearly smooth, by which time further change in P would occur on much longer time scales.

In analogy to the idea of a critical energy for 'maximum unfrustrated growth' discussed in Chapter 4, we might define a critical energy E_p at which the effect on perimeter/surface is maximised. Growth rates would be sufficient to give a fast early decrease in P, but the clusters would be able to restructure relatively fast so that the constant-P fractal regime was 'avoided'. In the 2D simulations at $\rho = 0.3$, for example, we estimate $2.5 \leq |E_p| \leq 3.0k_BT$; in 3D at $\rho = 0.05$, E_p is somewhere between $-1.5k_BT$ and $-3.0k_BT$. Note though that in contrast to the frustration of growth as seen in the scattering analysis (Chapters 3 and 4) the sharp 'near-freezing' of the total perimeter indicates the transition of the system to a system of ramified fractals, not to a space-filling gel. The perimeter/surface as measured here does not appear to be sensitive to gelation or space-filling. At gelation the fractals which make up the gel fill space and contact each other, but there is no reason to think this contact would involve

much more loss of perimeter than fractal aggregation in the dilute system well before gelation.

5.3 Characteristic length scales

We have already devoted considerable discussion to the structural scaling hypothesis which has been proposed and investigated for fractal aggregation [45, 52, 65, 67, 69, 81, 115, 117], concentrating in Chapters 3 and 4 on its application to scattering data from experiments and from the DLCA simulations. The fundamental idea that the scattering function $I(Q)$ (or more generally just 'the structure') of the system may be characterised by a single measure such as Q_m, the small-Q peak position in $I(Q)$, requires that the single measure is the only important or dominant scale in the system. All other scales must be proportional to this *characteristic scale* (for time-independent scaling, all important scales must evolve the same way with time). Scaling analyses of the scattering function or of the pair correlation function represent one way to study scaling in the system. In this section we take a simpler approach and directly compare the time-scaling of various length scales in the DLCA system.

Here four lengths are identified and compared: the average radius of gyration of clusters r_g; the radius of gyration of the largest (most massive) cluster in the system at any one time, R_g; the length scale equivalent to the position of the peak in the structure factor, $R_Q = 2\pi/Q_m$ (which as shown in Chapters 3 and 4 is in turn equivalent to the outer radius of the depletion zone in the pair correlation function $g(r)$); and finally the *inner* radius of the depletion zone g_1, that is the distance at which the $g(r)$ function first falls below 1.0. In Figures 5.6 to 5.9 we plot these lengths against time for irreversible and reversible DLCA simulations. (Note that monomers are excluded from the average radius of gyration r_g since they have a rather arbitrary radius of gyration.)

In all simulations the lengths R_Q and g_1 scale similarly with time, implying that the inner and outer radii of the depletion zone in $g(r)$ are proportional[3]. In other words, as

[3] Sintes and co-workers [81] actually used g_1 rather than Q_m to examine the scaling properties of their DLCA simulations.

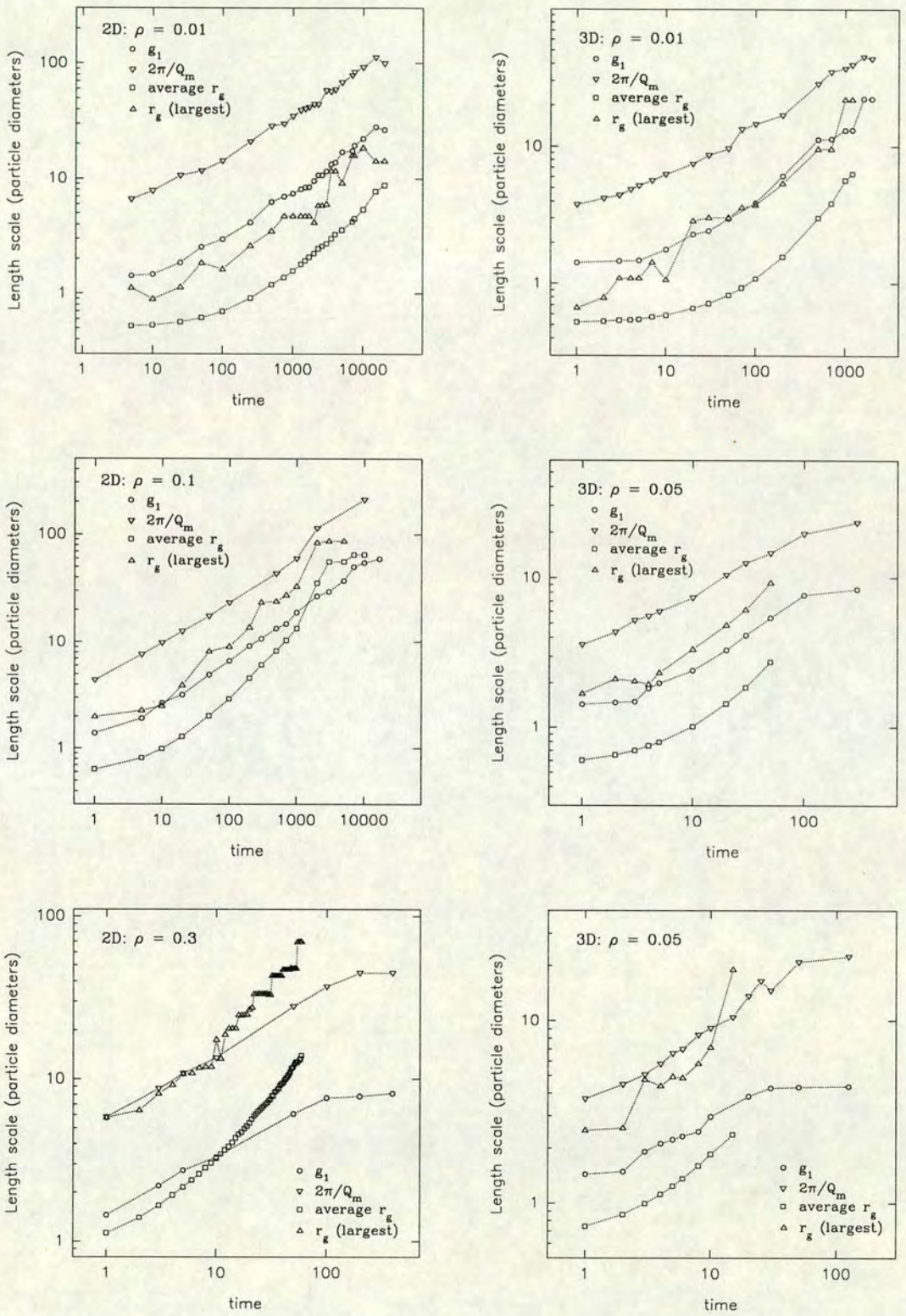

Figure 5.6. Comparison of the time evolution of various 'characteristic' length scales in the irreversible DLCA simulation. g_1 is 'inner radius' of the depletion zone in the $g(r)$ function (the distance at which $g(r)$ first goes below 1.0); Q_m is the position of the peak in the scattering function; r_g (largest) is the radius of gyration of the largest (most massive) cluster in the system; the average r_g is calculated excluding monomers (which have somewhat arbitrary radius of gyration).

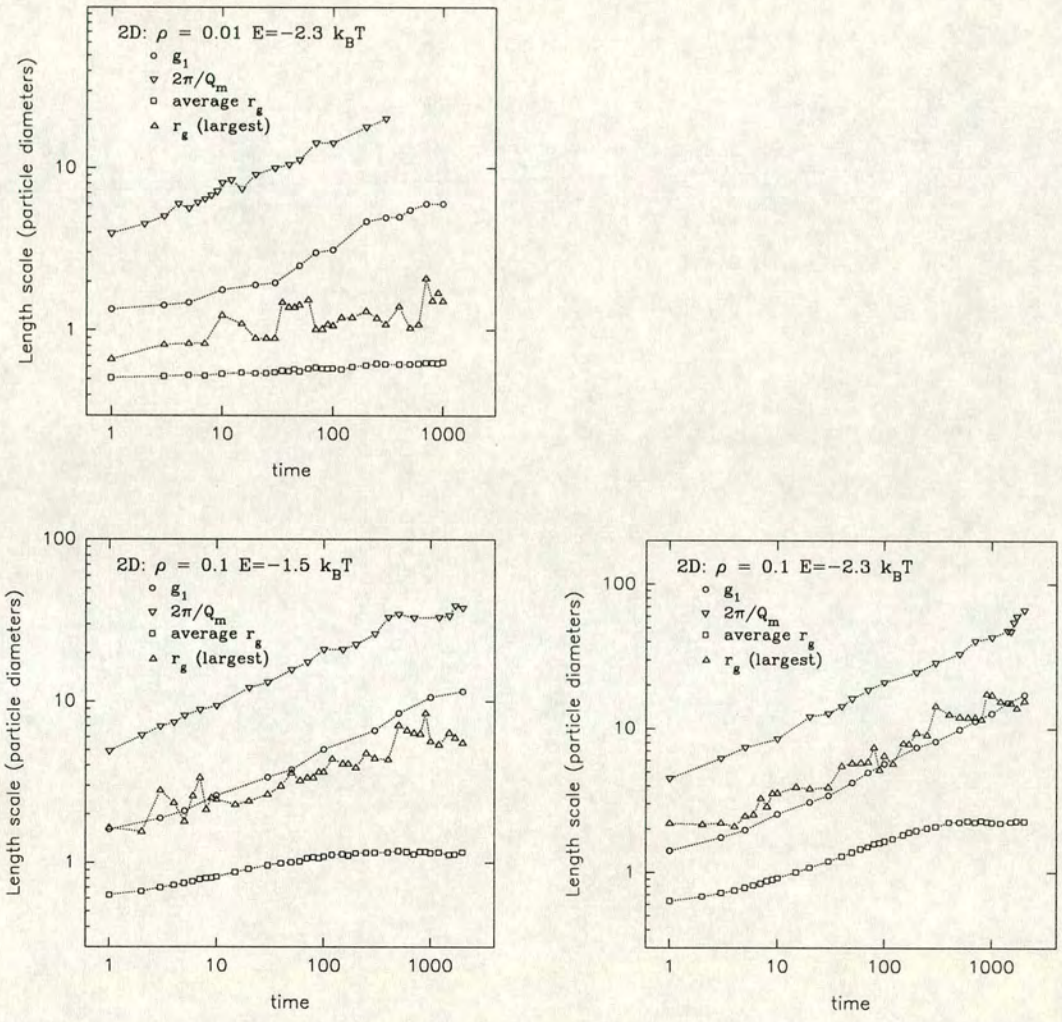

Figure 5.7. Comparison of the time evolution of various 'characteristic' length scales in 2D *reversible* DLCA simulations at densities $\rho = 0.01$ and $\rho = 0.1$. Symbols are as in Figure 5.6.

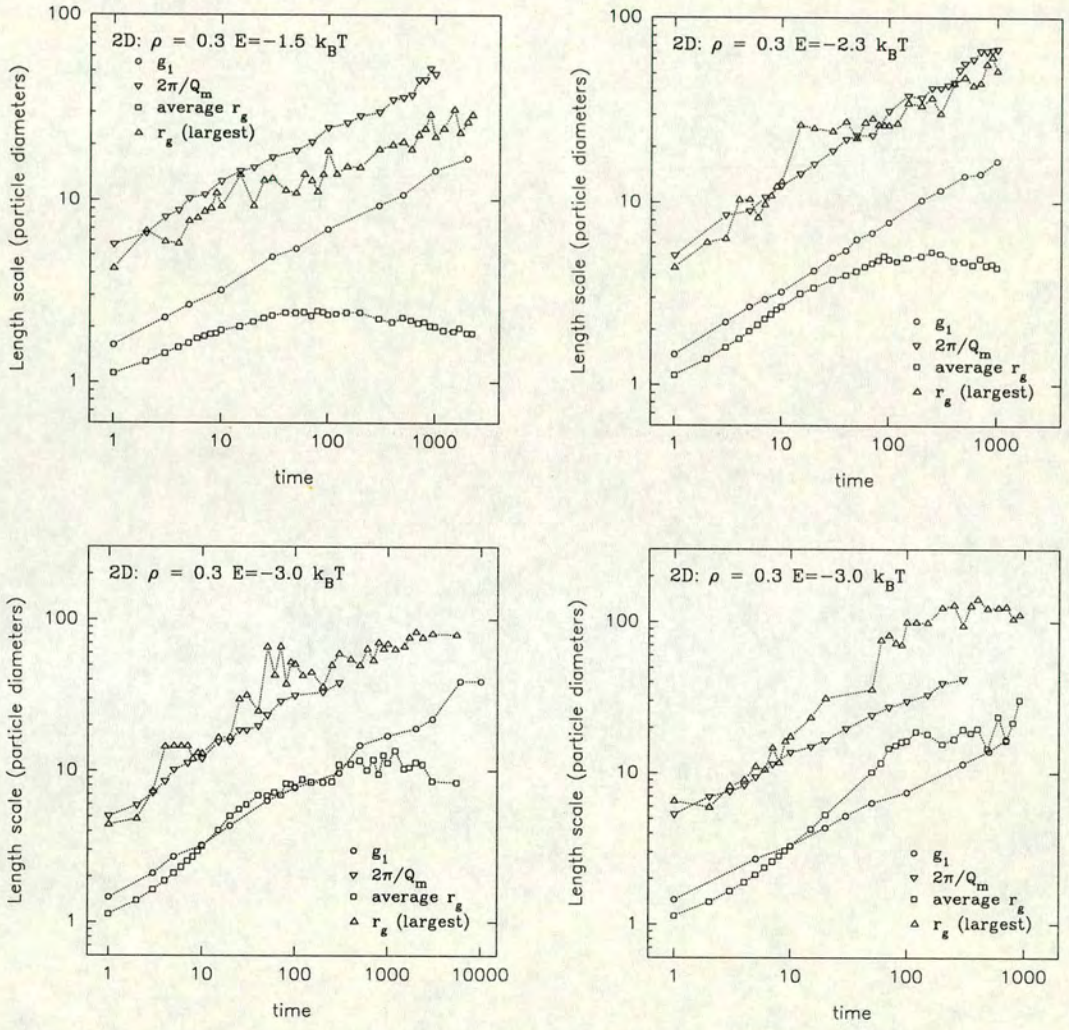

Figure 5.8. Comparison of the time evolution of various 'characteristic' length scales in 2D reversible DLCA simulations at density $\rho = 0.3$. Symbols are as in Figure 5.6.

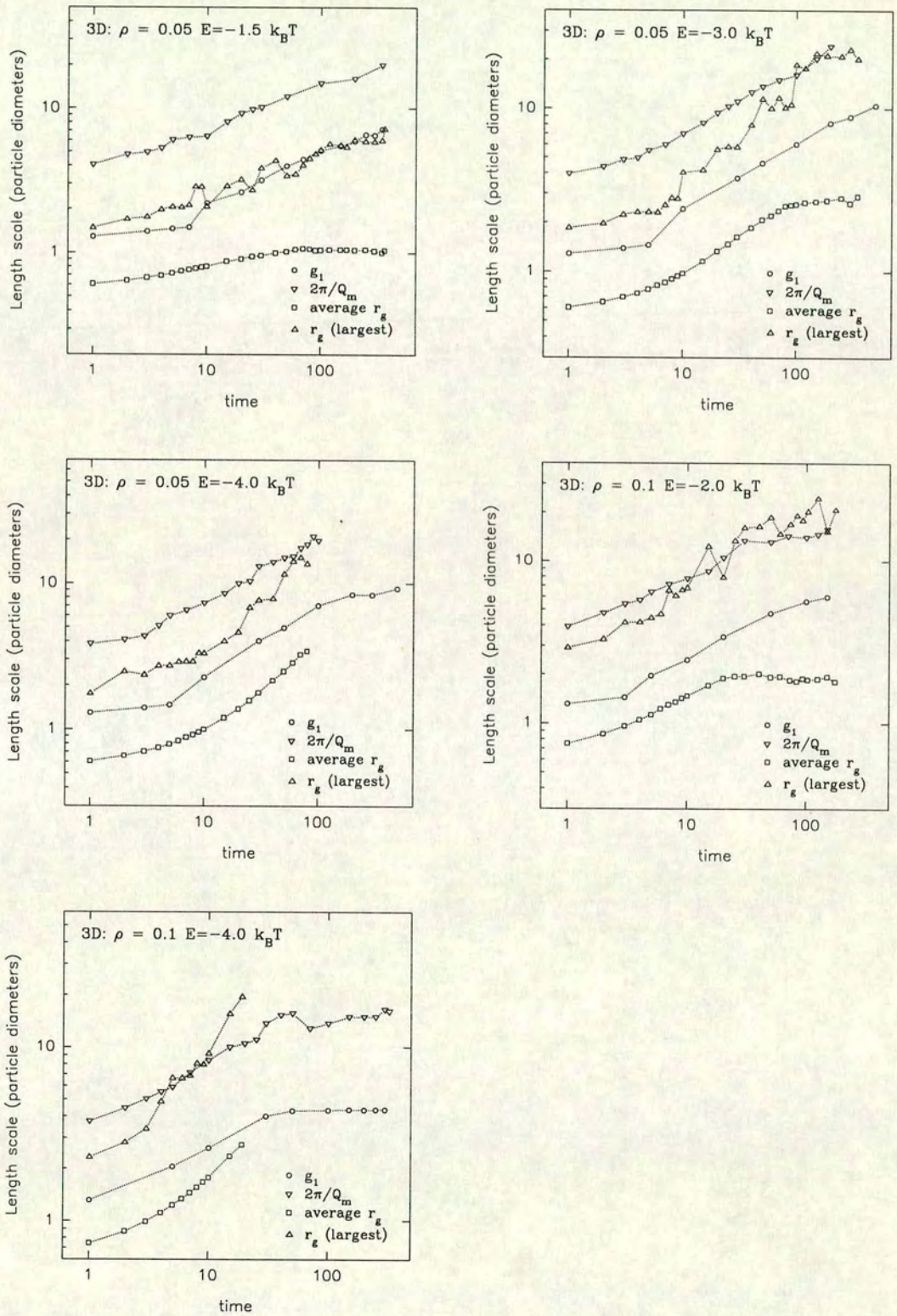

Figure 5.9. Comparison of the time evolution of various 'characteristic' length scales in 3D reversible DLCA simulations. Symbols are as in Figure 5.6.

the aggregation proceeds the depletion zone is simply *stretched*; it does not get wider relative to the inner radius. This is true even near gelation, where the slowing and 'freezing' of growth of the depletion zone or of Q_m is quite apparent (see the g_1 and $2\pi/Q_m$ curves for $\rho = 0.3$ in 2D and $\rho = 0.05$ and 0.1 in 3D); g_1 shows almost exactly the same freezing. Now if we were to treat g_1 as a nominal 'cluster size' and R_Q as the typical distance to the surrounding 'background' of clusters, this would seem to imply that even on gelation the typical cluster is not 'reaching' its neighbours and filling space. This implies then that g_1 is *not* a good measure of 'cluster size', at least not the cluster size important for gelation.

The depletion zone is not really the sharp-sided 'ditch' of the simple model (see Chapter 1 and Ref. [68]). It is important to realise that the depletion zone is not *empty*. We have pointed this out already in our examination of the cluster arrangement in Chapter 3. Some parts of the 'centre' cluster will extend into the depletion zone beyond g_1. In addition at the length scale of the outer edge where $g(r)$ reaches 1.0 the system is already homogeneous; there must be parts of clusters *within* this edge to make $g(r)$ begin to rise from the minimum back toward 1. Recall also that (except at low bond energies) the depth of the depletion zone decreases with time (Chapter 4). This implies that typically the fractal clusters 'grow into' their depletion zones, increasing the depletion zone density. This effect is not observed in compact growth models [68].

R_g, the radius of the largest cluster, is a more direct measure of a cluster size. While this is the size of the *largest* (most massive) cluster the scaling of the mass distribution (Appendix A) implies that, at least well before the appearance of the large 'gel cluster', we expect R_g to be reasonably representative of all clusters in the system. In fact it can be seen from the plots that R_g and the average radius of gyration r_a do scale with time in a similar way. Now for the irreversible aggregation, there is a clear trend in the behaviour of R_g with system density. At the low densities we find that the clusters are *smaller* than the scattering characteristic length $2\pi/Q_m$. The typical magnitude of R_g increases with density. (As density increases $R_g(t \to 0)$ is higher in the simulations, because of the lattice effect on the effective start time, see Chapter 2). *But R_g does not scale with time in the same way as R_Q*, especially at later time. At later times

R_g grows faster than R_Q, exactly what we expect from the simple picture of growing fractals approaching gelation: the fractal grows faster than the 'depleted zone' from which came its constituent particles (see Chapter 1). In the high density systems R_g increases rapidly above $2\pi/Q_m$. Now the largest cluster is the precursor of the gel, and its radius appears to diverge (R_g can only be calculated until the largest cluster spans the simulation system). In other words as the system approaches gelation the largest cluster or 'gel fraction' grows beyond the depletion zone. This is consistent with the idea of the gel being made up of an assembly of smaller fractal clusters, the gel structure being homogeneous on long length scales *but retaining the depletion zone in* $g(r)$ (retaining the frozen small-Q peak in $I(Q)$) at intermediate lengths.

In lower densities and early time, the time evolution of R_g and R_Q (or g_1) may *appear* quite similar. This may explain the 'approximate' scaling of the scattering functions found for the lower density systems (Chapter 3) [16, 45, 52, 65, 81, 115, 117]. Sciortino and co-workers [67, 69] have suggested indeed that all observed 'scaling' in *fractal growth* systems is only approximate. In low density systems especially the breadth of the time regime of such approximate scaling may be substantial [45]. Nevertheless, good scaling of the scattering functions has also been observed in higher density colloid-polymer systems [16]. It may alternatively be that one of the scales (e.g. R_g) is simply not important in determining the scattering function, and therefore a lack of proportionality between R_g and R_Q does not affect the scaling of $I(Q)$.

The direct examination of length scales as has been carried out here would be a useful further test of scaling in experimental systems. The problems of direct observation of experimental systems nevertheless remain. Comparison of length scales has been reported for the 2D colloidal aggregation experiment of Robinson and Earnshaw [154]. The average (median) radius of gyration of clusters was compared with the average nearest-neighbour separation of clusters. It was found that the two quantities did *not* scale in the same way with time, despite the fact that approximate scaling of the scattering function was observed [52]. Furthermore it was also shown that scaling of $I(Q)$ commenced only when the average cluster radius had grown larger than the cluster separation; in this regime in addition the $I(Q)$ peak position was identified

convincingly with the cluster separation. Earnshaw and Robinson point out [52, 154] that scaling at long length scales (near and on the low-Q side of the small-Q peak) implies some kind of long-range interaction or correlation. Our own findings from DLCA simulations are not totally consistent with this experiment, however. Where we do observe approximate scaling of $I(Q)$ (Chapter 3), for instance in 2D at $\rho = 0.1$ (comparable with the experiment), our R_g is still *smaller* than $2\pi/Q_m$. It may be then that other effects, for instance the early-time RLCA-DLCA crossover [7], are important in determining a 'scaling regime' in the experiment.

Somewhat more indirectly, Carpineti and co-workers have compared length scales in their 3D colloidal aggregation experiments [47]. In this case a functional form with two 'length scale' parameters R_1 and R_2 was derived and fitted to the measured light-scattering data. The two fitted length scales may be identified with the outer (R_2) and inner (R_1) radii of the depletion zone in $g(r)$. Once again differences between this experiment and our irreversible DLCA results are apparent. In the early-time regime where $I(Q)$ did not scale, it was found that R_2 actually drastically decreased while R_1 rose slowly. Thence R_2 'turned around' and, coinciding with the onset of the scaling of $I(Q)$, the two lengths increased approximately in proportion. The experiments of Carpineti and co-workers [45, 46, 47] were typically at very low volume fractions ($\Phi \leq 0.003$) compared to our simulations; it may be that at our higher volume fractions the lattice effect on the 'start time' precludes our observation of an early-time regime in which the outer radius of the depletion zone decreases. However a decrease in this radius is difficult to explain. Another difference between the experiment and our simulations is the *very* shallow depletion zone in $g(r)$ implied by the derived fit parameters of Carpineti and co-workers [47]. We find that the depletion zone in $g(r)$ is typically much deeper in lower density systems, as space around the clusters is more efficiently emptied. These points cannot yet be resolved; once again there may be effects in the experiment, especially at early time, which the DLCA model does not include.

We must conclude in any case that the full understanding of the scaling of the scattering functions and structure in fractal growth systems awaits further theoretical progress as well as more *direct* experimental measurement.

Effect of reversibility

In the reversible simulations the proportionality of R_Q and g_1 is again well demonstrated, especially for the low density/low bond energy systems. The effect of reversibility on the average cluster radius r_a is clear. At the lowest energies at all densities r_a, after an initial growth, approaches a constant. There is even a suggestion in some cases ($\rho = 0.3$ in 2D, for $E = -1.5$ and $E = -2.3k_BT$) that r_a begins to *decrease* at late time, which may be an indication of the continuing compactification of clusters. In addition in the reversible simulations the same general trend for the largest cluster's radius R_g to be higher at higher system density is observed. With the introduction of the finite bond energy though the time evolution of R_g is affected. At the lower energies ($E = -2.3k_BT$ for $\rho = 0.01$ and $E = -1.5k_BT$ for $\rho = 0.1$ and 0.3, in 2D) R_g seems to grow slower than R_Q. This presumably is because even the largest cluster is subject to substantial compactification as it grows. At intermediate bond energy the competing effects of growth and restructuring seem to lead to a very similar time-scaling of R_g and R_Q (2D, $\rho = 0.1, E = -2.3k_BT$, $\rho = 0.3, E = -2.3k_BT$ and $-3.0k_BT$, and 3D, $\rho = 0.05, E = -1.5k_BT$, $\rho = 0.1, E = -2.0k_BT$). In these cases then one might expect to see an 'apparent' time-independent scaling at least over a time regime equivalent to that studied in the simulations. Furthermore in these systems (again up to the times studied) R_g does not exceed R_Q and gelation is not observed. In the 2D simulation at $\rho = 0.3, E = -3.0k_BT$, R_Q seems likely to follow R_g for a very extended time regime of 4 decades (unfortunately due to the small size of the system and the small number of **Q** components at small Q, Q_m cannot be easily measured at the later times). Interestingly this system appears to be very near the 'critical limit' of gelation. From time $t = 2000$ onward a system-spanning cluster appears and reappears intermittently, continually forming and breaking up again. Subsequent structural evolution is very slow.

At the higher energies the effects of gelation are similar to those in the irreversible model: R_g tends to rise above R_Q at later time and diverges as gelation is approached. Once again, especially in the high density systems, no extended period of R_g/R_Q proportionality is observed.

Chapter 6

Conclusion

...et la Reine, la Sorcière
qui allume sa braise dans le pot de terre
ne voudra jamais nous raconter
ce qu'elle sait, et que nous ignorons.

Arthur Rimbaud
'Après le déluge'

6.1 Analysis of structure

In this thesis we have made a detailed study of the structure of the aggregating system using the DLCA computer simulation model. It has been demonstrated that analysis methods analogous to scattering experiments provide a wealth of information beyond that previously obtained in similar simulations. The results of such analyses may also be directly compared to experiment. In this Conclusion we give a summary of some of the main points raised by our analyses. We end with a final comparison of our simulations with experiments and with some suggestions for the future development of the study of aggregation and gelation with the DLCA model.

6.1.1 Summary of results

- The scattering properties of the DLCA system are in qualitative agreement with measurements in a wide range of experiments: the scattering function $I(Q)$ features a strong peak at small angle or small scattering vector magnitude Q. As the aggregation proceeds this peak grows in intensity and shifts to smaller Q.

- The pair correlation function $g(r)$ features a depletion zone of lower than average density surrounding each cluster.

- We have shown that the characteristic length scale indicated by the strong small-Q peak in the scattering function is equivalent to the outer radius of the depletion zone in $g(r)$. In other words the picture of clusters growing by 'draining' material from nearby regions, thereby creating depletion zones, appears to be reasonable, and is sufficient to qualitatively explain the strong scattering peak at small Q.

- As observed in experiments, gelation or the filling of the system by fractal clusters leads to a saturation in the scattering peak intensity and a cessation of growth of the characteristic length scale.

- The scattering function of the DLCA system is a complicated function involving the structure of individual clusters, the arrangement of clusters, the distribution of cluster masses and the spatial distribution of those masses, as well as shape correlation between neighbouring clusters.

- In the irreversible DLCA model far from gelation (e.g. in low density systems), the structure of individual clusters, studied by calculation of the cluster form factor, is approximately time-independent. In high density systems where gelation may be reasonably simulated, the structure of the typical aggregate changes in a complex way as gelation is approached.

- There is no strong order in the arrangement of clusters, as measured by the cluster structure factor. The time evolution of the structure factor indicates that the cluster arrangement has a more or less constant form, simply expanding to larger lengths as the aggregation proceeds.

- The cluster polydispersity generates a size-position correlation, especially strong in the reversible DLCA model where there are many small clusters, such that small clusters tend to weakly associate in the spaces between large clusters. Thus both the size distribution and the spatial distribution of sizes is important in determining the scattering function and the structure of the system.

- While there is evidence that the scattering functions have a time-independent form, at least in an intermediate time regime, direct comparison of length scales in the DLCA system indicates that the cluster separation and the cluster size are not truly proportional; instead a region of 'apparent' proportionality may be observed.

- In the reversible DLCA model, a near-continuous range of scaling exponents is found according to the bond energy, corresponding to the wide range of morphologies observed in the system; furthermore the scaling exponent itself appears to be time-dependent in some cases.

- The radius polydispersity of DLCA clusters is approximately constant far from gelation. Near gelation the polydispersity rises steeply.

- The main effect on the mass distribution (Appendix A) of the finite bond energy is to generate and maintain a 'pool' of clusters at small mass.

In the next sections we discuss some of the points made above in a little more detail, relating our own findings to those of previous simulation studies and experiments.

6.2 Effect of reversibility

We have simulated the effect of thermal fluctuations in particle kinetic energy in a system where the attractive interparticle potential is quite weak, by incorporating a 'bond-breaking' algorithm in the standard DLCA model. This is the first detailed study of the effect on the system structure of such reversible bonding. Limited studies of the bond-breaking model were first reported by Shih and co-workers [107], who

studied only the fractal dimension of clusters (by the mass-radius relation). We find agreement with the results of Shih *et. al.*: the apparent fractal dimension of clusters in the reversible system is a function of the bond energy E. For potentials stronger than about $E = -4.0k_BT$ the irreversible DLCA fractal dimension is recovered; weaker potentials lead to compactification of clusters.

However, in our detailed 'scattering' analysis we show that the structure of the reversible DLCA system cannot be adequately described with a single 'apparent fractal dimension'. The reversible system features a wide range of morphologies dependent on the bond energy E. At very weak bonding, there is almost no growth of clusters. At intermediate E, growing clusters are internally near-compact, but have ramified surfaces. The clusters are embedded in a 'low-density phase' of monomers and small clusters whose density also depends on E. At higher bond energy, we find very large clusters which are near-space filling (fractal on very long length scales) but which are quite compact on short lengths; we call this structure a 'fat filament gel'. At higher bond energy still, the system approaches the irreversible DLCA structure, a 'fine filament gel' fractal on short and long scales. This work may be compared with various other simulation models of phase separation [57, 58, 59, 64, 162], making clear the similarities between the reversible DLCA model and these other models of phase separation.

The reversible DLCA system may be viewed in terms of a competition between growth, restructuring, and frustration of growth. At the lowest interparticle bond energies, the fast collapse of small clusters means that growth is insignificant, and we expect the system to be stable as a 'single phase fluid'. (At higher energy presumably a metastable system may be found which eventually begins to phase-separate by nucleation of stable large clusters, though we have been unable to observe such a nucleation event.) At higher energy still, growth is more substantial, but restructuring happens quickly enough compared to growth that the growing clusters are internally compact. At still higher energy growth is faster than restructuring and the clusters are fractal on the longest length scales. Fractal growth leads to space filling: thus at high enough energy the clusters fill enough space that they begin to *frustrate* the growth of their neighbours.

Further growth slows down, and must 'wait' for slower restructuring to compactify the large clusters enough that more space is freed for further growth.

Study of the evolution in time of the scattering peak, $I(Q_m)$, provides a good comparison with the above picture. At low energy a very weak scattering peak is observed (possibly no peak at all at the lowest energies); at intermediate energy the peak grows slowly at first but eventually becomes strong and continues to grow; at higher energy, after faster initial growth the peak 'saturates' due to the frustration of growth by the space-filling fractals.

6.3 Structural scaling in DLCA

From our data there are some indications from scattering functions that the aggregating system may be characterised by a single important length scale *in a limited time regime* during the simulation. However, direct examination of length scales in Chapter 5 indicates that the cluster size and the depletion zone size (more or less the cluster separation) are not truly proportional to each other. Rather in some time regime they may scale *similarly* with time.

These observations must be considered in the context of other simulations and of experiments. In experiment the following fractal scaling form has been proposed for the measured scattering functions $I(Q,t)$:

$$I(Q/Q_m,t) \sim Q_m^{-\gamma}(t)F(Q/Q_m) \tag{6.1}$$

Sintes and co-workers [81] found good scaling of the scattering function of the DLCA simulation system over a limited time regime, in a 2D simulation at an area fraction $\Phi = 0.1$, with $\gamma \approx d_{f,DLCA}$, the fractal dimension of the clusters. Our own results for number density $\rho = 0.1$ are similar [117], though our smaller system sizes lead to more noise in the data and uncertainty about the extent of the data collapse. In experiments, Robinson and Earnshaw [52] in a 2D experiment again at $\Phi \approx 0.1$ found

approximate scaling of the calculated scattering functions with $\gamma \approx d_{f,DLCA}$. In 3D experiments at low volume fraction Carpineti and Giglio [45] found remarkably good scattering function scaling again in a limited time regime. Pirie and co-workers [16] found both 'fractal' scaling ($\gamma \approx d_{f,DLCA}$) and 'compact' (spinodal-like, $\gamma = 3$) scaling (depending on the strength of the interparticle potential) in colloid-polymer mixtures at *high* volume fractions in 3D, $\Phi \sim 0.2$.

There remains however little theoretical justification for the reported scaling of the structure over *all* length scales. Carpineti and Giglio [45] point out that for (isolated) fractal clusters with scattering function $I(Q) \sim Q^{-d_f}$ (on the high-Q side of the peak, i.e. in the fractal region) the scaling by Q_m^{γ} *on the high-Q side of the peak* with $\gamma = d_f$ is trivial. However that their data show good scaling collapse also near the peak and on the small-Q side of the peak implies then that the exponent or fractal dimension γ also characterises the structure of the system at length scales beyond the typical cluster size, i.e. that the clusters are somehow arranged fractally in space [154]. In fact when plotted on log scales our simulation data do not support such good scaling on the low-Q side of the peak. Meanwhile Sciortino and co-workers [67, 69] have argued that true scaling (in terms of a single characteristic length scale) should not be observed in fractal growth, and that the reported scaling is no more than 'approximate'. The simple picture of gelation implies that the fractal clusters *must* grow faster than their surrounding depletion zones for gelation to occur at all; thus there are at least two length scales in the problem. Even so, scattering function scaling may still be observed if one of these lengths is not important in determining the scattering.

To summarise our own observations, at low and intermediate densities we find approximate scaling of the scattering functions at least as good as some experiments [52], with $\gamma \approx d_{f,DLCA}$, though only in a limited time regime. At higher density the scattering functions do not follow the fractal scaling hypothesis with $\gamma \approx d_{f,DLCA}$; however it is of course more difficult to define a fractal dimension at high density. $I(Q)$ does have a time-independent form (i.e. $I(Q)$ can be scaled by the two characteristic values Q_m and $I(Q_m)$, but instead of $\gamma \approx d_{f,DLCA}$ we seem to observe $I(Q_m) \sim Q_m^{-1}$, or a scaling exponent $\gamma \approx 1.0$, especially in 2D systems. We have tentatively ascribed this to the

inability for small near-linear 'pre-fractals' formed early in the aggregation to grow into fully-branched 'DLCA fractals' due to the fast space-filling at high density. (We observe good scaling with $\gamma \approx 1.0$ in early time at lower densities too.) But further direct confirmation of this picture would be desirable.

In reversible DLCA we find that the scaling exponent γ is dependent on the bond energy E. Generally $\gamma(E)$ is consistent with the changed morphology of the reversible DLCA clusters (i.e. $\gamma \to D$, the space dimension, for compact clusters at low E, and γ decreases as clusters become more and more ramified at higher and higher bond strength). However because the cluster morphology is time-dependent (especially in the 'early' stages of the aggregation studied here) we expect also a time-dependent γ. While the scattering functions may retain a time-independent form (the scaling function $F(Q/Q_m)$ is unchanged) we must at least then have a further time-dependent characteristic value, $\gamma(t)$, to add to $Q_m(t)$. Once again, at high density we observe low γ, with $\gamma \to \gamma_{irrev} = 1.0$ near $E = -4.0k_BT$ (for density $\rho = 0.3$ in 2D and $\rho = 0.1$ in 3D).

There is continued controversy over the origin of the scattering function scaling, and even over the validity of experimental observations. It seems clear from experiment that the scattering functions, in some time regime, do have a very similar form. To what extent factors like measurement resolution and even the clarity of data presentation [69] affect this remains a point of argument. In simulation, it is difficult to obtain good data without an inordinate amount of computational effort. Even then there remains no good theoretical or even intuitive justification of structural scaling over long length scales: one is left with the feeling of being in rather thankless pursuit of a kind of large bird, white, wild, formerly popular at Christmastime. Our own results are consistent with other simulation and experiment at low densities, and do demonstrate that even in high density DLCA systems where it is more difficult to define a fractal dimension, the scaling function does have a time-independent shape at least until quite close to gelation.

6.4 Comparison with experiments

We have shown that qualitatively the DLCA model does generate similar observations to those of recent experiments: the aggregating system contains a characteristic length scale which is indicated by a strong scattering peak at small scattering vector magnitude [11, 45, 49, 52, 65, 81, 115, 117]. The peak intensity increases with time, but in systems where gelation occurs the intensity 'saturates' as the growing clusters fill space [16, 117]. Under certain conditions the scattering functions demonstrate approximate scaling with an exponent approximately equal to the cluster fractal dimension [52, 117]. We have shown that the arrangement of clusters in the DLCA system has a time-independent form which simply expands at the same rate as the characteristic length scale, as observed in experiment [138]. The DLCA mass distribution (Appendix A) has a similar form to that measured in aggregation experiments [7, 41] and demonstrates similar scaling properties. When the interparticle potential is weak enough that thermal fluctuations may lead to structural changes, the morphology of the system is found to be sensitive to the strength of the potential: the reversible DLCA model generates structures from no growth through compact clusters to space-filling fractals, consistent with the interpretations of experiments [16]. In these respects our studies of the DLCA model and experiments therefore appear to be in good agreement.

There remain differences between the DLCA model results and some experimental observations. Firstly, in many phase separation and aggregation experiments the growth rate, as measured by the rate of change of the scattering peak position Q_m, shows a late-time increase (from an approximate $Q_m \sim t^{-1/3}$ scaling to a $Q_m \sim t^{-1}$ scaling). We do not observe this in the DLCA simulations, but this is probably not surprising. The transition to linear scaling in time has been shown to be associated with a hydrodynamic 'channelling' behaviour of the separating phases (for liquid phase separation) or of the solvent (in colloidal aggregation) [16, 151]. Fluid moves from narrow channels between clusters into more open regions, generating a new growth mechanism. Of course nothing like this is included in the simple DLCA model. Simulations of spinodal decomposition incorporating hydrodynamic approximations do find a similar effect [175].

There are certain differences between the DLCA simulation results and the 3D charged-colloid experiments of Carpineti and co-workers [45, 46, 47]. The most noticeable difference arises in the early-time regime where scaling of the scattering functions is not observed. While such a non-scaling regime is observed in both simulation and experiment, in the experiment [45] the early-time peak intensity grows faster than expected (or the peak position decreases more slowly than expected). In the simulation the converse is true, the intensity growing more slowly than in the late-time, approximate scaling regime. The reasons for this are unclear. One problem with other studies in which an early-time non-scaling regime is reported is that such non-scaling data is rarely presented, making comparisons difficult (e.g. [81]). Thus there are indications that at least the experiment of Carpineti *et al.* cannot be fully described by the DLCA simulation model. It is also possible that the DLCA model might behave differently at the very low volume fractions of the experiments ($\Phi \leq 0.003$). The failure to observe a characteristic scattering peak in this system under reaction-limited conditions [46] while such a peak is observed in other systems [52] and in simulations [65] may indicate other divergences between this experimental system and the 'standard' cluster aggregation models.

As mentioned, many experiments and other simulations report an early-time regime wherein the scaling of the scattering functions fails [16, 45, 47, 52, 65, 81]. As far as we are aware our observation that scaling does work in this regime if one uses an exponent $\gamma = 1.0$ has not been made elsewhere. It would be of great interest to compare these results with experimental systems.

In Brownian dynamics (BD) simulations of aggregation with 'weak' potentials [108, 110] a qualitative difference in the effect of interparticle potential depth upon cluster structure is observed: at stronger interparticle potential clusters are *more* compact rather than less. In the BD simulations the 'bonds' are flexible. It is also not clear what effect the finite range of the BD potential has on the aggregate structure (e.g. in the colloid-polymer system the range of the attractive potential has major effects on the observed phase diagram [12]). However the reversible DLCA model does seem to give results more consistent with experiments (e.g. colloid-polymer systems [16], charged systems

[107, 155], temperature-induced aggregation of sterically-stabilised colloids [176]). It is probably the case then that these experimental systems involve rather 'rigid' bonding such that the major mode of restructuring is the thermal 'escape' of particles from the attractive potential rather than the flexible reshaping of aggregates. Further investigation of 'weak' aggregation in the colloid-polymer system where the range of the potential is easily variable would probably lead to a better understanding of the difference between the two reversible aggregation models.

6.5 Gelation—and future developments

Perhaps one of the most intriguing aspects of aggregation and phase separation phenomena is *gelation*. Particle gelation is very important in applications in food science, paints and cosmetics, detergents, and biophysics. It remains relatively unstudied. Chemical gelation in polymeric systems has been a subject of great activity for some years and is reasonably well understood [8]; however there seem to be significant differences between polymer and particle gelation (for instance the particle gel retains a characteristic length scale [45, 49, 52]). Particle gels are also often rather unstable structures which may collapse under gravity or shear or restructure under thermal fluctuations. (Reversible gelation in polymers is also an important field far less well understood than chemical gelation.) It seems that the *direct* study of the evolution of structure in systems very close to gelation has not been reported in any detail. The DLCA simulation model would seem to be a good candidate for such a study, especially if one carries out properly detailed structural studies as we have here. Such structural information may then be compared quite directly with experimental measurements. The main problem with studying particle gelation with the DLCA model is then one of resources: one must study very large systems (especially at lower densities) in order to ensure that the gelation process is not seriously affected by finite size effects.

In this study limitations on computational resources mean that we have been able to make only a preliminary study of gelation. However from the high number density simulations we can make some observations about gelation in the DLCA system. The

polydispersity of cluster radii increases steeply near gelation, and the typical cluster structure becomes rather complex as the system approaches gelation. Study of the typical cluster 'form factor' by scattering in experiments would be a good way to obtain a direct structural description of gelation. It appears that time-independent scaling of the DLCA scattering function fails near gelation. By contrast, in experiments [45, 52] scaling is reported to work all the way to gelation. The disagreement may be because we can only study scaling close to gelation in high density systems, while these experiments have involved quite low area/volume fractions. In high density colloid-polymer gels scaling of the scattering function is also observed to fail at late time [16]. Examination of length scales in the DLCA system indicates that the radius of the largest cluster (and the average radius) rise steeply close to gelation, while the characteristic length scale indicated by the scattering peak 'freezes' at some substantially lower value. The indication for the gel structure is then that the gel retains the depletion zone of lower than average density at some intermediate length scale. At greater length scales the gel is near-homogeneous (there is little scattering on these longer lengths).

The simple picture of gelation is one of a system of similarly-sized clusters which grow reasonably 'independently', and at approximately the same rate, throughout the large system; because the clusters are fractal they tend to fill the intervening space until at the gelation time all the clusters contact each other to form a very large, system-spanning structure. But this picture has not been directly confirmed. Do the clusters contact each other across the whole system simultaneously (is gelation an instantaneous event) ? Or does a single large spanning cluster appear to which the leftover clusters in the system gradually attach themselves—rather like a percolation model [65, 123] ? How does the polydispersity of the cluster size distribution affect the gelation kinetics and structure ? These are questions upon which, with our limited-size simulations, we cannot give definitive answers. A study by Gimel and co-workers [123] indicates that the 'gel clusters' *percolate* the macroscopic system rather than pack homogeneously. To obtain a direct measure of the structure of the gel at such large length scales would require a gel system containing a very large number of 'gel clusters', quite impossible to simulate under realistic computational constraints. One problem is that neither the percolated system nor the homogeneous system generate substantial scattering, so

that study of the scattering function at very long length scales may not be much use. On the other hand study of the *evolution* close to gelation of the typical cluster form factor may at least provide information on structural *changes* in the system as it nears gelation, giving clues as to whether gelation involves packing or percolation.

There are also some interesting questions concerning the evolution of the gel structure in 'weak bonding' systems [16]: how does the bond strength affect the 'lifetime' of the gel ? How do gravity and shear stresses interact with thermal restructuring, and for that matter with growth in the early stages [125, 169, 166] ? How can one relate the measured dynamics of the system [11, 16] to the restructuring processes ? There is a lot of scope here for further study and improved understanding of experimental systems.

It may be argued that more complex models than the DLCA simulation are required given the complexity of the various experimental systems. However we have shown here that a *physical* understanding of the processes of aggregation and the important elements which determine the structure of the aggregating system, as well as a useful direct comparison with experiments, may be obtained with the DLCA model. It seems that a relatively simple model like DLCA remains a useful approach from which to derive a general understanding. The problems faced by the theorist in trying to understand far from equilibrium systems like gels seem to be substantial [60], and a general physical picture derived from direct observation of the behaviour of simple models would seem a useful step toward further progress.

Appendix A

Mass distribution in DLCA

Abstract

In this Appendix, for completeness we include studies of the distribution of cluster masses in the irreversible and reversible DLCA simulations, as well as an examination of the 'fractal' structure of aggregates via the scaling of cluster mass with radius. Mass distributions consistent with previous simulation and experiments are obtained. The main effect of the finite bond energy in the reversible simulations is to generate a 'pool' of small clusters in the system. Fractal dimensions derived from mass-radius scaling are consistent with previous simulation and with the results discussed in the previous Chapters of this thesis; however it is clear that, especially at high density and in the reversible model, the fractal dimension is inadequate to fully describe the structure of aggregates.

A.1 Cluster mass distribution

The distribution of cluster masses in the aggregating system has been the subject of many studies involving the DLCA simulation model [85, 86, 122, 170, 177] and other simulation models and theoretical approaches [73, 91, 93, 95]. Mass distributions for 2D and 3D aggregating colloidal systems have been measured in experiment [7, 41, 35,

42, 87]. In this section we examine the distribution of masses of clusters in the DLCA model and in particular consider its time dependence, comparing the irreversible DLCA model with the reversible model where interparticle attractive potential energy is finite and clusters may fragment.

To plot a distribution of the masses (number of monomers) of clusters it is necessary to assign the clusters into mass 'bins', i.e. to form a histogram. If regular (equal width) mass bins are used this is straightforward. However because there always tend to be few clusters of large mass, a better estimate of the mass distribution, especially at late time, is obtained by using *logarithmic* mass bins, that is bins which are equally-spaced powers of 10. A consequence of this is that the mass bins are wider at larger mass. To correctly form the histogram then it is necessary to normalise by the bin width, so that we count the number of clusters in unit bin width at each given mass. Note that because the 'edges' of the logarithmic bins used are not generally integers but all masses are integers (the number of particles in a cluster), in practice we actually normalise by the *number of integers* in each mass-bin.

All the histograms here are constructed using mass bins of either $\delta m = 2.0$ particles (where linear bins are used, at early times when all clusters are small) or $\delta(logm) = 0.2$ (where logarithmic bins are used; in other words mass bins at $m \leq 10^{0.2}$, $m \leq 10^{0.4}$, ... $m \leq 10^{0.2n}$). In some cases (particularly for the irreversible model) in order to increase the statistical quality of the data averages are taken over repeat runs of simulations at given number densities, by adding in all clusters at a given time step from all simulations.

A.1.1 Mass distribution of irreversible DLCA

In Figure A.1 (lattice model) and Figure A.2 (off-lattice model) we show cluster mass distributions $N(m,t)$ for irreversible DLCA simulations at various system densities at various times t. Data for very late times is generally not available due to the limited size of the simulation systems and the consequently small number of clusters, which makes it difficult to measure a continuous distribution. Especially then at late times

empty mass-bins (mass bins containing no clusters) may appear in the histogrammed distributions. In the log-log plots empty bins have been included by plotting separate points on or near the x-axis.

Typically the mass distribution at early time shows a decay with increasing mass at small masses, followed by a fast 'cut-off' near some mass m_{cut}. In one of the earliest studies of 2D DLCA mass distributions Vicsek and Family [85] showed that at fixed time t the decay for masses $m < m_{cut}$ was well-represented by a power-law, $N_t(m) \sim m^{-\tau}$. In fact the data reported here demonstrate that the mass distribution tends to flatten as time increases until, at the latest times where good data is available, a *broad peak* may appear in $N(m,t)$. More extensive simulations and examination of the effect of the cluster diffusivity prescription (Chapter 2) [86] have similarly shown that, *under conditions where larger clusters diffuse more slowly than small clusters*, a peak in $N(m,t)$ at $m > 1$ is expected to develop at later times. All the monomers and small clusters, which diffuse relatively quickly compared to the larger clusters, are 'absorbed' into the large clusters, so depleting $N(m,t)$ at small m. By contrast in Ref. [85] a constant, cluster size-independent diffusivity was employed, under which conditions [86] a peaked mass distribution does not develop. It is worth pointing out though that often in experiments a well-defined peak has not been convincingly demonstrated [7, 41]. It is not clear to what extent the finite size of any observable system affects the late-stage evolution of the mass distribution. The limited size of the observable system is a major difficulty even in experiments, so that at later times when a peak might be found the number of clusters is too small to give a reasonably continuous mass distribution.

The broad peak in $N(m,t)$ is most evident for the lower density systems. In the high density system, fast *gelation* interferes and the mass distribution is unable to evolve toward the 'dilute DLCA' form [69]. It is easily seen from the snapshots of the 2D, $\rho = 0.3$ irreversible DLCA simulation (Chapter 3) that well-defined separate clusters cannot form at such high number density. We would expect this to have substantial effects on the evolution of the mass distribution. Instead of the 'dilute DLCA' process of well-separated fractal clusters diffusing through space and meeting each other to

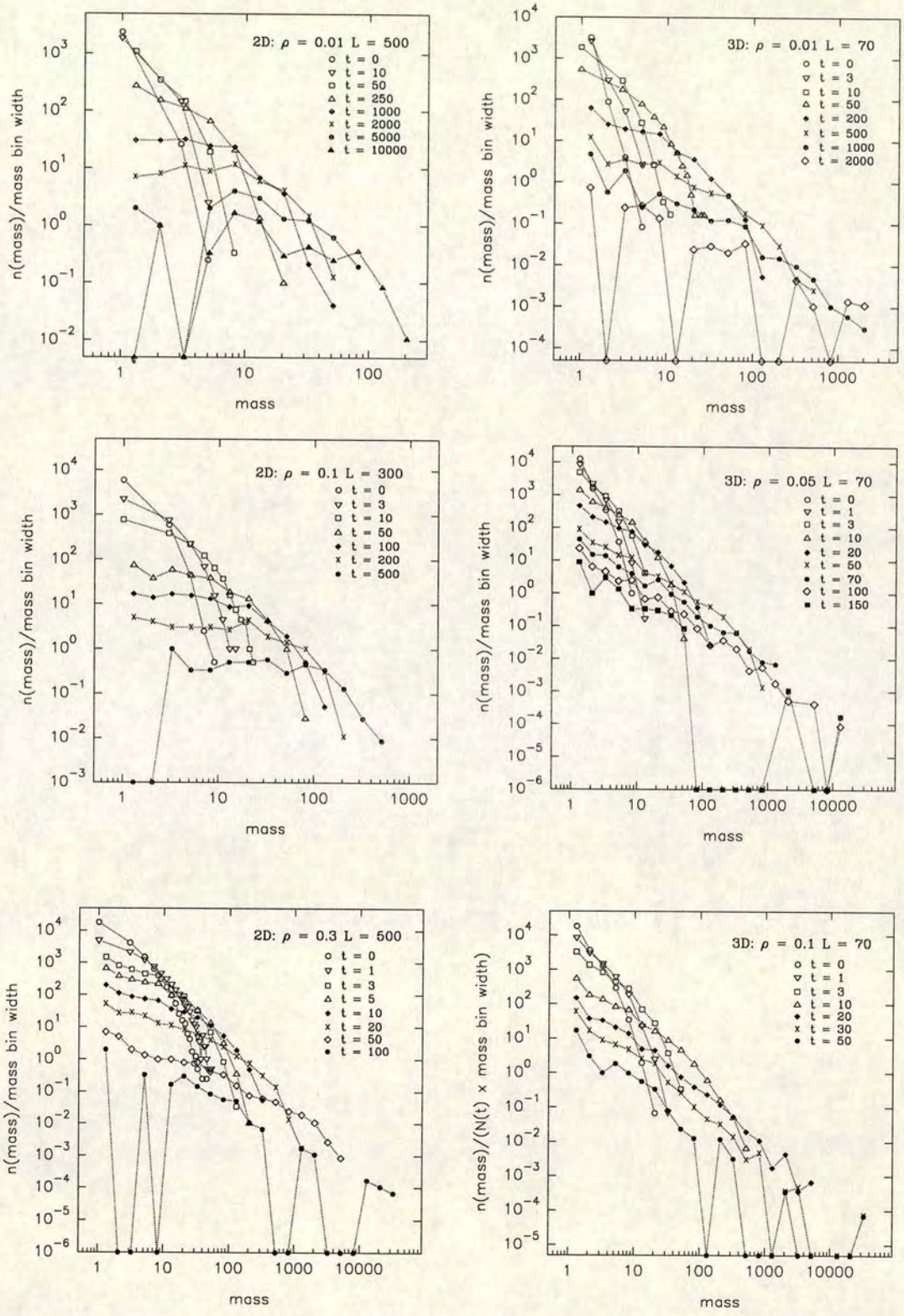

Figure A.1. Cluster mass distributions for 2D and 3D lattice-based irreversible DLCA simulations. The data are 'binned' to form a histogram, using at early times a linear bin width of $\delta m = 2$ and at late times a *logarithmic* bin width of $\delta(logm) = 0.2$. $n(mass)$ is the number of clusters in the mass-bin centred at the given mass, *normalised by the bin width.*

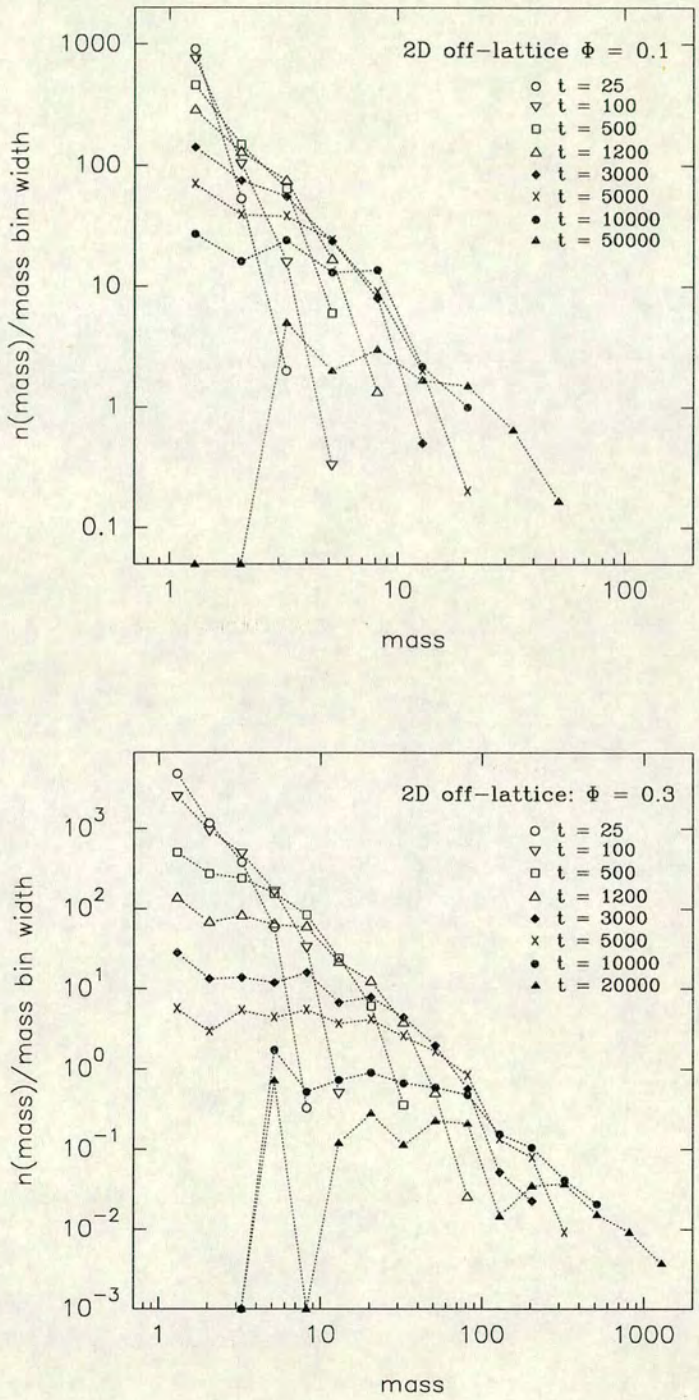

Figure A.2. Cluster mass distributions for 2D off-lattice irreversible DLCA simulations. The data are 'binned' to form a histogram, using at early times a linear bin width of $\delta m = 2$ and at late times a logarithmic bin width of $\delta(logm) = 0.2$. $n(mass)$ is the number of clusters in the mass-bin centred at the given mass, it normalised by the bin width.

form bigger self-similar structures, we have instead a highly confined set of clusters packed into the system, hardly able to diffuse before colliding with neighbours.

Cut-off mass and weight-average mass

It is evident from Figures A.1 and A.2 that the cut-off masses from different times form an 'envelope' which can be described by a power law. In other words, the number of clusters at the cut-off mass depends on the cut-off mass according to

$$N(m_{cut}) \sim m_{cut}^{-a}. \tag{A.1}$$

Proposed scaling relations for the mass distributions [85, 86] combined with conservation of mass lead to the prediction of an 'envelope' power-law exponent $a = 2.0$. This is supported reasonably well by the data here as we shall see. It is of interest first to relate m_{cut} to other statistics. The *weight-average* of the mass distribution, $M_2(t)$ is defined as follows:

$$M_2(t) = \sum_m m^2 N(m,t) / \sum_m mN(m,t). \tag{A.2}$$

In scaled plots of the mass distribution (plotting $mass/M_2(t)$ on the x-axis, see section A.1.3) the cut-off in the distributions for all times comes at $mass/M_2 \approx 1$, showing that the cut off mass is equivalent to the weight-average mass [82]:

$$m_{cut}(t) \approx M_2(t) \tag{A.3}$$

Equations (A.1) and (A.3) therefore imply that

$$n(M_2(t)) \sim M_2^{-a}(t). \tag{A.4}$$

$n(M_2(t))$ is plotted *vs.* $M_2(t)$ for 2D and 3D irreversible DLCA simulations in Figure A.3. For clarity on the plots only example fitted lines to a few of the datasets are shown; estimates of the power-law exponent a for all data are given in Table A.1. The power-law relation is supported quite well over a large range of $n(M_2)$ and M_2, failing

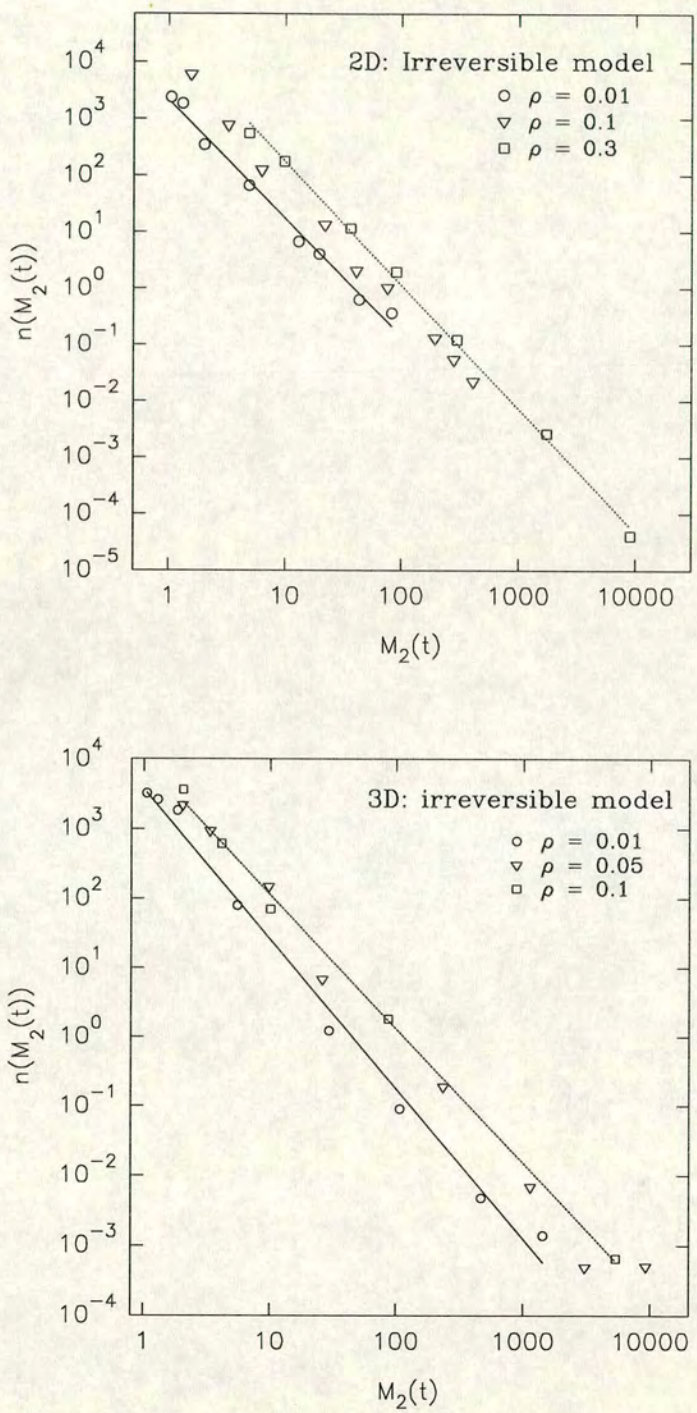

Figure A.3. The number of clusters at mass M_2, where M_2 is the weight-average mass, for irreversible DLCA simulations. Note that $n(M_2)$ can be less than one because it is taken from the histogrammed mass distribution, where $n(mass)$ is normalised by the (usually logarithmically-spaced) bin width; see Figure A.1. Fitted lines are shown for $\rho = 0.01$ and 0.3 (2D) and $\rho = 0.01$ and 0.1 (3D).

2D or 3D	Density	Bond energy	a	No. points
(a) Irreversible simulations				
2D	0.01	–	2.09	8
	0.1	–	2.03	7
	0.3	–	2.18	7
3D	0.01	–	2.16	8
	0.05	–	1.99	9
	0.1	–	1.94	5
(b) Reversible simulations				
2D	0.1	-1.5	2.57	5
	0.1	-2.3	2.13	7
	0.3	-1.5	2.01	5
	0.3	-2.3	1.92	6
	0.3	-3.0	2.03	6
	0.3	-4.0	1.94	5
3D	0.05	-1.5	2.45	5
	0.05	-3.0	2.08	5
	0.05	-4.0	2.17	4
	0.1	-2.0	2.04	5
	0.1	-4.0	2.04	3 (!)

Table A.1. The scaling of the number of clusters at the weight-average mass, $n(M_2)$, with M_2. Bond energies are in units of k_BT. a is the power-law exponent in the relation $n(M_2) \sim M_2^{-a}$, estimated by least-squares fitting. The fits exclude large late-time values of M_2 in those cases where a 'gel cluster' forms. (In the last case, density $\rho = 0.1$ in 3D at energy $E = -4.0k_BT$, this leaves only 3 points for the power-law fit...the reader is left to judge the reliability of this exponent for him/herself !)

only in high density systems where M_2 becomes limited by the finite size of the system (see the M_2 *vs.* time curves below). Consistent with scaling predictions [85, 86] we do find $a \approx 2$.

Time evolution of the weight-average mass

Figure A.4 shows the behaviour of M_2 as the irreversible aggregation proceeds for 2D and 3D simulations. Consistent with previous simulation [86], experiment and with predictions derived from Smoluchowski theory [92], we find after an early-time 'pre-scaling' period, an approximate power-law time-scaling of M_2,

$$M_2(t) \sim t^z. \tag{A.5}$$

This is only valid however for the lower densities. At high density the influence of *gelation* is clear; M_2 diverges as a 'proto-infinite' cluster forms in the system. In the simulations M_2 cannot truly diverge to infinity; the finite system contains only a finite number of particles N_0, so that M_2 hits a 'ceiling' $M_2 \approx N_0$ at late time. Beyond this time the 'precursor gel' cluster *should* be connecting very quickly with other clusters *outside* the part of the system which is simulated.

2D or 3D	Density	Time range	z
2D	0.01	$t > 300$	0.76
	0.1	$t > 100$	1.16
3D	0.01	$100 \leq t \leq 1000$	1.54

Table A.2. Fitted exponents z for the power-law growth of the weight-average mass, $M_2 \sim t^z$, for irreversible DLCA. Only the lower densities exhibit reasonably clear power-law regimes; at higher density M_2 tends to diverge due to approaching gelation (see text).

For the lower densities where some power-law region in M_2 *vs.* t is observable, estimates of the exponent z are given in Table A.2. Fluctuations in M_2 become quite severe at late time when there are only a few clusters left in the system (whether proper 'gel' clusters or just single fractals approaching the system size), demonstrating the difficulty

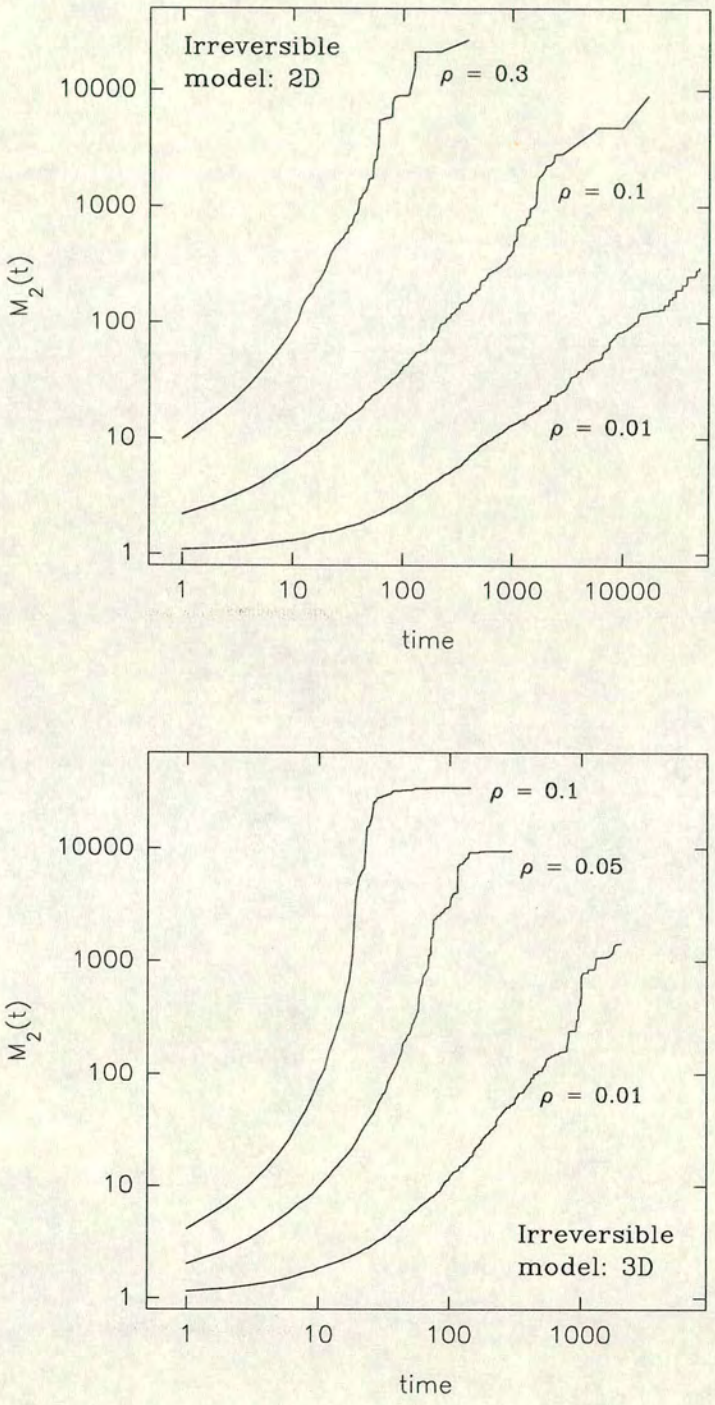

Figure A.4. Time evolution of weight-average mass for irreversible DLCA. At the highest densities M_2 tends to diverge on gelation, but becomes limited by the finite size of the system.

of obtaining a substantial 'scaling region' even with the large 2D systems used here. Thus estimating z with any precision is rather difficult. We find z on the order of 1, which is consistent with previous simulations and with scaling theories [83, 86].

A.1.2 Effect of finite bond energy on mass distribution

We go on now to consider how the mass distribution is affected when a finite bond energy or interparticle potential is introduced into the DLCA model. Figures A.5, A.6 and A.7 show mass distributions from 2D and 3D reversible DLCA simulations at various bond energies E. The mass distribution in the reversible simulations never loses the early-time peak at small clusters/monomers. At the weak potentials considered here there is always some reasonable probability of monomers breaking away from the surface of clusters (even if only temporarily before being 'caught' again), so that there is always a substantial number of small clusters and monomers in the system. This is true even for the quite high bond energy and high density systems which are in other ways quite close in character to the irreversible DLCA (see the structural analysis in Chapter 4). For instance in 3D, for $\rho = 0.1$ and $E = -4.0k_BT$, a very large cluster ($\sim$ 32000 particles out of the system's total number 34500) forms early in the simulation (Figure A.7), but there remains a noticeable curve upward in the mass distribution at very small masses (compare with the irreversible model, Figure A.1).

At the higher energies there is a tendency for the distribution to develop a shoulder at intermediate mass or even a slight peak, that is to approach a broad 'bimodal' distribution (these 'shoulders' are more apparent in the scaled mass distribution plots as is shown in section A.1.3). This is consistent with the approach to the irreversible model, where a broad peak develops at $m > 1$ (Figure A.1); at finite bond energy the 'signature' DLCA peaked mass distribution is broadened toward smaller masses due to the collapse and fragmentation of clusters. This broadening and the persisting peak at small masses are the two major effects of the finite bond energy on the form of the mass distribution.

Some kinetic effects of the finite bond energy may be studied by examining the time

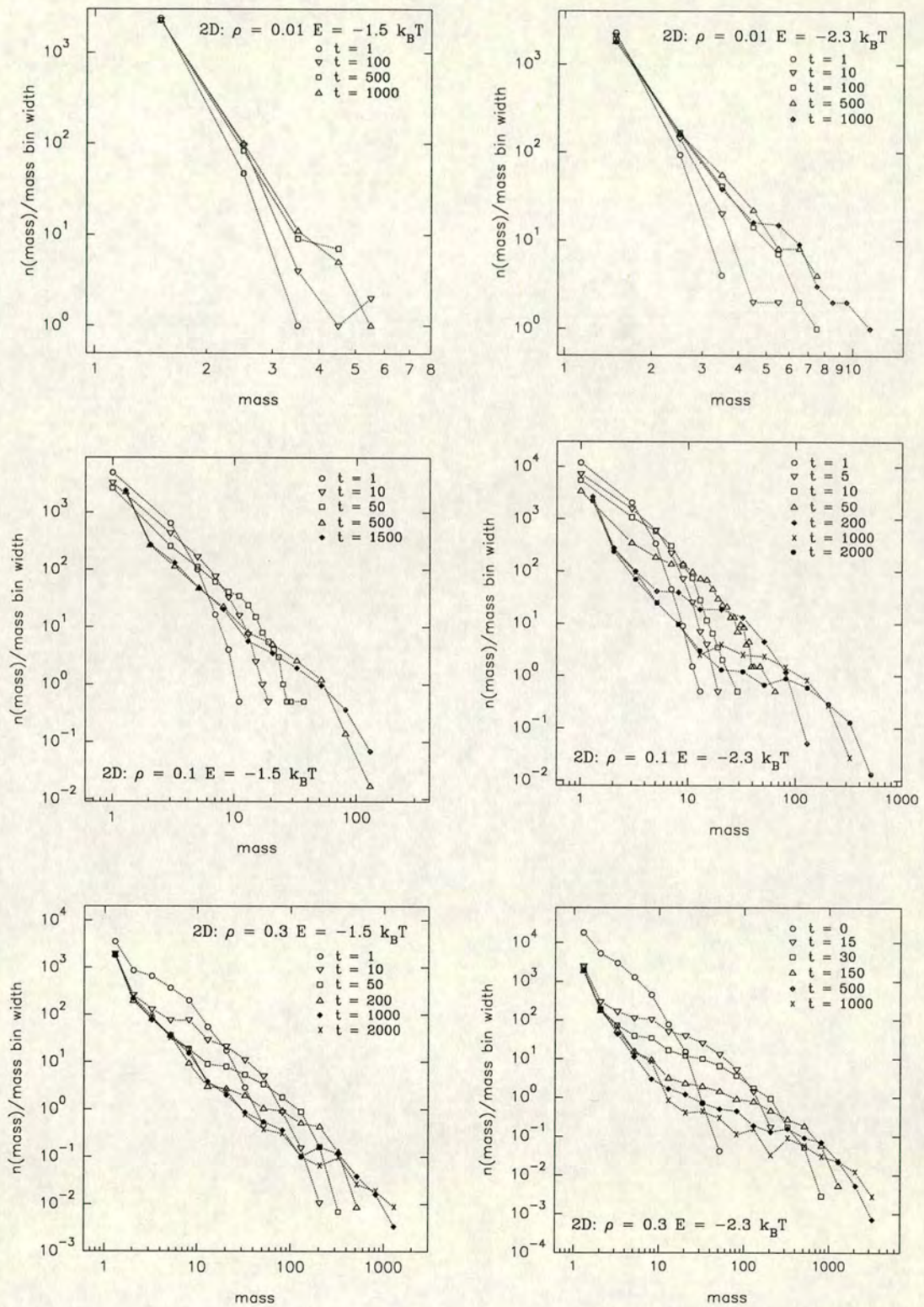

Figure A.5. Cluster mass distributions for 2D *reversible* DLCA simulations at 'low' bond energies $E = -1.5k_BT$ and $E = -2.3k_BT$. The data are 'binned' to form a histogram, using at early times a linear bin width of $\delta m = 2$ and at late times a logarithmic bin width of $\delta(logm) = 0.2$. $n(mass)$ is the number of clusters in the mass-bin centred at the given mass, normalised by the bin width.

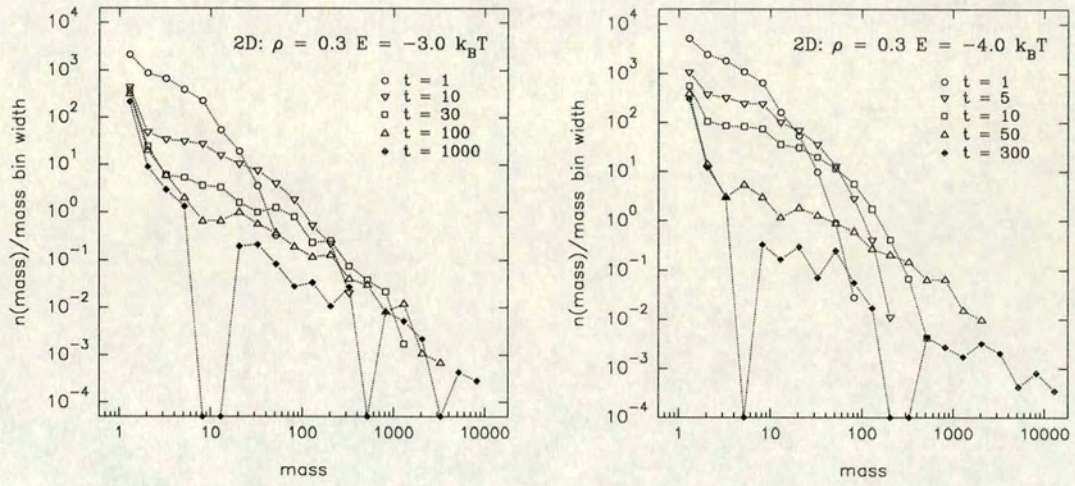

Figure A.6. Cluster mass distributions for high-density ($\rho = 0.3$) 2D reversible DLCA simulations at bond energies $E = -3.0k_BT$ and $E = -4.0k_BT$. The data are 'binned' to form a histogram, using at early times a linear bin width of $\delta m = 2$ and at late times a logarithmic bin width of $\delta(logm) = 0.2$. $n(mass)$ is the number of clusters in the mass-bin centred at the given mass, normalised by the bin width. Empty bins are indicated by the points near the x-axis.

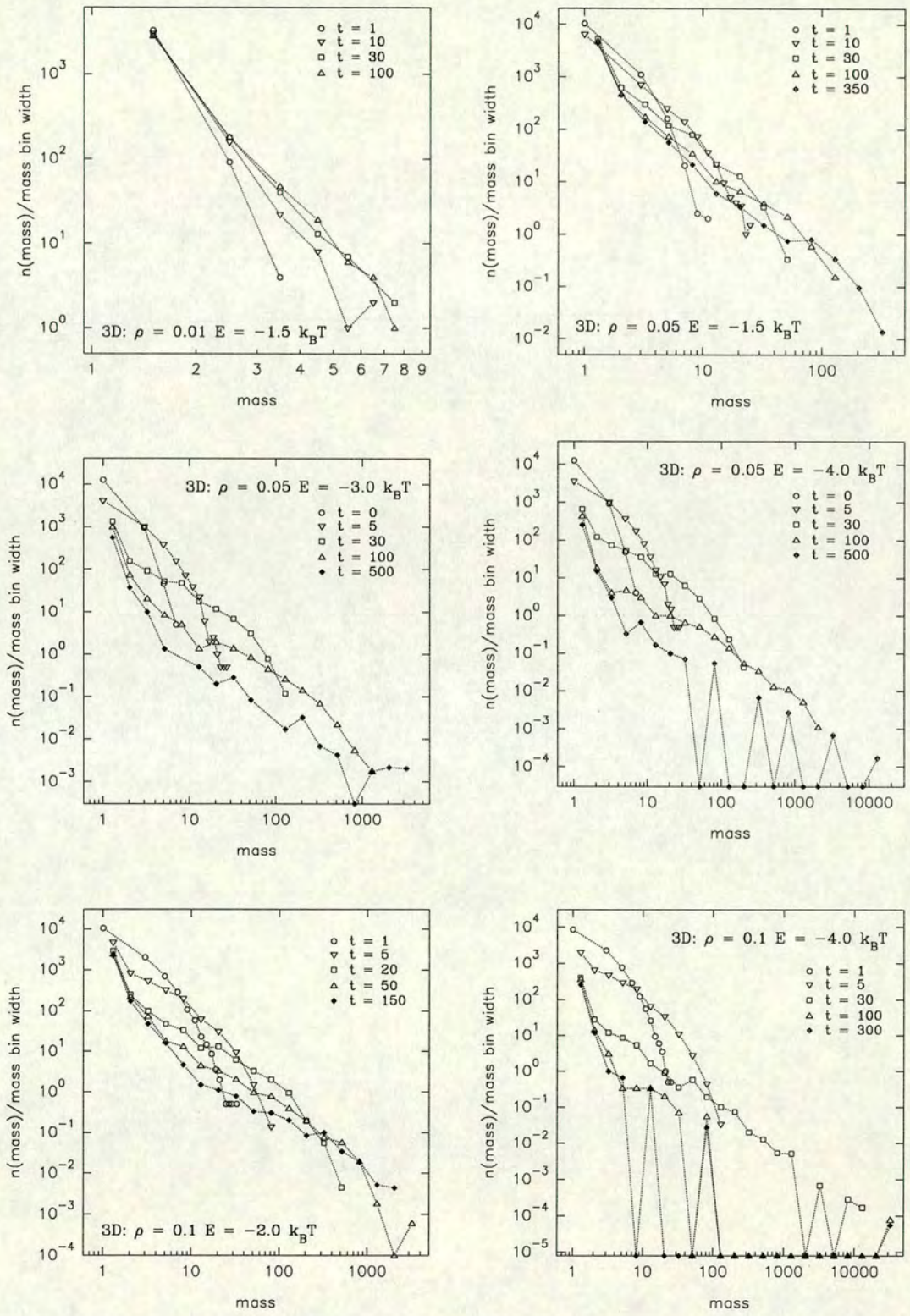

Figure A.7. Cluster mass distributions for 3D reversible DLCA simulations. The data are 'binned' to form a histogram, using at early times a linear bin width of $\delta m = 2$ and at late times a logarithmic bin width of $\delta(logm) = 0.2$. $n(mass)$ is the number of clusters in the mass-bin centred at the given mass, normalised by the bin width. Empty bins are indicated by the points near the x-axis.

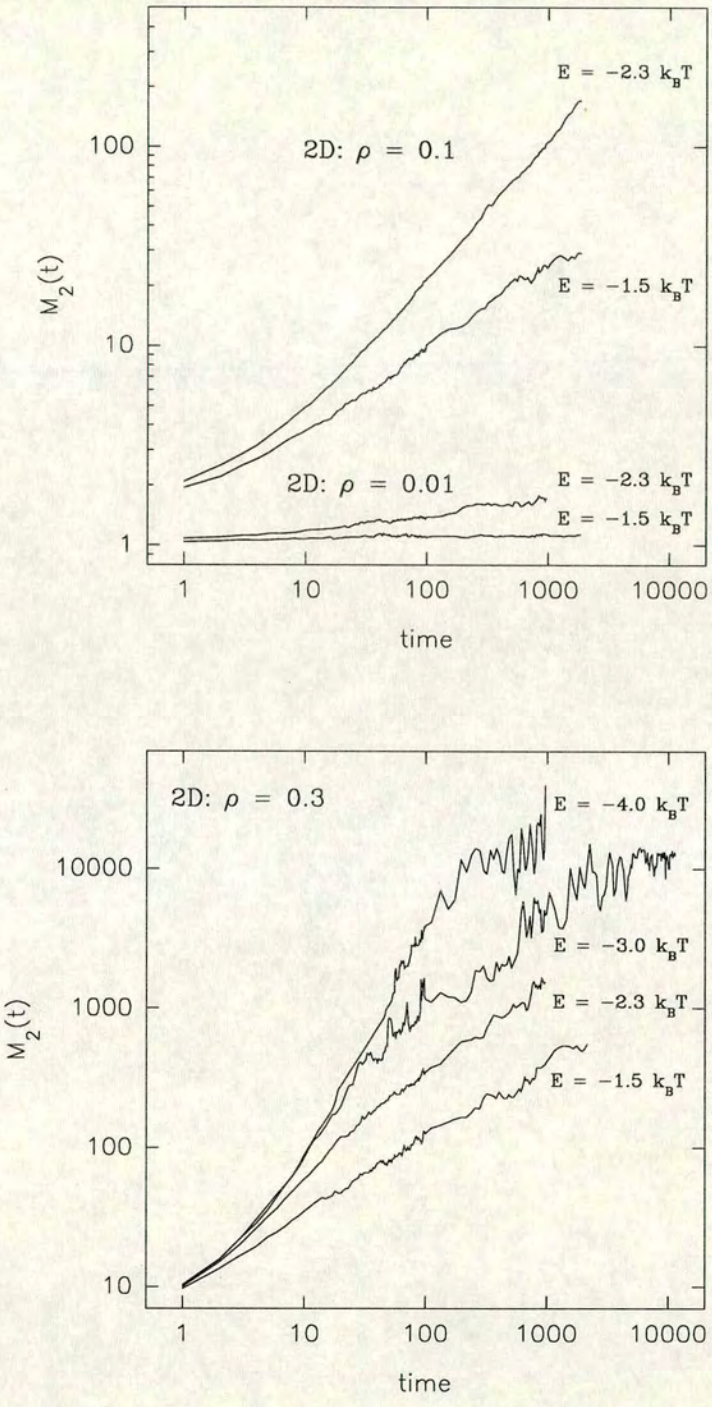

Figure A.8. Time evolution of weight-average mass for 2D *reversible* DLCA. In the reversible model M_2 fluctuates continually as clusters fragment. In these plots, at later times M_2 values calculated at each simulation time step have been averaged over time intervals of 50 steps.

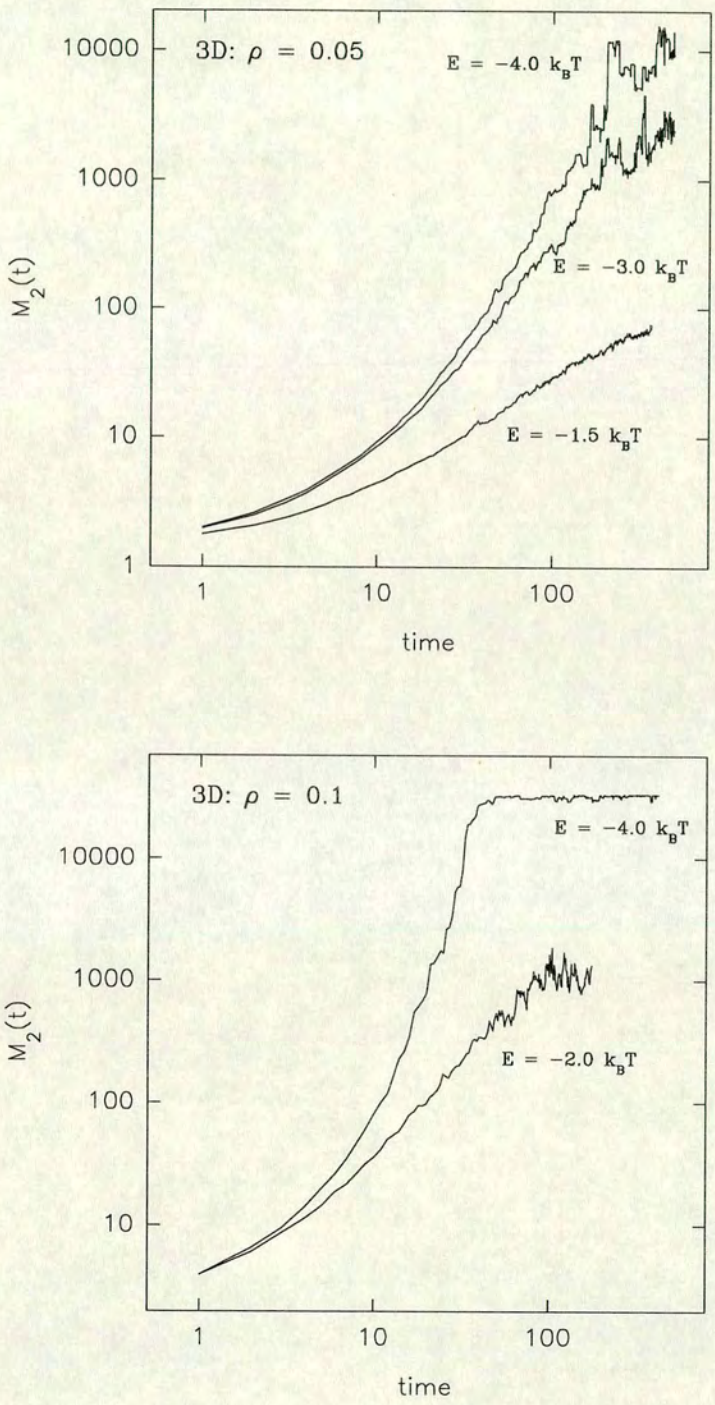

Figure A.9. Time evolution of weight-average mass for 3D *reversible* DLCA. In the reversible model M_2 fluctuates continually as clusters fragment. In these plots, at later times M_2 values calculated at each simulation time step have been averaged over time intervals of 50 steps.

evolution of the weight-average mass M_2. M_2 is plotted *vs.* time for the reversible simulations in Figures A.8 and A.9. Lower bond energy slows down the growth of M_2. In some cases ($E = -1.5k_BT$, $\rho = 0.1$ in 2D and $\rho = 0.05$ and 0.1 in 3D) there are indications that the growth of M_2 is slowing toward a constant. Mean-field approaches to reversible aggregation using a Smoluchowski equation with fragmentation as well as coagulation rates [93, 95] have predicted that a 'dynamic equilibrium' is achieved at late time with $M_2 \rightarrow$ constant. However it is not easy to relate these models very directly to the reversible DLCA model since in DLCA we have the parameter E, whereas in the Smoluchowski analysis the parameters are the coagulation and fragmentation 'kernels' (which determine the rates of these two processes). In addition of course the Smoluchowski approach ignores all spatial correlation of clusters, thus discarding many of the interesting features of the aggregation problem.

At higher bond energies M_2 continues to rise to the latest times to which we have run the simulations. For $E = -3.0k_BT$ and $E = -4.0k_BT$ we observe an interesting slowing down of growth (between $t = 10$ and $t = 100$), accompanied by the onset of large fluctuations in M_2. (At the very latest times, e.g. $t \approx 10000$ for $\rho = 0.3, E = -3.0k_BT$ in 2D, the 'ceiling' effect on M_2 of the finite size of the system may be important; M_2 cannot fluctuate above N_0, the total number of particles in the system.) These fluctuations demonstrate the breaking and reforming of clusters, and are so large because of the small number of separate clusters in the system at late times; at these densities and bond energies the systems are quite close to gelation (see the pictures in Chapter 4). Experimental observation of M_2, for instance by scattering methods, would presumably demonstrate the same large fluctuations.

The dependence of $n(M_2)$ on M_2 in the reversible model is shown in Figure A.10. As in the irreversible model we observe a power-law dependence (equation (A.4)) with exponent $a \approx 2.0$ (see Table A.1), with little clear dependence on bond energy or density. This would imply then that the finite bond energy does not affect the scaling of the mass distribution *near the weight-average mass.* This is supported by the scaling analysis as discussed in the next section. In other words, the major effect of the finite bond energy is to maintain a 'pool' of smaller clusters and monomers which in the

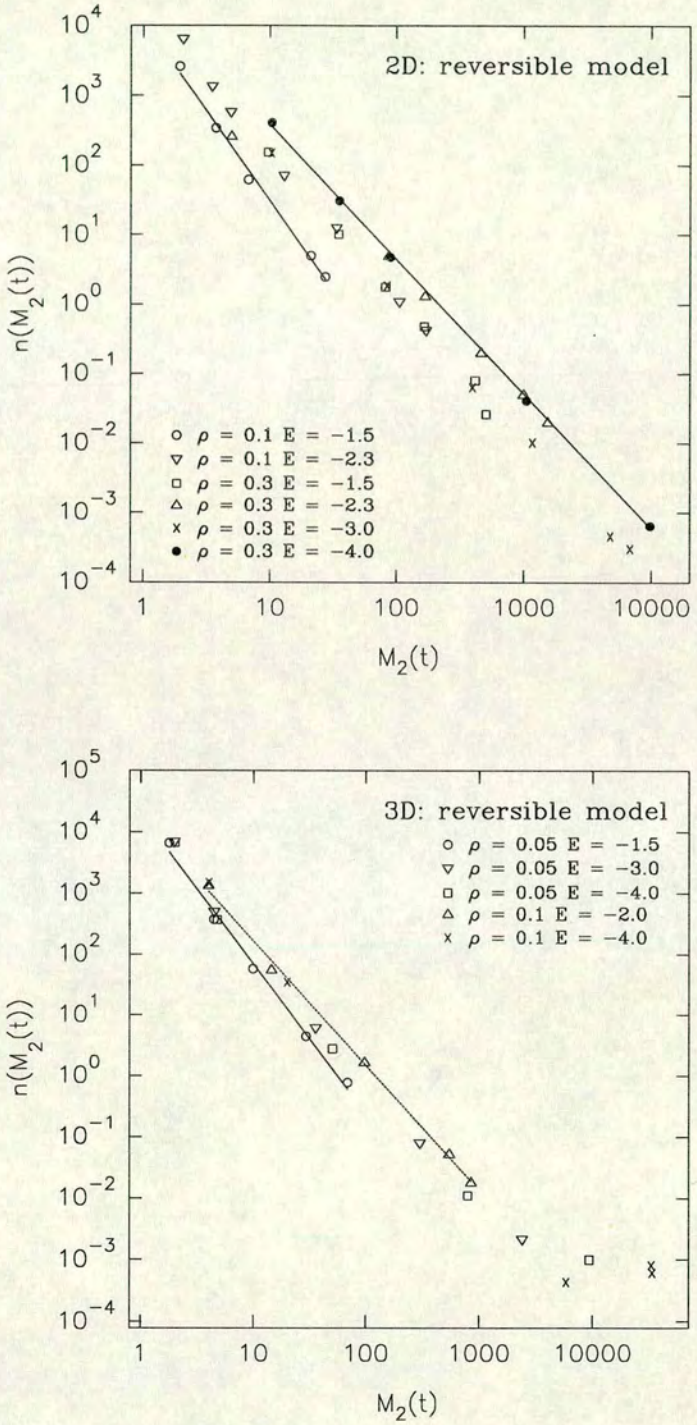

Figure A.10. The number of clusters at mass M_2, where M_2 is the weight-average mass, for *reversible* DLCA simulations. For clarity fitted lines are shown only for $\rho = 0.1, E = -1.5k_BT$ and $\rho = 0.3, E = -4.0k_BT$ (2D) and $\rho = 0.05, E = -1.5k_BT$ and $\rho = 0.1, E = -2.0k_BT$ (3D). Estimates of exponents for all datasets are given in Table A.1.

irreversible model would be quickly absorbed by the larger clusters. These show up in the mass distributions as the peak at small mass. At larger mass the number of clusters seems to scale with mass in the same way regardless of bond energy, though there will remain *kinetic* effects because the absolute rate of growth (Figures A.8 and A.9) does depend on bond energy.

A.1.3 Scaled form for the mass distribution

Proposing 'phenomenological' forms for the DLCA mass distribution, various authors have investigated whether the mass distribution may be characterised by some time-dependent *scale*, the distribution retaining otherwise a time-independent shape. Vicsek and Family [85] give a power-law form for the mass distribution (power-law in both mass and time) adopted from critical phenomena and percolation [178, 179]. Various exponents then appear in the problem. Simulation data has been shown to follow the proposed forms well [82, 86]. Rather than repeat this analysis, we will simply investigate directly to what extent the DLCA mass distribution may be characterised by single scale parameters, in particular comparing results from the irreversible simulations with those from reversible DLCA.

Figure A.11 shows plots of $n(m,t)/n(M_2(t))$ *vs.* $m/M_2(t)$ for the irreversible DLCA simulations in 2D and 3D. There is indeed a rather good data collapse, indicating that the mass distributions have a time-independent shape. As the aggregation proceeds the scales of the mass distributions are simply 'stretched' on the mass axis by the growing weight-average mass M_2 and 'shrunken' on the number axis by the falling $n(M_2)$. *But at a given fraction of the weight-average mass, the number of clusters as a fraction of the number at M_2 is approximately constant.* This is the physical meaning of the time-independent scaling of the mass distribution. Specifically, for example, the number of clusters with mass of half the weight-average mass is always some constant fraction a of the number at M_2. This is a rather striking result, implying as it does that M_2 'controls' the entire mass distribution. We discuss the experimental implications of this further below.

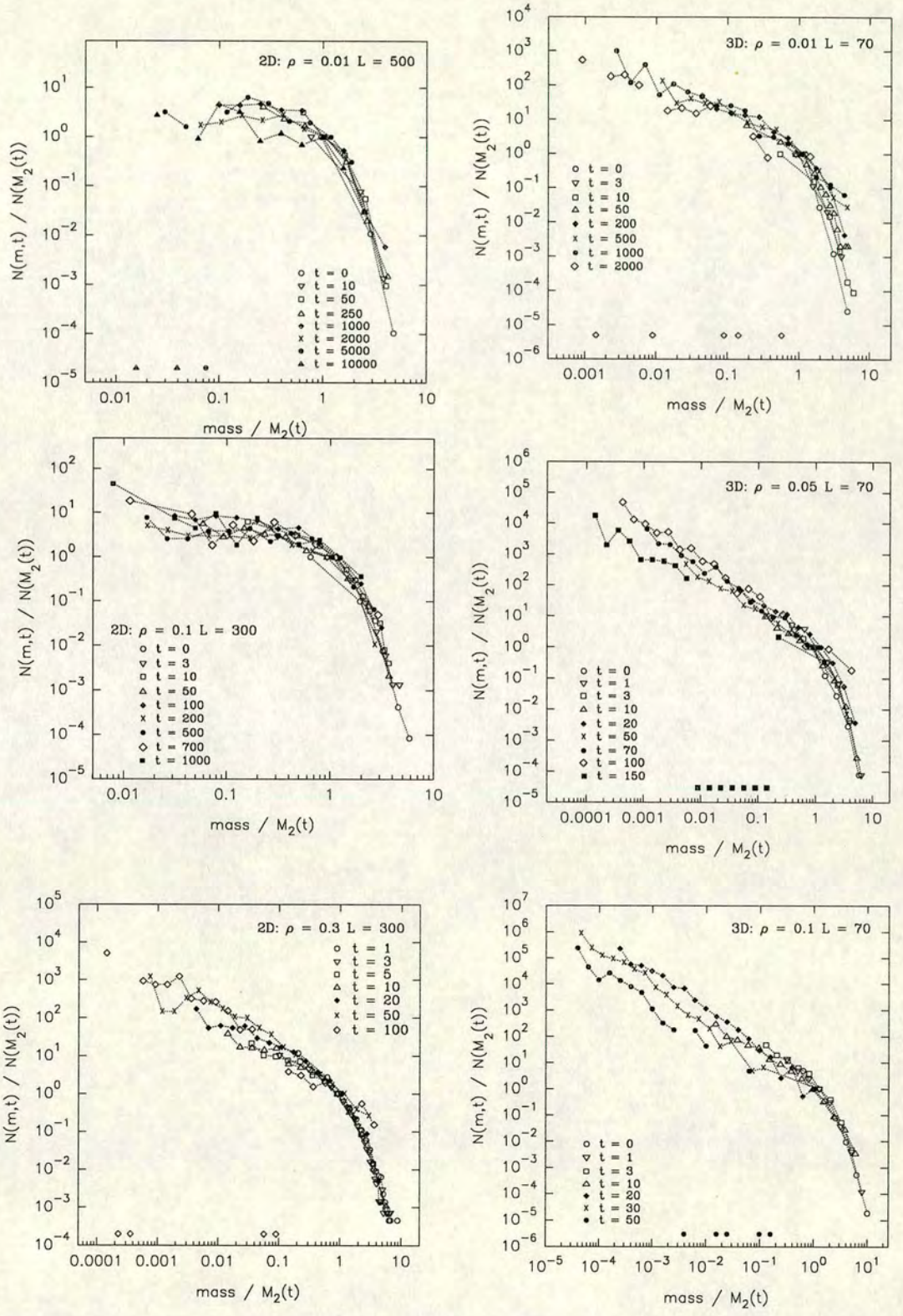

Figure A.11. Scaling form of the cluster mass distributions for 2D and 3D irreversible DLCA simulations. The data are scaled by the two 'characteristic' values, the weight-average M_2 for the mass on the x-axis and the number of clusters with mass M_2, $n(M_2)$ on the y-axis. The 'cut-off' in the distributions comes at $mass/M_2 \approx 1$, or $m_{cut} = M_2$, as discussed in section A.1.1.

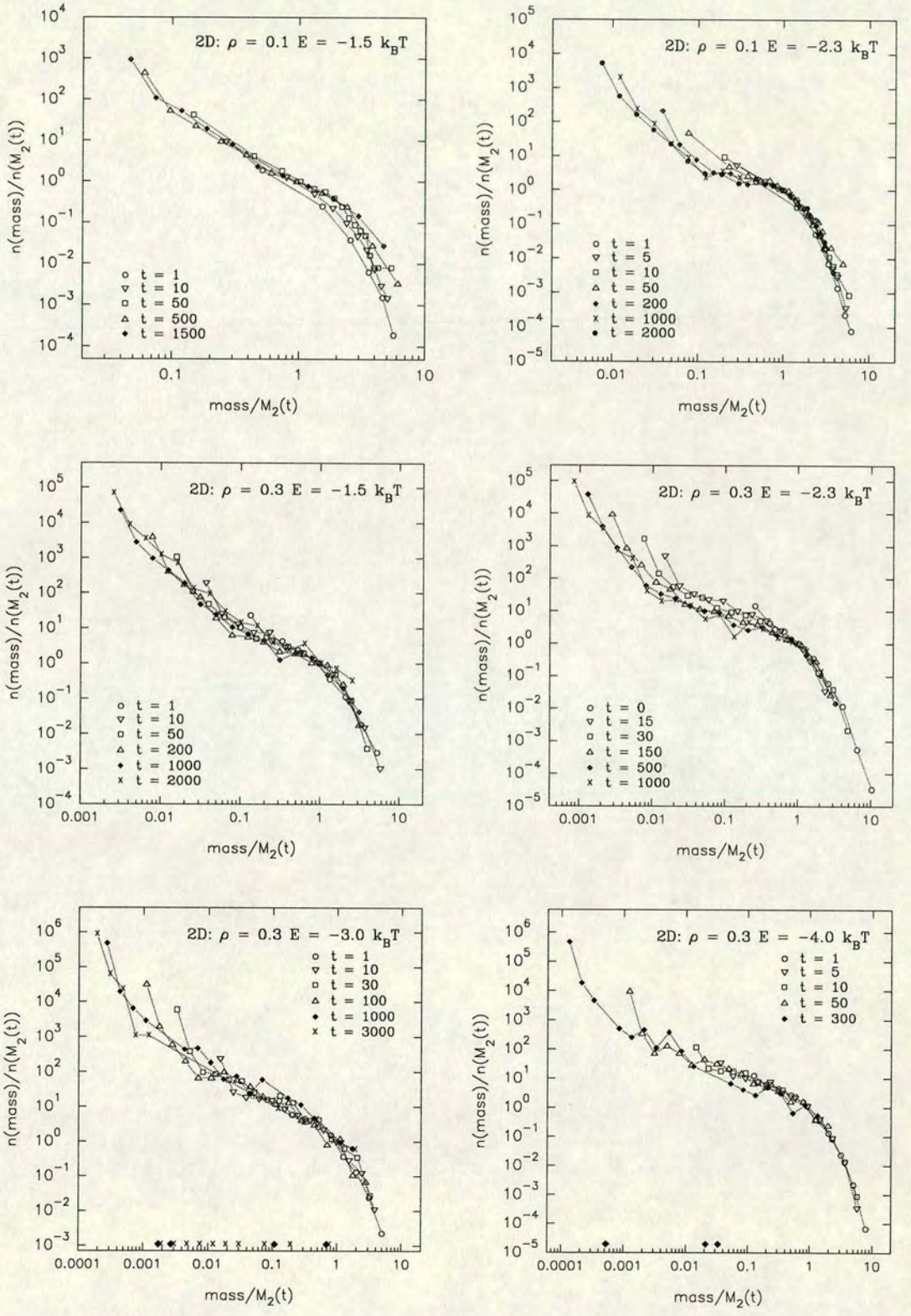

Figure A.12. Scaling form of the cluster mass distributions for 2D *reversible* DLCA simulations. The data are scaled as in Figure A.11 by the two 'characteristic' values M_2 and $n(M_2)$.

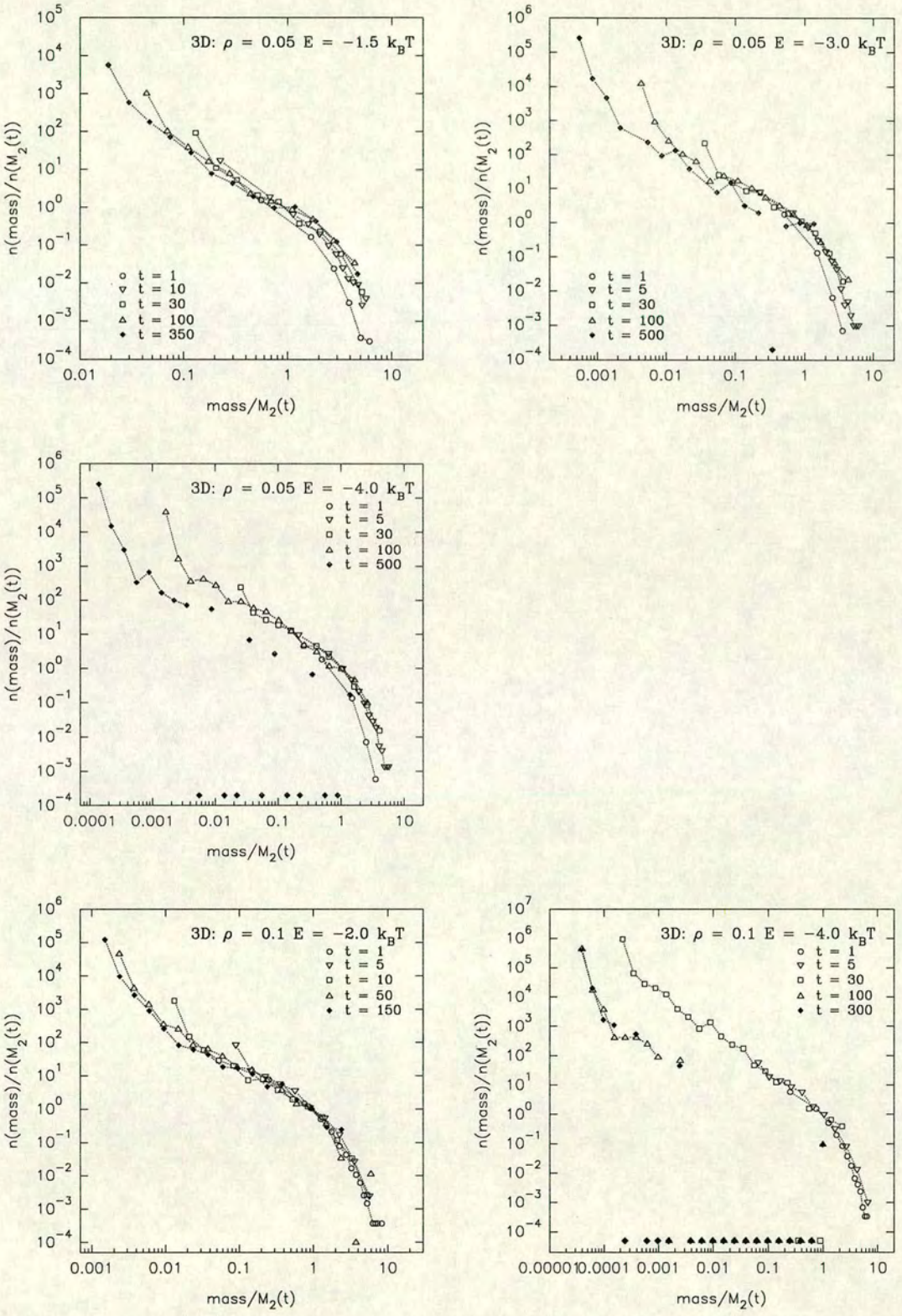

Figure A.13. Scaling form of the cluster mass distributions for 3D *reversible* DLCA simulations. The data are scaled as in Figure A.11 by the two 'characteristic' values M_2 and $n(M_2)$.

In the lower density systems where we can begin to see the development of a broad peak in $n(m,t)$ at $m > 1$, we would expect the early-time (pre-peak) scaling form and the late-time (peak regime) scaling form to differ. Unfortunately with the system sizes of these simulations we cannot obtain a peaked regime substantial enough to examine the scaling of $n(m,t)$ at these later times. Interestingly even when empty bins appear in the histograms, breaking up the continuous distribution, the values of $n(m,t)$ in non-empty bins still appear (at least at low enough density) to follow the scaling form.

At late times in higher density systems there is some indication that the scaling of $n(m,t)$ begins to fail. At high density, when M_2 begins to rise quickly due to the onset of gelation, one might expect M_2 no longer to characterise the complete distribution. However added to this is the problem of the finite size of the simulation (Figure A.4) which affects the late-time evolution of M_2. M_2 also shows strong fluctuations from time step to time step at late time when there are few clusters in the system, meaning that it is not so easy to estimate this 'characteristic' mass. Thus it is difficult to conclude with certainty how the scaling of $n(m,t)$ is affected as the DLCA system approaches gelation. A similar problem affects experiments (e.g. [7]) where the observable part of the system is quite limited in size.

The scaled plots for the irreversible 2D systems may be compared with the experimental data reported for a 2D charged colloidal system by Robinson and Earnshaw [7]. The experimental particle area fraction was $\Phi \approx 0.1$, so that we have simulation data at a comparable system concentration. In Ref. [7] the mass distribution was scaled by plotting $M_2(t)^2 n(m,t)$ *vs.* $m/M_2(t)$, equivalent to our scaling given that $n(M_2,t) \sim M_2^{-a}$ with $a \approx 2.0$. The shape of the scaled distributions from simulation and experiment is very similar, indicating that, according to the kinetic evolution of the mass distribution at least, the DLCA model is a good model for the 2D colloidal system. The lack of an obvious peak in the mass distribution measured in the experiment is probably due to limited observable system size, a similar problem to that met in the simulations. Interestingly the comparison of the results holds despite some extra complications in the experiment, such as an RLCA-DLCA 'crossover' at early time, some anomalous diffusion of large clusters in the experiment, and the other elements of the real system

which are not modelled in the simulations (hydrodynamic effects, rotational diffusion, and so on). Additionally the time-evolution of M_2 in the experiment is rather different to that in the simulation (Figure A.4). Thus the scaling of the mass distributions does not appear to be sensitive to these details. The very simple DLCA model is adequate to generate results which compare very well with the experimental system.

Weitz and Lin [41] reported one of the first direct measurements of the mass distribution in an 3D aggregating colloidal system. Again the form of the mass distributions is similar to our simulation data, and again a well-defined peak in the mass distribution was not convincingly demonstrated; as in the simulations the small number of clusters at late times led to difficulties in measuring a reasonably continuous distribution. Weitz and Lin showed that the measured mass distributions scaled in time, giving a scaling form again in agreement with the simulations reported here.

Effect of reversibility

Figures A.12 and A.13 show scaled mass distributions from the reversible simulations at various bond energies E. Once again the peak in the number of clusters at small masses $m << M_2$ is the most obvious change caused by the introduction of the finite bond energy. In particular, the data still scale well close to the weight-average mass M_2 (except at late time in the high density systems). This is consistent with our earlier observation that the $n(M_2)$ *vs.* M_2 scaling is not affected by the bond energy (see above).

At small mass the time-independent scaling breaks down. The scaling collapse proceeds to smaller and smaller m/M_2 as time increases. M_2 grows and so a given value of m/M_2 corresponds to larger and larger m; larger clusters are relatively less affected by the bond-breaking.

In the scaled plots the 'shoulder' below $m = M_2$ is quite apparent. Between the peak at small masses and the cut-off near $m = M_2$ the distribution follows roughly a power law in m/M_2, similarly to the irreversible model. In other words, the main difference in the scaling form of the mass distribution caused by the introduction of the finite bond energy is at the smallest mass fractions. This is perfectly reasonable: fragmentation of

a dimer is clearly a relatively more significant change than evaporation of a monomer from a large cluster.

Interestingly, the mass distribution measured by Weitz and Lin [41] for *reaction-limited* cluster aggregation conditions looks rather similar to that found in the reversible DLCA simulations. It may be that the experiment's 'slow aggregation' condition, interpreted as an indicator of reaction-limited aggregation, also involved some reversibility in the aggregation leading to a slowing down of growth. However given the preponderance of long-lived small clusters characteristic of both reaction-limited aggregation [7, 40] and reversible DLCA it is perhaps not surprising that the mass distributions look qualitatively similar.

A.1.4 Mass distributions—Conclusions

In these simulations we have measured mass distributions consistent (for the irreversible model) with those measured both in previous simulations [85, 86] and in experiment [7, 41]. There are indications that in high density systems space-filling or gelation occurs too quickly for the mass distribution to attain the familiar 'broad-peaked' form[1]. Essentially there is insufficient space in the high density system for the typical 'DLCA' process of self-similar aggregation of larger and larger fractal clusters to be realised [69]. However *this effect does not appear to invalidate the time-independent scaling properties of the mass distribution.* Therefore it appears that despite the striking differences in the appearance of systems at high density and low density (see e.g. the pictures in Chapter 3), the scaling of the mass distributions is not substantially affected. Unfortunately study of the mass distribution very close to gelation is (almost by definition) difficult, especially in simulations.

There are conflicting reports as to whether strong small-Q scattering peaks at $Q > 0$ are observed in *reaction limited* cluster aggregation systems. Carpineti and co-workers found no peak in their (3D) RLCA experiments [46]. In contrast, Robinson and Earnshaw [52] do see a peak in $I(Q)$ for a 2D RLCA system. In 3D RLCA simulations

[1] The peak is *broad*, that is the cluster system remains quite polydisperse; see Chapter 5.

Gonzalez and Ramirez-Santiago also find a small-Q peak [65]. These contradictions are, to our knowledge, so far unresolved. The possible *lack* of a strong scattering peak in RLCA has been linked with the similar lack of a strong peak in the RLCA mass distribution [49]. It has been suggested in other words that the characteristic length scale indicated by the scattering peak is reflected in a strongly characteristic mass. However, whether RLCA has a scattering peak or not, the peak we observe in the mass distribution in the DLCA system (at the lower densities) does not appear until quite late time, whereas the peak in the scattering appears very quickly. Additionally there is never a single strong peak in $n(m,t)$ for the reversible simulations, where larger masses are fragmented to broaden the distribution at smaller masses, while the reversible systems (except possibly at very low bond energy) of course do show strong scattering peaks. Thus there seems to be no direct correspondence between the appearance in the aggregating system of a characteristic length scale and the existence of a strongly peaked mass distribution. The differences between scattering results from DLCA and RLCA systems still require explanation. There *is* a characteristic mass in DLCA (and it is characteristic from the earliest times, consistent with the scattering) but it appears in the mass distribution more as the edge of a shoulder than as a strong peak. The characteristic mass M_2 is connected to the scattering via the average form factor $P(Q)$ ($P(Q \to 0) \simeq M_2$, see Chapter 3). In other words, the clusters at mass M_2, while they are not especially numerous in the number distribution (there is no strong peak) do dominate the scattering *form factor* at long length scales; this may be the origin of the connection between characteristic length scale and characteristic mass. (In fact RLCA mass distributions have also been shown to scale [7, 41], indicating that there is a characteristic mass in RLCA too; again it does not appear as a strong peak but rather as a shoulder or cut-off at high masses.)

The main effect of reversibility in the aggregation, at least at the bond energies studied here, is that the system retains a substantial population of small clusters and monomers. This is true even at the higher bond energies, because even at (say) $E = -4.0k_BT$ there is a reasonable probability that single-bonded particles can escape and 'survive' for at

least some time as free monomers[2]. Note that the scattering behaviour (as measured for instance by the saturation of growth of the small-Q peak) in the higher-energy systems approaches quite closely the irreversible model (e.g. by $E = -4.0k_BT$), but the systems still differ in the substantial population of small clusters; *these small clusters do not play much of a part in the scattering function near the peak or in the space-filling.* Measurements besides $I(Q_m)$ are required to detect the presence of the small clusters and to fully describe the system.

The irreversible DLCA process features a mass distribution with a *time-independent shape* whose scale is determined by only two characteristic parameters, the weight-average mass M_2 and the number of clusters at M_2, $n(M_2)$. Since $n(M_2) \sim M_2^{-a}$ it may be argued that only a single parameter is required in addition to the time-independent functional form to fully characterise the mass distribution at all times far from gelation (however then an estimate of a is required). Even when the interparticle potential is weak so that fragmentation of clusters is possible, the mass distribution away from the smaller masses retains an approximately time-independent scaled form. Such reversibility makes the scaling break down at small clusters, however, as might be expected given the substantial population of small clusters which remain in the system at all times in the reversible model. This population is maintained regardless of the growth of M_2, that is M_2 does not strongly 'characterise' the mass distribution at the small masses. In this way the evaporation and condensation of small clusters and monomers might be seen as a process almost 'separate' from the larger scale growth.

Experimentally, the existence of the time-independent scaling form for the mass distribution implies that one need only measure the full mass distribution at one time; thereafter (at times well before gelation) the full distribution may be obtained simply by measuring the characteristic values M_2 and $n(M_2)$ (or measuring M_2 and making some assumption about a). M_2 may typically be measured quite simply in many systems via scattering (see Chapter 3) by measuring the average form factor of the clusters. In practice this can only be done though in dilute systems; in concentrated systems some

[2] Of course most of the mass at high bond energy is contained in the large clusters, but the *number fraction* of small clusters is still significant.

method of dilution which does not change the individual cluster structure (or at least not sufficiently to affect the scattering measurement of M_2) must be employed.

A.2 The mass-radius relation

Finally for completeness we return to a point where many previous studies of DLCA have started (and often finished): estimation of the fractal dimension of individual clusters from the mass-radius relation:

$$m \sim R_g^{d_f}. \tag{A.6}$$

We have estimated the fractal dimension d_f from linear least-squares fitting to the logarithms of the data, at various time steps through the aggregation in each simulation; results are given in Tables A.3 to A.5. Note that all fits exclude clusters of less than 5 particles, in order to try to minimise the effect of very small non-fractal clusters. It is clear that in most cases the estimated exponent d_f changes during the simulation. We have 'combined' data from sets of time steps in order to present more concise plots; these combined 'scatter' plots of the masses of clusters *vs.* their radii are given in Figures A.14, A.15, A.16 and A.17. The Tables give the 'combined' d_f estimates too. Essentially where significant evolution of d_f is observed we have tried to select for the 'combined' m *vs.* R_g plots data from late times where changes in d_f have stopped or at least slowed down. It should be noted though that there is a complex interdependence of many of the data points in the scatter plots, since parts of clusters which are plotted from an early time combine to make larger clusters at later times. Thus estimation of a variance from the scatter plots would be problematic. We do not attempt to estimate error bars here anyway, since we are more interested in the general evolution/size dependence of d_f. The estimates of d_f we obtain for the irreversible model are in reasonable agreement with other simulations [30, 31, 34, 120] in which larger statistical samples were used to obtain error bars. Note however that such statistical estimation

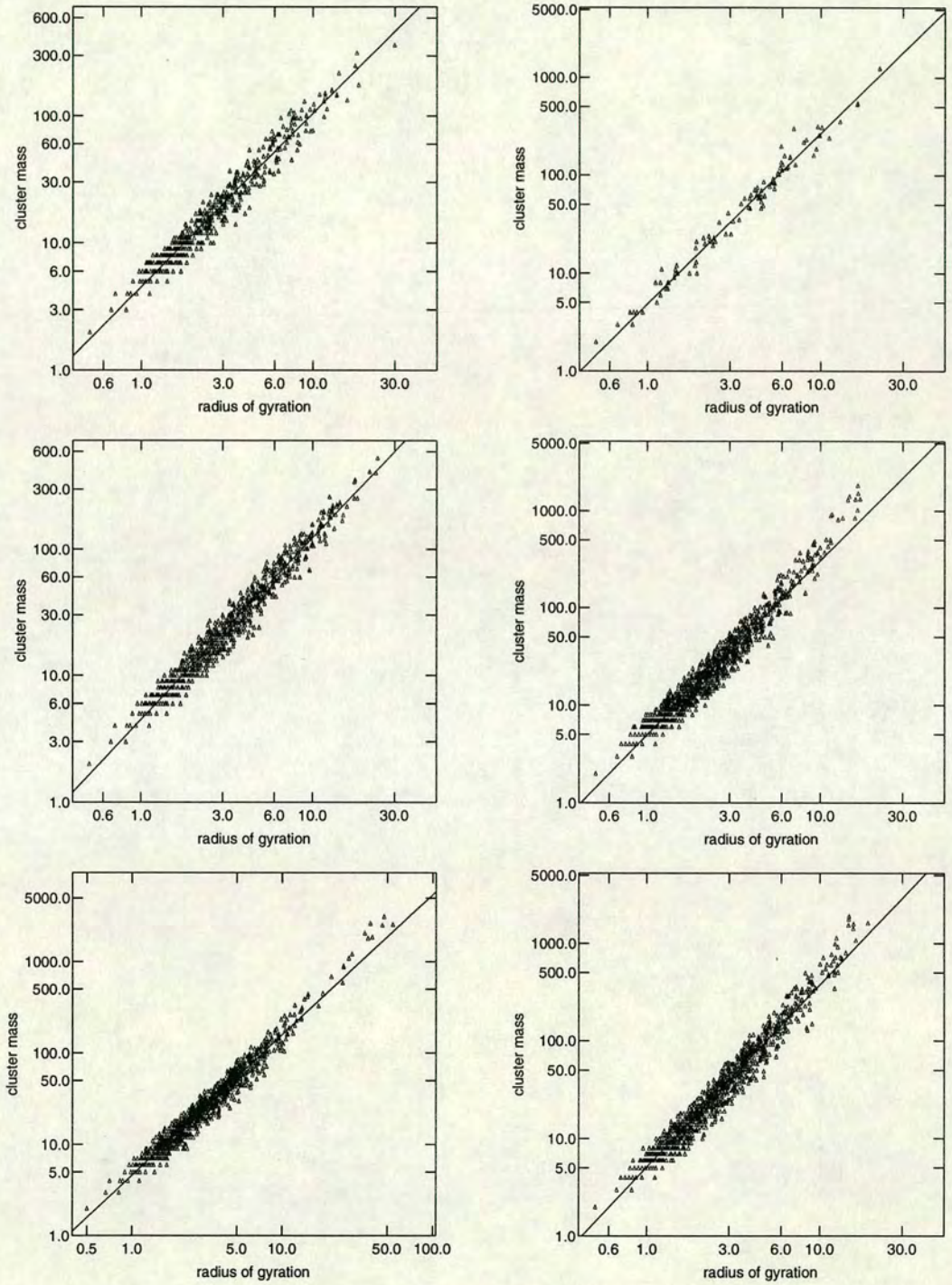

Figure A.14. Scatter plot of cluster mass *vs.* cluster radius in irreversible lattice-based DLCA simulations. Each of the plots shows data for a set of time-steps as described in the text and detailed in Table A.3. Lines are least-squares fits to the logarithms of the data, excluding all clusters of less than 5 particles. The left column shows results from 2D simulations at densities $\rho = 0.01$, $\rho = 0.1$ and $\rho = 0.3$; the right column 3D results at densities $\rho = 0.01, 0.05$ and 0.1.

Density	Time	d_f	No. clusters	
(a) 2D lattice				
0.01	1000	1.21	201	
	3000	1.29	126	
	10000	1.38	47	
0.01	50-10000	1.36	3444	Combined
0.1	50	1.32	517	
	100	1.38	337	
	200	1.45	188	
0.1	50-500	1.44	1587	Combined
0.3	5	1.47	1216	
	10	1.54	676	
	50	1.66	63	
0.3	5-50	1.54	1955	Combined
(b) 3D lattice				
0.01	100	1.40	261	
	500	1.72	60	
	1000	1.76	21	
0.01	500-3000	1.74	152	Combined
0.05	10	1.43	1242	
	50	1.87	256	
	100	1.98	53	
0.05	20-200	1.79	2043	Combined
0.1	5	1.63	2011	
	10	1.81	1036	
	30	1.94	85	
0.1	10-30	1.87	1813	Combined
(c) 2D, off-lattice				
0.1	20000	1.33	80	
	50000	1.44	51	
	100000	1.44	25	
0.1	50000-900000	1.47	422	Combined
0.3	700	1.28	91	
	1200	1.45	76	
	3000	1.51	37	
	10000	1.68	10	
0.3	900-10000	1.56	235	Combined

Table A.3. Fitted fractal dimensions d_f from the mass-radius relation, $m \sim R_g^{d_f}$, for irreversible DLCA simulations. All the fits exclude clusters smaller than 5 particles. At each density a 'combined' fit is also given, where all clusters from a number of time steps between the given times are included in the fit.

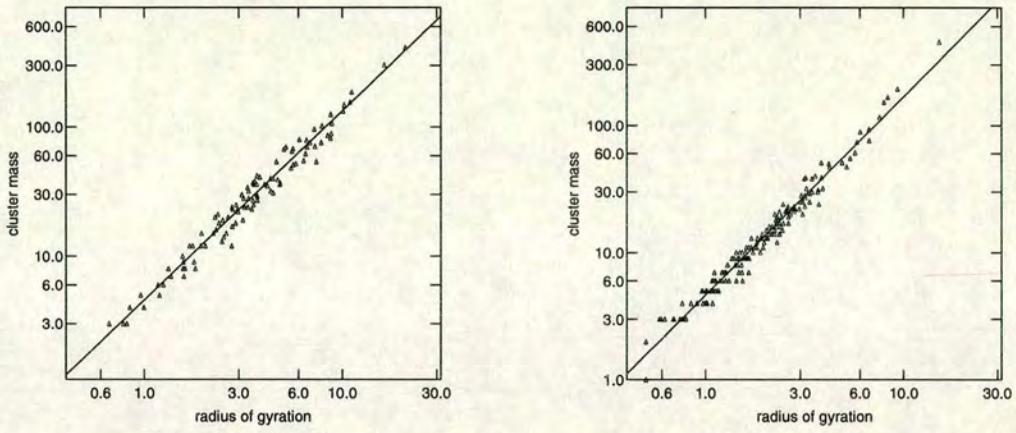

Figure A.15. Cluster mass *vs.* cluster radius in 2D irreversible off-lattice DLCA simulations. Each of the plots shows data for a set of time-steps as described in the text. Lines are least-squares fits to the logarithms of the data, excluding all clusters of less than 5 particles. The left plot shows results for area fraction $\Phi = 0.1$, the right plot area fraction $\Phi = 0.3$.

of error bars assumes that the data do follow a single power law and so does not take into account the possibility of structural differences at different length scales. This point becomes more important in the reversible model.

Irreversible DLCA

In the irreversible simulations at low density the estimates of d_f agree quite well with previous simulations and the 'accepted' DLCA fractal dimensions, $d_{f,DLCA} \approx 1.45 \pm 0.05$ (2D) and $d_{f,DLCA} \approx 1.75 \pm 0.05$ (3D). However estimates show an increase from smaller d_f at early times toward the 'accepted' values, as if the smaller clusters which dominate at early time have lower fractal dimensions. This may be an effect of the use of the lattice in the simulations. With the restriction of the lattice structure at short length scales, small clusters may tend to be more ramified than would be the case in a continuum. However results from small-scale off-lattice simulations in 2D show a similar trend for d_f to increase over time as more larger clusters appear in the system (Figure A.15 and Table A.3). The time/size dependence of the estimated d_f is more likely simply a reflection of the fact that the fractal structure of the clusters will always be better defined for larger clusters. On small length scales self-similarity will be less

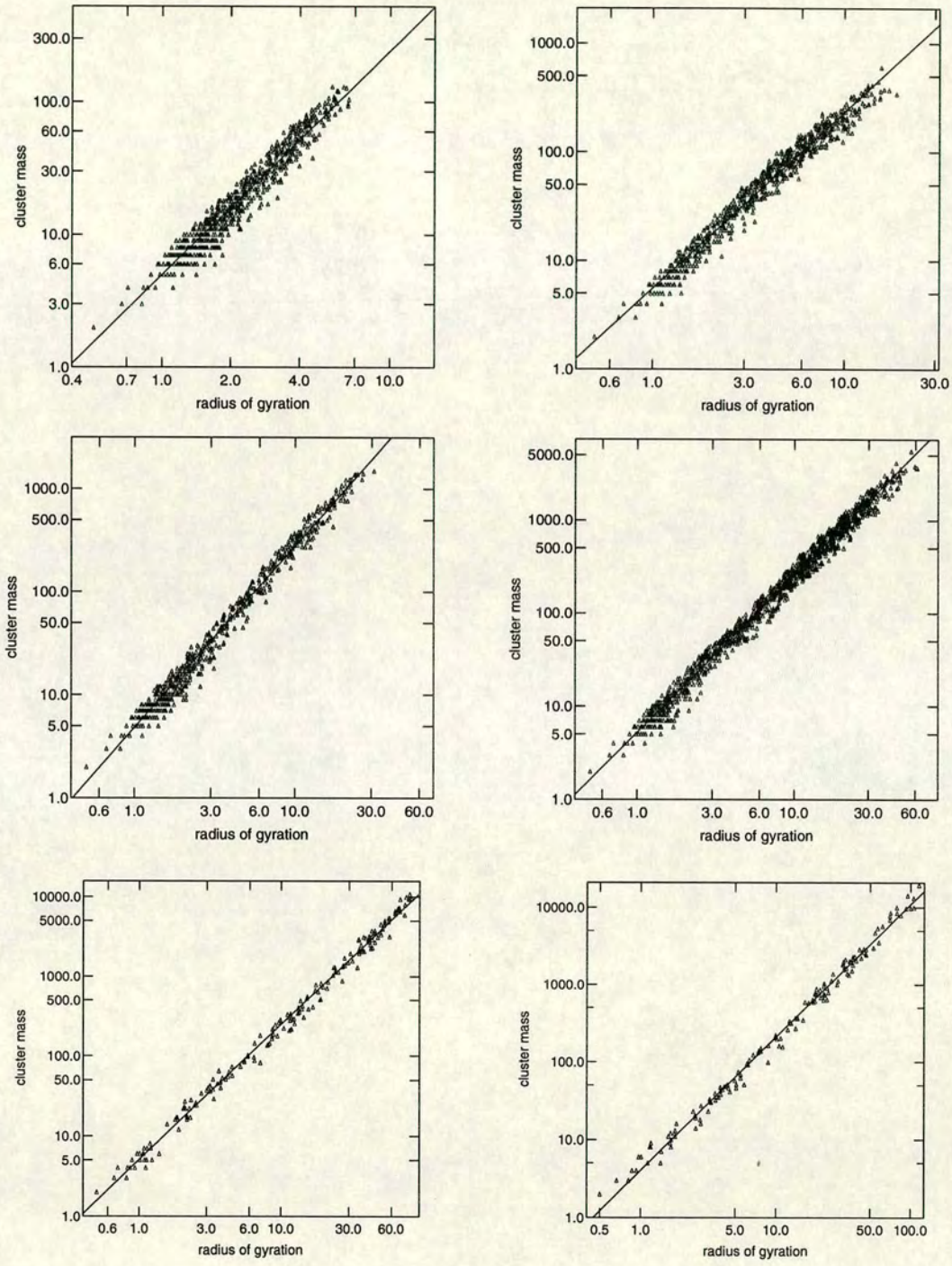

Figure A.16. Cluster mass *vs.* cluster radius in 2D reversible DLCA simulations. Lines are least-squares fits to the logarithms of the data, excluding all clusters of less than 5 particles. The top row shows density $\rho = 0.1$, $E = -1.5k_BT$ (left) and $E = -2.3k_BT$; the middle row shows $\rho = 0.3$, $E = -1.5k_BT$ (left) and $E = -2.3k_BT$; the bottom row $\rho = 0.3$, $E = -3.0k_BT$ (left) and $E = -4.0k_BT$.

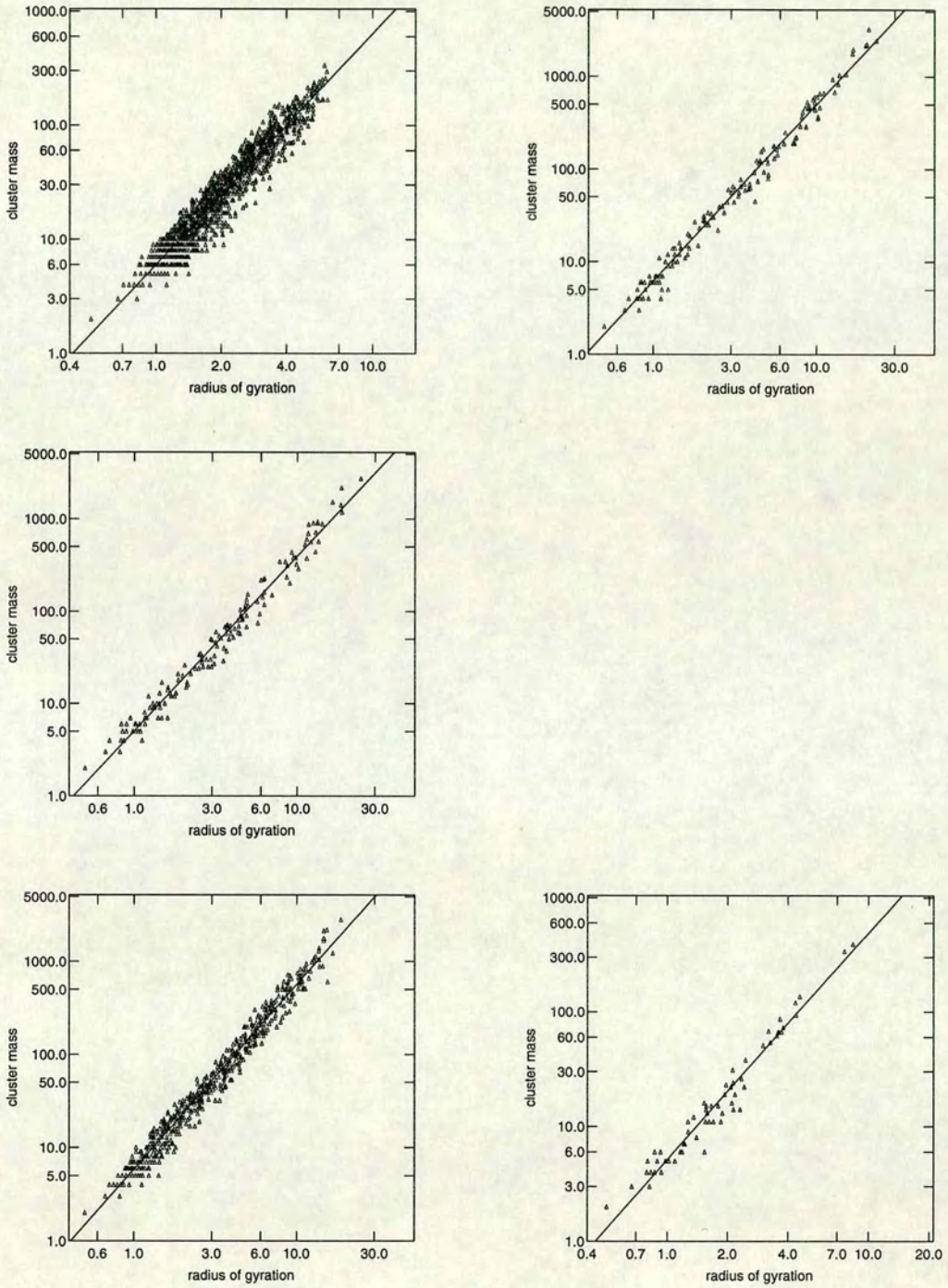

Figure A.17. Cluster mass *vs.* cluster radius in 3D reversible DLCA simulations. Lines are least-squares fits to the logarithms of the data, excluding all clusters of less than 5 particles. The upper three plots are density $\rho = 0.05$, $E = -1.5k_BT$ (top left) and $-3.0k_BT$ (top right) and $E = -4.0k_BT$ (middle). The bottom row are density $\rho = 0.1$, $E = -2.0k_BT$ (left) and $E = -4.0k_BT$.

Density	Bond energy	Time	d_f	No. clusters	
2D					
0.1	-1.5	100	1.47	429	
		500	1.65	327	
		1000	1.66	287	
0.1	-1.5	1000-2000	1.69	1096	Combined
	-2.3	100	1.37	1167	
		500	1.53	478	
		1000	1.57	337	
0.1	-2.3	1000-2000	1.62	878	Combined
0.3	-1.5	10	1.45	1079	
		100	1.63	397	
		500	1.72	273	
0.3	-1.5	1000-2000	1.76	911	Combined
	-2.3	10	1.50	2164	
		150	1.61	383	
		500	1.67	198	
0.3	-2.3	500-1000	1.68	1845	Combined
	-3.0	10	1.50	665	
		100	1.61	88	
		1000	1.66	27	
		5000	1.70	11	
0.3	-3.0	500-5000	1.69	196	Combined
	-4.0	10	1.53	1784	
		50	1.66	218	
		100	1.72	71	
		500	1.71	22	
0.3	-4.0	100-1000	1.72	142	Combined

Table A.4. Fitted fractal dimensions d_f from the mass-radius relation, $m \sim R_g^{d_f}$, for reversible DLCA simulations in 2D. Bond energy is in units of K_BT. The fits exclude clusters smaller than 5 particles. 'Combined' fits are also given, where all clusters from a number of time steps between the given times are included in the fit.

evident. This point demonstrates once again the problem of trying to fully characterise the aggregating system using the single statistic d_f.

Density	Bond energy	Time	d_f	No. clusters	
3D					
0.05	-1.5	50	1.75	636	
		100	1.92	485	
		200	2.03	373	
0.05	-1.5	100-350	2.03	2187	Combined
	-3.0	50	1.73	1145	
		100	1.82	152	
		300	1.88	47	
0.05	-3.0	200-500	1.91	137	Combined
	-4.0	30	1.72	607	
		50	1.81	306	
		100	1.91	95	
0.05	-4.0	100-500	1.89	140	Combined
0.1	-2.0	20	1.81	710	
		50	1.96	275	
		100	1.95	168	
0.1	-2.0	50-150	1.99	584	Combined
	-4.0	10	1.80	1095	
		30	1.93	100	
0.1	-4.0	50-400	1.98	57	Combined

Table A.5. Fitted fractal dimensions d_f from the mass-radius relation, $m \sim R_g^{d_f}$, for reversible DLCA simulations in 3D. Bond energy is in units of K_BT. The fits exclude clusters smaller than 5 particles. 'Combined' fits are also given, where all clusters from a number of time steps between the given times are included in the fit.

At higher density especially in 2D there is some indication that the fractal dimension of clusters is higher than the 'accepted' estimates. For instance in the combined plots (Figure A.14, $\rho = 0.3$ in 2D and $\rho = 0.05$ and 0.1 in 3D) there seems a tendency for the largest clusters to begin to 'stray' upward from the fitted power-law, in other words for the fractal dimension of the largest clusters to be higher. A previous study of 2D DLCA at high number density [120] reached a similar conclusion. However the range of length scales over which fractal structure might be observed becomes severely limited at higher density because of gelation; the gel cluster size (Chapter 1) is sensitively dependent on density. The large clusters may have somewhat different structure on

long length scales (as the gel clusters begin to contact each other and aggregate near-homogeneously). Given the tightly-packed nature of the high density system (see the pictures in Chapter 3) one would expect structural changes at high density, and it would seem that trying to quantify these changes solely with an estimate of a single exponent over a limited scale is not likely to be adequate.

Reversible DLCA

In the reversible simulations the time-dependent nature of the mass-radius dimension d_f is more noticeable. In all simulations at finite bond energy there is a marked rise in the estimated d_f with time (Tables A.4 and A.5). In the reversible model this is consistent with the expected compactification of the clusters as particles move into more stable multiply-bonded configurations. The increase of d_f is more substantial the lower the bond energy. The time-evolution of d_f found here is consistent with that studied in previous simulations of reversible DLCA by Shih and co-workers [107] whose results were limited to estimates of d_f. Time-dependent fractal dimensions have been measured in experiments and ascribed to restructuring effects [97, 155, 180]. However it has been shown clearly in previous Chapters that the effects of the finite bond energy are too substantial to hope to fully describe them with a single parameter like the fractal dimension of individual clusters. It is clear that in the reversible model clusters can have different structure on different length scales, so that a single power-law relation between mass and radius is less applicable, and may indeed give misleading results.

Bibliography

[1] E. Dickinson, *An Introduction to Food Colloids*, Oxford University Press, 1992; A. M. Donald, *Rep. Prog. Phys.* 57 (1994) 1081.

[2] P. N. Pusey, in *Liquids, Freezing, and the Glass Transition*, eds. J.P. Hansen, D. Levesque and J. Zinn-Justin. Elsevier Science, 1991.

[3] J. L. Harland, S. I. Henderson, S. M. Underwood and W. van Megen, *Phys. Rev. Lett.* 75 (1995) 3572.

[4] R. J. Hunter, *Introduction to Modern Colloid Science*, Oxford University Press, 1993.

[5] W. B. Russel, D. A. Saville and W. R. Schowalter, *Colloidal Dispersions*, Cambridge University Press, 1989.

[6] M. Carpineti, F. Ferri, M. Giglio, E Paganini and U. Perini, *Phys. Rev. A* 42 (1990) 7347.

[7] D. J. Robinson and J. C. Earnshaw, *Phys. Rev. A* 46 (1992) 2045; D. J. Robinson and J. C. Earnshaw, *Phys. Rev. A* 46 (1992) 2055; D. J. Robinson and J. C. Earnshaw, *Phys. Rev. A* 46 (1992) 2065.

[8] P. G. de Gennes, *Scaling Concepts in Polymer Physics*, Cornell University Press, 1979.

[9] H. N. W. Lekkerkerker, J. K. G. Dhont, H. Verduin, C. Smits and J. S. van Duijneveldt, *Physica A* 213 (1995) 18.

[10] J. W. Jansen, C. G. de Kruif and A. Vrij, *J. Coll. Int. Sci* 114 (1986) 481; C. G. de Kruif, P. W. Rouw, W. J. Briels, M. H. G Duits, A. Vrij and R. P. May, *Langmuir* 5 (1989) 422.

[11] P. N. Pusey, A. D. Pirie and W. C. K. Poon, *Physica A* 201 (1993) 322.

[12] S. M. Ilett, A. Orrock, W. C. K. Poon and P. N. Pusey, *Phys. Rev. E* 51 (1995) 1344.

[13] W. C. K. Poon and P. N. Pusey, in *Observation, Prediction and Simulation of Phase Transitions in Complex fluids*, eds. M. Baus, L. F. Rull and J.-P. Ryckaert. NATO ASI Series, Kluwer, 1995.

[14] S. Asakura and F. Oosawa, *J. Chem. Phys.* 22 (1954) 1255.

[15] H. N. W Lekkerkerker, W. C. K. Poon, P. N. Pusey, A. Stroobants and P. B. Warren, *Europhysics Lett.* 20 (1992) 559.

[16] A. D. Pirie, Ph.D. Thesis. University of Edinburgh, 1995 (unpublished).

[17] P. Bartlett, R. H. Ottewill and P. N. Pusey, *Phys. Rev. Lett.* 68 (1992) 3801; P. Bartlett, R. H. Ottewill and P. N. Pusey, *J. Chem. Phys.* 93 (1990) 1299.

[18] A. D. Dinsmore, A. G. Yodh and D. J. Pine, *Phys. Rev. E* 52 (1995) 4045.

[19] A. Imhof and J. K. G. Dhont, *Phys. Rev. Lett.* 75 (1995) 1662.

[20] C. A. Murray, W. O. Sprenger and R. A. Wenk, *Phys. Rev. B* 42 (1990) 688; C. A. Murray, W. O. Sprenger and R. A. Wenk, *J. Phys. Cond. Matter* 2 (1990) SA385.

[21] M. Kerker, *The scattering of light and other electromagnetic radiation*, Academic Press, 1969.

[22] P. N. Pusey and W. van Megen, *Nature* 320 (1986) 340.

[23] J. V. Sanders, *Acta Cryst.* A 24 (1968) 427.

[24] J. E. Martin and A. J. Hurd, *J. Appl. Crystallography* 20 (1987) 61.

[25] D. A. Weitz, J. S. Huang, M. Y. Lin and J. Sung, *Phys. Rev. Lett.* 54 (1985) 1416.

[26] M. Y. Lin, H. M. Lindsay, D. A. Weitz, R. Klein, R. C. Ball and P. Meakin, *J. Phys. Cond. Matter* 2 (1990) 3093.

[27] A. Guinier and G. Fournet, *Small-angle scattering of X-rays*, Wiley, 1955.

[28] S. R. Forrest and T. A. Witten, *J. Phys. A: Math. Gen.* 12 (1979) L109.

[29] T. A. Witten and L. M. Sander, *Phys. Rev. Lett.* 47 (1981) 5686.

[30] P. Meakin, *Phys. Rev. Lett.* 51 (1983) 1119.

[31] M. Kolb, R. Botet and R. Jullien, *Phys. Rev. Lett.* 51 (1983) 1123.

[32] D. W. Schaefer, J. E. Martin, P. Wiltzius and D. S. Cannell, *Phys. Rev. Lett.* 52 (1984) 2371.

[33] D. A. Weitz and M. Oliveria, *Phys. Rev. Lett.* 52 (1984) 1433.

[34] R. Jullien, M. Kolb and R. Botet, *J. Physique Lett.* 45 (1984) L211.

[35] A. J. Hurd and D. W. Schaefer *Phys. Rev. Lett.* 54 (1985) 1043.

[36] P. Richetti, J. Prost and P. Barois, *J. Physique Lett.* 45 (1984) L1137.

[37] A. J. Armstrong, R. C. Mocklet and W. J. O'Sullivan, *J. Phys. A: Math. Gen.* 19 (1986) L123.

[38] A. T. Skjeltorp, *Phys. Rev. Lett.* 58 (1987) 1444.

[39] D. Asnaghi, M. Carpineti, M. Giglio and M. Sozzi, *Phys. Rev. A* 45 (1992) 1018.

[40] M. Y. Lin, H. M. Lindsay, D. A. Weitz, R. C. Ball, R. Klein and P. Meakin, *Phys. Rev. A* 41 (1990) 2005.

[41] D. A. Weitz and M. Y. Lin, *Phys. Rev. Lett.* 57 (1986) 2037.

[42] J. Feder, T. Jossang and E. Rosenqvist, *Phys. Rev. Lett.* 53 (1984) 1403.

[43] J.-F. Roussel, R. Blanc and C. Camoin, *J. Physique* 50 (1989) 3269.

[44] G. Helgesen, A. T. Skjeltorp, P. M. Mors, R. Botet and R. Jullien, *Phys. Rev. Lett.* 61 (1988) 1736.

[45] M. Carpineti and M. Giglio, *Phys. Rev. Lett.* 68 (1992) 3327.

[46] M. Carpineti and M. Giglio, *Phys. Rev. Lett.* 70 (1993) 3828.

[47] M. Carpineti, M. Giglio and V. DeGiorgio, *Phys. Rev. E* 51 (1995) 590.

[48] F. Ferri, B. J. Frisken and D. S. Cannell, *Phys. Rev. Lett.* 67 (1991), 3626.

[49] J. Bibette, T. G. Mason, H. Gang and D. A. Weitz, *Phys. Rev. Lett.* 69 (1992) 981.

[50] J. Bibette, T. G. Mason, H. Gang, D. A. Weitz and P. Poulin, *Langmuir* 9 (1993) 3352.

[51] W. C. K. Poon, A. D. Pirie and P. N. Pusey, *Faraday Disc.* (1995), in press.

[52] D. J. Robinson and J. C. Earnshaw, *Phys. Rev. Lett.* 71 (1993) 715

[53] M. Takenaka, T. Izumitani and T. Hashimoto, *J. Chem. Phys.* 92 (1990) 4566; T. Hashimoto, M. Takenaka and T. Izumitani, *J. Chem. Phys.* 97 (1992) 679.

[54] P. W. Rouw, A. T. J. M. Woutersen, B. J. Ackerson and C. G. de Kruif, *Physica A* 156 (1989) 876.

[55] J. D. Gunton, M. San Miguel and P. S. Sahni, in *Phase Transitions and Critical Phenomena*, Vol. 8, p. 267, eds. C. Domb and J. L. Lebowitz. Academic Press, 1983.

[56] K. Schatzel and B. J. Ackerson, *Phys. Rev. Lett.* 68 (1992) 337; K. Schatzel and B. J. Ackerson, *Phys. Rev. A* 48 (1993) 3766.

[57] J. W. Cahn, *J. Chem. Phys.* 42 (1965) 93; A. B. Bortz, M. Kalos, J. L. Lebowitz amd M. Zendejas, *Phys. Rev. B.* 10 (1974) 535; J. Marro, A. B. Bortz, M. Kalos and J. L. Lebowitz, *Phys. Rev. B* 12 (1975) 2000.

[58] J. Marro, J. L. Lebowitz and M. Kalos, *Phys. Rev. Lett.* 43 (1979) 282.

[59] K. Binder, C. Billotet and P. Mirold, *Z. Phys. B* 30 (1978) 183.

[60] J. S. Langer, in *Solids far from Equilibrium*, p. 297, ed. C. Godreche. Cambridge University Press, 1992.

[61] B. Mandelbrot, *The Fractal Geometry of Nature*, Freeman, 1983.

[62] T. Vicsek, *Fractal Growth Phenomena*, World Scientific, 1994.

[63] C. Allain and B. Jouhier, *J. Physique Lett.* 44 (1983) L421.

[64] B. D. Butler, H. J. M. Hanley, D. Hansen and D. J. Evans, *Phys. Rev. Lett.* 74 (1995), 4468.

[65] A. E. Gonzalez and G. Ramirez Santiago, *Phys. Rev. Lett.* 74 (1995) 1238.

[66] J. W. Cahn, *Trans. Metall. Soc. AIME* 242 (1968) 166.

[67] F. Sciortino and P. Tartaglia, *Phys. Rev. Lett.* 74 (1994) 282.

[68] S. W. Koch, R. C. Desai and F. F. Abraham, *Phys. Rev. A* 27 (1983) 2152.

[69] F. Sciortino, A. Belloni, and P. Tartaglia, *Phys. Rev. E* 52 (1995) 4068.

[70] D. N. Sutherland, *J. Coll. Int. Sci.* 25 (1967) 373.

[71] R. M. Brady and R. C. Ball, *Nature* 309 (1984) 225; L. Niemeyer, L. Pietronero and H. J. Wiesmann, *Phys. Rev. Lett.* 52 (1984) 1033; M. Matsushita, M. Sano, Y. Hayakawa, H. Honjo and Y. Sawada, *Phys. Rev. Lett.* 53 (1984) 286; J. Nittmann, G. Daccord and H. E. Stanley, *Nature* 314 (1985) 141; J. Zhang, D. Liu and K. Colbow, *Phys. Rev. B* 48 (1993) 9130; P. Jensen, A.-L. Barabasi, H. Larralde, S. Havlin and H. E. Stanley, *Nature* 368 (1994) 22.

[72] L. Finegold, *Biochim. Biophys. Acta* 448 (1976) 393.

[73] A. E. Gonzalez, *Phys. Rev. E* 47 (1993) 2923.

[74] A. DiBiasio, G. Bolle, C. Cammetti, P. Codestefano, F. Sciortino and P. Tartaglia, *Phys. Rev. E* 50 (1994) 1649.

[75] M. P. Allen and D. J. Tildesley, *Computer simulation of Liquids* Oxford University Press, 1990.

[76] P. Meakin, Z. Chen and J. M. Deutch, *J. Chem. Phys.* 82 (1987) 3786.

[77] D. Stauffer, *Introduction to Percolation Theory*, Taylor and Francis, 1994.

[78] P. Meakin, *J. Chem. Phys.* 81 (1987) 4637.

[79] O. P. Behrend, PhD. Thesis. University of Edinburgh, 1995 (unpublished).

[80] W. H. Press, S. A. Teukolsky, W. T. Vetterling and B. P. Flannery, *Numerical Recipes*, Chapter 12. Cambridge University Press, 1993.

[81] T. Sintes, R. Toral and A. Chakrabarti, *Phys. Rev. E.* 50 (1994) R3330.

[82] P. Meakin, in *Phase Transitions and Critical Phenomena*, vol. 12, pp 430-489. Eds. C. Domb and J. L. Lebowitz. Academic Press, 1983.

[83] P. Meakin, *Physica Scripta* 46 (1992) 295.

[84] P. Meakin, *Phys. Rev. A* 27 (1983) 1495.

[85] T. Vicsek and F. Family, *Phys. Rev. Lett.* 52 (1984) 1669.

[86] P. Meakin, T. Vicsek and F. Family, *Phys. Rev. B* 31 (1985) 564.

[87] J. Stankiewicz, M. A. Cabrerizo Vilchez and R. Hidalgo Alvarez, *Phys. Rev. E* 47 (1993) 2663.

[88] M. von Smoluchowski, *Z. Phys. Chem.* 92 (1917) 129; S. Chandrasekhar, *Rev. Mod. Phys.* 15 (1943) 59.

[89] R. M. Ziff, E. M. Hendriks and M. H. Ernst, *Phys. Rev. Lett.* 49 (1982) 593.

[90] R. Botet and R. Jullien, *J. Phys. A: Math. Gen.* 17 (1984) 2517.

[91] M. Thorn and M. Seesselberg, *Phys. Rev. Lett.* 72 (1994) 3622.

[92] B. Cabane, in *Neutron, X-Ray and Light Scattering*, eds P. Lindner and Th. Zemb. North Holland, 1991.

[93] F. Family, P. Meakin and J. Deutch, *Phys. Rev. Lett.* 57 (1986) 727; C. Sorenson, H. Zhang and T. Taylor, *Phys. Rev. Lett.* 59 (1987) 363.

[94] P. Meakin and M. H. Ernst, *Phys. Rev. Lett.* 60 (1988) 2503.

[95] T. Sintes, R. Toral and A. Chakrabarti, *Phys. Rev. A* 46 (1992) 2039.

[96] M. Kolb and R. Jullien, *J. Physique Lett.* 45 (1984) L977.

[97] C. Aubert and D. S. Cannell, *Phys. Rev. Lett.* 56 (1986) 738.

[98] J. C. Earnshaw and D. J. Robinson, *Phys. Rev. Lett.* 72 (1994) 3682.

[99] J. C. Earnshaw and D. J. Robinson, *Physica A* 214 (1995) 23.

[100] J.-M. Debierre and L. Turban, *J. Phys. A: Math. Gen.* 19 (1986) L131; *J. Phys. A: Math. Gen.* 20 (1987) L239.

[101] G. C. Ansell and E. Dickinson, *Phys. Rev. A* 35 (1987) 2349.

[102] G. C. Ansell and E. Dickinson, *Faraday Disc. Chem. Soc.* 83 (1987) 167.

[103] E. Dickinson, *J. Chem. Soc. Fara. Trans.* 90 (1994) 173.

[104] R. F. Voss, *J. Stat. Phys.* 36 (1984) 861.

[105] P. Meakin and M. Muthukumar, *J. Chem. Phys.* 91 (1989) 3212.

[106] R. Botet and R. Jullien, *J. Phys. A: Math. Gen.* 19 (1986) L907.

[107] W. Y. Shih, J. Liu, W. H. Shih and I. A. Aksay, *J. Stat. Phys.* 62 (1991) 961; W. Y. Shih, I. A. Aksay and R. Kikuchi, *Phys. Rev. A* 36 (1987) 5015.

[108] E. Dickinson, C. Elvingson and S. R. Euston, *J. Chem. Soc. Fara. Trans. 2* 85 (1989) 891.

[109] E. S. Sorensen, H. C Fogedby and O. G. Mouritsen, *Phys. Rev. A* 39 (1989) 2194.

[110] M. C. Bujan-Nunez and E. Dickinson, *Mol. Phys.* 80 (1993) 431.

[111] P. Meakin and R. Jullien, *J. Physique* 46 (1985) 1543.

[112] M. Kolb, *J. Phys. A: Math. Gen.* 19 (1986) L263.

[113] P. Meakin, *J. Chem. Phys.* 83 (1985) 3645.

[114] A. Hasmy, M. Foret, J. Pelous and R. Jullien, *Phys. Rev. B* 48 (1993) 9345.

[115] M. D. Haw, W. C. K. Poon and P. N. Pusey, *Physica A* 208 (1994) 8.

[116] A. Hasmy, E. Anglaret, M. Foret, J. Pelous and R. Jullien, *Phys. Rev. B.* 50 (1994) 6006.

[117] M. D. Haw, M. Sievwright, W. C. K. Poon and P. N. Pusey, *Physica A* 217 (1995) 231.

[118] H. F. van Garderen, W. H. Dokter, T. P. M. Beelen, R. A. van Santen, E. Pantos, M. A. J. Michels and P. A. J. Hilbers, *J. Chem. Phys.* 102 (1995) 480.

[119] M. D. Haw, M. Sievwright, W. C. K. Poon and P. N. Pusey, *Adv. Coll. Int. Sci.* 62 (1995) 1.

[120] M. Kolb and H. J. Herrmann, *J. Phys. A: Math Gen* 18 (1985) L435.

[121] M. Kolb and H. J. Herrmann, *Phys. Rev. Lett.* 59 (1987) 454.

[122] H. J. Herrmann and M. Kolb, *J. Phys. A: Math Gen* 19 (1986) L1027.

[123] J. C. Gimel, D. Durand and T. Nicolai, preprint.

[124] Y. Kantor and T. A. Witten, *J. Physique Lett.* 45 (1984) 675.

[125] R. Wessel and R. C. Ball, *Phys. Rev. A* 46 (1992) R3008.

[126] F. F. Abraham, S. W. Koch and R. C. Desai, *Phys. Rev. Lett.* 49 (1982) 923

[127] M. Schobinger, S. W. Koch and F. F. Abraham, *J. Stat. Phys.* 42 (1986) 1071.

[128] A. Vrij, *J. Chem. Phys.* 69 (1978) 1742; A. Vrij, *J. Chem. Phys.* 71 (1979) 3267.

[129] P. van Buerten and A. Vrij, *J. Chem. Phys* 74 (1981), 2744.

[130] D. Frenkel, R. J. Vos, C. G. de Kruif and A. Vrij, *J. Chem. Phys* 84 (1986) 4625.

[131] W. L. Griffith, R. Triolo and A. L. Compere, *Phys. Rev. A* 35 (1987) 2200.

[132] M. Kotlarchyk and S.-H. Chen, *J. Chem. Phys.* 79 (1983) 2461.

[133] J. B. Hayter and J. Penfold, *Colloid Polym. Sci.* 261 (1983) 1022.

[134] M. Kallala, C. Sanchez and B. Cabane, *Phys. Rev. Lett.* 48 (1993) 3692.

[135] M. E. Fisher and R. J. Burford, *Phys. Rev.* 156 (1967) 583.

[136] A. Barbero, unpublished.

[137] M. S. Ripoll and C. F. Tejero, *Mol. Phys.* 85 (1995) 423.

[138] J. C. Earnshaw, personal communication.

[139] B. D'Aguanno and R. Klein, *J. Chem. Soc. Fara. Trans.* 87 (1991) 379.

[140] N. C. Wong and C. M. Knobler, *Phys. Rev. A* 24 (1981) 3205; Y. C. Chou and W. I. Goldburg, *Phys. Rev. A* 20 (1979) 2105.

[141] W. I. Goldburg, in *Light Scattering near Phase Transitions*, eds. H. Z. Cummins and A. P. Levanyuk. North Holland, 1983.

[142] See Ref. [55], p. 331.

[143] I. M. Lifshitz and V. V. Slyozov, *J. Phys. Chem. Solids* 19 (1961) 35.

[144] K. Binder and D. Stauffer, *Phys. Rev. Lett.* 33 (1974) 1006.

[145] W. H. Press, S. A. Teukolsky, W. T. Vetterling and B. P. Flannery, *Numerical Recipes*, Chapter 15. Cambridge University Press, 1993.

[146] H. L. Snyder and P.Meakin, *J. Chem. Phys.* 79 (1983) 5588.

[147] T. Sintes, personal communication.

[148] S. C. Glotzer, M. F. Gyure, F. Sciortino, A. Coniglio and H. E. Stanley, *Phys. Rev. E* 49 (1994) 247.

[149] F. Sciortino, R. Bansil, H. E. Stanley and P. Alstrom, *Phys. Rev. E* 47 (1993) 4615.

[150] M. R. Mruzik, F. F. Abraham and G. M. Pound, *J. Chem. Phys.* 69 (1978) 3462.

[151] H. Furukawa, *Adv. Phys.* 34 (1985) 703.

[152] R. C. Desai and A. R. Denton, in *On Growth and Form*, eds. H. E. Stanley and N. Ostrowski. Nijhoff, 1986; W. Klein, *Phys. Rev. Lett.* 65 (1990) 1462; E. K. Hobbie, B. J. Bauer and C. C. Han, *Phys. Rev. Lett.* 72 (1994) 1830.

[153] B. J. Berne and R. Pecora, *Dynamic Light Scattering*, p. 165. Wiley, 1976.

[154] J. C. Earnshaw and D. J. Robinson, in *Proceedings of the 1st meeting on Scaling concepts and complex fluids* (Copanello, Italy, July 1994), ed. F. Mallamace, 1995.

[155] J. Liu, W. Y. Shih, M. Sarikaya and I. A. Aksay, *Phys. Rev. A* 41 (1990) 3206.

[156] J. M. Yeomans, *Statistical Mechanics of Phase Transitions*, Oxford University Press 1992.

[157] S. Hayward, D. W. Heermann and K. Binder, *J. Stat. Phys.* 49 (1987) 1053.

[158] G. Lironis, D. W. Heermann and K. Binder, *J. Phys. A: Math. Gen.* 23 (1990) L329.

[159] L. G. B. Bremer, B. H. Bijsterbosch, P. Walstra and T. van Vliet, *Adv. Coll. Int. Sci.* 46 (1993) 117.

[160] J. G. Amar, F. E. Sullivan and R. D. Mountain, *Phys. Rev. B* 37 (1988) 196.

[161] O. T. Valls and J. E. Farrell, *Phys. Rev. E* 47 (1993) R37.

[162] T. M. Rogers and R. C. Desai, *Phys. Rev. B* 39 (1989) 11956; N. Akaiwa and P. W. Voorhees, *Phys. Rev. E* 49 (1994) 3860; R. Yamamoto and K. Nakanishi, *Phys. Rev. B* 51 (1995) 2715.

[163] R. J. Baxter, *J. Chem. Phys.* 49 (1968) 2770.

[164] W. G. T. Kranendonk and D. Frenkel, *Mol. Phys.* 64 (1988) 403.

[165] I. Webman and Y. Kantor, in *Kinetics of Aggregation and Gelation*, eds. F. Family and D. P. Landau. Elsevier, 1984.

[166] C. Camoin and R. Blanc, *J. Physique Lett.* 46 (1985) 67.

[167] G. C. Ansell and E. Dickinson, *J. Coll. Int. Sci.* 110 (1986) 73.

[168] A. A. Potanin, *J. Coll. Int. Sci.* 157 (1993) 399.

[169] C. Allain and M. Cloitre, *Adv. Coll. Int. Sci.* 46 (1993) 129.

[170] M. Kolb, *Phys. Rev. Lett.* 53 (1984) 1653.

[171] W. G. Griffin and M. C. A. Griffin, *J. Chem. Soc. Fara. Trans.* 89 (1993) 2879.

[172] S. Schwarzer, S. Havlin and H. E. Stanley, *Phys. Rev. E* 49 (1994) 1182.

[173] P. Meakin and Z. B. Djordjevic, *J. Phys. A: Math. Gen.* 19 (1986) 2137.

[174] E. Dickinson, *J. Chem. Soc. Fara. Trans.* 91 (1995) 51.

[175] T. Koga and K. Kawasaki, *Phys. Rev. A* 44 (1991) R817; S. Puri and B. Dunweg, *Phys. Rev. A* 45 (1992) R6977.

[176] P. W. Zhu and D. H. Napper, *Phys. Rev. E* 50 (1994) 1360.

[177] K. Kang and S. Redner, *Phys. Rev. A* 30 (1984) 2833.

[178] P. C. Hohenberg and B. I. Halperin, *Rev. Mod. Phys.* 49 (1977) 435.

[179] D. Stauffer, *Phys. Rep.* 54 (1979) 1.

[180] P. Dimon, S. K. Sinha, D. A. Weitz, C. R. Safinya, G. S. Smith, W. A. Varady and H. M Lindsay, *Phys. Rev. Lett.* 57 (1986) 595.

List of Publications

Aggregation dynamics in a model colloid-polymer mixture

W. C. K. Poon, A. D. Pirie, M. D. Haw and P. N. Pusey, *Analytical Proceedings* 30 (1993) 493.

Structure factors from cluster-cluster aggregation simulation at high concentration

M. D. Haw, W. C. K. Poon and P. N. Pusey, *Physica A* 208 (1994) 8.

Structure and characteristic length scales in cluster-cluster aggregation simulation

M. D. Haw, M. Sievwright, W. C. K. Poon and P. N. Pusey, *Physica A* 217 (1995) 231.

Cluster-cluster gelation with finite bond energy

M. D. Haw, M. Sievwright, W. C. K. Poon and P. N. Pusey, *Adv. Coll. Int. Sci.* 62 (1995) 1.